2018

Functional Magnetic Interface Phenomena in Nano-Architectures

Grace L. Causer
University of Wollongong

Functional Magnetic Interface Phenomena in Nano-Architectures

GRACE L. CAUSER

BSc Advanced (Physics) Honours - Class 1

A dissertation submitted in fulfilment of
the requirements for the award of the degree of

Doctor of Philosophy

UNIVERSITY OF
WOLLONGONG

Institute for Superconducting and Electronic Materials
and
School of Physics

2018

CERTIFICATION

I, Grace L. Causer, declare that this thesis, submitted in fulfilment of the requirements for the award of Doctor of Philosophy, in the School of Physics, Faculty of Engineering and Information Sciences, University of Wollongong, is wholly my own work unless otherwise referenced or acknowledged. The document has not been submitted for qualifications at any other academic institution.

Grace L. Causer
August 2018

To my Family.

Contents

List of Tables . . . iii
List of Figures . . . x

Abstract . . . xi
Acknowledgements . . . xii
Statement of Contribution . . . xiv
Publications and Conferences . . . xv

1 Introduction **2**
1.1 The Fundamental Sharpness of Magnetic Interfaces Formed by Chemical Disorder Using a He^+ Beam . . . 3
1.2 Hydrogen-Driven Switching of the Magnetic Surface Anisotropy at the Co/Pd Interface . . . 7
1.3 Thesis Overview . . . 10

2 Experimental Techniques **13**
2.1 X-ray Diffraction . . . 15
2.2 Reflectometry . . . 18
2.3 Polarised Neutron Reflectometry . . . 20
2.4 X-ray and Neutron Data: Measurement and Fitting . . . 23

3 The Fundamental Sharpness of Magnetic Interfaces Formed by Chemical Disorder Using a He^+ Beam **27**
3.1 Motivation . . . 28
3.1.1 Introduction to $FePt_3$ . . . 31
3.2 Sample Growth and Characterisation . . . 33
3.3 Ion-Beam Theory and Monte Carlo Simulation . . . 42
3.4 Sample Irradiation and Characterisation . . . 48
3.4.1 Magnetometry . . . 49
3.4.2 Transmission Electron Microscopy . . . 52
3.4.3 Polarised Neutron Reflectometry . . . 60
3.5 Density Functional Theory . . . 69
3.6 Sample Annealing and Characterisation . . . 77

3.6.1 Introduction to Exchange Bias . . . 78
3.6.2 Magnetometry . . . 81
3.6.3 Transmission Electron Microscopy . . . 84
3.6.4 Polarised Neutron Reflectometry . . . 86
3.7 Conclusion . . . 91

4 Hydrogen-Driven Switching of the Magnetic Surface Anisotropy at the Co/Pd Interface 94
4.1 Motivation . . . 95
4.1.1 Magnetic Anisotropy . . . 98
4.1.2 Magnetic Proximity Effect . . . 100
4.1.3 Ferromagnetic Resonance . . . 100
4.1.4 Pd-Hydride Phase Diagram: Bulk and Thin Film . . . 103
4.1.5 Neutrons and Hydrogen . . . 107
4.2 Commissioning of Sample Environment . . . 108
4.2.1 PNR with *in situ* FMR Chamber . . . 110
4.2.2 Methodology . . . 115
4.2.3 Feasibility Study . . . 117
4.3 Sample Growth and Characterisation . . . 124
4.3.1 *Ex situ* Characterisation . . . 125
4.3.2 PNR with *in situ* FMR Characterisation . . . 130
4.4 Conclusion . . . 148

5 Summary and Outlook 151

A Units of Measurement 157

Bibliography 194

List of Tables

3.1 Experimental parameters of the peak positions (2θ), FWHMs and the integrated X-ray diffraction intensities (I_β) of the four ($00l$)-type $FePt_3$ Bragg reflections displayed in Figure 3.3. 37

3.2 Parameters used in the calculation of the theoretical integrated intensities (I_α) for an $FePt_3$ specimen with perfect chemical order (i.e., of $S = 1$). 41

3.3 Nominal rates of energy loss occurring via electronic and nuclear processes for energetic ($0.01 - 30$ keV) He^+ ions incident upon a bulk density $FePt_3$ target, and the resulting R_z and δ characteristics. All values are calculated using SRIM. 46

3.4 Parameters of the nuclear model obtained from best fits to the PNR data of the as-prepared $FePt_3$ film at 300 K. 63

4.1 Comparison of the X-ray and neutron scattering lengths of hydrogen and palladium. 107

4.2 Parameters used in the calculation of the average C_H absorbed by the Pd layer of each Co/Pd bilayer in a 3.5% H_2/N_2 atmosphere. Parameters were obtained from best fits to the PNR data sets of each bilayer between the N_2 (subscript: Pd) and the 3.5% H_2/N_2 (subscript: Pd+H) atmospheres of the first cyclic exposure. 139

A.1 List of magnetic quantities and the corresponding SI and CGS units. To obtain the values of the quantities in CGS units, the corresponding SI unit should be multiplied by the conversion factor. 157

List of Figures

2.1 Scattering measurements in the $\omega/2\theta$ Bragg-Brentano geometry. An incident beam of wavevector $\mathbf{k}_i$ is scattered by a sample resulting in an outgoing beam of wavevector $\mathbf{k}_f$. $\mathbf{k}_f$ scatters at an angle 2θ relative to $\mathbf{k}_i$, which is incident at an angle ω to the sample surface. 15

2.2 Reciprocal-space lattice showing the Bragg condition for diffraction where the wavevector transfer $\mathbf{Q}_z$ must equal some reciprocal-space lattice vector $\mathbf{G}$ in order for diffraction to occur. 17

2.3 The typical naming convention employed in the neutron reflection process. The neutron spin $\mathbf{S}$ lies in the plane of the film, and either parallel $(+)$ or anti-parallel $(-)$ to the external magnetic field $\mathbf{H}$. The in-plane magnetisation $\mathbf{M}$ of the film, which can take any arbitrary angle α with respect to $\mathbf{H}$, is assigned the vector components M_x and M_y. 21

2.4 The PLATYPUS time-of-flight polarised neutron reflectometer located at ACNS, ANSTO [122]. 24

3.1 Atomic arrangements of $FePt_3$ in the (a) chemically ordered and the (b) chemically disordered states, showing low-temperature magnetic ordering. Formally, the crystallographic symmetry of $FePt_3$ transforms from simple-cubic with bi-atomic basis atoms to face-centred-cubic between the chemically ordered and the chemically disordered states, respectively. 32

3.2 XRD spectrum of the as-prepared $FePt_3$ film and a clean MgO substrate (shown for comparison). The presence of $(00l)$-type $FePt_3$ reflections reveals the preferred epitaxial growth direction of the film along the [001] crystallographic axis 35

3.3 Enlarged views of the (001), (002), (003), (004) $FePt_3$ reflections. Each data set has been fitting with a Voigt function. The low-2θ shoulders of the (002) and the (004) $FePt_3$ reflections most likely originate from the thin epitaxial Pt seed and capping layers of the film. 36

3.4 ω-rocking curves of the (002) film and substrate reflections used in determining the absolute divergence of the $FePt_3$ crystallite orientations from the epitaxial axis. 38

3.5 The ion-target interaction volume generated by the intrinsic straggling behavior of a point irradiation incident upon a sample surface. The ion comes to rest at the end of the path range R_p at a projected distance equal to $R_z + \delta$ beneath the target surface. 42
3.6 DPA profiles obtained using Equation 3.16 for 15 keV He^+ ions with fluences of 2 $\times 10^{16}$ ions cm^{-2} and 2 $\times 10^{17}$ ions cm^{-2} incident upon a bulk density amorphous $FePt_3$ target. 47
3.7 *m-H* behaviours of the (a) as-prepared and the (b) irradiated $FePt_3$ films measured at 10 K and 300 K. 50
3.8 (a) Cross-sectional TEM image of the as-prepared film, showing the 280 nm $FePt_3$ film thickness. DF-TEM morphologies of the (b) as-prepared film and the (c) irradiated (2 $\times 10^{16}$ He^+ ions cm^{-2}) $FePt_3$ film. The red boarders are guides for the eye to separate domains of high chemical order (bright-contrast level) and high chemical disorder (dark-contrast level). (d) Low-magnification DF-TEM image of the irradiated (2 $\times 10^{16}$ He^+ ions cm^{-2}) $FePt_3$ film. (e) DF-TEM morphology and (f) low-magnification DF-TEM image of the irradiated-reference (2 $\times 10^{17}$ He^+ ions cm^{-2}) $FePt_3$ film. The location of the film surface and the 120 nm-thick ion-induced chemically disordered layer are shown. 53
3.9 Schematic of the expected change in position among the $L1_2$ chemically ordered lattice atoms of $FePt_3$ during low-energy He^+ irradiation, showing the formation of ion-induced chemically disordered $FePt_3$ domains. The simulated [103] zone axis diffraction patterns for the fully chemically ordered and fully-chemically disordered arrangements of $FePt_3$ show the presence and absence of {010} diffraction peaks, respectively. 55
3.10 SAED patterns of the (a) as-prepared, (b) irradiated (2 $\times 10^{16}$ He^+ ions cm^{-2}) and (c) irradiated-reference (2 $\times 10^{17}$ He^+ ions cm^{-2}) $FePt_3$ films, with corresponding normalised intensity profiles through the {000}, {0-10} and {0-20} reflections. Using the relative intensity ratio between the {0-10} and {0-20} reflections, the chemical-order parameter S of each film can be determined. 56
3.11 (a) Filtered HR-TEM image measured within the irradiated volume of the 2 $\times 10^{16}$ He^+ ions cm^{-2} irradiated $FePt_3$ film in the [110] zone axis. Corresponding SAED pattern displays single crystalline diffraction peaks. (b) Filtered HR-TEM image measured within the irradiated volume of the 2 $\times 10^{17}$ He^+ ions cm^{-2} irradiated-reference $FePt_3$ film in the [110] zone axis. (c) High-magnification image of the marked area in (b) with FFT areas. (d) Chemically disordered domains are modelled as precipitates of the chemically ordered phase, and (e) simulated HR-TEM image map. 58

3.12 PNR data (open symbols) and best fits (solid curves) to the R^+ and R^- channels of the (a) as-grown and the (c) irradiated $FePt_3$ films, each measured at 300 K and 5 K. For clarity, the 5 K PNR data sets and best fits are shifted on the ordinate. Corresponding nuclear and magnetic SLD profiles obtained from best fits to the PNR data of the (b) as-grown and (d) irradiated $FePt_3$ films. 62
3.13 DPA profiles calculated for 15 keV He^+ ions at a fluence of 2 $\times 10^{16}$ ions cm^{-2} incident upon: a bulk density $FePt_3$ target (grey DPA profile), and a 95% bulk density $FePt_3$ target (yellow DPA profile). The DPA profiles are plotted on a logarithmic scale for clarity. The magnetic depth-profile of the irradiated $FePt_3$ film (obtained from best fits to the 300 K PNR data) is plotted for comparison. 66
3.14 Magnetic interface roughness R models of the FM/non-FM boundary. (a) 5 K PNR data (open symbols) and selected fits (solid curves) corresponding to $R = 0$, 2, 3, 4, 5 and 10 nm. (b) Corresponding nuclear and magnetic SLD profiles and (c) a magnified view of the sharp transition-width of the R models at the FM/non-FM boundary. 68
3.15 Stability plot of the thickness of the non-FM layer relative to the roughness R of the FM/non-FM interface. The thickness of the non-FM layer was constrained to 97.4 nm throughout the fitting procedure. A unique and stable solution is identified by the minimum corresponding to a FM/non-FM interface roughness R of $2.5 - 3$ nm. 69
3.16 The four, potential long-range magnetically ordered configurations of the chemically ordered $FePt_3$ supercell. The relative internal energies Δ are given for (a) (½ ½ ½) g-type AFM, (b) FM, (c) (½ 0 0) a-type AFM and (d) (½ ½ 0) c-type AFM structures in order of descending energy. (Top) The simplified structure shows only the Fe spins corresponding to the different propagation vectors used in the calculations. (Bottom) A detailed representation of the corresponding spin-density isosurfaces indicates patches of small quadrupolar and induced moments surrounding the Pt sites, together with a much larger component localised on the Fe sites. The isosurface is drawn at a value of 5% of the maximum difference density. 72

3.17 The lowest energy states of (½ ½ 0) c-type $FePt_3$ under variable degrees of anti-site disorder (Fe ↔ Pt) were calculated to model the effect of ion-irradiation upon the magnetic state of $FePt_3$. (Left) Without anti-site disorder, the (½ ½ 0) c-type AFM solution is strongly preferred over the FM state. (Centre, Top) By interchanging a neighbouring Fe and Pt site, the global magnetic energy is dramatically modified, and the AFM state is only weakly preferred. (Centre, Bottom) A second symmetrically unique configuration for a single anti-site defect can be created if a Fe atom effectively jumps two Pt sites; however, the energy is essentially comparable to the (Centre, Top) configuration. (Right) By creating two anti-site defects, the system can be driven towards an energetically favourable FM state. 74
3.18 (a) DPA surface plot calculated for a beam of 15 keV He^+ ions incident upon the surface of a $FePt_3$ target. The ion-beam is centred at the origin of the abscissa. The plane through the surface plot at 0.125 DPA identifies the critical disorder level, at and above which, the DFT result indicates that ferromagnetism can be induced in $FePt_3$ by anti-site disorder. (b) A two-dimensional top-down projection of the surface plot in Figure 3.18(a). The area enclosed by the purple contour encompasses the FM element. Note: The colour grading in Figure 3.18(b) is scaled to 0.125 DPA. 76
3.19 Structure of the (a) as-prepared ≈ 280 nm-thick chemically ordered $FePt_3$ film and the (b) irradiation process resulting in a ≈ 180 nm-thick chemically disordered (near-surface irradiated) / ≈ 100 nm-thick chemically ordered (un-irradiated) $FePt_3$ bilayer. The chemically ordered and the chemically disordered unit cells of $FePt_3$ are shown which exhibit AFM and FM character, respectively. 78
3.20 (a) 5 K *m-H* data of the $FePt_3$ FM/AFM bilayer before and after annealing at several temperature stages between 800 K and 1000 K. Insets show the magnified low-field (top, left) and high-field (bottom, right) regions of the hysteresis loops. (b) Annealing-temperature dependence on the exchange bias field (H_{EB}) and the magnetic coercivity (H_C) of the $FePt_3$ FM/AFM bilayer. The solid curves are guides for the eye. . . 82
3.21 SAED images recorded within the nominally FM layers of the (a) 840 K and the (b) 1000 K annealed $FePt_3$ FM/AFM bilayers. DF-TEM images formed with an {001} diffracted beam for the cross-sections of the (c) 840 K and (d) 1000 K annealed $FePt_3$ bilayers. Arrowheads indicate the expected low-temperature magnetic ordering of each specified domain. . 85

3.22 PNR data (closed symbols) and best fits (solid and broken curves) to the R^+ and R^- channels of the 840 K annealed $FePt_3$ FM/AFM bilayer, measured at (a) 300 K and (b) 5 K in 10 kOe. The spin-asymmetry of the annealed $FePt_3$ FM/AFM bilayer is plotted below the corresponding PNR data set. For comparison the spin-asymmetry of the $FePt_3$ FM/AFM bilayer prior to any annealing treatment is also plotted. . . . 87
3.23 (a) The nuclear SLD profiles of the $FePt_3$ FM/AFM bilayer before and after annealing at 840 K. (b) The temperature-dependent magnetic SLD profiles of the $FePt_3$ FM/AFM bilayer before annealing (reproduced from Figure 3.12). (c) The temperature-dependent magnetic SLD profiles of the $FePt_3$ FM/AFM bilayer after annealing at 840 K, showing a roughened magnetic interface at the non-irradiated/irradiated boundary. A re-crystallisation of the chemically ordered $FePt_3$ phase propagates from the centre of the irradiation layer which effectively increases the number of magnetic interfaces potentially exchange biased within the film. 88

4.1 Schematic of the typical geometry employed in the measurement of the FMR of a FM film. An AC magnetic field $\mathbf{H}_{ac}$ is used to perturb the equilibrium (static) direction of $\mathbf{M}$, placing it into gyroscopic motion about $\mathbf{H}_{eff}$. The resonance condition is met when the frequency of $\mathbf{H}_{ac}$ coincides with the precessional eigenfrequency of $\mathbf{M}$. 101
4.2 Pd-H phase diagrams. (a) The pressure-concentration isotherms of bulk Pd (available from [155] under Creative Commons from Johnson Matthey Plc). At room temperature the α'-phase boundary is located at $PdH_{0.6}$ (or $PdH_{0.57}$ at 30 °C). (b) The room-temperature pressure-concentration isotherms of nanoscale Pd (reprinted from [83] with permission from Elsevier). As the Pd thickness decreases the maximum hydrogen solubility reduces. 104
4.3 Schematic of the chemical potential across the Co/Pd-hydride/Co interface. (a) Isolated lattices of Co and Pd have low and high hydrogen solubilities, respectively. (b) Upon nanostructuring, the chemical potential of interfacial Pd increases which reduces the density of energetically favourable hydrogen absorption sites (denoted in red). 105
4.4 Comparison of the (a) isotropic three-dimensional expansion of bulk crystalline Pd lattices after hydrogen absorption, and the (b) anisotropic one-dimensional expansion of thin-film crystalline Pd lattices after hydrogen absorption. 106
4.5 Cross-sectional schematic and beamline geometry of the PNR with *in situ* FMR sample chamber. 111
4.6 External circuitry required to facilitate PNR with *in situ* FMR measurements. The sample chamber described in Figure 4.5 (denoted in yellow) is placed between the poles of an electromagnet (denoted in grey). 112

4.7 Field-resolved FMR spectra of the CNP alloy film recorded (a) before hydrogenation in the presence of nitrogen gas (solid green line), (b) in the hydrogenated state after 1.5 hours of hydrogen gas flow (solid blue line) and (c) in the hydrogenated state, after 12 hours of hydrogen gas flow (dotted blue line). All data sets were measured at a microwave frequency of 8 GHz. 119
4.8 (a) Time-resolved FMR spectrum of the CNP alloy film during the initial stages of hydrogen-gas absorption. (b) Consecutive R^+ PNR patterns measured in parallel with the data of pane (a). 120
4.9 (a) R^+ and (b) R^- PNR patterns obtained for the CNP alloy film before hydrogenation (red data points and fits) and in the hydrogenated state (blue data points and fits). For clarity, the R^- data sets have been offset by an order of magnitude on the ordinate axis. Error bars lie within the data set symbols. (Inset) The nuclear and magnetic SLD profiles extracted from fitting the PNR data before hydrogenation (red) and in the hydrogenated state (blue). 122
4.10 XRR data (closed symbols) and best fits (solid curves) to the (a) Co/Pd(3 nm), (b) Co/Pd(5 nm), (c) Co/Pd(10 nm) and (d) Co/Pd(15 nm) bilayers. The X-ray SLD profiles obtained from best fits to the XRR data are correspondingly shown in the inset of each figure. Measurements were recorded in air at room temperature. 126
4.11 High-angle XRD spectrum of the Co/Pd(15 nm) bilayer measured in air at room temperature, showing evidence of the Pd(111) and the Pd(113) Bragg reflections. 127
4.12 (a) Filtered HR-TEM image of the Co/Pd(10 nm) bilayer measured in the [110] zone axis. High-magnification images of the (b) Co layer and the (c) Pd layer taken from the marked areas in (a). FFT of the high-magnification images of the (d) Co layer and the (e) Pd layer which display diffraction patterns consistent with face-centred-cubic Co and Pd, respectively. 128
4.13 The (a) in-plane and the (b) out-of-plane M-H behaviours of the Co/Pd(10 nm) bilayer measured at 300 K. The M-H behaviours shown are representative of all Co/Pd bilayers. 129
4.14 PNR data sets of the Co/Pd(15 nm) bilayer during the first and second cyclic exposures to a 3.5% H_2/N_2 atmosphere. The H_2/N_2 data sets are shifted on the ordinate axis for clarity. 132
4.15 FMR spectra of the Co/Pd(15 nm) bilayer during the first and second cyclic exposures to a 3.5% H_2/N_2 atmosphere. All data sets were acquired at a microwave frequency of 4.4 GHz. 133

4.16 PNR data (open symbols) and best fits (solid curves) to the R^+ and R^- cross-sections of the Co/Pd(10 nm) bilayer (a) before hydrogenation (measured in N_2), (b) after hydrogenation (measured in 3.5% H_2/N_2), and (c) after dehydrogenation (measured in N_2). Data sets (b) and (c) are shifted on the ordinate axis for clarity. 135
4.17 Nuclear and magnetic SLD profiles of the Co/Pd(10 nm) bilayer (a) before hydrogenation (measured in N_2), (b) after hydrogenation (measured in 3.5% H_2/N_2) and (c) after dehydrogenation (measured in N_2). Modelled SLDs are obtained from best fits to the PNR data and are plotted as a function of sample depth from the SiO_2-terminated Si substrate. Solid and dashed lines denote the SLD arising from nuclear and magnetic components of the bilayer, respectively. 136
4.18 Time-resolved FMR spectra of the Co/Pd(10 nm) bilayer during the initial stages of (a) hydrogen-gas absorption and (b) hydrogen-gas desorption. 137
4.19 (a) XRR data (closed symbols) and best fits (solid curves) to the Co/Pd(10 nm) bilayer before hydrogenation and after dehydrogenation. (b) Corresponding X-ray SLD profiles obtained from best fits to the XRR data in either state. Measurements were recorded in air at room temperature. 140
4.20 Evolution of the spin-asymmetry of the Co/Pd(10 nm) bilayer during primary hydrogen-gas absorption. Closed symbols denote data points, and solid lines denote magnetic models obtained from fitting the asymmetric influence of the samples' in-plane FM magnetisation on the R^+ and R^- scattering potentials. (b) The magnified critical-edge region of the spin-asymmetry, which is proportional to the total in-plane FM magnetisation of the interface. 142
4.21 Evolution of the spin-asymmetry of the (a) Co/Pd(3 nm), (b) Co/Pd(5 nm), and (c) Co/Pd(15 nm) bilayers during primary hydrogen-gas absorption. Closed symbols denote the data points, and solid lines denote the magnetic models obtained from fitting the asymmetric influence of each film's in-plane FM magnetisation on the R^+ and R^- scattering potentials. 143
4.22 Field-resolved FMR spectra of the Co/Pd(10 nm) bilayer during primary hydrogen absorption. All data sets were measured at a microwave frequency of 9.354 GHz. 145

Functional Magnetic Interface Phenomena in Nano-Architectures

Grace L. Causer

Abstract

The work embodied in this thesis aims to investigate the occurrence of magnetic interface phenomena in low-dimensional thin-film systems which have conceivable utility in future condensed-matter technologies. Namely, the magnetic interface quality of an $FePt_3$ nano-magnet formed via ion-induced chemical disorder will be critically analysed, in addition to a Co/Pd bilayer which features modifiable magnetic surface anisotropy upon exposure to hydrogen gas. The studies are enabled chiefly through advanced X-ray and neutron scattering techniques specifically chosen to probe interface structure as well as chemical and magnetic orders, and supplemented by traditional lab-based characterisation tools.

To begin, a much-anticipated experimental confirmation of the intrinsic sharpness of magnetic interfaces formed by locally driving magnetic phase transitions in materials using ion beams is presented. This is achieved through a unique experimental design whereby a room-temperature ferromagnetic nano-layer is encoded with depth-control onto a paramagnetic $FePt_3$ film by inducing chemical disorder using energy-specific He^+ ions. The magnetic transition is investigated through theoretical modelling, whereby the first density functional theory results for the entire suite of potential long-range magnetically ordered states of $FePt_3$ are presented. In doing so, the energetically favourable ground-state spin structure is identified. By analysing several localised defect structures which may form in $FePt_3$ under ion irradiation, the fundamental mechanism of the disorder-driven magnetic transition is revealed and shown to be caused by an intermixing of Fe and Pt atoms in anti-site defects above a threshold density.

In a second study, hydrogen-induced modifications to the layer-averaged static magnetisation and macroscopic magneto-dynamic behaviours of a Co/Pd heterostructure are investigated. The modifications are observed and examined in detail through simultaneously probing the magnetic anisotropy energy and studying the changing chemical and magnetic depth-profiles across the entire bilayer during primary hydrogen-gas absorption. It is revealed that the in-plane interfacial magnetisation of the Co/Pd bilayer irreversibly increases after primary hydrogen-gas absorption, indicating a weakening of the perpendicular magnetic anisotropy energy. To aid in conducting this analysis, an original experimental method is first developed which innovatively combines neutron scattering and microwave spectroscopy; equipment is then commissioned, and feasibility studies are performed.

Acknowledgements

- Prof. Xiaolin Wang of the Institute for Superconducting and Electronic Materials at the University of Wollongong for supervising this thesis.

- Prof. Frank Klose of the Guangdong Technion-Israel Institute of Technology (formerly of the Australian Nuclear Science and Technology Organisation, ANSTO) for going above and beyond the duties of a supervisor — for providing ample opportunities for me to learn, grow, and lead, as well as for introducing me to a sport I now love! Thank you.

- Prof. Gary Mankey of the Department of Physics and Astronomy at the University of Alabama for preparing high-quality samples which were imperative to the success of the project on $FePt_3$, as well as for valued contributions to the proof reading of manuscripts.

- Prof. Mikhail Kostylev, Dr. Chris Lueng and Mr. Thomas Schefer of the School of Physics at the University of Western Australia for continued partnership during the Co/Pd project — for preparing the samples, commissioning the sample environment, attending the neutron beamtimes and for the many helpful discussions about ferromagnetic resonance.

- Prof. Mihail Ionescu of the Centre for Accelerator Science at ANSTO for performing the ion irradiations on the $FePt_3$ samples, and for many insightful discussions on the topic.

- Dr. David Cortie of the Institute for Superconducting and Electronic Materials at the University of Wollongong for contributing to the theoretical description of the $FePt_3$ work, and for continued research guidance and many enlightening discussions over the years.

- Dr. Hanliang Zhu and Mr. Joel Davis of ANSTO for assistance with TEM measurements, and for many valuable discussions and contributions to the proof reading of manuscripts.

- Prof. Ko-Wei Lin of the Department of Materials Science and Engineering at the National Chung Hsing University for a steady supply of samples and the opportunity to work on many collaborative projects, as well as for being a valued team member during your 2015 sabbatical.

- The sample-environment team of the Australian Centre for Neutron Scattering (ACNS) at ANSTO for fantastic 24-hour technical support for when things didn't go to plan. Special thanks to Dr. Norman Booth, Dr. Paolo Imperia and Stan Lee for assistance during the commissioning of the sample chamber associated with the Co/Pd project.

- Dr. Robert Robertson (retired), Dr. Jamie Schulz and Prof. Garry McIntyre of ACNS at ANSTO for always having an open door, for providing desk space for me to work, and for the financial support to attend local and international conferences.

- All the instrument scientists, technical and administration staff, post-docs and students of ACNS at ANSTO for making me feel welcome and valued, and for helping me in many and varied ways. Special thanks to my colleagues of the magnetism group (past and present) for every advice, support and helping hand.

- The Australian National Fabrication Facility at the Centre for Microscopy, Characterisation and Analysis at the University of Western Australia for the facilities, scientific and technical assistance provided as part of the Co/Pd project.

- The team at the ANSTO Discovery Centre for the endless opportunities to talk to visiting school groups, parents and teachers about the fundamentals, importance and applications of neutron science. Special thanks to Robin Davis for championing me all these years. It was a real privilege and I am truly grateful.

- Dr. Herma Buttner (formerly of ANSTO) for her friendship, assistance and organisational support during my time as the ANSTO Young Researchers Club president.

- My high-school physics and chemistry teacher Dr. Tristan Burg for being the first to spark my interest in science, and ultimately being responsible for all of this. Thank you.

- The Australian Institute for Nuclear Science and Engineering and the Australian Government for continued financial support during my post-graduate studies, and the Royal Society of New South Wales for financial support during 2017.

- Most of all, I would like to thank my family for supporting me through this journey. I would not have achieved what I have without them.

Statement of Contribution

The projects outlined in this thesis have been supported by collaborations with several institutions and university groups across Australia and the United States of America. Each project was initiated by me as the principal investigator responsible of project management and output. Below I outline my personal contributions to each project, and the individual contributions made by others.

The $FePt_3$ project forms a collaboration between the University of Wollongong (UOW), the Australian Nuclear Science and Technology Organisation (ANSTO) and the University of Alabama (UA). Prof. G. J. Mankey (UA) prepared the $FePt_3$ films. Prof. M. Ionescu (ANSTO) performed the ion irradiations. Dr. H. Zhu and J. Davis (ANSTO) performed the transmission electron microscopy measurements. I worked jointly with Dr. D. L. Cortie (UOW) to design and perform the density functional theory calculations. I ran the Monte Carlo simulations, performed the X-ray diffraction, magnetometry and polarised neutron reflectometry measurements, and completed analysis of all the experimental data. I prepared the manuscripts published in *Appl. Surf. Sci.*, *J. Phys.: Condens. Matter* and *ACS Appl. Mater. Interfaces*.

The Co/Pd project constitutes a collaboration between the UOW, ANSTO, the University of California-Berkeley (UC) and the University of Western Australia (UWA). The group of Prof. M. Kostylev (UWA) modified one of their existing ferromagnetic resonance chambers such that measurements could be performed *in situ* with polarised neutron reflectometry. The alterations were conducted following technical guidance provided by myself in conjunction with the neutron reflectometry and sample-environment teams at ANSTO. The Kostylev Group also prepared the Co/Pd films and assisted during the polarised neutron reflectometry experiments. Prof. S. Salahuddin and Dr. C.-H. Lambert (UC) provided the feasibility samples. Dr. H. Zhu (ANSTO) performed the transmission electron microscopy measurements. I performed the X-ray reflectometry, X-ray diffraction, magnetometry and polarised neutron reflectometry measurements, and completed analysis of all the experimental data. I made an 80% contribution to the manuscript published in *J. Appl. Cryst.*, and contributed the Co/Pd section to the feature article published in *Metals*.

Publications and Conferences

Published articles included in this thesis

1. The microstructural evolution of chemical disorder and ferromagnetism in He^+ irradiated $FePt_3$ films
   G. L. Causer, H. Zhu, J. Davis, M. Ionescu, G. J. Mankey, X. L. Wang, F. Klose
   Appl. Surf. Sci. **459**, 672-677 (2018).

2. Tailoring exchange bias in ferro/antiferromagnetic $FePt_3$ bilayers created by He^+ beams
   G. L. Causer, H. Zhu, M. Ionescu, G. J. Mankey, X. L. Wang, F. Klose
   J. Phys.: Condens. Matter **30**, 315804 (2018).

3. Direct measurement of the intrinsic sharpness of magnetic interfaces formed by chemical disorder using a He^+ beam
   G. L. Causer, D. L. Cortie, H. Zhu, M. Ionescu, G. J. Mankey, X. L. Wang, F. Klose
   ACS Appl. Mater. Interfaces **10**, 16216-16224 (2018).

4. *In situ* ferromagnetic resonance capability on a polarised neutron reflectometry beamline
   M. Kostylev†, G. L. Causer†, C.-H. Lambert, T. Schefer, C. Weiss, S. J. Callori, S. Salahuddin, X. L. Wang, F. Klose
   J. Appl. Cryst. **51**, 9-16 (2018).

5. Hydrogen absorption in metal thin films and heterostructures investigated *in situ* with neutron and X-ray scattering
   S. J. Callori, C. Rehm, G. L. Causer, M. Kostylev, F. Klose
   Metals **6**, 125 (2016).

Forthcoming articles related to this thesis

6. Hydrogen-driven switching of the magnetic surface anisotropy at the Co/Pd interface
   G. L. Causer, M. Kostylev, D. L. Cortie, C. Lueng, S. J. Callori, X. L. Wang, F. Klose
   In preparation.

Additional articles published in the course of this thesis

7. Surface engineering with Ar^+/O_2^+ ion beam bombardment: Tuning the electronic and magnetic behaviour of $Ni_{80}Fe_{20}/La_{0.7}Sr_{0.3}MnO_3/SrTiO_3(001)$ junctions
   I. Bergenti, P. K. Manna, C.-H. Lin, P. Graziosi, X. Liu, G. L. Causer, F. Liscio, A. Ruotolo, V. A. Dediu, J. van Lierop, F. Klose, K.-W. Lin
   J. Appl. Phys. **124**, 183903 (2018).

8. Structural evolution of a Ni/NiO_x based supercapacitor in cyclic charging-discharging: A polarised neutron and X-ray reflectometry study
   Z. Li[†], X. Liu[†], G. L. Causer, K.-W. Lin, P. Pong, S. A. Holt, F. Klose, Y.-Y. Li
   Electrochim. Acta. **290**, 118-127 (2018).

9. Field dependence of the ferromagnetic/superconducting proximity effect in a YBCO/STO/LCMO multilayer
   O. H. C. Paull, A. V. Pan, G. L. Causer, S. A. Fedoseev, A. Jones, X. Liu, A. Rosenfeld, F. Klose
   Nanoscale **10**, 18995 (2018).

10. Modifying exchange bias in Mn/NiFe bilayers by *in situ* Ar^+ bombardment
    G. L. Causer, P. K. Manna, C.-C. Chiu, J. van Lierop, M. Ionescu, K.-W. Lin, F. Klose
    Nucl. Instr. Meth. Phys. Res. B **409**, 121-125 (2017).

11. Fe/FeO/Fe/FeV characterised by magnetometry and polarised neutron reflectometry
    S. J. Callori, K.-H. Chao, G. L. Causer, B. Nagy, L. F. Kiss, A. Sulyok, L. Bottyan, K.-W. Lin, F. Klose
    IEEE Magn. Lett. **8**, 4102205 (2017).

Forthcoming articles prepared in the course of this thesis

12. Controlling the magnetic reversal mechanism of exchange biased $Mn_xO_y/Ni_{80}Fe_{20}$ bilayers through O^+ implantation
    J. Zhang†, G. L. Causer†, X. Liu, M. Ionescu, S. Li, K.-W. Lin, F. Klose
    Under review at *J. Magn. Magn. Mater.*

13. Interfacial exchange bias and spin-glass in $CaMnO_3/La_{0.7}Ca_{0.3}MnO_3$ heterostructures
    A. Tseng†, J. Zhang†, G. L. Causer, F. Klose, S. Li, L. Qiao, A. Pham
    In preparation.

14. Enhanced interfacial magnetism in $SrRuO_3/BiFeO_3$ bilayers deposited on $SrTiO_3$ (111) and $SrTiO_3$(001) substrates
    J. Zhang†, X. Liu†, G. L. Causer, O. H. C. Paull, P.-H. Xiang, S. Li, F. Klose
    In preparation.

15. High-field neutron diffraction investigation of the meta-magnetic transition in $FeTiO_3$
    G. L. Causer, D. L. Cortie, A. J. Studer, R. O. Piltz, D. Cheng, X. L. Wang, J. Horvat, F. Klose
    In preparation.

† equal contributions

Conference Presentations

1. One PLATYPUS plus some ion beams equals SIRIUS disorder
   G. L. Causer, D. L. Cortie, H. Zhu, M. Ionescu, G. J. Mankey, X. L. Wang, F. Klose
   Talk presented at the ANSTO Young Researchers Mini-Conference, 2018, Sydney, Australia (Awarded 2nd Place Travel Scholarship)

2. Depth profiling magnetic interfaces formed intrinsically in $FePt_3$ by ion beams
   G. L. Causer, D. L. Cortie, H. Zhu, M. Ionescu, G. J. Mankey, X. L. Wang, F. Klose
   Talk presented at the American Physical Society March Meeting, 2018, Los Angeles, United States (Awarded a Forum on International Physics Distinguished Student Scholarship)

3. Uncovering hidden nanoscale worlds with neutrons
   G. L. Causer
   Invited talk presented at the Royal Society of New South Wales — Scholars Open Lecture, 2018, Sydney, Australia (Awarded a Royal Society of NSW Scholarship)

4. Depth control of ferromagnetism in thin films by ion irradiation
   G. L. Causer, D. L. Cortie, H. Zhu, M. Ionescu, G. J. Mankey, X. L. Wang, F. Klose
   Talk presented at the International Conference on Nanoscience and Nanotechnology, 2018, Wollongong, Australia

5. Direct measurement of the intrinsic sharpness of magnetic interfaces formed by ion beams
   G. L. Causer, D. L. Cortie, H. Zhu, M. Ionescu, G. J. Mankey, X. L. Wang, F. Klose
   Poster presented at the ANSTO User Meeting, 2017, Melbourne, Australia (Awarded 1st Place Poster Prize)

6. Crafting room temperature ferromagnetism by ion irradiation of ordered $FePt_3$: A PNR and DFT study
   G. L. Causer, D. L. Cortie, H. Zhu, M. Ionescu, G. J. Mankey, X. L. Wang, F. Klose
   Talk presented at the Gordon Research Seminar on Neutron Scattering, 2017, Kowloon, Hong Kong

7. Depth control of ferromagnetism in $FePt_3$ films by ion irradiation
   G. L. Causer, D. L. Cortie, H. Zhu, M. Ionescu, G. J. Mankey, X. L. Wang, F. Klose
   Talk presented at the International Conference on Neutron Scattering, 2017, Daejeon, South Korea

8. Magneto-electronic hydrogen gas sensing
   G. L. Causer, C. Lueng, S. J. Callori, P. Metaxas, M. Kostylev, F. Klose
   Talk presented at the Condensed Matter and Materials Meeting, 2017, Wagga Wagga, Australia (Awarded Best Talk)

9. Hydrogen gas sensing in Co/Pd bilayers characterised by polarised neutron reflectometry with *in situ* ferromagnetic resonance
   G. L. Causer, C. Lueng, S. J. Callori, K.-W. Lin, P. Metaxas, X. L. Wang, M. Kostylev, F. Klose
   Poster presented at the International Conference of the Asian Union of Magnetics Societies, 2016, Tainan, Taiwan

10. Meta-magnetism of single crystal $FeTiO_3$ investigated by high-field neutron diffraction
    G. L. Causer, D. L. Cortie and F. Klose
    Poster presented at the Asia-Oceania Conference on Neutron Scattering, 2015, Sydney, Australia

Abbreviations

ACNS	Australian Centre for Neutron Scattering
AFM	Antiferromagnetic
ANSTO	Australian Nuclear Science and Technology Organisation
CNP	Cobalt-Nickel-Palladium
DF-TEM	Dark-Field Transmission Electron Microscopy
DFT	Density Functional Theory
DPA	Displacements per Atom
EB	Exchange Bias
FFT	Fast-Fourier Transforms
FMR	Ferromagnetic Resonance
FM	Ferromagnetic
FWHM	Full-Width-at-Half-Maximum
HGS	Hydrogen Gas Sensor
HR-TEM	High-Resolution Transmission Electron Microscopy
ISEM	Institute for Superconducting and Electronic Materials
OPAL	Open Pool Australian Light-Water
PMA	Perpendicular Magnetic Anisotropy
PM	Paramagnetic
PNR	Polarised Neutron Reflectometry
PPMS	Physical Properties Measurement System
SAED	Selected-Area Electron Diffraction
SLD	Scattering Length Density
SRIM	Stopping and Range of Ions in Matter
TEM	Transmission Electron Microscopy
TRIM	Transport of Ions in Matter
VSM	Vibrating Sample Magnetometry
XRD	X-ray Diffraction
XRR	X-ray Reflectometry

Chapter 1

Introduction

In 1959 Richard Feynman delivered a visionary lecture in which he theorised that if matter could be assembled at the atomic level, then materials could be designed 'at will' to exhibit properties which are unobtainable in bulk specimens [79]. Feynman envisaged a world where these artificial nanostructures could be used to solve a myriad of challenges facing electronics, engineering and medicine [230]. In the decades that have since followed, the words of Feynman have been credited to laying the foundations of modern nanoscience and are continually reflected in the ever-growing number of technological developments which lie in their wake. For example, energy-gap variations across the interfaces of semiconductor heterostructures have provided high-speed opto-electronics, for which Herbert Kroemer won the 2000 Nobel Prize in Physics and coined the phrase 'the interface is the device' [142]. The ability to control and transport spin through atomically-thin magnetic layers led to the discovery of giant-magnetoresistance [16, 29], giving birth to the spintronics paradigm [27, 15], and acquiring Albert Fert and Peter Grünberg the 2007 Nobel Prize in Physics. More recent Nobel laureates have highlighted the importance of surface-state topology and

have outlined novel frameworks for predicting and characterising exotic forms of matter — some of which may even form the basis of quantum computing [205, 104, 137]. Feynman's ideas brought the realisation that completely new and tuneable properties could be obtained by manipulating the physical dimensions of matter [264, 183]. And, as touched on by Kroemer, a further concept which underpins much of all condensed-matter nanoscience is the importance of interfaces in communicating low-dimensional phenomena between heterostructure components [70], and which act as anchor points for the direct control and tunability of device functionality.

In this thesis, the concepts put forward by Feynman and Kroemer are explored through two magnetic thin-film architectures which are united in the utility of interfacial effects and dimensionality. The first study, which is introduced in Section 1.1, reports on the fundamental sharpness of magnetic interfaces formed by ion-induced chemical disorder in $FePt_3$ films. A second study, which is introduced in Section 1.2, investigates hydrogen-induced modifications to the magnetic surface anisotropy of Co/Pd bilayers. The interface physics of the nanostructures detailed in this thesis have the potential to support a manifold of future magnetic thin-film devices, namely in the areas of computing and advanced sensing technologies.

1.1 The Fundamental Sharpness of Magnetic Interfaces Formed by Chemical Disorder Using a He^+ Beam

In order for storage densities in magnetic recording devices to exceed 5 Tbit in^{-2}, the current approach to information-storage engineering will drastically need to change [144, 270]. Up until now, the delicate balance of maintaining workable signal-to-noise

ratios, while pursuing increased storage densities in conventional hard-disks, has been managed by reducing the bit size over a fixed number of weakly interacting grains per bit [271]. However, below a certain finite size the small volume of an individual grain will render it highly susceptible to thermal-induced switching [196, 289], resulting in a loss of stored information. To avoid this data-storage dilemma, research focus has now expanded to consider the potential of storing information on artificially-formed bit-patterned structures, where each bit constitutes a single-domain ferromagnetic (FM) entity [270, 162, 196]. This design construction is particularly attractive, because as each bit comprises of one magnetic domain only, the switching volumes have enhanced size (on the order of some 10 nm^3) and therefore enhanced thermal stability with respect to conventional hard-disk media [272, 271].

Traditionally, the geometric FM-dot arrays typical of bit-patterned media have been fabricated using lithographic techniques such as X-ray, electron- or ion-beam lithography [180, 270]. These methods require the use of both template and resist materials, plus several chemical treatments to develop the resist, deposit the FM-dot material, and then lift-off the resist layer. In short, these multiple steps take time and require numerous equipment set-ups, not to mention the quality of the resist after chemical development often plays a significant role in determining the definition of the resulting FM bits [66, 294]. Furthermore, once the film is stripped of the resist layer the lithographically deposited FM islands are revealed, which are not only chemically inequivalent to the template material, but also have a different topography [270, 144]. The latter hinders prospective applications in magnetic data-storage because the discrete bits can disturb the stable flying of the giant-magnetoresistance recording heads which traverse over the media at distances of only a few nanometres. For example, it is estimated that a 4 nm head-to-media clearance will be required to reach the 5 Tbit in^{-2} areal-density point [182], otherwise recording errors will be incurred.

Consequently, an alternative nano-fabrication technique to lithography is sought which can preserve surface topography while allowing for the local modification of magnetic properties within a thin film. One approach which is highly capable of delivering such structures on a commercial scale, is to employ energetic-ion beams produced by particle accelerators to synthesise detailed magnetic nanostructures from continuous non-magnetic templates [246, 48, 19, 154, 144]. Generally, there are two mechanisms for inducing magnetic-property modifications in materials using ion beams. The first is to introduce impurity dopants through ion implantation [191, 154, 131], which openly introduces additional chemical factors. The second is to drive magnetic phase transitions by rearranging lattice structure and introducing chemical disorder, without doping, by irradiating with chemically-inert light-ions such as He^+ [73]. This dopant-free approach has the merit of preserving the chemical stoichiometry of the template while modifying the band structure in the region of exposure. However, it is only effective in certain material classes [19, 234, 174, 190]. In saying this, both mechanisms provide the capability to engineer magnetic properties in three dimensions on the nanometre length scale, with a greater spatial resolution than traditional lithography. These will be important considerations for several emerging magnetic technologies. For instance, ion implantations are increasingly being used to prepare novel logic and spintronic devices [54], and to sculpt the conducting edge states of topological insulators [253, 84]. While focussed-ion irradiations are adept to machine superior, three-dimensional, yet planar, spatial arrays of FM components which are ideally suited to the tribology of bit-patterned devices [272, 74, 270]. Ultimately, the performance and functionality of these devices will hinge on the spatial definition of the incorporated magnetic nano-elements. The parameter of spatial definition is set by the inherent tendency of the ion beam to widen its energy distribution and angular momentum through statistical scattering processes within the non-magnetic template [301, 92]. This 'straggling' be-

haviour (which is intrinsic to all low-energy ion beams) will have a profound influence on the maximum storage-densities achievable in bit-patterned devices, as it will be the limiting factor to define the minimum separation distance required to prevent magnetic coupling among adjacent bits. As such, gaining a quantitative understanding of the magnetic transition-width of FM/non-FM interfaces formed by ion beams is of topical importance to the future success of these devices.

The investigation presented in Chapter 3 elucidates the fundamental sharpness of magnetic interfaces which can be formed locally by driving magnetic phase transitions in materials using ion beams. The term *fundamental* is used here, namely, to describe a magnetic interface arising solely from the ion-matter interaction itself. This is achieved through a unique experimental design in which the ion distribution is made independent of all external factors which commonly act to reduce magnetic interface quality in ion-beam-designed nanostructures (e.g., shadowing effects typical of masked irradiations) [294, 66].

The investigations are carried out on the intriguing model system — $FePt_3$ — motivated by its unique quantum chemical feature which allows either a paramagnetic (PM) or FM state to be selected at room temperature depending on the level of atomic-site disorder in the material [243, 244, 173, 174]. Through careful selection of the irradiating ion energy and fluence, room-temperature ferromagnetism is locally induced into a fractional volume of a PM $FePt_3$ film through dopant-free chemical order modification. A combination of transmission electron microscopy, magnetometry, and polarised neutron reflectometry measurements demonstrate that the interface over which the PM-to-FM modulation occurs in this model system is confined to a few atomic monolayers only, while the structural boundary transition is less well-defined. Using complementary density functional theory calculations, the mechanism for the ion-beam induced magnetic transition is revealed and shown to be caused by an in-

termixing of Fe and Pt atoms in anti-site defects above a threshold density. The results presented in Chapter 3 are closely based on the self-publications contained in References [43], [45] and [46], but also include some additional and unpublished data.

1.2 Hydrogen-Driven Switching of the Magnetic Surface Anisotropy at the Co/Pd Interface

While the investigation of Chapter 3 takes advantage of the binary magnetic states unique to $FePt_3$ and is pertinent to understanding the utmost areal-densities achievable in forthcoming bit-patterned technologies prepared by ion beams, the $FePt_3$ alloy itself is far from a competitive data-storage material. Although many previous works into $FePt_3$ have been motivated by spintronic, magnonic and data-storage applications [174, 173, 234, 244, 243, 164], the alloy is mostly a convenient prototype for demonstrating the reported concepts. This is because, while $FePt_3$ may be able to display FM and PM phases simultaneously at room temperature, it is nevertheless magnetically soft meaning that (in a device) individual FM bits could easily lose their written data through stray-field interactions or via thermal excitation.

Instead, for application, high-anisotropy materials which display square hysteresis loops, high coercive fields and which orient their magnetic easy-axis perpendicular to the plane of the film are required. The myriad of candidate materials exhibiting this so-called 'perpendicular magnetic anisotropy' (PMA) comprise of Co/Pt [288, 42], Co/Au [279, 278], Co/Pd [267, 266], Fe/Pd [152, 226], and Fe/Pt [185] heterostructures as well as $L1_0$ FePt [23, 146, 299, 94, 55], $L1_0$ MnAl [214], and $L1_2$ $CrPt_3$ [268, 128] alloys. The occurrence of PMA in these systems is reported to emerge from the co-operative effects between the spin moments of the FM 3d transition metals and the large spin-orbit interactions of the PM 4d transition metals [211, 282, 247]. The proximity interaction

of the elemental species induces a spontaneous magnetic polarisation of the heavier 4d moments (originating from their large Stoner factors [236, 113]) [50, 107], which then presents as an interfacial or bulk derived PMA within heterostructure and alloyed films [271], respectively.

According to Néel theory [202], the reduced coordination of interfacial atoms in heterostructure films plays a significant role in redistributing the spin-polarised electron density, which alters the spin-orbit energy responsible for the system's state of magnetic anisotropy [41]. Consequently, by rearranging interfacial structure it is possible to modify the PMA. Accordingly, ion beams have been employed to induce interface atomic-mixing in PMA heterostructures to either rotate the magnetic easy-axis direction [288, 66, 77, 279] or destroy magnetism in the region of exposure altogether [67, 74]. This has afforded the preparation of arrayed PMA nano-elements separated by either in-plane magnetised or PM spacer regions, respectively. The latter arrangement represents that of an 'ideal' bit-patterned assembly as there is no opportunity for the PMA elements to exchange couple to their neighbouring spacer elements. Furthermore, in terms of the high-anisotropy alloys, ion-induced chemical disorder has been shown to lead to the local creation or destruction of magnetism throughout the irradiated regions of $A1$ FePt [23, 231] and $L1_2$ $CrPt_3$ films [111, 213], respectively.

Among the many high-anisotropy heterostructures the FM/Pd interface represents a special case in which the interfacial PMA is not only modifiable through ion-beam irradiation, but rather remarkably, also upon exposure to hydrogen gas [47, 171, 172]. This is made possible by the strong affinity of Pd to absorb large volumetric quantities of hydrogen whereby it undergoes a chemical, mechanical and optical transformation [156]. This unique tendency of Pd opens a fascinating possibility for the interfacial PMA effect to not only be employed in the realm of data-storage media but also in a multitude of hydrogen sensing and storage applications. Increasingly, hydrogen as

an energy carrier as well as the development of associated hydrogen technologies, such as fuel-cells and sensors, are establishing themselves as key and important ingredients in the race to find economical, renewable and safe solutions to our ever-increasing demand for energy in the face of dwindling fossil fuel reserves [1, 260]. Kostylev *et al.* were the first to exploit the magnetic anisotropy of Co/Pd bilayers to demonstrate the concept of a hydrogen gas sensor (HGS) which utilises magnetic interface effects [47]. Since then numerous works have extended the appreciation of magnetic HGSs to systems such as Fe/Pd bilayers [148, 158] and CoPd alloyed films [160]. In general, these works have demonstrated the commercial viability of PMA-based HGSs; however, a comprehensive understanding of the fundamental mechanism which drives the changes to the Pd layer magnetisation at the FM/Pd interface is still lacking. Progress in this area has been hindered primarily due to the complexity in characterising the interfacial effect during hydrogenation, especially since there is a likelihood of the process leading to a partial irreversibility of the interfacial properties [212, 197]. Under these circumstances it is essential to record as much information about the FM/Pd interface step-wise throughout a single exposure to hydrogen gas, because once perturbed by the environment the initial state of the sample is unable to be revisited at any later stage. Addressing this requires the use of an experimental probe which is sensitive to magnetic anisotropy, while capable of simultaneously resolving the depth-profile of magnetic polarisation throughout a heterostructure during hydrogen-gas absorption.

In Chapter 4 we devise an experimental procedure capable of mutually extracting information about the static magnetisation and the magnetic anisotropy of a FM film while its properties are gradually transformed in the presence of an external stimulus. This is achieved through commissioning an original sample chamber which combines polarised neutron reflectometry and ferromagnetic resonance. Feasibility studies performed using the commissioned equipment reveal the profound capacity of

the measurement approach in being able to detect minute changes between extrinsically driven states of matter. The commissioned equipment is then used to characterise hydrogen-induced changes to the magnetic and structural properties of Co/Pd bilayers of varying Pd layer thickness. It is shown that the total in-plane magnetisation of the Co/Pd bilayers irreversibly increases after primary hydrogen-gas absorption indicating a weakening of the PMA strength, and which displays a dependence on the thickness of the Pd layer. The results presented in Chapter 4 are based on the self-publications contained in References [40], [44] and [140], but also include some additional and unpublished data.

1.3 Thesis Overview

As the majority of the experimental conclusions contained in this thesis are obtained by X-ray and neutron scattering techniques (specifically applied to thin films), the fundamental principles of the relevant methods are first introduced in Chapter 2. References to complementary lab-based characterisation tools which have also been utilised as part of this work are also provided. At the beginning of each research chapter, in Chapters 3 and 4, a more thorough motivation section will prelude the work and outline the current state-of-play for the topics covered. Following this, in Chapter 3, the growth conditions, and initial characterisation of the $FePt_3$ films will be presented. Ion-beam theory is then introduced, and Monte Carlo simulations are employed to model the disorder distributions anticipated within the $FePt_3$ films resulting from the specified irradiation conditions. Following this, a comprehensive materials investigation of the structural properties of the irradiated $FePt_3$ films as a function of the He^+ fluence is presented. Experimental investigations of the magnetic interface quality are then provided, and theoretical calculations are performed to rationalise the experimental

findings. Finally, a supplementary investigation into the low-temperature magnetic coupling generated at the FM/PM interface within the irradiated $FePt_3$ film is presented. In Chapter 4, a description of the polarised neutron reflectometry with *in situ* ferromagnetic resonance sample chamber commissioned at the Australian Centre for Neutron Scattering (ACNS) of the Australian Nuclear Science and Technology Organisation (ANSTO) over the course of this thesis is presented. The methodology and the first experimental results obtained from feasibility studies using the commissioned equipment are provided and discussed. A detailed *ex situ* and *in situ* characterisation of the hydrogen-driven switching of interfacial PMA in Co/Pd bilayers of varying Pd layer thickness is then presented and analysed. Chapter 5 summarises all the main experimental and theoretical results presented throughout the thesis and provides suggestions for the future directions of each project.

Although the two research projects outlined in Chapters 3 and 4 of this thesis are very different in nature and in operation, the investigations are motivated by the same set of research questions. These are:

- How do the chemical, structural and magnetic properties of a material behave on the nanoscale and/or near an interface?
- How do external factors, such as hydrogen gas or ion irradiations, modify the chemical structure of thin films, and what role do these factors play in modifying the magnetic landscape on the nanoscale and/or near an interface?
- How can X-ray and neutron scattering techniques be used to resolve the depth-dependent chemical and magnetic signatures of nano-architectures?
- How can the magnetic phenomena of low-dimensional systems (e.g., exchange bias and perpendicular magnetic anisotropy) be exploited in the operation of

forthcoming solid-state technologies?

Chapter 2

Experimental Techniques

X-rays and neutrons are complementary and ideal matter probes routinely employed to investigate the structure, atomic order and magnetism of thin films [298, 183, 241, 68]. X-rays and neutrons constitute high-resolution probes because they mutually possess wavelengths comparable to interatomic distances in solids. Both X-rays and neutrons have enabled studies into bulk materials because each interacts only very weakly with matter to permit larger depth-penetrations compared to that of proton or electron probes which are restricted to surface studies [62]. In addition, while X-rays scatter from the electron cloud, neutrons interact with the atomic nuclei and the unpaired electrons of an atom, and therefore each provides complementary information about a specimen — be it electronic, nuclear or magnetic. It follows that neutrons are sensitive to the isotopes of a given element and are also acutely sensitive to light (low atomic number Z) elements [225], whereas X-ray sensitivity scales linearly with Z across the periodic table. Hence, X-ray and neutron scattering techniques employed in synergy provide a pathway to directly resolve the atomic and magnetic structures of thin films, and as such have been used to facilitate a large portion of the experimental work pre-

sented in this thesis. In general, lab-based techniques such as transmission electron microscopy (TEM) [290] and vibrating sample magnetometry (VSM) [274] are also commonly used to supplement scattering measurements. However, structural investigations utilising microscopy are restricted to surface measurements, and as such cannot provide insight into the nature of buried chemical and/or magnetic interfaces within thin films. While magnetometry provides indirect and volume-averaged information which cannot spatially resolve variations in magnetisation across film thicknesses. The fundamental principles of the TEM and VSM techniques will not be discussed in this thesis, but can be found in several excellent sources [290, 90, 36, 274, 22, 81].

This chapter introduces the scattering theories relevant to the techniques presented in this thesis. The discussions are intended to be brief, and will focus on scattering techniques applied to magnetic thin films. As such, discussions will be limited to scattering which is both elastic ($E_i = E_f$) and specular ($\theta_i = \theta_f$). Extensive reviews covering descriptions of the basic principles towards full theoretical derivations of scattering theory (and the numerous techniques which it supports) can be found in the literature [262, 165, 257, 286, 91, 106].

The principle of scattering is centred around the process whereby an incident beam of wavevector $\mathbf{k}_i$ is scattered by a sample resulting in an outgoing beam of wavevector $\mathbf{k}_f$ (as depicted in Figure 2.1). For a scattering event which is both specular and elastic, the difference between the incident and scattered wavevectors contains information regarding the component of the wavevector transfer $\mathbf{Q}_z$ normal to the sample surface [257, 134],

$$\mathbf{Q}_z = \mathbf{k}_f - \mathbf{k}_i. \tag{2.1}$$

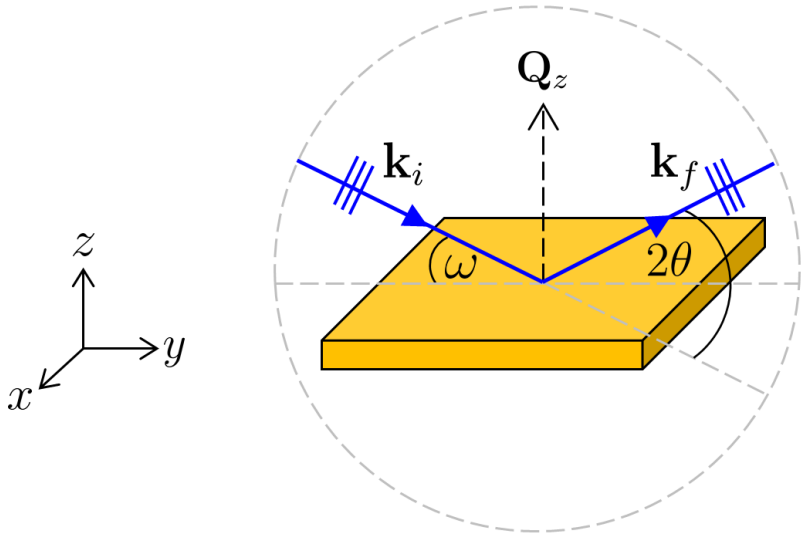

Figure 2.1: Scattering measurements in the $\omega/2\theta$ Bragg-Brentano geometry. An incident beam of wavevector $\mathbf{k}_i$ is scattered by a sample resulting in an outgoing beam of wavevector $\mathbf{k}_f$. $\mathbf{k}_f$ scatters at an angle 2θ relative to $\mathbf{k}_i$, which is incident at an angle ω to the sample surface.

2.1 X-ray Diffraction

W. L. Bragg was the first to realise that X-rays striking a crystal at an angle θ constructively interfere to produce a diffracted beam, only if the path difference between rays reflected from adjacent planes of the lattice are an integer multiple of wavelengths λ [34]. The condition is termed Bragg's Law [134], and is given by

$$n\lambda = 2d_{hkl}\sin\theta, \tag{2.2}$$

where n is the harmonic of the diffraction and d_{hkl} is the distance in real-space between consecutive lattice planes in a given Miller direction denoted by the indices (hkl) [13]. The Bragg angle θ is related to the modulus of the component of the scattering vector

Q_z normal to the sample surface [257], and is given by

$$Q_z = \left(\frac{4\pi}{\lambda}\right) \sin\theta, \tag{2.3}$$

which is inversely proportional to d_{hkl} (i.e., $Q_z = 2\pi/d_{hkl}$).

Because a crystal represents a three-dimensional periodic spatial array of atoms, it is convenient to take the Fourier transform of the real-space lattice to define a reciprocal-space [257]. Each point of the reciprocal-space lattice can be described by a reciprocal lattice vector $\mathbf{G}$ [134],

$$\mathbf{G} = h\hat{\mathbf{a}}^* + k\hat{\mathbf{b}}^* + l\hat{\mathbf{c}}^*, \tag{2.4}$$

where $\hat{\mathbf{a}}^*, \hat{\mathbf{b}}^*, \hat{\mathbf{c}}^*$ are reciprocal-space lattice vectors related to the real-space lattice vectors $\hat{\mathbf{a}}, \hat{\mathbf{b}}, \hat{\mathbf{c}}$. By substituting Equations 2.2 and 2.4, Bragg's Law can be used to determine the distance between the adjacent planes of any crystalline lattice described by the lattice parameters (a, b, c). For the particular case of a cubic lattice with lattice parameter a $(= b = c)$ this becomes [134],

$$d_{hkl} = \left(\frac{h^2 + k^2 + l^2}{a^2}\right)^{-1/2}. \tag{2.5}$$

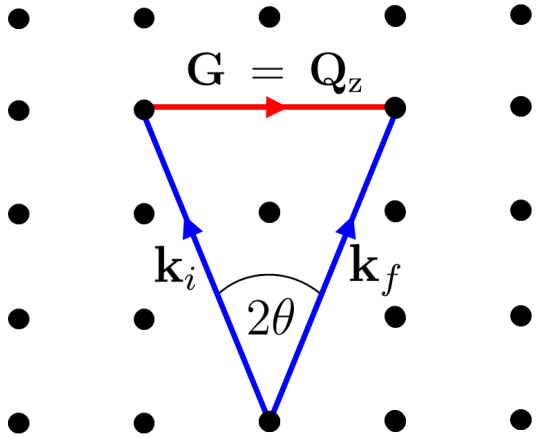

Figure 2.2: Reciprocal-space lattice showing the Bragg condition for diffraction where the wavevector transfer $\mathbf{Q}_z$ must equal some reciprocal-space lattice vector $\mathbf{G}$ in order for diffraction to occur.

As depicted in Figure 2.2, the Bragg condition for diffraction is satisfied when $\mathbf{G} = \mathbf{Q}_z = \mathbf{k}_f - \mathbf{k}_i$. However, because of the differing scattering powers and of the relative locations of individual atoms within the unit cell of a crystalline lattice, not all diffracted beam intensities recorded at each Bragg angle will be equivalent. Instead, one must consider the structure factor $\mathbf{S}_\mathrm{G}$ of a lattice [134],

$$\mathbf{S}_\mathrm{G}(hkl) = \sum_j f_j \exp\left[-2\pi i(hx_j + ky_j + lz_j)\right], \tag{2.6}$$

which is taken as the summation over all the atoms j positioned at (x, y, z) within the unit cell. The atomic form factor f_j describes the scattering amplitude of a given atom, which (for X-rays) is related to the electron density and can therefore be approximated by the atomic number Z of the atom.

2.2 Reflectometry

While diffraction is suitable for determining the atomic structure and lattice spacings of a crystalline film, it cannot provide information regarding its thickness, layering sequence and/or interfacial qualities. These latter parameters are obtainable by setting ω in Figure 2.1 at a glancing angle to the sample surface. In this low-momentum transfer regime, the plane waves of $\mathbf{k}_i$ partially reflect and refract from each of the film's interfaces undergoing interference with $\mathbf{k}_f$ to subsequently form a reflectivity pattern (analogous to optical interference phenomena observed during the reflection of visible light) [68, 225].

To aptly conduct a reflectometry investigation, it is essential that the film being studied comprises of a planar surface, and any buried layers or interfaces are laterally homogeneous across the sample dimension on the length scale of the incident beam's wavelength [176]. In this way, each layer can be approximated to be invariant in the xy-plane (as defined in Figure 2.1) and the scattering problem reduces to one dimension. In this simplified form, the scattering potential V is only influenced by variations in the bound coherent scattering length b and atomic density ρ which occur perpendicular to the sample surface (i.e., in the z-direction), and is expressed as

$$V = \frac{2\pi\hbar^2}{m} \sum_i \rho_i b_{i,nuc} \ , \tag{2.7}$$

where m is the neutron mass and the summation is performed over all elemental and/or isotopic (in the case of neutrons) constituents i of a given layer. The product of b and ρ is termed the scattering length density (SLD) of the layer.

By measuring the reflected intensity R of a sample (where $R = |r^* r|^2$ and r is the sample reflectance [80]) as the incident angle (or wavelength) is varied, a reflectivity

pattern as a function of Q_z is produced, from which a SLD profile normal to the sample surface can be obtained. The SLD profile which is sensitive to optical-index deviations on the nanometre length scale can be used to identify the individual layers of a system and provide information regarding material and interface properties. A prominent feature of the reflectivity pattern is the critical edge Q_c

$$Q_c = \sqrt{16\pi\rho b_{nuc}}\ , \tag{2.8}$$

which corresponds to a material-specific critical angle below which $\mathbf{k}_i$ undergoes total external reflection from the sample surface. At incident angles greater than Q_c the reflectivity falls asymptotically as Q_z^{-4} [6]. The appearance of Kiessig fringes, formed as a result of the changing SLD throughout the sample depth, provide information regarding the thicknesses and chemical compositions of the constituent layers within the sample [85].

At low-momentum transfer (i.e., as $Q_z \to 0$), through enhanced incidences of the self-absorption and refraction of $\mathbf{k}_i$, the major assumptions of the kinematical Born approximation are violated [257]. As such, the analysis of reflectivity data (unlike diffraction data) cannot simply rely on the reciprocity of Fourier transforms. Instead, dynamical approaches such as those developed by Parratt [221] need to be implemented in order to solve the scattering problem. The Parratt formalism solves the matrix equation [300],

$$\begin{pmatrix} t \\ ik_{n+1}t \end{pmatrix} \exp\left(ik_{n+1}\right)l_{n+1} = \begin{pmatrix} \cos(k_n l) & \sin(k_n l)/k_1 \\ -k_1\sin(k_n l) & \cos(k_n l) \end{pmatrix} \begin{pmatrix} 1+r \\ ik_{n-1}(1-r) \end{pmatrix}, \tag{2.9}$$

recursively for a sample consisting of n layers of thickness l in order to obtain the reflectance r and transmittance t amplitudes of the neutron wavevector k across each

layer (or, equivalently, in three neighbouring mediums). For example, the distinct wavevectors of a single-layer film are: k_{n-1} = vacuum, k_n = film, k_{n+1} = substrate. The primary quantity of interest is the reflectivity $R = |r^* r|^2$.

2.3 Polarised Neutron Reflectometry

It is beneficial at this stage to draw attention to the detail, that, reflectometry measurements which employ neutrons as the material probe, are particularly well-suited to the study of magnetic films [62, 225]. This is because neutrons themselves possess a magnetic moment μ given by

$$\mu = \gamma_n \mu_n \hat{\sigma}, \tag{2.10}$$

where γ_n is the neutron gyromagnetic ratio, μ_n is the nuclear magneton and $\hat{\sigma}$ is the Pauli spin operator [176]. Hence, neutrons can be thought of as tiny bar magnets which are able to interact with the uncompensated spins of a magnetic sample through the magnetic induction $\mathbf{B}$ (where $\mathbf{B} = \mu_0(\mathbf{H} + \mathbf{M})$ and $\mathbf{H}$ is the external magnetic field and $\mathbf{M}$ is the sample magnetisation), to provide an additional magnetic scattering potential $V = -\mu \cdot \mathbf{B}$ during a reflectivity measurement. Due to the fermionic property of the neutron, its angular momentum or 'spin' $\mathbf{S}$ is quantised such that it can occupy one of two possible discrete eigenstates, either spin-up (+) or spin-down (−), in the presence of $\mathbf{B}$. For the study of thin films, the typical naming convention stipulates that spin-up neutrons align parallel to an external magnetic field $\mathbf{H}$, while spin-down neutrons align anti-parallel to $\mathbf{H}$. As shown in Figure 2.3, $\mathbf{H}$ is applied in the plane of the film along the y-direction, such that $\pm\,\mathbf{S} \parallel \hat{\mathbf{y}} \perp \mathbf{Q}_z$ and can take any arbitrary angle α with respect to the sample magnetisation $\mathbf{M}$. From Maxwell's equations, $\mathbf{B}_z$ is continuous and can therefore be neglected, such that only M_x and M_y contribute to

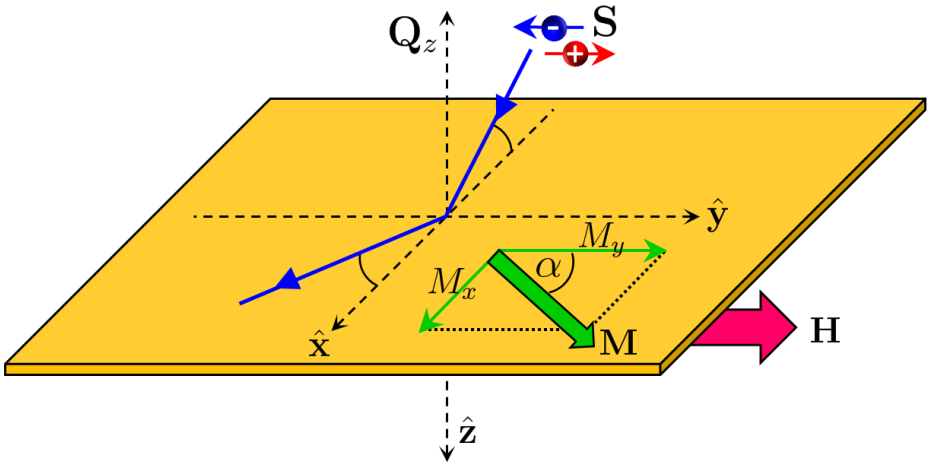

Figure 2.3: The typical naming convention employed in the neutron reflection process. The neutron spin **S** lies in the plane of the film, and either parallel (+) or anti-parallel (−) to the external magnetic field **H**. The in-plane magnetisation **M** of the film, which can take any arbitrary angle α with respect to **H**, is assigned the vector components M_x and M_y.

the reflectivity at any interface.

By performing a reflectivity measurement using a beam of polarised neutrons — that is, to perform a polarised neutron reflectometry (PNR) measurement — the scattering potential of Equation 2.7 is extended to account for the interaction between μ and **B** such that

$$V_{\pm} = V_{nuc} \pm V_{mag} = \frac{2\pi\hbar^2}{m}(\sum_i \rho_i b_{i,nuc} \pm \sum_i \rho_i b_{i,mag}), \tag{2.11}$$

where the $\pm$ sign denotes the polarisation state of the neutron. The concluding term of Equation 2.11 is commonly referred to as the magnetic SLD, and can be equally expressed as

$$\text{SLD}_{mag} = \sum_i \rho_i b_{i,mag} = C \sum_i \rho_i \mu_i, \tag{2.12}$$

where $C = m\mu_n\mu_B/2\pi\hbar^2 = 2.645$ x10^{-5} Å$/\mu_B$ and μ_i is the magnetic moment of the sample per formula unit [80].

Typically, the scattering potential of Equation 2.11 is expressed in the form of a 2×2 matrix, by incorporating the Pauli matrices and an appropriate rotational transformation [176], to define four interaction potentials

$$\begin{pmatrix} V^{++} & V^{+-} \\ V^{-+} & V^{--} \end{pmatrix} = \frac{2\pi\hbar^2}{m}\rho \left[b_{nuc} \begin{pmatrix} 1 & 0 \\ 0 & 1 \end{pmatrix} + b_{mag} \begin{pmatrix} \cos\alpha & \sin\alpha \\ \sin\alpha & -\cos\alpha \end{pmatrix} \right]. \tag{2.13}$$

The first and second subscript of each potential denotes the spin state of the incident and outgoing neutron beam, respectively, and is used to account for instances where the incident spin state undergoes a π-phase change (is flipped) upon reflection from the sample to emerge in an opposing spin state. The diagonal elements, V^{++} and V^{--}, are referred to as the non-spin-flip scattering potentials, and probe the sample's nuclear structure and the component of the magnetic moment parallel to the neutron polarisation axis [177]. The off-diagonal elements, V^{+-} and V^{-+}, are referred to as the spin-flip scattering potentials, and probe the component of the sample's magnetic moment perpendicular to the neutron polarisation axis only. The four scattering potentials correspond to the four measurable reflectivity cross-sections R^{++}, R^{+-}, R^{--} and R^{-+}. In instances where all four reflectivity cross-sections are measured, the in-plane vectorial components of the sample's magnetisation parallel and perpendicular to the neutron polarisation axis can be spatially resolved (e.g., during magnetic reversal) to provide a quantitative measure of a sample's magnetic moment per unit volume as a function of sample depth. Specifically, by taking the normalised difference between the R^{++} and R^{--} cross-sections as a function of Q_z, a depth-profile arising purely from the magnetic signature of the sample can be obtained. This quantity is commonly referred to as the spin-asymmetry and is expressed as

$$\text{spin-asymmetry} = \frac{R^{++} - R^{--}}{R^{++} + R^{--}}. \tag{2.14}$$

Hence, regardless of a sample's chemical composition (even if it is homogeneous throughout the sample depth), lateral fluctuations in the internal magnetic structure can be detected by PNR. Furthermore, due to the quantisation of the neutron it follows that the degeneracy of Q_c in Equation 2.8 is lifted for experiments involving polarised neutrons, to become

$$Q_{c_\pm} = \sqrt{16\pi\rho(b_{nuc} \pm b_{mag})}, \tag{2.15}$$

where the differences in the Q_z locations of $Q_{c_\pm}$ provides a direct measure of the sample's total magnetic moment. Overall, PNR is a powerful technique offering nanoscale resolution for the determination of magnetic and nuclear depth-profiles across thin films and multilayered structures [178, 91]. The PNR technique is ideally suited to analysing interfacial structure, as well as the microscopic composition of layer-averaged FM specimens.

2.4 X-ray and Neutron Data: Measurement and Fitting

X-ray diffraction (XRD) and X-ray reflectometry (XRR) measurements presented in this thesis were collected using a lab-based Panalytical X'Pert Pro X-ray diffractometer located at ACNS, ANSTO. The diffractometer was operated with Cu-K_α radiation (λ = 1.5406 Å) in the Bragg-Brentano configuration depicted in Figure 2.1 [90]. During XRD measurement, a Ni filter was used to limit contamination from Cu-K_β radiation as well as W and Ni impurities in the Cu anode of the X-ray source. XRR data were modelled using MOTOFIT [203, 204] to obtain a least-squares determination of the best-fit structural parameters (i.e., layer thickness, interfacial roughness) of the measured sample.

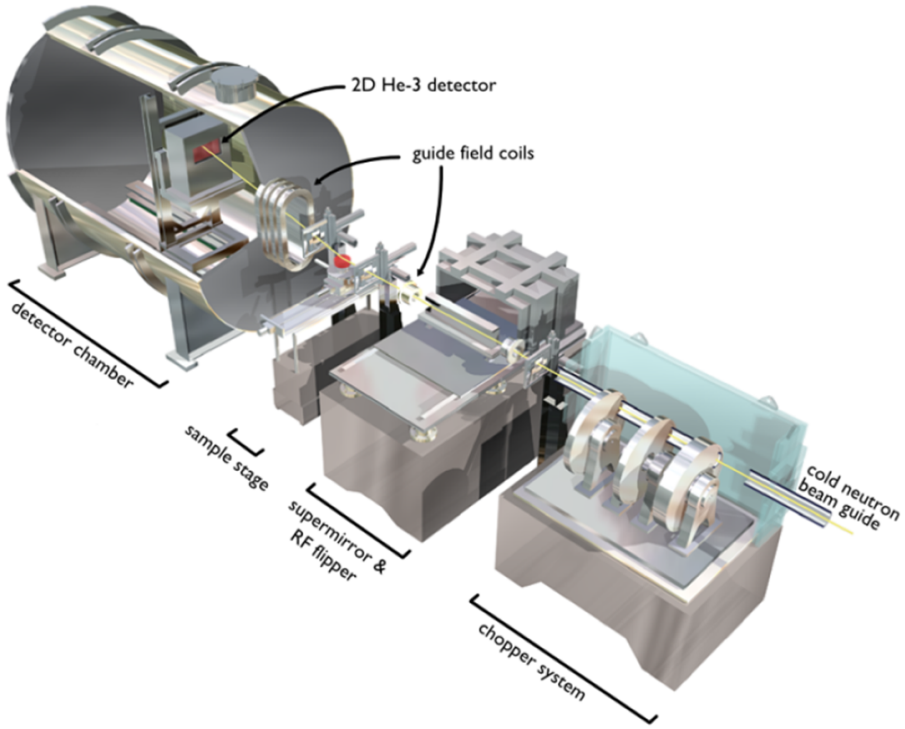

Figure 2.4: The PLATYPUS time-of-flight polarised neutron reflectometer located at ACNS, ANSTO [122].

PNR measurements were performed on the PLATYPUS reflectometer located at ACNS, ANSTO [122, 242]. A schematic of the PLATYPUS instrument is shown in Figure 2.4. The instrument uses low-energy neutrons with typical wavelengths ranging from 1 Å $< \lambda <$ 21 Å produced from the cold source of the 20 MW open pool Australian light-water (OPAL) research reactor. The PLATYPUS beamline operates with a horizontal sample surface geometry (vertical scattering plane) and employs the time-of-flight method to acquire data in which the travelling time of the neutron beam between two points is recorded to provide a retrospective measure of the velocities (and therefore the wavelengths) of the reflected neutrons. Four in-series dual-selectable boron-coated disc choppers operating at frequencies of 33 Hz are used to generate broad bandwidth neutron pulses to complement the efficiency spectrum of the polarising Fe/Si supermirror (2.5 Å $< \lambda <$ 12.5 Å) located upstream of the sample position

[242]. Because the transmitted (−) neutron spin state is the only spin state to emerge from the polariser, a radio-frequency spin flipper is employed post-supermirror to initiate spin precession through the application of a time-varying longitudinal field (198 kHz) to flip the neutron spin during experiments where the non-transmitted (+) state is required. To enable investigations into the four interaction potentials outlined in Equation 2.13, a secondary spin-flipper and supermirror package may accordingly be placed in the beam to analyse the neutron spin state downstream of the sample position. From Equation 2.3 it follows that the resolution of a reflectometry experiment is a combination of wavelength and angular resolutions

$$\frac{\Delta Q_z}{Q_z} = \sqrt{\left(\frac{\Delta\lambda}{\lambda}\right)^2 + \left(\frac{\Delta\theta}{\theta}\right)^2}. \tag{2.16}$$

By selecting different disc chopper pairings, the wavelength resolution of the PLATYPUS instrument can be varied between 1% and 9% [122], while the angular resolution is dependent on the vertical divergence of the incident beam at the sample position which is controlled by four absolute-encoded slit towers. Sample environments consisting of an electromagnet capable of applying a 10 kOe in-plane magnetic field to the sample position and/or a cryostat to provide sample cooling/heating over a 5 − 300 K temperature range are also available for use on the instrument.

For all PNR measurements presented in this thesis, PNR data was collected with a moderate wavelength resolution of 4.3% and an angular resolution of 3% to deliver a $\Delta Q_z/Q_z$ experimental resolution of 5.2%. The 10 kOe electromagnet was used to magnetise each sample's magnetic moment along the applied field direction parallel to the neutron polarisation axis. Spin analysis was not performed and only the $R^+(= R^{++} + R^{+-})$ and $R^-(= R^{--} + R^{-+})$ channels were recorded for each sample. The experimental PNR data was reduced, background subtracted, corrected for beam

footprint and polarisation efficiency through the POLSLIM add-in for Igor Pro developed by A. Nelson and T. Saerbeck [242]. PNR data analysis was performed using SIMULREFLEC [216] which utilises Parratt's recursive matrix formalism to simulate PNR patterns through the construction of real-space models which account for the thickness, density, scattering length, magnetisation and root-mean-square roughness of each layer within a multilayered system. The software employs least-squares fit procedures to continually adjust the parameters of the model (within physical limits) until a reasonable agreement to the experimental data is achieved. The residual error χ^2 of the modelled reflectometry pattern M_i to the experimental reflectometry data R_i is given by

$$\chi^2 = \frac{1}{n-p} \sum_{i=1}^{n} \left(\frac{R_i - M_i}{\sigma_{R_i}} \right)^2, \tag{2.17}$$

where n is the number of experimental data points, p is the number of fitting parameters in the model, and σ_{Ri} is the weighted statistical error of the experimental data. The goal of the fitting procedure is to minimise the divergence between M_i and R_i until, ideally, a χ^2 of 1 is achieved.

Chapter 3

The Fundamental Sharpness of Magnetic Interfaces Formed by Chemical Disorder Using a He^+ Beam

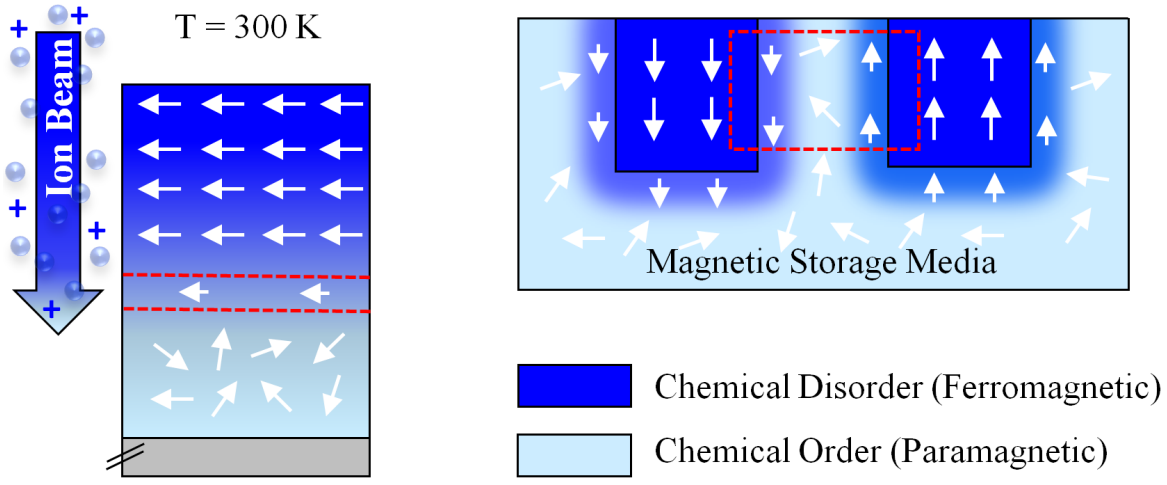

(left) Illustration of chemical disorder induced in a thin film by ion irradiation, resulting in a magnetic phase transition at room temperature. (right) From a device viewpoint, the finite width of the magnetic boundary formed at the chemical order/disorder interface will influence the minimum separation distance required to prevent data loss between adjacent magnetic bits in next-generation magnetic-storage media designed by ion beams.

3.1 Motivation

Artificial magnetic nanostructures synthesised by ion beams exhibit novel properties which are envisaged to become centrally important to the future functionality of ultra-high density magnetic recording devices [246, 19] and to the scalability of magnetic logic-gates in the spintronics paradigm [54, 237, 33, 59, 189]. Aiding a move away from the traditional nano-fabrication technique of lithography, focused light-ion (e.g., H^+, He^+, N^+, O^+) irradiations have demonstrated an aptitude for crafting superior quality, three-dimensional nano-elements through a single-step, dopant-free fabrication process which preserves film topography [213, 144, 234, 73]. This advent has fostered a revolution in nanostructure design. It is now possible to tune electronic properties and artificially drive phase transitions through the introduction of chemical disorder in a wide range of materials with nanoscale selectivity. Cybart *et al.* patterned thin insulating barriers into $YBa_2Cu_3O_{7-\delta}$ films using H^+ ions to form high-transition-temperature Josephson superconducting tunnel junctions [64]. Matczak *et al.* used He^+ ions to continuously modify the effective magnetic anisotropy gradient along Co/Au multilayer stripes to produce field-controllable magnetic domain walls [186]. Ramirez *et al.* suppressed long-range electronic correlations to tune the metal-to-insulator transition in V_2O_3 via disorder-induced O^+ irradiation [228]. Bernas *et al.* reported that the converse is also true in certain systems — chemical disorder can be driven to chemical order — after irradiating $A1$ FePt films with He^+ ions to obtain $L1_0$ FePt [23].

PM precursors, such as $Fe_{60}Al_{40}$ and $FePt_3$, which display an attractive interplay between chemical order and magnetism have also been explored [19, 190, 234, 174], because they constitute ideal systems for investigating the phenomenon of chemical disorder-driven ferromagnetism. In these model architectures, impinging ions act as mixing agents to knock magnetic and non-magnetic atoms from their chemically

ordered PM sites. The vacancies created during the irradiation process are filled randomly by the diffusion of atoms to form a non-equilibrium solid solution accommodating a modified band structure [19]. Ferromagnetism is then locally generated in the disordered regions due to a change in the magnetic exchange interactions which are tied to the Fe-Fe interatomic distances and bond angles. The irradiation leads exclusively to the substitution of atoms within a few atomic distances of the ion-path, without the formation of interstitial defects [74], due to the low momentum of the impinging ions which undergo nuclear stopping and later diffuse from the target material. In this way, by actively tailoring the chemical properties of non-magnetic frameworks, ion beams provide an avenue for direct stylus-type 'writing' of nano-compact FM dot arrays characteristic of ultra-high density magnetic recording devices [19, 190, 234]. Ultimately, the maximum achievable FM-dot density of these types of devices will be limited by the intrinsic nature of the ion beam itself, which widens its energy distribution and angular momentum through statistical scattering processes in the host material [301, 92]. This character, which is fundamental to all low-energy ions, is thought to have the potential to blur the intended definition of the resulting magnetic bit, which could hinder applications. Moreover, as there is generally a dissociation between ion-induced magnetic and structural property changes [48], this, in turn, raises further questions about the overall magnetic uniformity of the irradiated volume.

Recently, a semi-empirical model was developed by Bali *et al.* to account for the inhomogeneous depth penetration and lateral scattering of ions in matter [19]. The model revealed an acute sensitivity of the ion-induced FM moment on the number of displacements undergone by an atom during the irradiation, that is, the displacements per atom (DPA) [112]. As an outcome, it was modelled that nearly-discrete magnetic elements with non-depth-varying saturated magnetisation profiles could be obtained by ion irradiation. A typical FM/PM interface sharpness on the order of 10 nm was

predicted, and found to be in line with experimental observations [234, 19]. However, as the collected data were affected by a marginal experimental depth-resolution and also by the mechanical precision of the resist layer used, the ultimate achievable sharpness of interface transitions between ion-beam-designed FM and PM regions remains yet to be experimentally demonstrated.

The work presented in this chapter provides direct evidence of a superior, fundamental magnetic interface quality which outstrips the predictions of the model developed by Bali *et al*. The investigations are carried out on single crystalline $FePt_3$ films, whereby, through tailoring the ion energy and fluence, a depth-controlled room-temperature PM-chemical-order to FM-chemical-disorder transition induced by He^+ irradiation is reported. Section 3.2 outlines the growth conditions and structural analysis of the as-prepared $FePt_3$ films. Section 3.3 provides a brief introduction to the relevant concepts of ion-beam theory, alongside Monte Carlo simulations and an outline of the unique irradiation configuration implemented in this work. The magnetic and microstructural properties of un-irradiated and irradiated $FePt_3$ films are comparatively characterised in Section 3.4. PNR is employed to fingerprint the FM profile throughout an irradiated volume to provide insight into the fine resolution of the terminating FM boundary to the underlying PM framework. In Section 3.5, density functional theory (DFT) calculations are used to rationalise our experimental result, as well as to showcase the fine tunability of ferromagnetism in $FePt_3$ lattices occupying varying degrees of chemical disorder. Finally, a supplementary experiment is outlined in Section 3.6 which investigates the low-temperature magnetic exchange coupling generated at the FM/PM interface within the irradiated $FePt_3$ film.

3.1.1 Introduction to $FePt_3$

The family of intermetallic XPt_3 (X = Cr, Mn, Fe, Co, Ni) alloys are ideal frameworks for studying magnetic nano-elements synthesised by ion beams, because each displays dual magnetic characteristics depending on the level of chemical order occupied by their constituent atoms [24, 7, 192, 39]. Formally, chemical order in these crystal lattices is exemplified by the preference of symmetrically-equivalent lattice sites to be occupied by a particular element, which precedes to a long-range ordered distribution of atoms across the superlattice. In the case of $CrPt_3$, Cr moments align antiparallel to Pt moments to support a ferrimagnetic chemically ordered state, which then transforms to a non-magnetic state when the lattice is fully chemically disordered [24]. The FM moments of chemically ordered $MnPt_3$ likewise give way to a non-magnetic structure in the chemically disordered state [7]. While $CoPt_3$ and $NiPt_3$ mutually exhibit chemically ordered FM states which are modified, yet not destroyed, by chemical disorder [192, 39]. Of particular interest within the series is $FePt_3$, which uniquely features tailorable low-temperature antiferromagnetic (AFM) and FM properties (or equivalently room-temperature PM and FM properties) between the chemically ordered and the chemically disordered states [173, 243], respectively.

As shown in Figure 3.1, fully chemically ordered $FePt_3$ crystallises in the pseudo face-centered-cubic $L1_2$ structure, which is formally described as a simple-cubic lattice comprised of bi-atomic basis atoms [57]. In stoichiometric compositions, Fe atoms occupy the corner sites and Pt atoms occupy the face centers of a cubic unit cell with a lattice parameter of a = 3.87 Å [14]. Cooling the bulk material through the Néel temperature T_N of 160 K, a (½ ½ 0) c-type AFM superlattice structure develops, where the Fe moments order in alternating FM sub-sheets in the (110) planes [173]. Below T_N the Fe atoms carry magnetic moments of 3.3 μ_B per atom (extrapolated to 0 K),

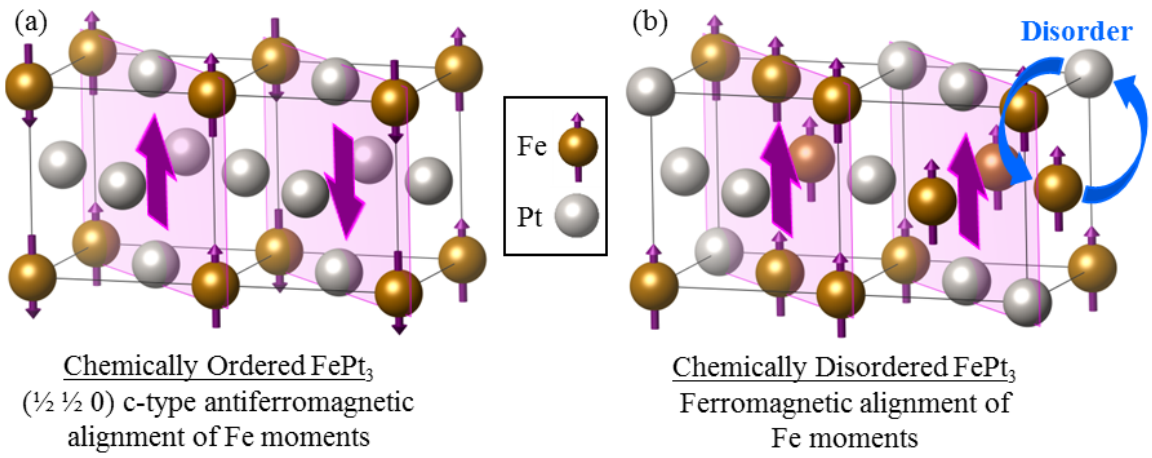

Figure 3.1: Atomic arrangements of $FePt_3$ in the (a) chemically ordered and the (b) chemically disordered states, showing low-temperature magnetic ordering. Formally, the crystallographic symmetry of $FePt_3$ transforms from simple-cubic with bi-atomic basis atoms to face-centred-cubic between the chemically ordered and the chemically disordered states, respectively.

while the Pt atoms are non-magnetic [14]. Above T_N paramagnetism is observed. In off-stoichiometric Fe-rich compositions, an additional first-order transition to a (½ 0 0) a-type AFM spin structure is exhibited below a $T_N = 100$ K, causing the Fe moments to organise into alternating FM sub-sheets along the (100) planes. The occurrence of this second AFM transition has been attributed to an excess of Fe atoms randomly occupying face-centre sites of the unit cell [14], which couple ferromagnetically to their nearest neighbours but retain long-range AFM order if FM clustering of the Fe atoms is avoided [218].

In the perfectly chemically disordered state of $FePt_3$, cubic symmetry and unit cell parameters are conserved; however, the occupancy of each face-centred-cubic lattice site is represented, on average, by ¼ Fe + ¾ Pt atoms. Governed by the random occupation of each lattice site and a reduction in the average Fe-Fe interatomic distance, positive exchange interactions develop between Fe nearest neighbour atoms and strong ferromagnetism prevails below a Curie temperature T_C of 425 K [14]. Robust

3.3 μ_B moments on each Fe site align parallel to accompanying 0.2 μ_B moments on the Pt sites. Above T_C the chemically disordered state remains structurally invariant up to approximately 1000 K at which point thermal activation leads to a chemical re-ordering of the superlattice [57].

The growth of chemically ordered $FePt_3$ films can be achieved via high-temperature deposition [167, 173], or by post-deposition annealing [14]. Chemical disorder — which is ascribed to an asymmetric distribution of Fe + Pt basis atoms over the face-centred-cubic $FePt_3$ lattice — can be mediated in $FePt_3$ by lowering the substrate temperature during film deposition [243], cold working [269], or by light-ion irradiation [174]. Because the transformation from chemical order to chemical disorder occurs via the partial and random growth of disordered domains throughout an ordered domain-structure, the characteristics of any physical $FePt_3$ sample will be a mixture of the two aforementioned crystal structures, which are displayed in Figure 3.1, and their respective magnetic properties arising from the growth conditions.

3.2 Sample Growth and Characterisation

The $FePt_3$ films studied in this chapter were grown by magnetron sputter deposition at the University of Alabama, in a four-target ultra-high vacuum deposition system consisting of confocal sputtering guns with independent shutters. The base pressure of the chamber was better than 2.6 $\times 10^{-4}$ mPa prior to deposition. One-side-polished 15 $\times$ 15 mm (001)-oriented MgO substrates purchased from MTI Corporation were loaded into the chamber and annealed for 12 hours at a temperature of 1023 K to remove surface contaminants prior to deposition. Deposition took place in an ultra-high purity (99.999%) argon gas atmosphere at a working pressure of 4 $\times 10^{-1}$ Pa.

Composite $Fe_{25}Pt_{75}$ sputter targets (99.99% purity) purchased from ACI Alloys were employed to predetermine the correct stoichiometric ratio between Fe and Pt atoms in the deposited $FePt_3$ films. To obtain the chemically ordered phase of $FePt_3$, the MgO substrate was held at a temperature of 1023 K throughout the deposition process. The optimal growth temperature had been determined from preliminary investigations [167]. The substrate to target distance was 125 mm, and the angle of incidence relative to the substrate normal was approximately 20 degrees. Thin epitaxial seed layers of Cr (3 nm) and Pt (6 nm) were deposited prior to the $FePt_3$ film to improve the crystalline orientation of the film, and largely suppress the (111)-oriented $FePt_3$ impurity phase. The power to the magnetron guns was fixed to 40 W during the deposition of Cr and Pt layers, and 60 W for the deposition of $FePt_3$. Deposition rates of 0.02, 0.12 and 0.10 nm sec^{-1} were calibrated for the Cr, Pt and $FePt_3$ targets, respectively, from preliminary X-ray reflectivity measurements. During deposition, the surface epitaxy of the film was monitored by *in situ* reflection high-energy electron diffraction. The $FePt_3$ film grew epitaxially on the (001)-oriented MgO substrate to a nominal thickness of 280 nm. To inhibit film oxidation, the $FePt_3$ film was capped with a 9 nm Pt cover layer.

Structural analysis of the epitaxy and chemical order of the as-prepared $FePt_3$ film was conducted by high-angle XRD. The film was positioned on the horizontal sample stage of the diffractometer and the X-ray beam aligned to the film surface by scanning 2θ at an incident angle of zero degrees. Alignment to the film lattice then proceeded by performing a further 2θ scan with the incident X-ray beam fixed to the ω position of a film diffraction peak (i.e., at $\omega = 2\theta/2$). The resulting XRD spectrum of the as-prepared $FePt_3$ film measured along the Q_z direction (i.e., normal to the film surface) is shown in Figure 3.2, alongside the XRD spectrum of a clean MgO substrate for comparison. The data sets were recorded over a 2θ range from 20° to

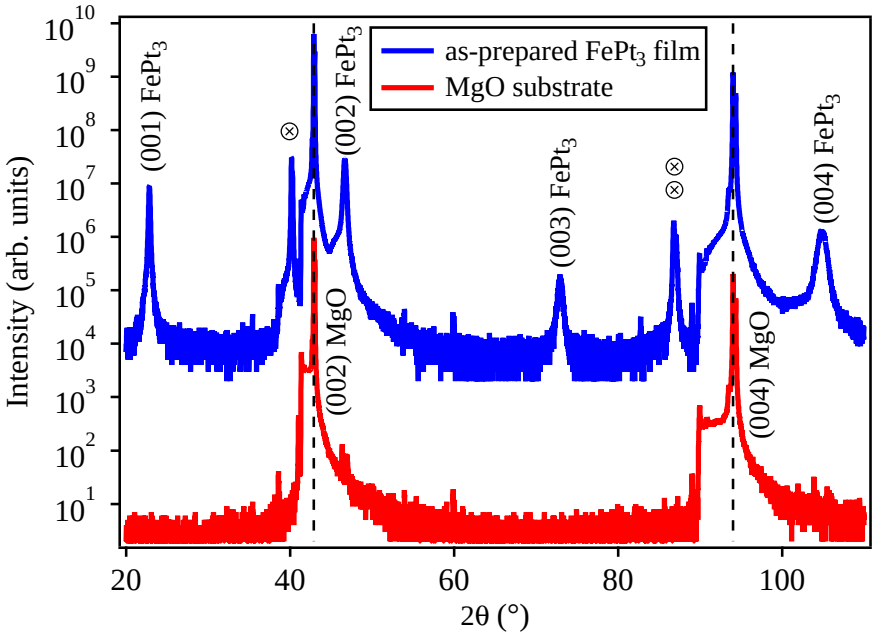

Figure 3.2: XRD spectrum of the as-prepared $FePt_3$ film and a clean MgO substrate (shown for comparison). The presence of $(00l)$-type $FePt_3$ reflections reveals the preferred epitaxial growth direction of the film along the [001] crystallographic axis

110° and obtained with a constant ω-offset of 0.03° to reduce the relative intensity of the substrate reflections. The XRD pattern of the $FePt_3$ film (which is shifted on the ordinate axis for clarity) displays four $(00l)$-type $FePt_3$ Bragg reflections. Figure 3.3 displays enlarged views of each reflection, and the corresponding Voigt function fit (i.e., the convolution of a Gaussian and a Lorentzian fit) used to extract the 2θ position, full-width-at-half-maximum (FWHM) and integrated intensity I_β of the diffraction peak. The fitting results are summarised in Table 3.1. The low-2θ shoulders which surround the (002) and (004) $FePt_3$ reflections in Figure 3.3 most likely originate from the thin epitaxial Pt seed and capping layers of the as-prepared film. Using Equation 2.5, the average out-of-plane lattice parameter of the film is calculated to be $c = 3.89 \pm 0.01$ Å. This value is consistent with reported bulk ($c = 3.87$ Å) [14] and previous thin-film values ($c = 3.88$ Å) [174, 53]. Because the total unit cell volume of the film must be conserved, this implies the lattice is strained by 0.5% in the out-of-plane direction.

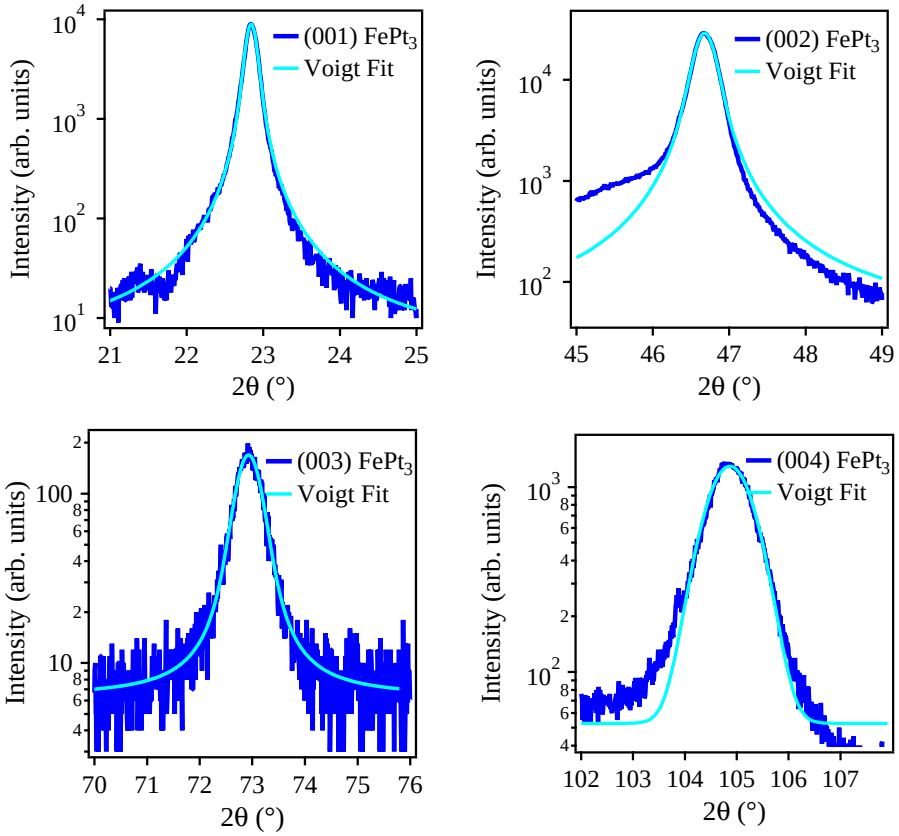

Figure 3.3: Enlarged views of the (001), (002), (003), (004) $FePt_3$ reflections. Each data set has been fitting with a Voigt function. The low-2θ shoulders of the (002) and the (004) $FePt_3$ reflections most likely originate from the thin epitaxial Pt seed and capping layers of the film.

The reflections labelled $\otimes$ and $\otimes\otimes$ in Figure 3.2 originate from diffraction from the (111) and (222) crystal planes of the $FePt_3$ film, respectively. While every effort was made to suppress the formation of [111]-oriented crystallites — namely, through the combined use of Cr and Pt seed layers — these impurity phases are difficult to avoid during $FePt_3$ film deposition.

The strong Bragg intensity of the (002) and (004) film reflections reveals the preferred epitaxial growth direction of the $FePt_3$ film along the [001] crystallographic axis. An assessment of the degree of epitaxy is made by measuring ω-rocking profiles, which are obtained by fixing 2θ while scanning ω across a shallow range either side of the

$FePt_3$ reflection	2θ (°)	FWHM (°)	I_β (arb. units)
(001)	22.84 ± 0.01	0.17	5.30
(002)	46.68 ± 0.04	0.32	31.91
(003)	72.93 ± 0.14	0.56	0.31
(004)	104.87 ± 0.18	0.97	4.95

Table 3.1: Experimental parameters of the peak positions (2θ), FWHMs and the integrated X-ray diffraction intensities (I_β) of the four ($00l$)-type $FePt_3$ Bragg reflections displayed in Figure 3.3.

specular $\omega = 2\theta/2$ condition. As a result, ω-rocking curves provide a measure of the divergence of crystallite orientations from the out-of-plane epitaxial axis to give an overall indication of the structural quality of the film. Both the film and the substrate are assessed via ω-rocking because the FWHM of the substrate reflection gives the experimental resolution of the diffractometer, which is then subtracted from the FWHM of the film reflection to obtain the true mosaicity of the crystal lattice. Furthermore, because the uncertainty in the experimental XRD data varies as $\theta(\Delta\lambda/\lambda)$, only reflections which are positioned low in 2θ are used in the final evaluation of the film's epitaxial quality. Accordingly, Figure 3.4 displays the normalised ω-rocking profiles of the (002) $FePt_3$ film and (002) MgO substrate reflections. The $FePt_3$ reflection is notably broader than the MgO substrate reflection, indicating a greater texture in the film. This texture, is however less than 1°, and thus indicates good structural alignment of the lattice planes distributed over the entire film thickness. By comparing the FWHMs of the (002) film and substrate reflections, it is determined that the $FePt_3$ crystallites exhibit an absolute mosaic spread of 0.81 ± 0.03° from the [001] crystallographic axis.

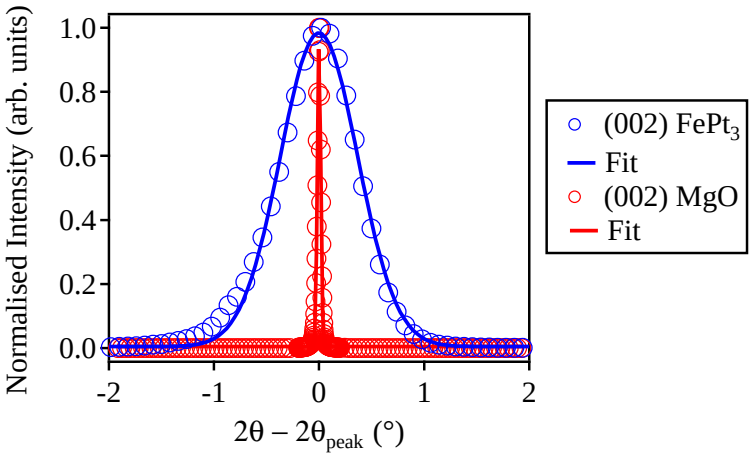

Figure 3.4: ω-rocking curves of the (002) film and substrate reflections used in determining the absolute divergence of the $FePt_3$ crystallite orientations from the epitaxial axis.

The amplitude of scattering from the hkl planes of a unit cell consisting of n basis atoms at coordinates (x_i,y_i,z_i) is defined by the structure factor F_{hkl} [134],

$$F_{hkl} = \sum_i f_n(Q) e^{2\pi i(hx_i+ky_i+lz_i)}, \tag{3.1}$$

where $Q_z = 4\pi \sin\theta/\lambda$. The atomic form factor $f_n(Q)$ is given by

$$f_n(Q) = (f_0(Q) + f'(\lambda) + if''(\lambda))e^{-DW}, \tag{3.2}$$

where $f_0(Q)$ is the first-order cross section, which can be calculated over the Cromer-Mann coefficients [60],

$$f_0(Q) = c + \sum_{i=1}^{4} a_i e^{(-b_i Q^2)}. \tag{3.3}$$

$f'(\lambda)$ and $f''(\lambda)$ are the real and imaginary parts of the dispersion correction for forward scattering [58], and the exponent $(-DW) = (-BQ^2)$ is the Debye-Waller factor where B is a temperature-dependent constant [252]. By assigning f as the real part of the

dispersion correction, so that $f = f_0 + f'$, Equation 3.1 becomes,

$$F_{hkl} = (f_{\mathrm{Fe}} + if''_{\mathrm{Fe}})e^{-DW_{\mathrm{Fe}}} + (f_{\mathrm{Pt}} + if''_{\mathrm{Pt}})e^{-DW_{\mathrm{Pt}}}[e^{2\pi i(h+k)} + e^{2\pi i(h+l)} + e^{2\pi i(k+l)}] \quad (3.4)$$

for the case of chemically ordered $FePt_3$ where Fe is located at (0,0,0) and Pt is located at (½, ½, 0), (½, 0, ½) and (0, ½, ½) within the cubic unit cell. It follows that,

$$F_{hkl} = \begin{cases} (f_{\mathrm{Fe}} + if^{"}_{\mathrm{Fe}})e^{-DW_{\mathrm{Fe}}} + 3(f_{\mathrm{Pt}} + if^{"}_{\mathrm{Pt}})e^{-DW_{\mathrm{Pt}}}, & \text{if } hkl \text{ all even/odd} \\ (f_{\mathrm{Fe}} + if^{"}_{\mathrm{Fe}})e^{-DW_{\mathrm{Fe}}} - (f_{\mathrm{Pt}} + if^{"}_{\mathrm{Pt}})e^{-DW_{\mathrm{Pt}}}, & \text{if } hkl \text{ mixed even/odd.} \end{cases} \quad (3.5)$$

The implication of this result is that the structure factor prevents diffraction from mixed-integer hkl reflections in the chemically disordered state where the Fe and Pt sites are non-unique. Hence, the existence of mixed-integer hkl reflections — also known as superstructure reflections — is evidence of long-range chemical order in $FePt_3$. Consequently, the integrated intensities of superstructure reflections I_{Super} in a diffraction spectrum can be used to provide a quantitative measure of the long-range chemical-order parameter S of a specimen [240],

$$S = \sqrt{\frac{(I_{\mathrm{Super}}/I_{\mathrm{Fund}})_\beta}{(I_{\mathrm{Super}}/I_{\mathrm{Fund}})_\alpha}}, \quad (3.6)$$

where I_{Fund} are the integrated intensities of fundamental reflections which are independent of the degree of long-range chemical order in the specimen. I_β denotes integrated intensities obtained experimentally by fitting Voigt functions to the diffraction peaks of the specimen whose S is to be measured. I_α describes integrated intensities for a theoretical specimen with perfect chemical order (i.e., of $S = 1$) calculated over

$$I_\alpha = |F_{(hkl)}F^*_{(hkl)}| \times L \times D, \quad (3.7)$$

where L is the Lorentz polarisation factor [63],

$$L = \frac{1 + \cos^2(2\theta)}{2\sin(2\theta)}. \tag{3.8}$$

D is used to correct for the film thickness t [30],

$$D = 1 - \exp\left(\frac{-2\mu t}{\sin\theta}\right), \tag{3.9}$$

where the linear absorption coefficient μ,

$$\mu = \rho \sum_n w_n \times (\mu/\rho)_n, \tag{3.10}$$

is calculated from the mass attenuation coefficient $(\mu/\rho)_n$ weight fraction w_n of each basis atom n in a lattice of density ρ. At an X-ray wavelength λ (E = 8.052 keV) = 1.5406 Å, the mass density of $FePt_3$ (ρ = 18.37 g cm^{-3}) gives μ_{FePt_3} = 4141 cm^{-1} [116].

The long-range chemical order parameter S of the as-prepared $FePt_3$ film has been calculated based on the four possible $(I_{\text{Super}}/I_{\text{Fund}})_\beta$ combinations of the experimental intensities provided in Table 3.1. The parameters used to calculate the corresponding fundamental and superstructure I_α values are summarised in Table 3.2. The values of f''_{Fe} and f''_{Pt} are 3.20 and 6.93, respectively [58]. Using Equation 3.6, the average S of the as-prepared $FePt_3$ film (with t = 280 nm) is found to be 82 ± 4 %, where the error in S originates from the uncertainty in the Voigt fit of the experimental data. As such, the film can be described as a homogeneous mixture of chemically ordered domains which occupy 82% (and chemically disordered domains which occupy 18%) of the whole film volume. The computed value of S is comparable to those previously obtained for $FePt_3$ films grown by following the same optimised sample preparation

(hkl)	2θ (°)	f_{Fe}	DW_{Fe}	f_{Pt}	DW_{Pt}	L	D	I_α (arb.units)
(001)	22.84	21.48	0.009	67.45	0.006	2.38	0.69	3.46
(002)	46.68	16.99	0.038	57.18	0.024	1.01	0.44	15.35
(003)	72.93	13.09	0.086	48.21	0.056	0.57	0.32	0.21
(004)	104.87	10.08	0.150	40.95	0.100	0.55	0.25	2.07

Table 3.2: Parameters used in the calculation of the theoretical integrated intensities (I_α) for an $FePt_3$ specimen with perfect chemical order (i.e., of $S = 1$).

conditions [167, 244].

The average size of the chemically ordered crystallites Λ which occupy 82% of the as-prepared $FePt_3$ film can be approximated using the Scherrer equation [63],

$$\Lambda = \frac{K\lambda}{A\cos(2\theta)}, \tag{3.11}$$

where the Scherrer constant K describes the geometry of the crystallite, λ is the X-ray wavelength, A is the FWHM of the diffraction peak (corrected for the resolution of the X-ray instrument) at the corresponding 2θ diffraction angle. Adopting a K of 0.94 to reflect spherical crystallites of cubic symmetry [286], an out-of-plane crystallite size of 62 nm is approximated for the as-prepared film from the (001) $FePt_3$ diffraction peak. An estimate of the error in the calculated value is not provided because the Scherrer formulation neglects peak broadening contributions originating from inhomogeneous strain and crystal lattice imperfections (e.g., grain boundaries, dislocations, stacking faults) and therefore provides a lower bound approximation only of the average crystallite size.

3.3 Ion-Beam Theory and Monte Carlo Simulation

When energetic ions pass through matter they lose their energy E via electronic and nuclear scattering processes with the atomic nuclei of the target [92, 275, 71]. At ion speeds much lower than the Bohr speed of the target electrons v_0, the ion is neutralised by electron capture, and in this regime collisions are dominated by elastic momentum-transfer resulting in nuclear-energy loss [32]. At increased ion speeds, energy losses occurring via nuclear processes decrease as $1/E$ and inelastic collisions with the target electrons becomes the dominant energy-loss mechanism [161]. In the range of ion speeds from $0.1v_0$ to $Z^{2/3}v_0$ (with Z being the atomic number of the ion), electronic-energy losses are proportional to $E^{1/2}$ [302]. At ion speeds much higher than v_0, ion-energy loses are given by the Bethe-Bloch relation [25], and in this regime the ion can lose electrons up to the state of full-ionisation.

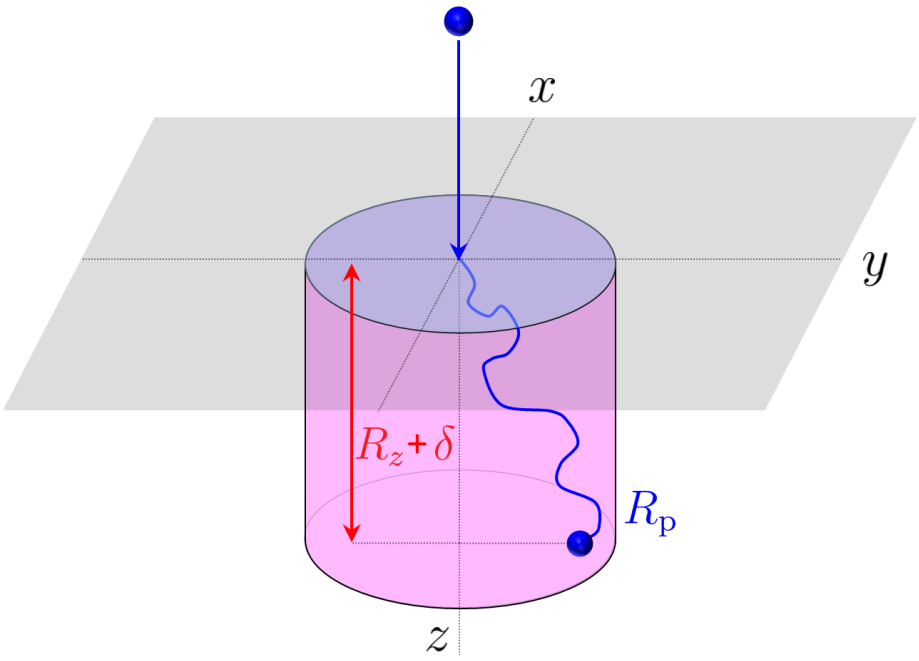

Figure 3.5: The ion-target interaction volume generated by the intrinsic straggling behavior of a point irradiation incident upon a sample surface. The ion comes to rest at the end of the path range R_p at a projected distance equal to $R_z + \delta$ beneath the target surface.

Because the amount of energy-transfer per interaction, and the number of interactions per ion path are both statistical quantities, the energy and momentum of the ion ensemble becomes distributed over a finite volume in the underlying target material [92]. Figure 3.5 illustrates this concept. The initial ion trajectory is perpendicular to the target surface (i.e., co-linear to the z-axis) which lies in the xy-plane. For convenience, we define the z-axis as the projected axis, and the xy-plane (which is governed by cylindrical symmetry) as the lateral axis. As the ion enters the material it scatters from the target's atomic lattice, forming a complex collision cascade, until coming to rest when the ion energy decreases below the minimum displacement energy. The mean projected range R_z of the i^{th} ion in an ensemble of N ions is given by [301],

$$R_z = \frac{1}{N}\sum_i z_i = \langle z \rangle. \tag{3.12}$$

The second moment of the projected range distribution, known as the projected straggling δ, is calculated at the square root of the variance [301],

$$\delta = \left(\sum_i \frac{(z_i - R_z)^2}{N}\right)^{1/2} = \langle \Delta z_i^2 \rangle^{1/2}, \tag{3.13}$$

where the variance is the expectation of the sum of the squared deviation of the ion ranges from R_z. The third and the fourth moments of the projected range distribution, respectively known as the skewness ξ [301],

$$\xi = \sum_i \frac{(z_i - R_z)^3}{N\delta^3} = \frac{\langle \Delta z_i^3 \rangle}{\langle \Delta z_i^2 \rangle^{3/2}}, \tag{3.14}$$

and the kurtosis γ [301],

$$\gamma = \sum_i \frac{(z_i - R_z)^4}{N\delta^4} = \frac{\langle \Delta z_i^4 \rangle}{\langle \Delta z_i^2 \rangle^2}, \tag{3.15}$$

are dimensionless quantities which provide information about the mode of the distribution (skewness) and the extent to which the tails of the distribution deviate from a true Gaussian distribution (kurtosis).

Essentially, there are two distinguishing parameters of an ion beam which can be used to predetermine, to a large extent, the three-dimensional spread of the final ion distribution in the target. These parameters are: the ion fluence and E. The ion fluence controls the disorder density by predetermining how many ions are active per unit target area. While E follows a power-law relationship with the path range R_{p} of the ion in a target, varying approximately between $R_{\mathrm{p}} \propto E^{1/2}$ to $E^{5/3}$ below and above the stopping power maximum, respectively [229]. For the investigations described in this chapter, we are exclusively concerned with employing He^{+} ions to chemically disorder $FePt_3$ films, because of their small size, chemical inertness and inability to ablate target surface-atoms. We place the following two requirements upon the characteristics of the He^{+} beam which is to be utilised in the proceeding experiments. The first restriction is placed upon E, to ensure that the resultant ion disorder profile remains confined to a fractional sub-surface volume of the total film thickness, such that a room-temperature FM/PM interface can be created within the 'bulk' of the $FePt_3$ layer. The second restriction is placed upon the ion fluence, to ensure that the chemically ordered Fe and Pt sites of the as-prepared $FePt_3$ film become markedly chemically disordered such that a PM-to-FM phase transformation can be achieved within the irradiated portion of the $FePt_3$ film.

In order to determine the optimal energy and fluence characteristics of the He^{+} beam, Monte Carlo simulations were performed. The Stopping and Range of Ions in Matter (SRIM) software [303] was used to compute energy-loss tables to provide details of the nominal R_z and δ of He^{+} ions in $FePt_3$ as a function of E. Within SRIM the Transport of Ions in Matter (TRIM) sub-routine can be used to compute with high

accuracy the stochastic interactions of energetic ions in targets, which are assumed amorphous [301]. TRIM was employed to model the collisional damage generated by He^+ ion cascades in a $FePt_3$ target to provide a prediction of the experimental three-dimensional ion distribution. However, it should be noted that TRIM does not account for mechanisms such as defect migration and damage accumulation, nor is it able to model crystalline effects such as ion-channeling [301, 166]. Ion-channeling occurs most frequently when an ion beam falls at an incident angle parallel to a major crystal direction of a crystalline target [249]. This results in ions predominately undergoing small-angle deflections (i.e., losing less energy per collision) along a specific crystal channel [5], which increases their mean projected range relative to an amorphous structure [166]. As such, if ion-channeling or defect migration plays a significant role in the crystalline $FePt_3$ film, we may expect the actual ion distribution to be elongated along the projected axis (when compared to the distribution modelled via TRIM).

The stopping power S_p of a material is defined as the average ion-energy loss per unit path length [275, 92], and is subsequently dependent upon E (i.e., $S_p = -\mathrm{d}E/\mathrm{d}z$). Table 3.3 presents the nominal rates for He^+ ion-energy losses occurring via electronic and nuclear processes per unit path length in a bulk density $FePt_3$ target. Based on the abovementioned experimental requirements, 15 keV is chosen as the preferred He^+ ion energy to be used in all the subsequent experimental irradiations presented in this chapter. According to Table 3.3, the nominal R_z and δ of 15 keV He^+ ions in $FePt_3$ are 34.3 nm and 41.9 nm, respectively. These two projected lengths imply that 15 keV He^+ ions can be used to produce a disorder contour which is symmetric across a 76.2 nm region of the $FePt_3$ film (neglecting the third and fourth moments of the ion-range distribution), which can subsequently be used to create a room-temperature FM/PM heterostructure from the as-prepared chemically-well ordered 280 nm-thick $FePt_3$ film.

He^+ energy (keV)	$dE/dz_{Elec.}$ (10^2 keV/nm)	$dE/dz_{Nucl.}$ (10^2 keV/nm)	R_z (nm)	δ (nm)
0.01	0.31	0.25	0.2	0.6
0.1	0.99	0.75	0.7	1.9
1	3.14	1.51	3.3	7
5	7.02	1.74	12.2	19.9
10	9.93	1.64	23.2	31.9
15	12.27	1.52	34.3	41.9
20	14.45	1.42	45.4	50.6
25	16.35	1.33	56.5	58.3
30	18.08	1.25	67.5	65.2

Table 3.3: Nominal rates of energy loss occurring via electronic and nuclear processes for energetic (0.01 − 30 keV) He^+ ions incident upon a bulk density $FePt_3$ target, and the resulting R_z and δ characteristics. All values are calculated using SRIM.

To evaluate the effect of ion fluence on the ion-target interaction gradient, DPA profiles were calculated over [112],

$$\text{DPA} = \frac{N(d) \times F \times M}{\rho \times N_A}, \tag{3.16}$$

where $N(d)$ is the summation of vacancies generated by the incident ion at depth d (obtained from Monte Carlo simulation), F is the ion fluence, M and ρ are the molar mass and mass density of the target material, respectively, and N_A is Avogadro's constant. Figure 3.6 displays the DPA profiles calculated using Equation 3.16 for 15 keV He^+ ions with fluences of 2 $\times 10^{16}$ ions cm^{-2} (low-fluence) and 2 $\times 10^{17}$ ions cm^{-2} (high-fluence) incident upon a $FePt_3$ target. To calculate these profiles, full-damage cascade calculations were performed in TRIM using a total of 10^6 incident ions directed perpendicular to the surface of a bulk density (ρ = 18.37 g cm^{-3}) amorphous $FePt_3$ target. A 9 nm Pt cover layer was initially considered as part of the calculation (to replicate the experimental sample), however later removed for simplicity, as it was found to have no sizable effect upon the simulation result. It should be noted that

the DPA profiles in Figure 3.6, unlike the R_z and δ data given in Table 3.3, account for the third and fourth moments of the ion distribution, giving the distributions an overall quasi-Gaussian character. The positive skewness of the distributions ($\xi = 0.368$) implies that the mode of each distribution is less than the mean depth, which causes the distributions to skew away from the surface. Furthermore, the constant kurtosis ($\gamma = 2.63$) of the two DPA profiles indicates that the ion distributions exhibit broader tails than a normal distribution.

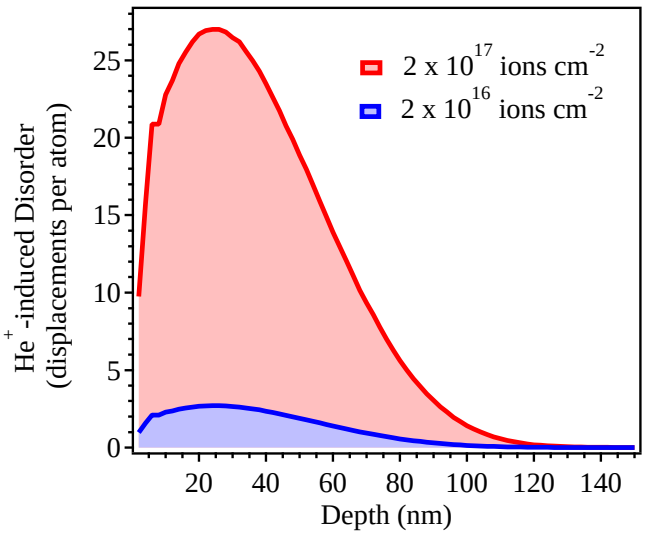

Figure 3.6: DPA profiles obtained using Equation 3.16 for 15 keV He^+ ions with fluences of 2 $\times 10^{16}$ ions cm^{-2} and 2 $\times 10^{17}$ ions cm^{-2} incident upon a bulk density amorphous $FePt_3$ target.

Independent of the ion fluence, it is computed that the quasi-Gaussian DPA profiles (which have a resolution of *ca.* 0.01 DPA) exhibit peak centroids located 28 nm beneath the target surface, and equally extend approximately 120 nm into the sub-surface region of the $FePt_3$ target. At the peak location, a fluence of 2 $\times 10^{16}$ He^+ ions cm^{-2} causes the $FePt_3$ target atoms to undergo approximately 2.5 lattice displacements on average. Increasing the ion fluence by an order of magnitude (from 2 $\times 10^{16}$ ions cm^{-2} to 2 $\times 10^{17}$ ions cm^{-2}) results in a comparative order-of-magnitude enhancement to the

DPA of the $FePt_3$ target at each corresponding depth (i.e., $\approx$ 25 lattice displacements at the peak location). This trend suggests that disorder, and therefore ferromagnetism, can be tailored in $FePt_3$ by modifying the fluence of the irradiating ion. This is because higher ion fluences support a greater probability of interaction between the ion and the target atom, which should then give rise to a greater density of chemical order-to-disorder transformations throughout the $FePt_3$ domain structure. However, as one may easily visualise, 25 DPA (corresponding to a fluence of 2×10^{17} ions cm^{-2}) would lead to an extreme over-saturation of the site disorder needed to drive the room-temperature PM-to-FM transition in $FePt_3$. For example, site disorder below 1 DPA resulting from light-ion irradiations (i.e., He^+, N^+, Ne^+) has been shown to be sufficient to drive magnetic phase transitions in a range of comparable alloyed systems, such as $Fe_{60}Al_{40}$, $Fe_{50}Rh_{50}$, $Fe_{50}Pd_{50}$ and $Fe_{50}Pt_{50}$, as well as $FePt_3$ itself [190, 108, 146, 23, 174]. As such, a fluence of 2×10^{16} ions cm^{-2}, analogous to a peak DPA of 2.5, is implemented as the primary ion fluence employed in the proceeding sections.

3.4 Sample Irradiation and Characterisation

To investigate the role of ion-induced disorder on the magnetic and microstructural properties of $FePt_3$, He^+ irradiations were performed on the chemically well-ordered $FePt_3$ films characterised in Section 3.2. The irradiations were performed at room temperature on the LEII-Surface Engineering beamline of the 6 MV SIRIUS Tandem Accelerator at the Centre for Accelerator Science, ANSTO [222]. 15 keV He^+ ions at a fluence of 2×10^{16} ions cm^{-2} were directed normal to the film surface. A broad-ion beam was employed during the irradiation to ensure the resulting atomic collision profile was invariant across the xy-plane of the film (creating a DPA profile with translational in-plane symmetry), while remaining heterogeneous over the projected

depth. Such an experimental configuration affords an artificial construction of a one-dimensional irradiation profile which is independent of all external lateral-scattering contributions (e.g., effects due to beam focusing and/or shadowing effects associated with masked irradiations), and only dependent upon the inherent depth-varying nature of the DPA curve. The reduction from a three-dimensional to a one-dimensional investigation of the magnetic interface is justified, because the ion undergoes nuclear stopping in the target material, forming a complex collision cascade comprising of large deflection angles, in which case the ion-beam scattering amplitude is form factor independent. This means the lateral (xy-plane) and projected (z-axis) interaction gradients are effectively commensurate. Hence, the magnetic and structural properties of the terminating one-dimensional FM/non-FM interface arising from this arrangement will be exclusively dependent upon the intrinsic straggling characteristic of the ion distribution in the $FePt_3$ film. In the proceeding section, the volume-averaged magnetic moment and the cross-sectional morphology of an un-irradiated (as-prepared) and an irradiated (15 keV, 2 $\times 10^{16}$ He^+ cm^{-2}) $FePt_3$ film are comparatively investigated by magnetometry and TEM. Detailed knowledge about the evolution of the magnetic, atomic and microstructural properties of $FePt_3$ upon He^+ irradiation is gained.

3.4.1 Magnetometry

The volume-averaged magnetic moments of the films were investigated by VSM magnetometry. The samples were measured in a Quantum Design Physical Properties Measurement System (PPMS) VSM located at ACNS, ANSTO. The films were field-cooled from room temperature to 10 K in a 10 kOe in-plane magnetic field, and field-cycled three times between $\pm$ 20 kOe to provide magnetic training prior to data acquisition. Magnetic hysteresis loops were measured at 10 K and 300 K upon warm-

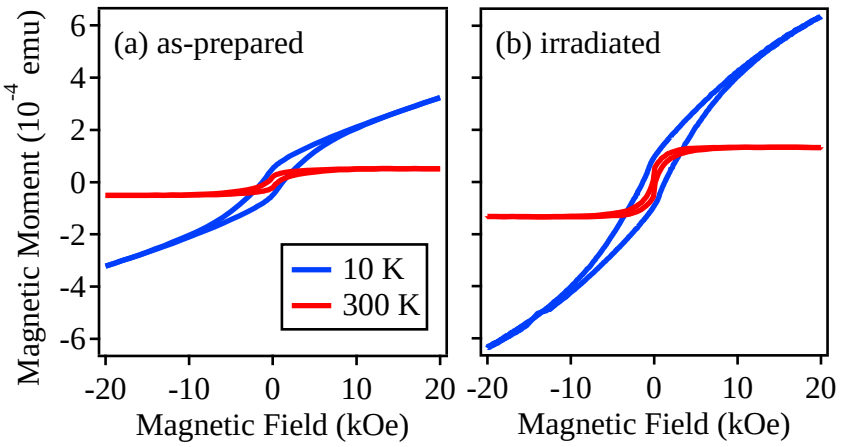

Figure 3.7: *m-H* behaviours of the (a) as-prepared and the (b) irradiated $FePt_3$ films measured at 10 K and 300 K.

ing across a ± 20 kOe field range. Data sets have been corrected for the diamagnetic response of the substrate. The 10 K and 300 K magnetic moment vs field (*m-H*) variations of the as-prepared and irradiated $FePt_3$ films are shown in Figure 3.7. The irradiated film displays a higher magnetic moment compared to the as-prepared film. At 10 K, in the presence of a 20 kOe external field, the magnetic moment of the sample increases from 3.2 x10^{-4} emu (as-prepared) to 6.3 ×10^{-4} emu after irradiation[1]. This is in agreement with ferromagnetism existing within chemically disordered grains, which take the largest volume fraction within the irradiated film. However, detailed quantitative conclusions of the former sample's magnetic properties are difficult, because magnetometry averages over both the irradiated and non-irradiated volumes of the film. Despite this, we observe the following: At the lowest temperature of 10 K, neither film can be fully saturated in the highest applied field of 20 kOe. In both cases we observe a hysteretic behaviour below |H| = 10 kOe and a non-hysteretic linear increase in magnetic moment above |H| = 10 kOe. This suggests there are two magnetic contributions to the overall moment of the sample. The hysteretic behaviour of

[1] A combination of SI and CGS units are used throughout this thesis. Appendix A provides a table of magnetic quantities and the corresponding conversion factor between SI and CGS units.

the low-field ($|H| < 10$ kOe) regions, which display enhanced coercivity and magnetic moment upon cooling to 10 K, highlights the presence of relatively soft FM domains throughout both films. While the non-saturation feature in the high-field ($|H| > 10$ kOe) region, and the general 'wasp-waisted' shape of the hysteresis curves, are equated to populations of superparamagnetic, PM, and weakly coupled AFM moments. These defect moments, which effectively work to increase the film's magnetic hardness, have the ability to align along the applied-field direction, giving the hysteresis curves linear characteristics in the high-field regions. The defects are believed to be more prevalent in the irradiated film because of the enhanced coercive fields and the enhanced positive slope of the data in the high-field region, when compared to the as-prepared film. Moreover, the weakly coupled AFM defect spins may either partially rotate into the field direction, or exchange couple to neighbouring FM domains, where the former act as pinning centres causing the moment to increase reversibly with the field. This picture is supported by the high-temperature (300 K) magnetometry data recorded well above the AFM T_N of $FePt_3$. Here the slope of the high-field region reduces to zero and both samples can be fully saturated in external fields of 10 kOe. As a final note, the 10 K hysteresis loops of the as-prepared and irradiated films are non-symmetric about the applied field axis, where this effect is greatest observed for the irradiated film. This is due to a particular type of exchange coupling — formally known as exchange bias [264, 135] — which is generated between neighbouring FM and AFM domains within the as-prepared film, and additionally at the FM/AFM interface within the irradiated film at low temperature. The relationship between chemical disorder and exchange bias has previously been studied for single-layer $FePt_3$ films similar to the as-prepared film considered in this work [244], as well as for magnetically stratified $FePt_3$ multilayers obtained by modifying the substrate temperature during deposition [243]. In Section 3.6, a detailed investigation into the exchange bias behaviour of the

irradiated $FePt_3$ film will be presented.

3.4.2 Transmission Electron Microscopy

The microstructural characteristics of the as-prepared and the irradiated films were comparatively investigated by TEM. Samples were fabricated using a Zeiss Auriga 60 crossbeam focussed-ion beam and TEM images were recorded using a JEOL 2200FS TEM device (operating at 200 kV) at ANSTO. Figure 3.8(a) shows the cross-sectional TEM image of the as-prepared $FePt_3$ film. The $FePt_3$ layer thickness is found to be approximately 280 nm, which agrees with the nominal film thickness estimated from the sputtering rate. To study the presence and growth of chemically disordered domains within irradiated $FePt_3$, the films were investigated by dark-field TEM (DF-TEM) [90]. Figure 3.8 shows the DF-TEM morphologies of the (b) as-prepared and the (c) irradiated $FePt_3$ films. The DF-TEM images of the irradiated film were recorded within the ion-impacted volume. The images were measured with a $\{001\}$ diffracted beam, where (for the same reasons as in Equation 3.5) diffractions along the $\langle 001 \rangle$ crystallographic directions are structure factor forbidden by the chemically disordered face-centred-cubic $FePt_3$ structure. Therefore, when ordered domains are viewed under the DF-TEM condition they will have a bright contrast-level, and correspondingly disordered domains will appear to have a darker contrast-level. The domain characteristics of the as-prepared film in Figure 3.8(b) are predominantly chemically ordered as seen by the high density of bright contrast areas. The average size of the chemically ordered domains in the as-prepared film complements the 62 nm lower-bound approximation obtained from Equation 3.11. After irradiating the $FePt_3$ film with 15 keV He^+ ions at a fluence of 2×10^{16} ions cm^{-2}, in Figure 3.8(c), the areal density of dark contrast domains increases slightly, and the average domain size noticeably reduces

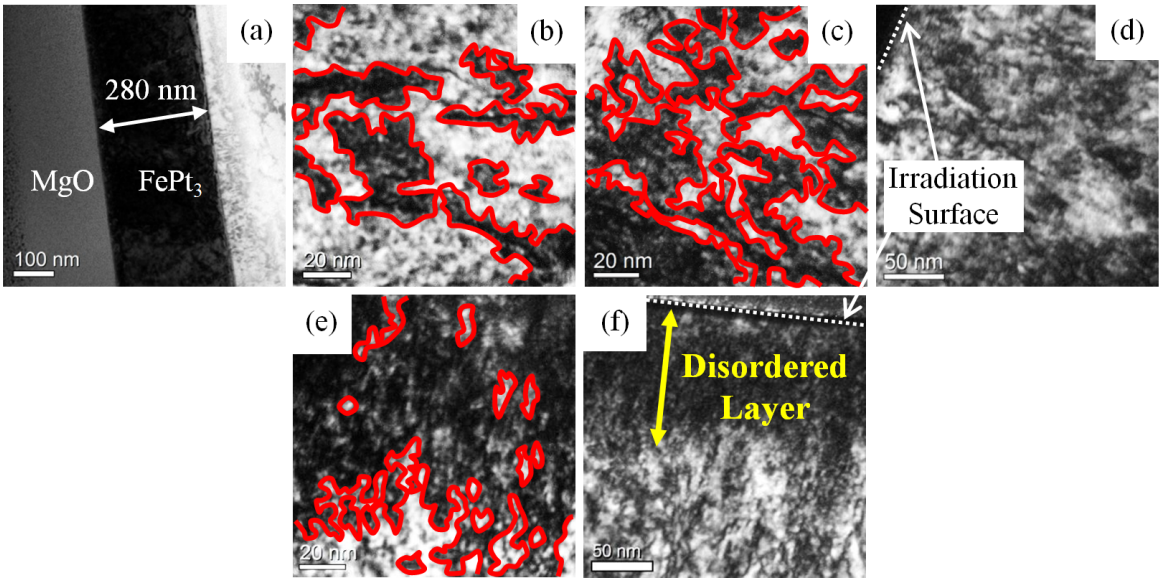

Figure 3.8: (a) Cross-sectional TEM image of the as-prepared film, showing the 280 nm $FePt_3$ film thickness. DF-TEM morphologies of the (b) as-prepared film and the (c) irradiated (2×10^{16} He^+ ions cm^{-2}) $FePt_3$ film. The red boarders are guides for the eye to separate domains of high chemical order (bright-contrast level) and high chemical disorder (dark-contrast level). (d) Low-magnification DF-TEM image of the irradiated (2×10^{16} He^+ ions cm^{-2}) $FePt_3$ film. (e) DF-TEM morphology and (f) low-magnification DF-TEM image of the irradiated-reference (2×10^{17} He^+ ions cm^{-2}) $FePt_3$ film. The location of the film surface and the 120 nm-thick ion-induced chemically disordered layer are shown.

to approximately 20 nm after irradiation. To observe the chemically disordered layer within the irradiated film, low-magnification DF-TEM imaging was performed. However, as seen in Figure 3.8(d) there is no appreciable change in colour contrast between the sub-surface (irradiated) and the bulk (un-irradiated) domains, despite the magnetometry data in Figure 3.7 showing evidence of ion-induced ferromagnetism. This is believed to be because of the disorder level, which according to Figure 3.6 is predicted to be no greater than ≈ 2.5 DPA, being below that required to observe dark contrast via TEM (while being above the VSM resolution of 10^{-6} emu). To overcome the TEM 'resolution' problem to enable an observation of the chemical order/disorder interface within the irradiated film, an additional 'reference' irradiation was performed at a fluence of 2×10^{17} ions cm^{-2}. According to Figure 3.6, irradiating with 15 keV He^+ ions

at a fluence of 2 $\times 10^{17}$ ions cm^{-2} will result in an order-of-magnitude enhancement to the DPA while preserving the maximum He^+ penetration depth (when compared to an irradiation using 15 keV He^+ ions at a fluence of 2 $\times 10^{16}$ ions cm^{-2}). Figure 3.8(e) and Figure 3.8(f) respectively show the high- and low-magnification DF-TEM images of the irradiated-reference $FePt_3$ film. In Figure 3.8(e), the microstructural domains of the film irradiated with the highest ion-fluence are shown to be approximately 10 nm in diameter and based on the observation of majority dark contrast domains, it is interpreted that a predominantly chemically disordered structure has been induced in the $FePt_3$ film by the irradiation process. Furthermore, a dark-contrast layer of chemical disorder is clearly observed in Figure 3.8(f). The thickness of the dark-contrast layer is approximately 120 nm, which is in good agreement with the He^+ ion penetration depths simulated in Figure 3.6. However, due to the resolution limitation of the TEM device (described above), the actual film thickness disordered by He^+ ions is expected to be broader than 120 nm (i.e., not equivalent to the thickness of the dark contrast layer). Moreover, due to the likelihood of ion-channeling and diffusion [5], the projected He^+ range may be even further increased beyond that simulated in Figure 3.6.

Selected-area electron diffraction (SAED) patterns were recorded for each $FePt_3$ film to enable a numerical evaluation of the degree to which chemically disordered domain formation occurs within $FePt_3$ subjected to varying He^+ ion fluences. Figure 3.9 models the expected change in position for chemically ordered $FePt_3$ lattice atoms during a low-energy He^+ irradiation. The $FePt_3$ crystal structures were modelled using CrystalMaker^{TM}, and SAED simulations were generated using SINGLECRYSTAL software [61]. The incident He^+ ions modify the site occupancy of the chemically ordered $L1_2$-type Fe-Pt nearest neighbours, resulting in the nucleation and growth of chemically disordered domains throughout the ion-impacted area. As seen by the

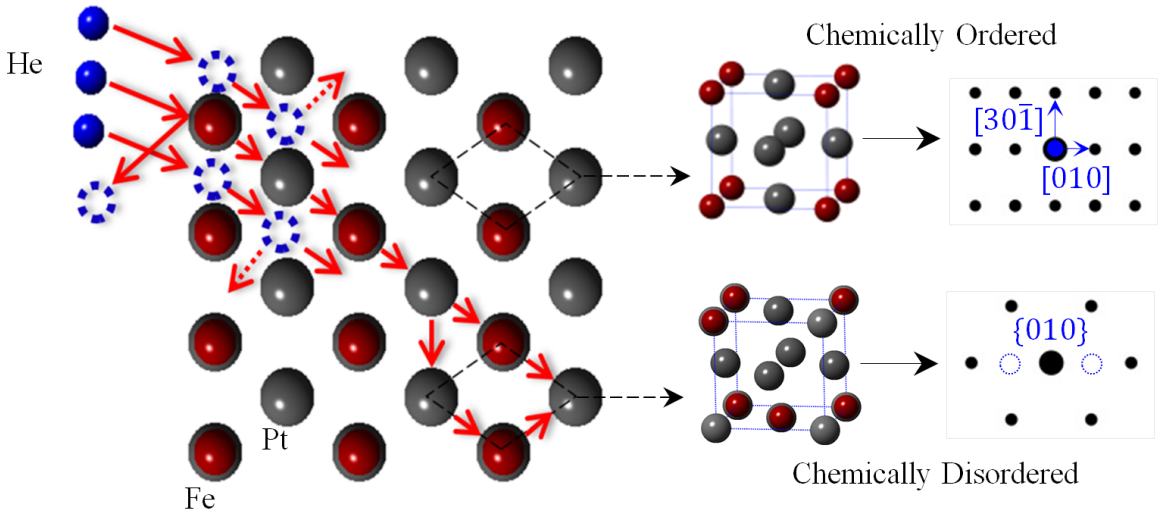

Figure 3.9: Schematic of the expected change in position among the $L1_2$ chemically ordered lattice atoms of $FePt_3$ during low-energy He^+ irradiation, showing the formation of ion-induced chemically disordered $FePt_3$ domains. The simulated [103] zone axis diffraction patterns for the fully chemically ordered and fully-chemically disordered arrangements of $FePt_3$ show the presence and absence of {010} diffraction peaks, respectively.

simulated SAED patterns, domains which are fully chemically disordered display the conventional face-centred-cubic structure and an absence of mixed even-/odd- integer (hkl) reflections, in contrast to domains which are fully chemically ordered. Figure 3.10 displays the SAED patterns obtained for the (a) as-prepared, (b) irradiated and (c) irradiated-reference $FePt_3$ films. Each SAED measurement was recorded in the [103] zone axis, and within the ion-impacted volumes of the two irradiated films. The presence of a single set of diffraction spots in all SAED images indicates that the single crystallinity of the $FePt_3$ lattice is preserved after irradiation. The line profiles through the fundamental (i.e., {000} and {0-20}) and superstructure (i.e., {0-10}) reflections are plotted as normalised intensity spectra to the right-hand side of each corresponding SAED pattern. The relative integrated intensity relationship between the {0-20} and the {0-10} reflections is proportional to the extent of chemical ordering, and as such, can be used to quantify directly the chemical-order parameter S of

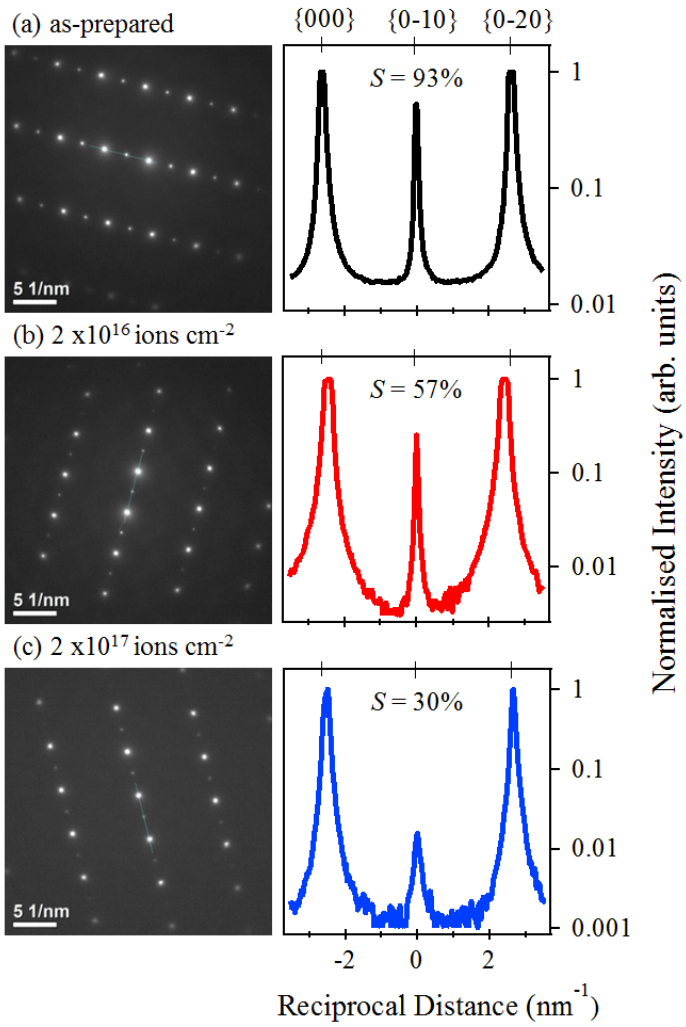

Figure 3.10: SAED patterns of the (a) as-prepared, (b) irradiated (2 $\times 10^{16}$ He^+ ions cm^{-2}) and (c) irradiated-reference (2 $\times 10^{17}$ He^+ ions cm^{-2}) $FePt_3$ films, with corresponding normalised intensity profiles through the {000}, {0-10} and {0-20} reflections. Using the relative intensity ratio between the {0-10} and {0-20} reflections, the chemical-order parameter S of each film can be determined.

each $FePt_3$ film. Performing the required calculations, using formalism described in Section 3.2, the S of the as-prepared film is found to decrease from 93% to 57% after irradiation with 2 $\times 10^{16}$ He^+ ions cm^{-2}. In Figure 3.10(c), irradiation with 2 $\times 10^{17}$ He^+ ions cm^{-2} substantially decreases the intensity of the {0-10} $FePt_3$ reflection, resulting in a calculated S of 30%. The general trend that S reduces as a function of the ion fluence is in collective agreement with the abovementioned DF-TEM re-

sults. It is duly noted that the calculated S is an average over the probed area which encompasses both higher-disorder (lower S) and lower-disorder (higher S) domains, which mirror the quasi-Gaussian trends of the simulated DPA profiles given in Figure 3.6. Nevertheless, for the current set of irradiated $FePt_3$ films, determining S from SAED patterns is a far more accurate approach than by, XRD, for instance, which can only provide a whole-film-averaged S due to the strong penetration of X-rays in matter (i.e., includes contributions from both the irradiated and un-irradiated volumes). This distinguishing point of difference between the two measurement techniques is further apparent when S of the as-prepared film obtained from global-probe XRD (82%) and local-probe SAED (93%) measurements is compared.

Figure 3.11 displays the filtered high-resolution TEM (HR-TEM) images of the (a) irradiated and the (b) irradiated-reference $FePt_3$ films. The measurements were recorded in the [110] zone axis over shallow depths in the near-surface ion-impacted regions of either film. The lattice parameter of the $FePt_3$ crystal structure in Figure 3.11(a) is found to be modified slightly by the ion-beam damage, however still displays a stacking sequence of $ABCABC$, and so forth, for example, for the close packing (-111) plane, which is consistent with the $L1_2$ crystalline structure. Even after irradiation with a substantial ion fluence, the $FePt_3$ lattice structure in Figure 3.11(b) retains its single crystallinity (in agreement with SAED data) with only minor evidence of dislocations and/or stacking-fault formation. Figure 3.11(c) is a magnification of the HR-TEM image in Figure 3.11(b), where fast-Fourier transforms (FFT) (outlined in red) have been applied to several sites across the image plane. The FFT of areas 2 and 4 contain {001} spots (shown by the blue arrowhead), while the same diffraction spot is absent from the respective FFT of areas 1 and 3. As such, the FFT verify the co-existence of chemically ordered and chemically disordered domains in the near-surface regions of the irradiated-reference $FePt_3$ film (which is analogous to the

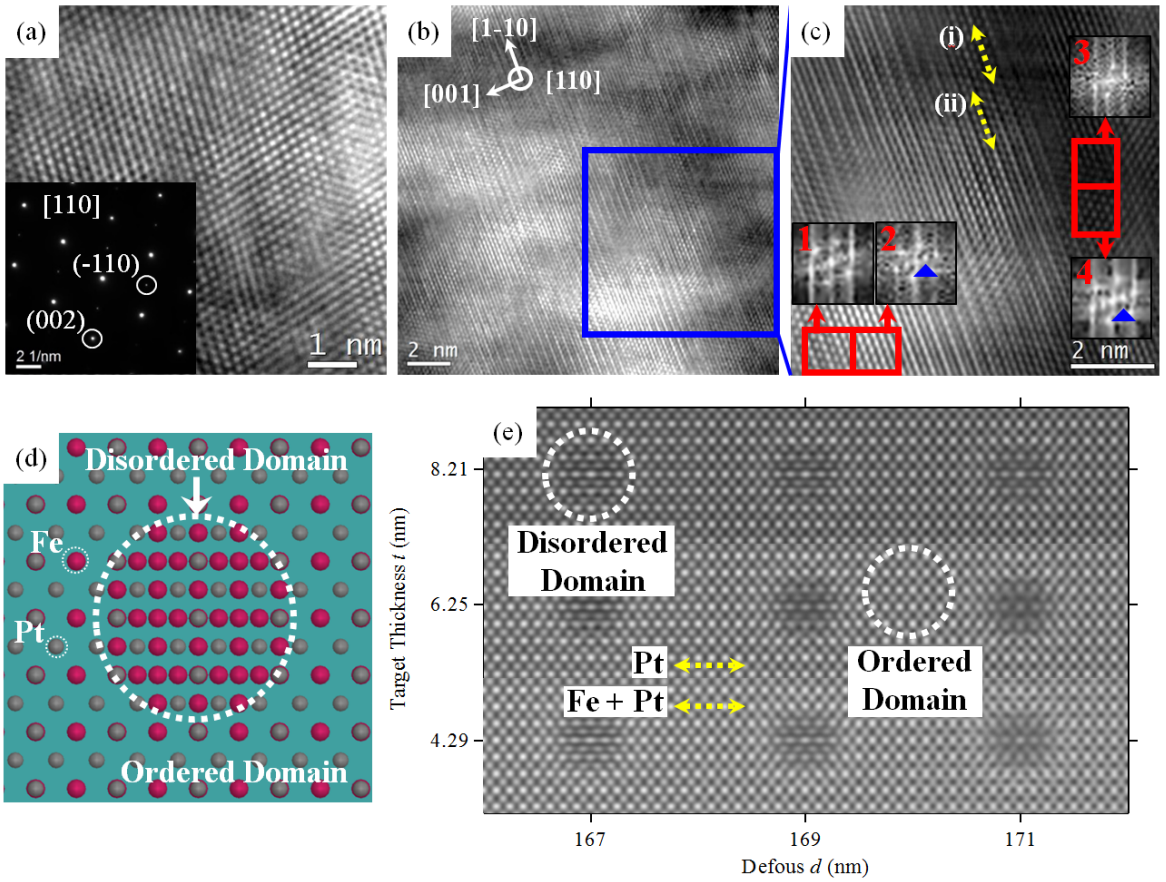

Figure 3.11: (a) Filtered HR-TEM image measured within the irradiated volume of the 2 $\times 10^{16}$ He^+ ions cm^{-2} irradiated $FePt_3$ film in the [110] zone axis. Corresponding SAED pattern displays single crystalline diffraction peaks. (b) Filtered HR-TEM image measured within the irradiated volume of the 2 $\times 10^{17}$ He^+ ions cm^{-2} irradiated-reference $FePt_3$ film in the [110] zone axis. (c) High-magnification image of the marked area in (b) with FFT areas. (d) Chemically disordered domains are modelled as precipitates of the chemically ordered phase, and (e) simulated HR-TEM image map.

domain structure throughout the irradiated film, but as previously discussed has a DPA below that required to observe dark contrast via DF-TEM). Referring to Figure 3.6, the near-surface (i.e., < 10 nm) regions of the film should remain predominantly chemically ordered, firstly, because the disorder concentration is comparatively low throughout the region and, secondly, because of the likelihood of ion-channeling [5]. As a result, the chemically disordered domains in the near-surface region of the film can be modelled as precipitates of the chemically ordered phase. Figure 3.11(d) dis-

plays the domain modelling results which were performed using JEMS software [263], and the unit-cell arrangements given in Figure 3.9. Because the apparent morphology of a HR-TEM image depends on the thickness of the sample and the focus of the TEM instrument, image-map simulations are performed over a range of target thicknesses t, $4.29 < t$ (nm) < 8.21 and defocus conditions d, $167 < d$ (nm) < 171, as shown in Figure 3.11(e). Because the actual structure of the film is inevitably very complex, and the exact thickness and defocus conditions are not known, a quantitative determination of the atomic arrangement by HR-TEM is difficult. Nevertheless, it is seen that the chemically disordered domain exhibits a different morphology to the surrounding chemically ordered domain. Qualitatively, the top right-hand side of the simulated HR-TEM image map defined by $t = 8.21$ nm and $d = 171$ nm in Figure 3.11(e), is morphologically equivalent to the experimental result shown in Figure 3.11(b). When viewed from the $\langle 110 \rangle$ direction, the chemically ordered domains of $FePt_3$ consist of atomic rows which alternate between Pt and (Pt + Fe) atoms, as shown in Figure 3.11(d). In the HR-TEM simulation of Figure 3.11(e) the dark and bright contrast planes consist of Pt and (Pt + Fe) atoms, respectively. Correlating these results to the atomic rows labelled (i) and (ii) in Figure 3.11(c) we are able to elucidate experimentally the lattice planes within chemically ordered domains which consist only of Pt atoms and those which consist of (Pt + Fe) atoms, respectively. Chemically disordered domains, on the other hand, are simulated to exhibit very little contrast between adjacent atomic rows (Figure 3.11(e)) due to the mismatched orientation of $FePt_3$ atoms between adjacent lattice planes within the three-dimensional domain volume (Figure 3.11(d)). These results are confirmed experimentally by Figure 3.11(c) where a larger contrast gradient between adjacent atomic rows is observed within chemically ordered domains (areas 2 and 4) compared to that of the chemically disordered domains (areas 1 and 3).

3.4.3 Polarised Neutron Reflectometry

So far, the $FePt_3$ films have been analysed by XRD, magnetometry and TEM. Each technique has a drawback when it comes to characterising the chemical order-to-disorder transition and the FM/PM interface of the He^+ irradiated $FePt_3$ film. Namely, XRD and magnetometry are both global-probe techniques which can only provide sample-averaged S and magnetisation information, respectively. On the other hand, while TEM is a localised technique, it is insensitive to magnetisation and suffers from a preparation step (i.e., focussed-ion beam cutting) which locally anneals and therefore chemically re-orders the sample region under investigation. Therefore, high-resolution PNR measurements were performed to compare the chemical and temperature-dependent magnetic depth-profiles of the as-prepared and the irradiated $FePt_3$ films. Because PNR probes small momentum-transfers at low angles of incidence, the technique is sensitive to magnetic periodicities on the sub-nanometre length scale. As such, PNR is capable of depth profiling layer-averaged FM moments, however is incapable of investigating AFM order on the atomic scale.

All PNR experiments were conducted in a 10 kOe external magnetic field on the PLATYPUS time-of-flight polarised neutron reflectometer at ACNS, ANSTO, after 10 kOe field-cooling from room temperature to 5 K. During the experiment, the specular reflected neutron spin-up R^+ and spin-down R^- intensities were recorded as a function of the incident angle θ using a time-of-flight data collection mode, which allows data to be analysed in terms of the wavevector transfer $Q_z = 4\pi\sin\theta/\lambda$ directed normal to the sample surface. The magnetisation detection limit of the PNR instrument (with $\Delta Q_z/Q_z = 5.2\%$) was approximately $35 - 85$ emu cm^{-3}, corresponding to $\approx 0.05 - 0.1$ μ_B per Fe atom. A determination of the nuclear and magnetic SLD profiles across all samples at each measured temperature were obtained by fitting model structures

to the respective PNR data sets using SIMULREFLEC.

Figure 3.12 displays the 5 K and 300 K PNR data collected for the (a) as-prepared and the (c) irradiated $FePt_3$ films. Open symbols show the R^+ and R^- cross-sections collected with the incident neutron polarisation oriented parallel (+) and antiparallel (−) with respect to a 10 kOe external magnetic field, respectively. The R^+ and R^- reflectivites encode information regarding the nuclear and magnetic SLD profiles of each film. The simulated SLD profiles obtained from the best fits (solid curves in Figure 3.12(a) and Figure 3.12(c)) to the PNR data are shown in Figure 3.12(b) and Figure 3.12(d) for the as-prepared and irradiated films, respectively. Magnetic SLD profiles are given in terms of the μ_B per Fe atom where 1 μ_B per Fe atom = 0.4697 $\times 10^{-6}$ Å^{-2} (note: the conversion has been calculated for a bulk $FePt_3$ lattice of ρ = 18.37 g cm^{-3} [14]).

In Figure 3.12(a), no significant asymmetry is observed between the two spin-dependent reflectivity channels (R^+ and R^-) for the as-prepared $FePt_3$ film at 300 K. Accounting for the magnetisation detection limit of the PNR instrument (i.e., 35 − 85 emu cm^{-3} corresponding to $\approx 0.05 - 0.1$ μ_B per atom for pure Fe), this indicates that the sample is very weakly FM, in agreement with the magnetometry data of Figure 3.7(a). The best-fit structural model of the as-prepared $FePt_3$ film, shown by the black nuclear SLD profile in Figure 3.12(b), consists of a MgO substrate (grey) with a 2.5 nm Cr (yellow) seed layer and a 5.4 nm Pt (red) buffer layer, upon which a 277.7 nm layer of $FePt_3$ (blue) sits below a 9.5 nm Pt (red) capping layer. Each layer is assigned a nuclear root-mean-square roughness between 1-2 monolayers, aside from the $FePt_3$ layer which has a surface roughness of 2 nm. Bulk scattering lengths and atomic number densities were used to model the MgO, Cr and Pt layers. To achieve a fitting to the critical edge, which is positioned at $Q_c = 0.0168$ Å^{-1}, the $FePt_3$ layer was modelled with an SLD of 6.28 $\times 10^{-6}$ Å^{-2} (note: SLD of bulk $FePt_3$ is 6.59 $\times 10^{-6}$ Å^{-2}

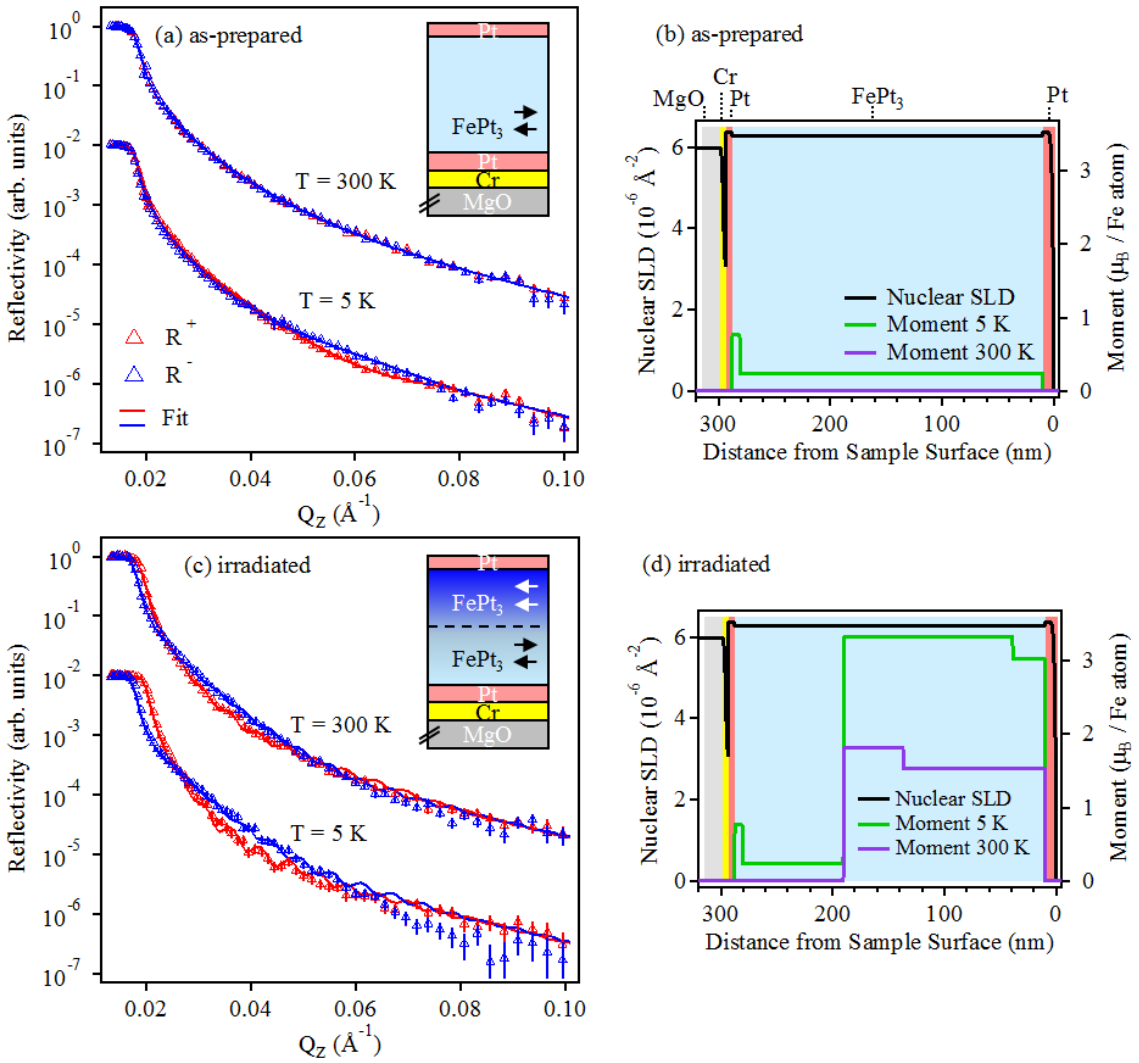

Figure 3.12: PNR data (open symbols) and best fits (solid curves) to the R^+ and R^- channels of the (a) as-grown and the (c) irradiated $FePt_3$ films, each measured at 300 K and 5 K. For clarity, the 5 K PNR data sets and best fits are shifted on the ordinate. Corresponding nuclear and magnetic SLD profiles obtained from best fits to the PNR data of the (b) as-grown and (d) irradiated $FePt_3$ films.

Layer	Thickness (nm)	Nuclear SLD (10^{-6} Å^{-2})	Roughness (nm)
MgO	Infinite	5.99	1.5
Cr	2.5	3.03	0.1
Pt	5.4	6.36	0.1
$FePt_3$	277.7	6.28	2.0
Pt	9.5	6.36	0.2

Table 3.4: Parameters of the nuclear model obtained from best fits to the PNR data of the as-prepared $FePt_3$ film at 300 K.

[82]). The SLD for the layer is reduced by approximately 5% relative to that of bulk $FePt_3$, which is a common feature in non-perfectly lattice-matched epitaxial films, and usually indicates a slightly reduced mass density or minor deviations in stoichiometry. The parameters of the structural model are summarised in Table 3.4. It should be noted that parameters of the structural model, including the film thickness and a distinction between the nuclear SLD of the $FePt_3$ and Pt layers, cannot be determined from fitting the PNR data directly (due to the resolution of the experiment). Instead, these parameters must be determined from independent measurements. For example, information about the total film thickness was obtained from the cross-sectional TEM image of Figure 3.8(a), while the nuclear SLDs of the $FePt_3$ and Pt layers were modelled on bulk structures. As there are no known structural phase transitions to occur in the materials over the temperature ranges considered here, the parameters of the nuclear model are held as constants during the subsequent fitting procedure performed at lower temperature.

At 5 K, a slight difference in the spin-dependent reflectivity is seen for the as-prepared film in the high Q_z region of Figure 3.12(a). The asymmetry most likely originates from a small net moment provided by a minority of chemically disordered domains, in the otherwise nominally chemically ordered $FePt_3$ film, at low tempera-

ture. The distribution of magnetic splitting which is minimal in the region surrounding the critical edge and maximum at $Q_z = 0.06$ Å^{-1} can be suitably described by a model which allocates a moment of 0.24 μ_B per Fe atom homogeneously throughout the $FePt_3$ layer, with the exception of a magnetically modified region close to the Pt buffer layer interface. In the latter region, the $FePt_3$ possesses an increased magnetic moment of 0.76 μ_B per Fe atom. The resulting magnetic SLD profile of the as-prepared film at 5 K used to obtain the best fit to the experimental data is shown in Figure 3.12(b).

Apart from changes to the magnetic structure, no chemical modulation is assigned to the $FePt_3$ film after irradiation. This is because the scattering lengths of Fe and Pt are comparable (9.45 fm and 9.6 fm, respectively [82]), and the size of the $FePt_3$ unit-cell is not reported to change in the chemically disordered state [14], and therefore the PNR technique is incapable of resolving any changes to the local chemical structure within the film resulting from the irradiation. As such, and for consistency, the chemical model established for the as-prepared film is likewise adopted to fit the PNR data for the irradiated film. As shown in Figure 3.12(c) and in contrast to the as-prepared film (Figure 3.12(a)), a clear spin splitting between the R^+ and R^- channels is found at the critical-edge location for the irradiated film at 300 K. Upon cooling to 5 K, an even greater spin-asymmetry develops, suggestive of a highly FM sample. In addition, the appearance of Kiessig fringes in both data sets — which result from the constructive and destructive interference of neutrons reflected from the FM/non-FM (AFM or PM, depending on the temperature) interface at the irradiation/non-irradiation boundary — provides a clear indication that magnetic contrast now exists within the chemically homogeneous $FePt_3$ layer. The period of the Kiessig fringes is determined by the thickness of the FM layer relative to the total film thickness, while the Q_z-dependence of the amplitude of the Kiessig fringes is determined by the quality (i.e., roughness) of the FM/non-FM interface. The magnetic SLD profiles of the irradiated film obtained

from best fits to the PNR data at both 5 K and 300 K are shown in Figure 3.12(d). Accurately fitting the period of the Kiessig fringes in Figure 3.12(c) determines that the lower 97.4 nm of the $FePt_3$ layer remains non-FM (on the layer average), while the remaining upper 180.3 nm thickness now carries a net in-plane magnetic moment because of the chemical disordering of the Fe and Pt atoms by the He^+ beam. During the fitting procedures, the magnetic SLD throughout the non-irradiated region of the $FePt_3$ layer was fixed to the model determined for the as-prepared film, and only the magnetic moment throughout the irradiated region was allowed to vary. This can be seen by comparing the magnetic SLD profiles of Figure 3.12(b) and Figure 3.12(d), in which the non-irradiated portion (>190 nm from the sample surface) of the $FePt_3$ layer's SLD profile is identical to the as-prepared film at the corresponding temperature. At this stage it is worth commenting that the data of Figure 3.12(c) could also be suitably described by a model consisting of an arrangement where the magnetic SLD profile of the $FePt_3$ layer in Figure 3.12(d) is inverted along the abscissa (i.e., resulting in a near-surface non-FM layer and a sub-surface FM layer). However, such a model is rejected because it is non-physical since the DF-TEM image of Figure 3.8(f) predetermines that the irradiation results in a sub-surface chemically disordered layer. To obtain a best fit to the 5 K data, a bulk $FePt_3$ FM moment of 3.3 μ_B per Fe atom was modelled throughout the majority of the layer. This moment decreased slightly to a value of 3 μ_B per Fe atom in proximity to the Pt capping layer. At 300 K, the FM moment carried by the disordered $FePt_3$ layer increases from 1.52 μ_B per Fe atom (at the surface) to 1.8 μ_B per Fe atom towards the interface which separates the chemically disordered and ordered regions of the $FePt_3$ layer. The suppression of the ion-induced moment at the sample surface is attributed to ion-channeling along the film's crystallographic axes. In addition, the thickness of the irradiated layer obtained from PNR analysis is slightly higher than the maximum ion-penetration depth determined from

Monte Carlo simulations. This suggests, firstly, that the $FePt_3$ film may have a lower density than the bulk $FePt_3$ density (ρ = 18.37 g cm^{-3}) used to simulate the DPA profiles in Figure 3.6. This picture is supported by the approximate 5% reduction from bulk SLD (i.e., 6.59 $\times 10^{-6}$ Å^{-2}) used to model the $FePt_3$ layer during the PNR analysis. Performing TRIM calculations based on the reduced number density of the $FePt_3$ layer extracted from the PNR fits, the modified DPA profile shown in Figure 3.13 is calculated. The DPA profile modelled for a 95% bulk density $FePt_3$ target, which is plotted alongside the magnetic depth-profile of the irradiated film obtained from the best fit to the 300 K PNR data, displays an increased ion-penetration depth compared to the DPA profile modelled using a bulk density $FePt_3$ target. Secondly, it is recalled that TRIM calculations neglect ion-channeling effects in crystalline materials, which have in our case significantly increased the projected ion-range compared to the mod-

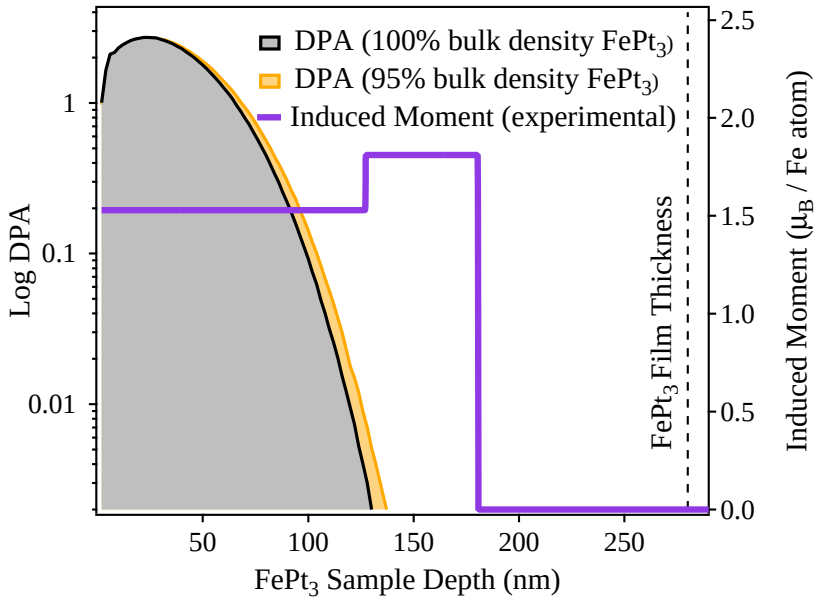

Figure 3.13: DPA profiles calculated for 15 keV He^+ ions at a fluence of 2 $\times 10^{16}$ ions cm^{-2} incident upon: a bulk density $FePt_3$ target (grey DPA profile), and a 95% bulk density $FePt_3$ target (yellow DPA profile). The DPA profiles are plotted on a logarithmic scale for clarity. The magnetic depth-profile of the irradiated $FePt_3$ film (obtained from best fits to the 300 K PNR data) is plotted for comparison.

elled amorphous structure. As a result of the significant influence of ion-channeling in our single crystalline $FePt_3$ film, we are prevented from providing a direct numerical relationship between the DPA and the ion-induced FM moment.

In order to account for the amplitude of the Kiessig fringes which appear in the data sets between $Q_z = 0.03 - 0.045$ Å^{-1}, various models of the magnetic interface roughness at the FM/non-FM boundary have been assumed. The models, which for simplicity are only shown in relation to the 5 K data, are summarized in Figure 3.14. The models assign a magnetic roughness R of 0, 2, 3, 4, 5 and 10 nm, respectively, to the FM/non-FM boundary of the irradiated film. Upon comparison of the fits it is evident that subtle changes to the roughness of the FM/non-FM interface have a strong bearing on the amplitude of the Kiessig fringe oscillations in the Q_z region of interest. To establish the best-fit parameter of the interfacial roughness, the stability plot of Figure 3.15 was computed. Stability plots compare model parameters against the residual error χ^2 obtained through the least-squares refinement process of the PNR data. This aids in determining a unique solution to a set of refined model parameters, which is denoted by a single and stable minimum within the two-dimensional parameter space. It is important to ensure that best-fit models represent unique and stable solutions because there is potential for non-unique solutions to arise when modelling PNR data, due to the loss of phase information during the scattering process [250]. However, in saying this, a definite minimum is observed in Figure 3.15 which is indicative of a convergent solution (for the parameters considered). The minimum identifies that the best-fit parameter to the roughness of the FM/non-FM interface within the irradiated $FePt_3$ film lies between 2.5 and 3 nm. This result, which essentially establishes that the FM/non-FM boundary transitions over a distance of less than 10 unit cells, is of experimental significance, as it highlights that for ferromagnetism to be induced in $FePt_3$ by ion-irradiation, it seems as though the target atoms must undergo

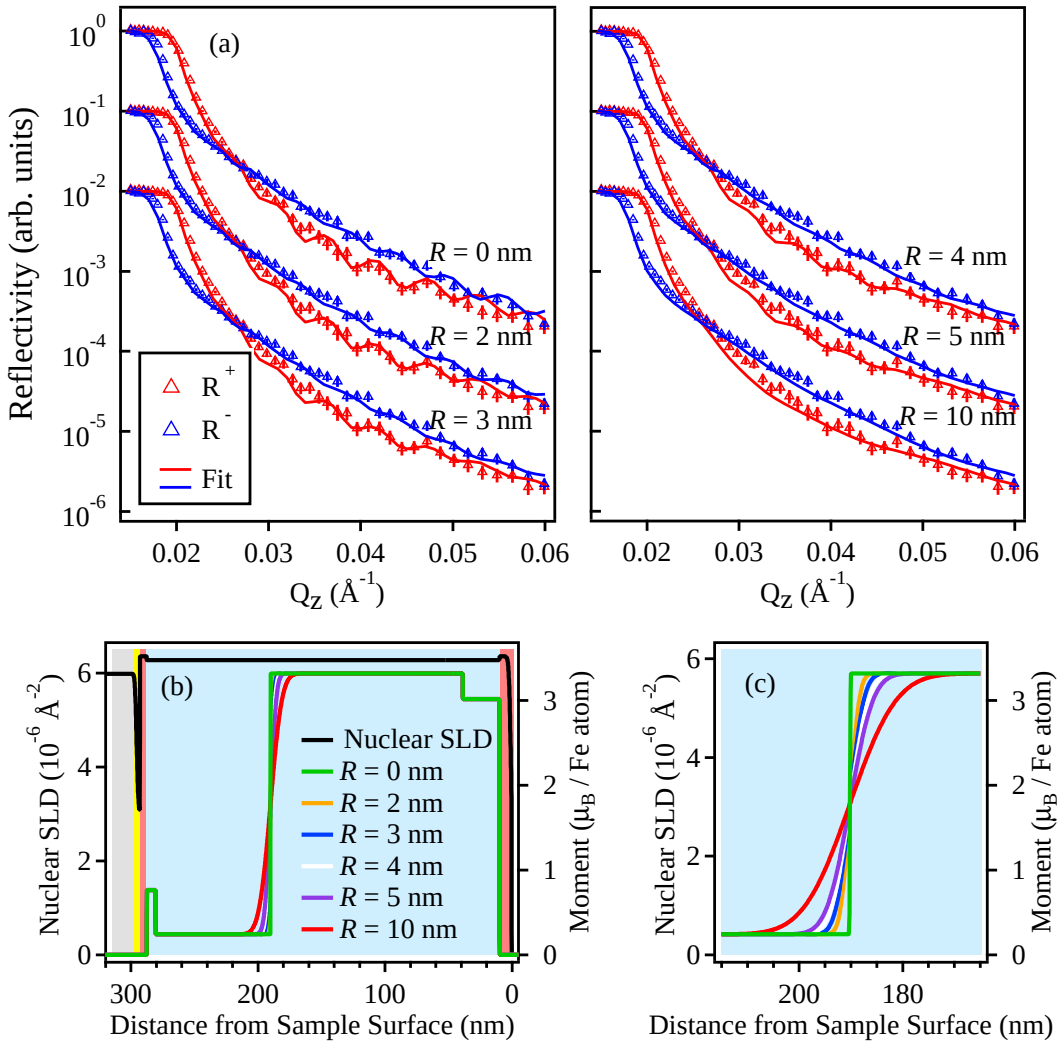

Figure 3.14: Magnetic interface roughness R models of the FM/non-FM boundary. (a) 5 K PNR data (open symbols) and selected fits (solid curves) corresponding to R = 0, 2, 3, 4, 5 and 10 nm. (b) Corresponding nuclear and magnetic SLD profiles and (c) a magnified view of the sharp transition-width of the R models at the FM/non-FM boundary.

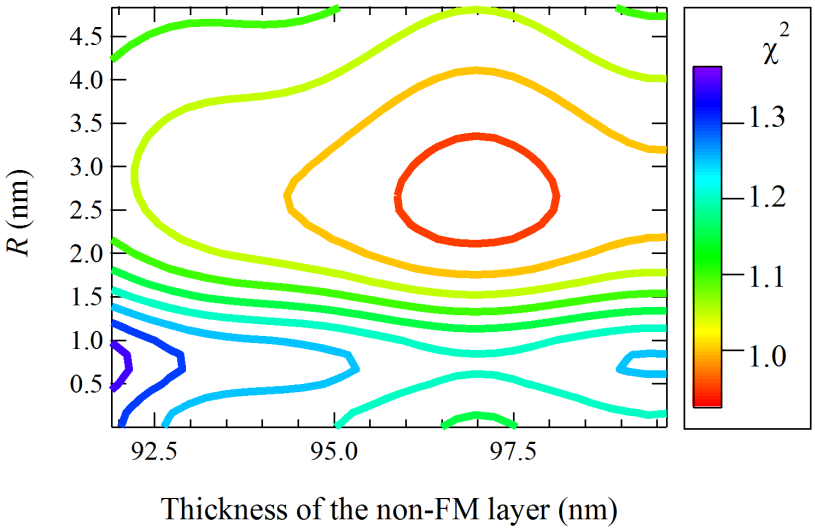

Figure 3.15: Stability plot of the thickness of the non-FM layer relative to the roughness R of the FM/non-FM interface. The thickness of the non-FM layer was constrained to 97.4 nm throughout the fitting procedure. A unique and stable solution is identified by the minimum corresponding to a FM/non-FM interface roughness R of $2.5 - 3$ nm.

a threshold number of atomic displacements. If, for instance, at a particular depth within the $FePt_3$ layer this condition is not met, the material will remain AFM or PM, depending on its actual degree of chemical order and temperature. From this perspective, unlike the quasi-Gaussian structural DPA distributions of Figure 3.6, an abrupt step-like magnetic interface would result in the material, between those depths within the $FePt_3$ layer that meet the condition for ferromagnetism, and those that do not.

3.5 Density Functional Theory

The previous section presents a comprehensive experimental data set that provides a solid foundation for constructing realistic models of the spin and chemical structure of ion-beam-disordered $FePt_3$. To that end, the next section discusses complementary

DFT calculations to draw additional insights into the underlying quantum chemical mechanisms that facilitate the low-temperature magnetic transition between the chemically ordered (and AFM) and the chemically disordered (and FM) states of $FePt_3$. Using the spin polarised DFT method, the electronic, ionic, and magnetic structure of $FePt_3$ is self-consistently solved for various models of chemical order and disorder.

DFT calculations were performed using Wien2K Version 14.2 (2016) [31], and the standard GGA-PBE(96) exchange functional were used allowing for collinear spin polarisation. Atomic sphere sizes were set to 2.43 atomic units for both Fe and Pt atoms. The separation between core and valence states was -6 Ry. The crystallographic data for the starting $FePt_3$ unit cell was taken from reference [38] (International Crystallographic Database Collection Code: 42588) which has the Pm-3m (221) space group and a bulk lattice parameter of $a = 3.872$ Å. Supercells were constructed of periodic 2×2×2 unit cells allowing for different types of magnetic order designation (i.e., FM, g-type AFM, a-type AFM, c-type AFM). Site disorder and vacancies were simulated by switching Fe-Pt positions, or by removing a Fe or Pt atom. To find the most stable local atomic configurations, ionic relaxation was performed to allow for a self-consistent crystal where forces converged to beneath 0.002 mRy $Å^{-1}$. The total energies were convergent to within 10^{-7} Ry. Final results are presented for a 10×10×10 reciprocal-space mesh used for integrations in the supercell, equivalent to 8000 points in the single Brillouin zone, providing well-converged energies tested to within 100 μeV. The local moment was extracted from the difference in spin density within the spheres, and the total spin density was extracted on a 40×40×40 Cartesian grid.

The trial models considered herein were chosen to reflect two well-established experimental ideals. Firstly, $FePt_3$ remains crystalline after moderate ion-irradiation (i.e., no amorphous regions can be detected) and secondly, the main effect of energetic ions is to introduce local defect structures while preserving the average cubic

symmetry and the overall lattice structure. Accounting for these constraints three types of defect structures were considered as perturbations within a large cubic lattice supercell of crystalline $FePt_3$: (i) anti-site defects (denoted by Fe $\leftrightarrow$ Pt) involving an interchange of Fe and Pt atoms between their respective sites, (ii) unoccupied vacancies (denoted by V^{Fe} or V^{Pt}), and (iii) rare-occurrences of He-vacancy pairs (denoted by He-V^{Fe} or He-V^{Pt}). For each isolated defect structure, the energetic differences between the disordered and ordered states after ionic relaxation were analysed. It is worth noting that there seems to be no prior *ab initio* calculations concerning the disordered magnetic state of $FePt_3$ for any of the three cases mentioned above in past literature. Nevertheless, high populations of Fe $\leftrightarrow$ Pt defects are directly analogous to the effect of thermal treatment, and consequently, the current proof-of-principle results are universally relevant to the many ways in which $FePt_3$ can be disordered (e.g., low-temperature deposited [243], cold worked [269], or ion-irradiated [174]).

To begin our calculations, it is first useful to study the magnetically ordered states of $FePt_3$. Figure 3.16 displays the four potential long-range magnetically ordered configurations which can be supported by the $FePt_3$ supercell. The types are labelled according to nomenclature first introduced by Wollan *et al.* for cubic lattices [291]. The top row of the figure shows a simplified representation of the corresponding detailed spin structure (bottom row of Figure 3.16) where, for clarity, only the Fe spins are shown labelled with a vector. The vector is used to denote either a spin-up (red) or spin-down (blue) site within the magnetic sub-lattice. Although there are several *ab initio* calculations published for the chemically ordered state of $FePt_3$ [8, 265, 276], it appears that the early works only treated the magnetic structure of $FePt_3$ as either FM (corresponding to Figure 3.16(b)) or the simplified planar form of antiferromagnetism (corresponding to Figure 3.16(c)). Meanwhile, our calculations show that overall the (½ ½ 0) c-type AFM structure (Figure 3.16(d)) is the most energetically favourable, in

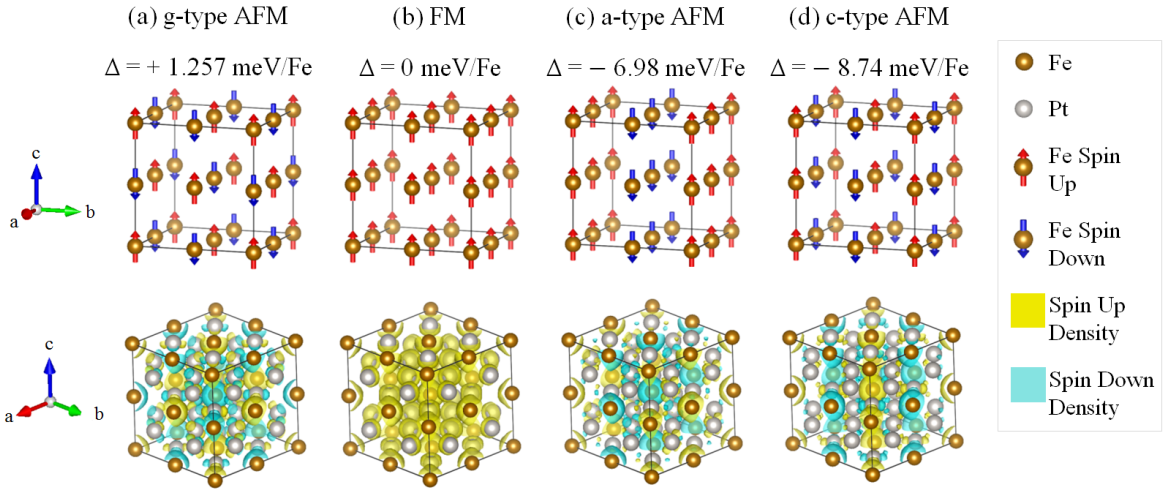

Figure 3.16: The four, potential long-range magnetically ordered configurations of the chemically ordered $FePt_3$ supercell. The relative internal energies Δ are given for (a) (½ ½ ½) g-type AFM, (b) FM, (c) (½ 0 0) a-type AFM and (d) (½ ½ 0) c-type AFM structures in order of descending energy. (Top) The simplified structure shows only the Fe spins corresponding to the different propagation vectors used in the calculations. (Bottom) A detailed representation of the corresponding spin-density isosurfaces indicates patches of small quadrupolar and induced moments surrounding the Pt sites, together with a much larger component localised on the Fe sites. The isosurface is drawn at a value of 5% of the maximum difference density.

direct agreement with previous neutron diffraction experiments [173]. Deeper analysis of the (½ ½ 0) c-type AFM structure reveals several interesting details. For instance, the structures in Figure 3.16 are arranged in terms of ascending relative enthalpy Δ. The FM state is higher in energy than the (½ 0 0) a-type and the (½ ½ 0) c-type AFM structures; however, it is lower in energy than the (½ ½ ½) g-type AFM structure. Nevertheless, in all cases the calculated magnetic moment per Fe atom remains close to 3.3 μ_B, in agreement with our experimental PNR results. This indicates that considerable magnetic frustration can be present in the Fe-Pt AFM exchange bonds while still preserving the site moment. Furthermore, in order to stabilise the (½ ½ 0) c-type AFM structure, the dominant interactions must extend beyond simple nearest-neighbour Fe-Pt-Fe exchange distances. The bottom row of Figure 3.16 shows the full set of fine details for the calculated spin electron densities of the four magnetically

ordered $FePt_3$ supercells. The majority of the spin density is located on the Fe sites, in agreement with past experiments [14]; however, small complex quadrupolar patterns are apparent on the Pt sites for certain AFM states. One can see that the quadrupolar order disappears in the FM state, and gives way to simple induced moments that appear on the Pt site with a magnitude of up to 0.3 μ_B per Pt atom. Using element-resolved X-ray magnetic circular dichroism, Pt moments of this magnitude have indeed been detected in FePt alloys [115].

Collectively the above results show that even the chemically ordered state of $FePt_3$ is very close to the magnetic critical point. It is therefore natural to expect that subtle perturbations of the chemical order may act as a strong control parameter to drive magnetic transitions by modifying the delicate local exchange pathways. To confirm this trait, Figure 3.17 shows a simplified model of chemical disorder in (½ ½ 0) c-type $FePt_3$, whereby the fully chemically ordered AFM state can be converted into an 87.5% chemically ordered cell simply by switching the atomic locations of a single Fe and Pt atom pair. This corresponds to creating a single Fe ↔ Pt defect. From calculations of the total energy difference between the FM and the (½ ½ 0) c-type AFM structures ($\Delta E_{\mathrm{FM}} - E_{\mathrm{AFM}}$), it is clear the Fe ↔ Pt defect has a significant effect on the magnetic state, effectively making the FM and AFM states degenerate to within a meV. We also investigated other forms of disorder, for example the $V^{Fe,Pt}$ and He-$V^{Fe,Pt}$ cases, but found in general these types of defects have much weaker effects on the magnetic energy of the system, such that an unrealistically high concentration of defects of this type would be required to modify the chemically ordered state of $FePt_3$.

To pinpoint the critical limit required to achieve an onset of ferromagnetism by Fe ↔ Pt type disorder in $FePt_3$, simulations were conducted as summarised by the sequence of images in Figure 3.17. The figure illustrates the crystal structure and

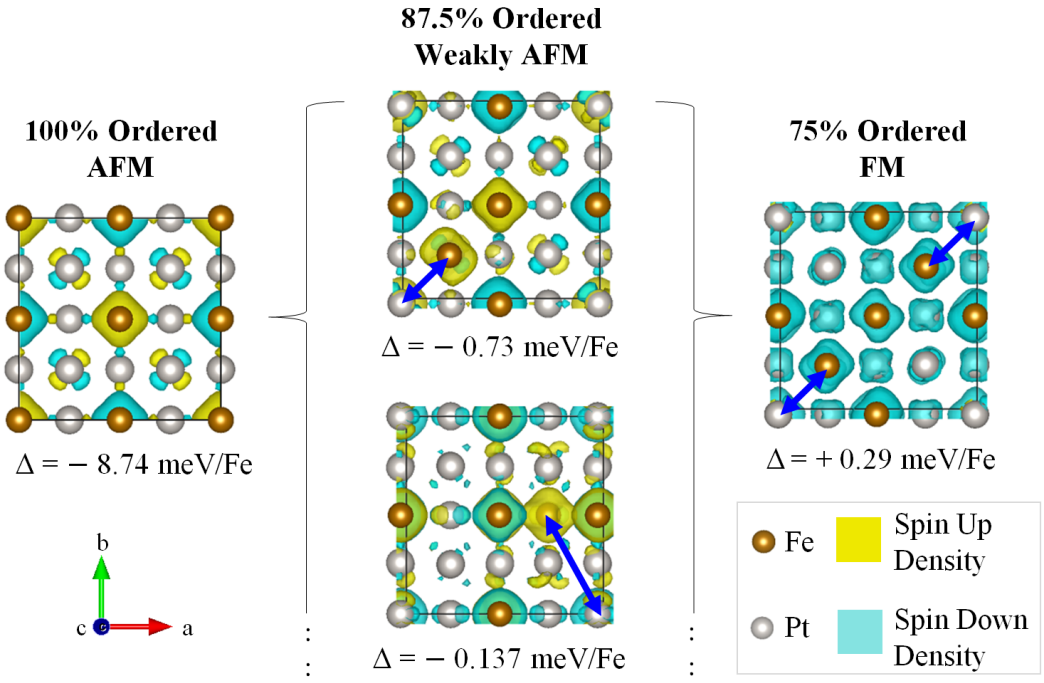

Figure 3.17: The lowest energy states of (½ ½ 0) c-type $FePt_3$ under variable degrees of anti-site disorder (Fe ↔ Pt) were calculated to model the effect of ion-irradiation upon the magnetic state of $FePt_3$. (Left) Without anti-site disorder, the (½ ½ 0) c-type AFM solution is strongly preferred over the FM state. (Centre, Top) By interchanging a neighbouring Fe and Pt site, the global magnetic energy is dramatically modified, and the AFM state is only weakly preferred. (Centre, Bottom) A second symmetrically unique configuration for a single anti-site defect can be created if a Fe atom effectively jumps two Pt sites; however, the energy is essentially comparable to the (Centre, Top) configuration. (Right) By creating two anti-site defects, the system can be driven towards an energetically favourable FM state.

the lowest-energy spin configuration of the $FePt_3$ supercell for several different Fe ↔ Pt configurations and concentrations. It is worth noting that statistically there are many more different possible disorder configurations than those shown here; however, it would be impractical to test all possible arrangements. The current results are intended merely to show the general trend, which indicates that a stable FM state in $FePt_3$ can become favored after flipping at least 25% of the Fe-Pt sites. Our computational result proposes that two anti-site defects per $FePt_3$ supercell are sufficient to induce ferromagnetism in $FePt_3$. This corresponds to a DPA of 0.125, which is in close agreement with reference [234]. Qualitatively, the result indicates that a threshold

level of ion-beam damage is required to trigger the chemically ordered (i.e., AFM) to chemically disordered (i.e., FM) phase transition in $FePt_3$. Meanwhile, lower levels of defects (Fe $\leftrightarrow$ Pt $< 25\%$) would push the system into a PM or a locally frustrated magnetic state. The surface plot in Figure 3.18(a) illustrates the impact of these findings in terms of the spatial extent of FM elements formed within damage cascades regions of ion-irradiated $FePt_3$. The three-dimensional DPA profile was produced using TRIM software for a 15 keV beam of He^+ ions incident upon the surface of a $FePt_3$ target. The approximate width of the ion-beam, set by the resolution of the TRIM calculation, is 5 nm. Nevertheless, the beam-width is an accurate depiction of the smallest beam sizes used in many modern-day focused-ion beam devices. Likewise, the needle-like shape of the beam enables a visualisation of the global (i.e., the lateral and the projected) intrinsic straggling behaviours for the specific ion-energy used in the calculation. The horizontal plane in Figure 3.18(a) which cuts the DPA axis at a constant value of 0.125 identifies the critical disorder level, at and above which, the DFT result indicates that ferromagnetism can be induced in $FePt_3$ by anti-site disorder. By examining the two-dimensional projection of the surface plot onto the lateral axis, it is noted that the critical DPA is located at a region on the quasi-Gaussian profile where the slope to the DPA data begins to increase rapidly over the lateral distance. This trend would warrant the formation of a relatively distinct magnetic interface at this boundary within the ion-impacted volume. We therefore propose that the concept of the threshold defect effect, put forward by the DFT result, may be the physical source of the abrupt magnetic interface observed experimentally by PNR in the irradiated $FePt_3$ film. Figure 3.18(b) displays the two-dimensional top-down projection of the surface plot from Figure 3.18(a), where the DPA colour grading has been scaled to the critical value. The purple contour represents the two-dimensional spatial boundary within the disorder profile where the DPA is equal to

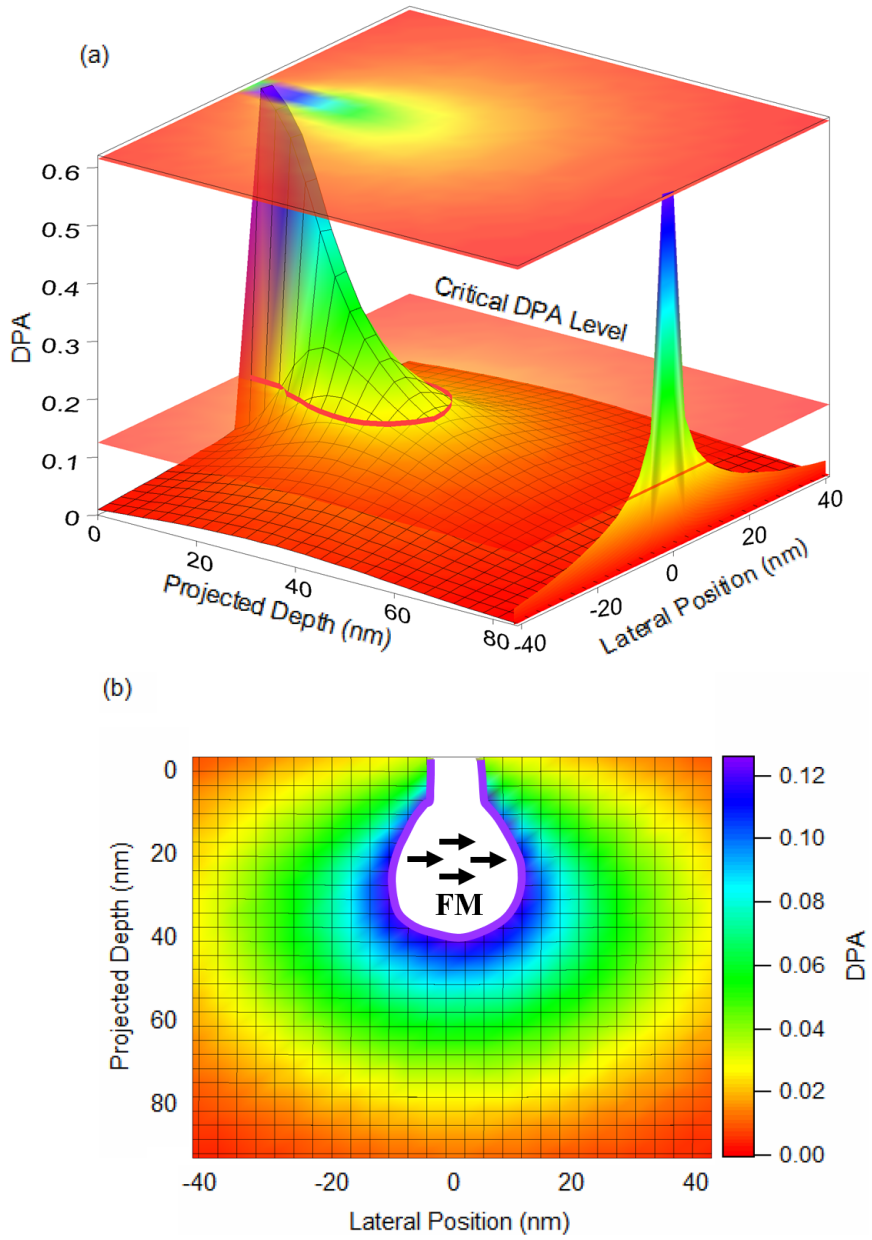

Figure 3.18: (a) DPA surface plot calculated for a beam of 15 keV He^+ ions incident upon the surface of a $FePt_3$ target. The ion-beam is centred at the origin of the abscissa. The plane through the surface plot at 0.125 DPA identifies the critical disorder level, at and above which, the DFT result indicates that ferromagnetism can be induced in $FePt_3$ by anti-site disorder. (b) A two-dimensional top-down projection of the surface plot in Figure 3.18(a). The area enclosed by the purple contour encompasses the FM element. Note: The colour grading in Figure 3.18(b) is scaled to 0.125 DPA.

0.125. Hence, this boundary separates the regions which exceed the critical DPA condition required to induce ferromagnetism in $FePt_3$ by anti-site disorder (shown in white), from the regions which experience lower levels of disorder. It is noted that the size of the FM element is confined spatially (i.e., 40 nm $\times$ 20 nm over the projected and lateral axes) relative to the broad length-scale of the entire ion-impacted area.

3.6 Sample Annealing and Characterisation

In the previous sections it has been established that through low-energy He^+ irradiation a FM ($\approx$ 180 nm)/AFM ($\approx$ 100 nm) bilayer — herein referred to as the $FePt_3$ FM/AFM bilayer — can be derived from an AFM chemically ordered $FePt_3$ film (at low-temperature) as depicted in Figure 3.19. In this section, a supplementary experiment is outlined which takes a deeper look at the low-temperature magnetic coupling which is artificially created at the FM/AFM interface within the chemically continuous $FePt_3$ film. The strength of the magnetic coupling is investigated and tailored through high-temperature annealing. In section 3.6.1 the specific type of exchange coupling generated exclusively at interfaces between FM and AFM domains is introduced and defined alongside the motivations for the project. The annealing-temperature dependence on the magnetometry and TEM behaviours of the $FePt_3$ FM/AFM bilayer are presented in Section 3.6.2. The magnetic model developed from fitting the characteristic PNR spectral features of the $FePt_3$ FM/AFM bilayer reveals that dual interfacial interactions can be attributed to the observed exchange coupling which is optimised after annealing at 840 K.

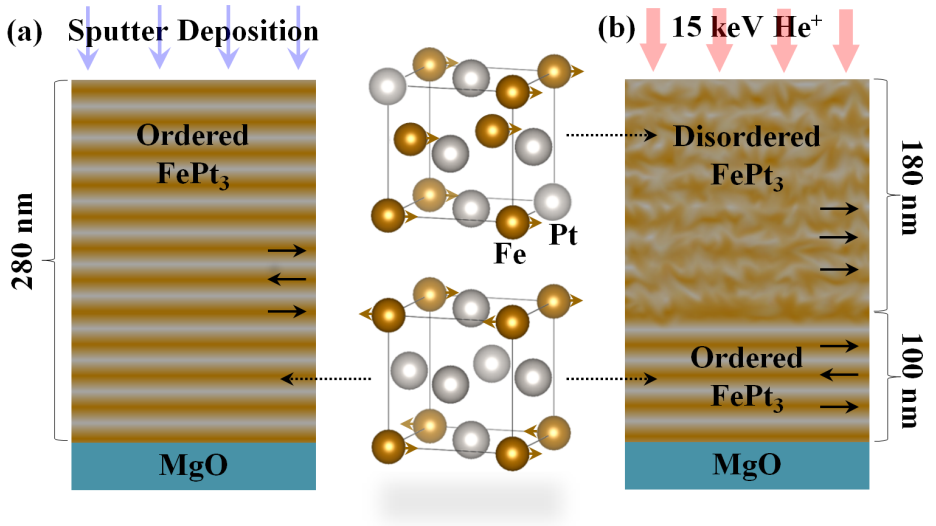

Figure 3.19: Structure of the (a) as-prepared ≈ 280 nm-thick chemically ordered $FePt_3$ film and the (b) irradiation process resulting in a ≈ 180 nm-thick chemically disordered (near-surface irradiated) / ≈ 100 nm-thick chemically ordered (un-irradiated) $FePt_3$ bilayer. The chemically ordered and the chemically disordered unit cells of $FePt_3$ are shown which exhibit AFM and FM character, respectively.

3.6.1 Introduction to Exchange Bias

Exchange bias (EB) is a unique type of magnetic exchange coupling which arises at the interface between FM and AFM domains, after cooling through the Néel temperature of the AFM component in an external magnetic field [187, 227]. These conditions impose a uni-directional magnetic anisotropy on the system, which horizontally offsets the origin of the magnetic hysteresis loop by an amount defined as the exchange bias field H_{EB}. The magnitude of the H_{EB},

$$H_{\mathrm{EB}} = (H_{\mathrm{C}_1} + H_{\mathrm{C}_2})/2, \tag{3.17}$$

is generally expressed in terms of the coercive fields of the ascending H_{C_1} and descending H_{C_2} field branches of the hysteresis loop. The formula implies that EB is

synonymous with the coercive field H_{C},

$$H_{\mathrm{C}} = |H_{\mathrm{EB}} - H_{\mathrm{C_1}}|, \tag{3.18}$$

which is enhanced in the EB state due to the pinning effect supplied by the antiferromagnet. EB has been widely researched for its fundamental scientific importance and for the numerous applications which it serves, including spin-orbit torque devices and spin-electronics implemented in magnetic sensors and non-volatile magnetic random-access memories [259, 201, 145, 207, 277]. For example, the effect of EB reduces the writing fields required by magnetic-storage media utilising exchange springs, while it can also act to magnetically pin FM layers in giant-magnetoresistance multilayers to separate the high and low resistivity states. In these devices, the magnitude of the H_{EB} can vary between a few Oersted to several kOe depending on various sample parameters, such as, size and shape, as well as the choice and individual thicknesses of the AFM and FM materials [264, 251, 195]. While, on the other hand, recent observations of EB in FM/spin-glass and FM/ferrimagnetic heterostructures generalise the requirement of the AFM spin structure [3, 297]. No attempt is made in this thesis to provide an overview of the historical development of EB, nor to review the material classes involved, or the current gamut of EB models which co-exist in the literature (for reviews see [207, 210, 227, 135, 248]). However, common to all models is an understanding of the importance of the FM/AFM interface. The interface has been shown to play a crucial role in communicating the exchange anisotropy between the FM and the AFM materials. It has been further shown that, the functionality of the FM/AFM interface is often modified by complex chemical structures, such as: incommensurate growth parameters, alloying, lattice mismatch, layer roughness and/or interdiffusion of atoms across the interface [206, 296, 293, 143, 26]. For this reason, it would be highly desirable to lift the structural constraints of the interface to enable a consid-

eration, purely, of the magnetic exchange across it. Doing so would enable a better quantitative determination of the EB mechanism, which continues to remain a topic of controversy to this day, partly due to the difficulty in ascertaining the microscopic magnetic structure of the FM/AFM interface [264, 135].

In this section, the low-temperature EB characteristics of the irradiated $FePt_3$ film are investigated. By design, the FM/AFM heterostructure exhibits stratified degrees of chemical order; however, the chemical composition and stoichiometry are invariant throughout the film volume. This uniquely allows for a consideration purely of the magnetic exchange across the FM/AFM interface without the added hindrance of structural boundary parameters which inherently affect EB quality. Such systems are scarcely reported in literature, because usually two chemically different materials are needed in order to show both FM and AFM phases at the same temperature [164]. The main objective here is to enhance the low-temperature magnetic coupling across the FM/AFM interface of the ion-beam-designed $FePt_3$ bilayer — which exhibits a very sharp magnetic interface — via thermal annealing. Annealing is a common post-deposition treatment effective in modifying the structural and magnetic properties of thin films [137, 223, 21]. It is anticipated that annealing may help to remove structural defects, such as dislocations and vacancies which may be acting to impede the magnetic stiffness of the AFM interface coupled to the FM region within the irradiated $FePt_3$ FM/AFM bilayer.

The $FePt_3$ FM/AFM bilayer was annealed in a PLD450 high-vacuum chamber system at the Institute for Superconducting and Electronic Materials (ISEM) of the University of Wollongong. The base chamber pressure was 3.6 $\times 10^{-4}$ Pa, and better than 5.9 $\times 10^{-4}$ Pa at each annealing temperature. The sample was annealed in 40 K intervals from 800 K to 1000 K for periods of 20 minutes each, and with a heating/cooling rate of 1.2 K min^{-1}.

3.6.2 Magnetometry

Between each annealing step, the m-H behaviours of the $FePt_3$ FM/AFM bilayer were measured using a Quantum Design PPMS DynaCool VSM at the ISEM of the University of Wollongong. Low-temperature hysteresis curves were acquired after 10 kOe field-cooling from room temperature to establish a preferential EB direction in the film. Data sets were recorded after first cycling the field three times to provide magnetic training to the film, and the data sets have been corrected for the diamagnetic response of the substrate. Figure 3.20(a) shows the 5 K m-H data of the $FePt_3$ FM/AFM bilayer before and after annealing at several temperatures between 800 K and 1000 K. The low-field regions of the m-H loops display the typical hysteretic behaviour of a soft ferromagnet, as evidenced by the relatively small coercive fields (top left-hand inset). In the high-field region (bottom right-hand inset), the magnetic moment of each data set increases linearly with field and is thought to originate from PM as well as weakly coupled AFM moments aligning with the applied field. It should be noted that none of the films were able to reach magnetic saturation over an extended $\pm$ 60 kOe applied field range. By comparing the data sets in Figure 3.20(a), it is established that the $FePt_3$ FM/AFM bilayer prior to annealing displays the highest volume-averaged magnetic moment. This is in agreement with ferromagnetism existing within chemically disordered domains, which take the largest volume fraction within the nominally FM layer of the $FePt_3$ FM/AFM bilayer before annealing. The maximum FM moment of the $FePt_3$ FM/AFM bilayer (in the high-field region) then steadily decreases as the annealing temperature is raised. This can be explained by considering that elevated annealing temperatures provide increased amounts of thermal energy which allow the substitutionally displaced Fe and Pt atoms within the chemically disordered domains to transform into a more long-range chemically ordered arrangement. Depending on the localised degree of chemical order, these 'higher order' domains will either have

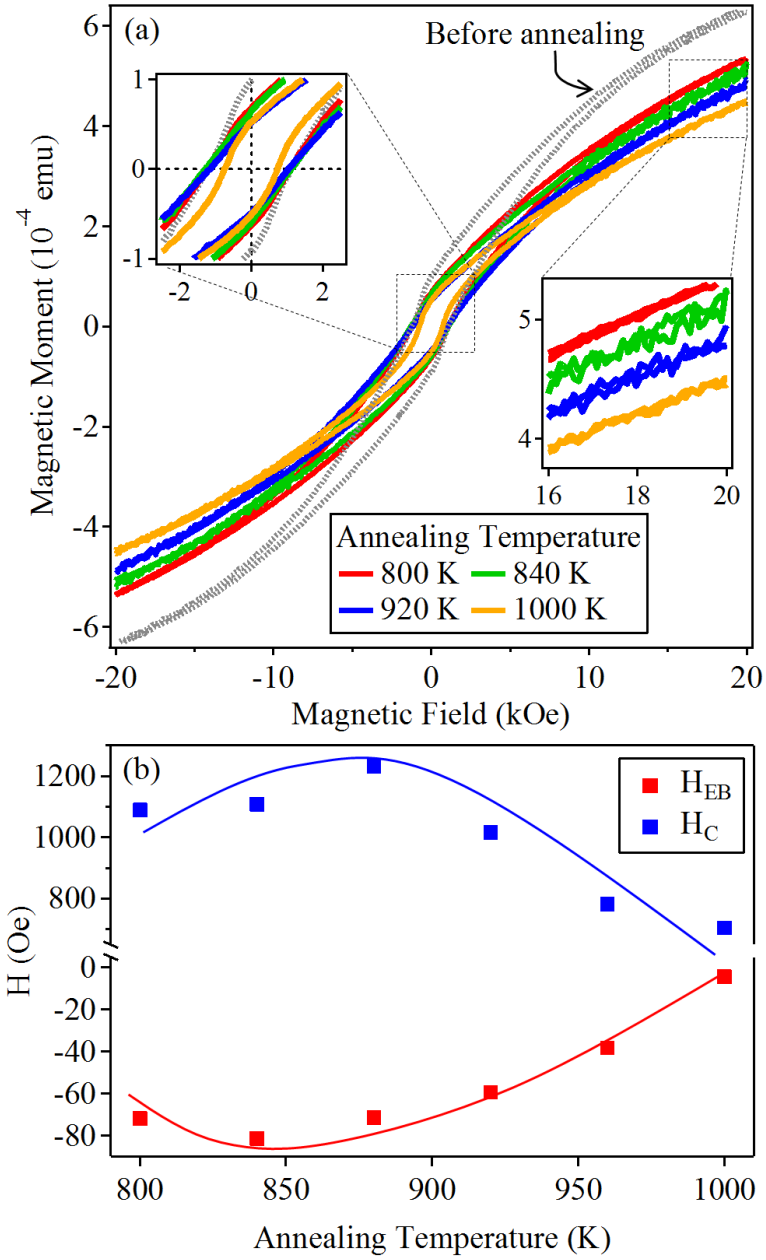

Figure 3.20: (a) 5 K m-H data of the $FePt_3$ FM/AFM bilayer before and after annealing at several temperature stages between 800 K and 1000 K. Insets show the magnified low-field (top, left) and high-field (bottom, right) regions of the hysteresis loops. (b) Annealing-temperature dependence on the exchange bias field (H_{EB}) and the magnetic coercivity (H_C) of the $FePt_3$ FM/AFM bilayer. The solid curves are guides for the eye.

PM or AFM character, such that increased annealing temperatures will systematically lower the volume-averaged FM magnetisation of the specimen. However, because magnetometry records the volume-averaged magnetic moment of a sample, it is difficult to decipher from which layer within the FM/AFM $FePt_3$ bilayer these changes originate. Furthermore, potential PM impurities within the MgO substrate [130], and their modification upon annealing, cannot be accounted for because their volume contributions are unknown. To assist in separating the film's FM response from AFM and PM contributions, magnetic depth-sensitive measurements are later conducted; however, for now it can be assumed that the majority of the changes occur throughout the domain structure of the nominally FM layer of the $FePt_3$ FM/AFM bilayer.

The dependence of annealing temperature on the H_{EB} and the H_C of the $FePt_3$ FM/AFM bilayer (extracted from the respective m-H loops) is shown in Figure 3.20(b). The H_{EB} and H_C characteristics of the $FePt_3$ FM/AFM bilayer prior to annealing were $-$ 49 Oe and 941 Oe, respectively. A peak in the H_{EB} curve is observed at an annealing temperature of 840 K. This signifies the annealing condition required to achieve the maximum magnetic stiffness within the EB system. The peak value of – 81 Oe represents a 66% increase in the H_{EB} of the $FePt_3$ FM/AFM bilayer prior to conducting any annealing procedures. Continued increase in the annealing temperature above 840 K results in a systematic decline in the H_{EB} as the interfacial coupling between the FM and the AFM domains weakens. In addition, the evolution of the H_C with annealing temperature is found to follow the typical EB behaviour, where a coercivity enhancement accompanies the effect.

3.6.3 Transmission Electron Microscopy

TEM examinations were conducted on the annealed $FePt_3$ FM/AFM bilayers to ascertain the dependence of microstructural characteristics on EB properties. TEM samples were fabricated using a Zeiss Auriga 60 crossbeam focussed-ion beam and TEM images were recorded using a JEOL 2200FS TEM device (operating at 200 kV) at ANSTO. Figure 3.21(a) and Figure 3.21(b) show the SAED patterns obtained from within the nominally FM layers (close to the irradiation surfaces) of the $FePt_3$ FM/AFM bilayers annealed at 840 K and 1000 K, respectively. These films were purposefully chosen for TEM analysis because they constitute the morphology of the strongest EB (840 K annealed) and the weakest EB (1000 K annealed) systems, as determined by magnetometry. The single-set of regular diffraction spots present in each image confirms that the FM layers of the $FePt_3$ FM/AFM bilayers remain single crystalline after He^+ irradiation and subsequent heat treatment. Both patterns can be indexed as the [110] zone axis of $FePt_3$ and each contain fundamental (all even-/odd-integer hkl) and superstructure (mixed even-/odd-integer hkl) reflections, the latter of which are evidence of chemical order in the specimen. Each mixed-integer hkl diffraction peak in Figure 3.21(a) clearly exhibits a weaker intensity compared to the equivalent diffraction peak presented in Figure 3.21(b). This indicates that the 1000 K annealed $FePt_3$ FM/AFM bilayer has an enhanced proportion of chemically re-ordered Fe and Pt atoms within the nominally FM layer, in comparison to the 840 K annealed bilayer. This trend agrees with the magnetometry data of Figure 3.20(a). A quantitative determination of the S for each annealed film from the respective SAED pattern is not provided here because it is unknown the effect of annealing on the volume of the nominally FM layers within the $FePt_3$ FM/AFM bilayers, where the thickness of the layer must be a known parameter to calculate S (see Equation 3.9). Nevertheless, the results collectively assert that the evolution of chemically 'higher order' domains are mutually

responsible for the systematic reduction in the FM response of the $FePt_3$ FM/AFM bilayer with increased annealing temperature.

The DF-TEM morphologies recorded within the nominally FM layers of the 840 K and the 1000 K annealed $FePt_3$ FM/AFM bilayers are correspondingly shown in Figures 3.21(c) and (d). To enable an evaluation of domain size, shape, and density, the DF-TEM images were recorded with a {001} diffracted beam. When viewing the films under this condition, bright regions correspond to highly chemically ordered domains, whereas dark areas identify those domains with a lower chemical-order percentage. The arrowheads in Figure 3.21(c-d) indicate the nominal low-temperature

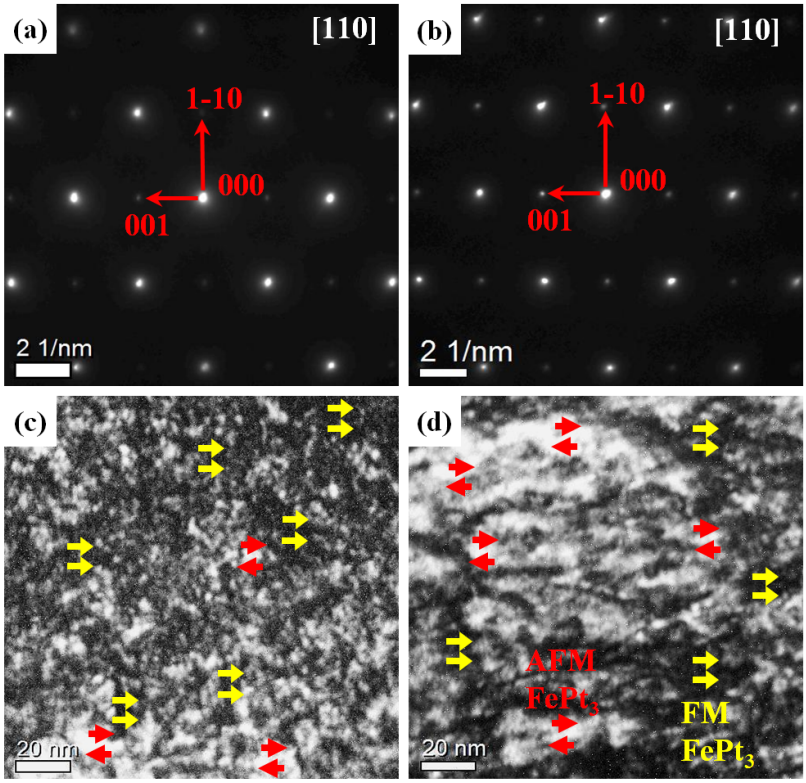

Figure 3.21: SAED images recorded within the nominally FM layers of the (a) 840 K and the (b) 1000 K annealed $FePt_3$ FM/AFM bilayers. DF-TEM images formed with an {001} diffracted beam for the cross-sections of the (c) 840 K and (d) 1000 K annealed $FePt_3$ bilayers. Arrowheads indicate the expected low-temperature magnetic ordering of each specified domain.

ordering of the Fe moments within the bright and dark contrast domains of each film. Primarily, it is most likely that the fine domain size (< 10 nm) of the 840 K annealed $FePt_3$ FM/AFM bilayer shown in Figure 3.21(c), in addition to a mixed population of chemically ordered and disordered domains, are the origins of the structure's strong EB characteristics. Besides this important feature, it is quite evident in Figure 3.21(d) that the 1000 K annealed $FePt_3$ FM/AFM bilayer has a greater areal density of bright contrast, and therefore a greater proportion of chemically ordered domains than that of the 840 K annealed film. Moreover, both the chemically ordered and disordered domains are larger within the nominally FM layer of the film annealed at 1000 K. These results collectively suggest that annealing can transform disordered domains into ordered domains, while the aggregation of equivalent domains occurs more frequently at elevated annealing temperatures. Similar trends between chemical order and domain size have been previously observed by Saerbeck *et al.* [244].

3.6.4 Polarised Neutron Reflectometry

To investigate further the origin of the peak EB in the $FePt_3$ FM/AFM bilayer annealed at 840 K, PNR measurements were performed. PNR data was recorded in 10 kOe after field-cooling from 300 K in the presence of a 10 kOe external magnetic field. This resulted in an identical field and temperature history of the bilayer to that used in the magnetometry measurements. The R^+ and R^- reflectivity data and best fits to the data sets for the 840 K annealed $FePt_3$ FM/AFM bilayer measured at 300 K and 5 K are shown in Figures 3.22(a) and (b), respectively. The reflectivity data is plotted against the Fresnel reflectivity $RQ_z{}^4$ which compensates for the intrinsic $Q_z{}^{-4}$ decay of the reflectivity curve, to better aid in visualising the features originating from the film's magnetic interface structure [56]. The Q_z-dependence of the neutron spin-asymmetry

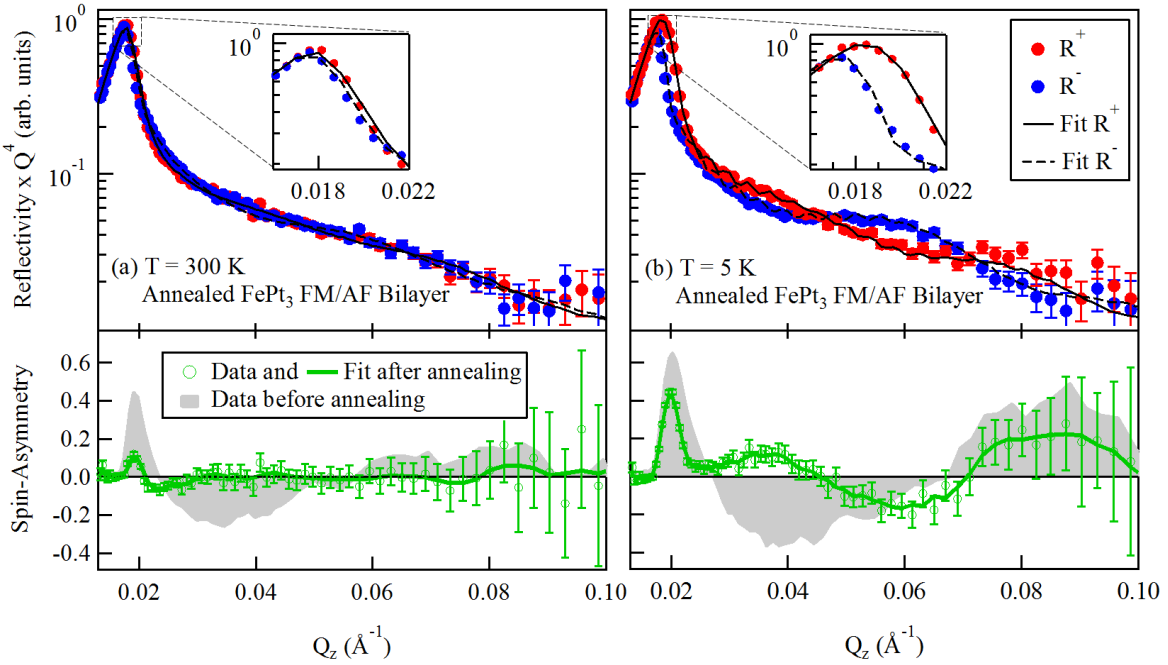

Figure 3.22: PNR data (closed symbols) and best fits (solid and broken curves) to the R^+ and R^- channels of the 840 K annealed $FePt_3$ FM/AFM bilayer, measured at (a) 300 K and (b) 5 K in 10 kOe. The spin-asymmetry of the annealed $FePt_3$ FM/AFM bilayer is plotted below the corresponding PNR data set. For comparison the spin-asymmetry of the $FePt_3$ FM/AFM bilayer prior to any annealing treatment is also plotted.

data (calculated via Equation 2.14) is displayed below the corresponding reflectivity data, and is compared to the spin-asymmetry of the bilayer prior to annealing (i.e., the spin-asymmetry of the PNR data presented in Figure 3.12). Figure 3.23 shows the (a) nuclear SLD profile, and the magnetic SLD profiles of the $FePt_3$ FM/AFM bilayer (b) before and (c) after annealing at 840 K. Each profile was selected from the best-fit parameters to the respective PNR data set. As prior established in Section 3.4.3, the structural model of the film prior to annealing consists of a uniform 277 nm-thick $FePt_3$ film, with a fitted nuclear SLD of 6.28 $\times 10^{-6}$ Å^{-2}. After annealing at 840 K, the increased Q_z-space location of the film's critical edge of neutron reflectivity (i.e., from Q_c(before) = 0.0168 Å^{-1} to Q_c(after) = 0.0175 Å^{-1}) corresponds to the same 277 nm-thick $FePt_3$ film, which now acquires a bulk $FePt_3$ nuclear SLD of 6.69

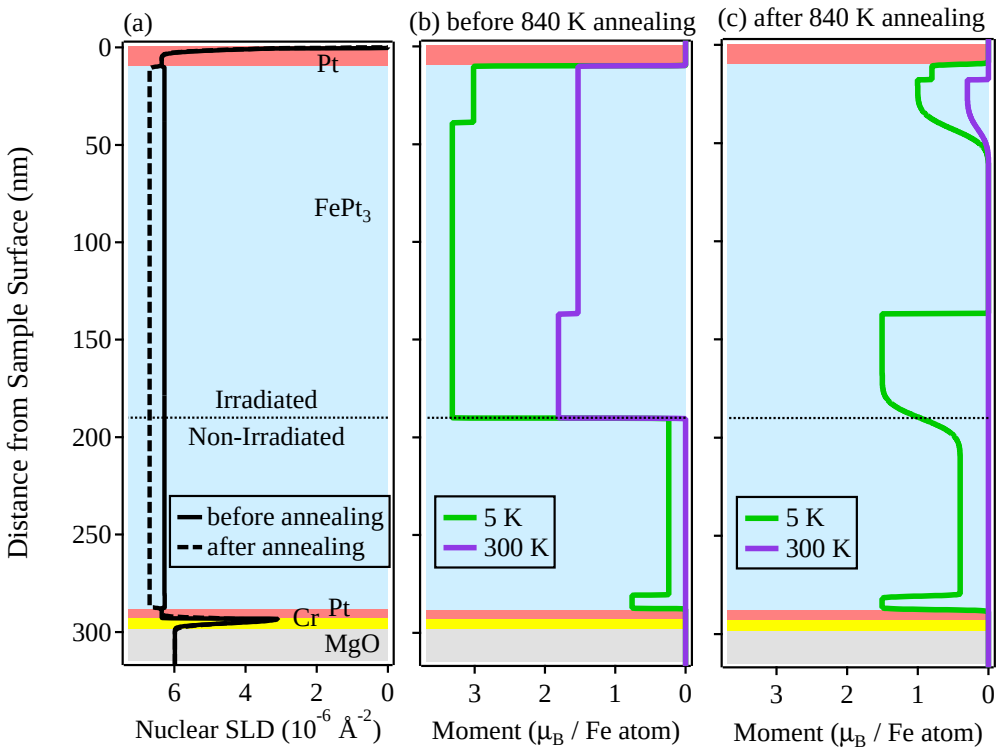

Figure 3.23: (a) The nuclear SLD profiles of the $FePt_3$ FM/AFM bilayer before and after annealing at 840 K. (b) The temperature-dependent magnetic SLD profiles of the $FePt_3$ FM/AFM bilayer before annealing (reproduced from Figure 3.12). (c) The temperature-dependent magnetic SLD profiles of the $FePt_3$ FM/AFM bilayer after annealing at 840 K, showing a roughened magnetic interface at the non-irradiated/irradiated boundary. A re-crystallisation of the chemically ordered $FePt_3$ phase propagates from the centre of the irradiation layer which effectively increases the number of magnetic interfaces potentially exchange biased within the film.

$\times 10^{-6}$ Å^{-2}, as shown in Figure 3.23(a). Overall, these changes indicate a 7% decrease in the average free-volume of the $FePt_3$ film post-annealing. This is attributed to the heat treatment reducing the density of crystal defects (e.g., voids, lattice distortions, stable point defects and defect clusters) within the film, allowing the atomic density of the $FePt_3$ lattice to increase towards the bulk value. Furthermore, the uniformity of the nuclear SLD across the irradiation/non-irradiation boundary in Figure 3.23(a) reinforces that the film remains free of chemical modulation after irradiation and subsequent heat treatment.

The size of the splitting between the R^+ and R^- channels at the critical edge of the specimen (i.e., where reflectivity = 1) defines the overall FM moment of the annealed $FePt_3$ FM/AFM bilayer at any given temperature. At 300 K, almost no spin-asymmetry is observed between the two spin states in the inset of Figure 3.22(a). This confirms a proximity to the T_C of the FM chemically disordered domains within the irradiated surface-layer of the $FePt_3$ bilayer. At 5 K a relatively large spin splitting at the critical-edge location is evident in the inset of Figure 3.22(b). It is noted that the magnitude of the spin-asymmetry, however, remains reduced in comparison to the bilayer measured at the same temperature prior to annealing. This result complements the magnetometry data discussed earlier, and suggests that the reduced FM moment of the film after annealing at 840 K is likely due to a reduction in the chemical disorder of the film. Overall, it is evident that annealing the $FePt_3$ FM/AFM bilayer at 840 K has strongly affected the depth dependence of the film's magnetisation. As previously analysed in Section 3.4.3 (and reproduced in Figure 3.23(b) for clarity), the magnetic SLD profile of the film prior to annealing can be described by an effective two-block model, consisting of a 97.4 nm-thick AFM chemically well-ordered (non-irradiated) layer extending from the substrate into a 180.3 nm-thick FM chemically disordered (irradiated) surface region. The average FM magnetisation of the chemically disordered layer is 3.25 μ_B per Fe atom at 5 K (1.60 μ_B per Fe atom at 300 K). The interface between the two layers has a magnetic roughness R between $2.5 - 3$ nm, as determined from Figure 3.15. In Figure 3.23(c), after annealing, the net moment of the irradiation layer degrades to an average of 0.62 μ_B per Fe atom at 5 K (0.04 μ_B per Fe atom at 300 K). It is noted that the reduction in magnetic moment of the film before and after annealing obtained by PNR (approximately 80%) does not reflect the reduction in magnetic moment obtained by magnetometry. This is attributed to the 'bulk' nature of magnetometry measurements, and the differing magnetic signals

which are obtainable via each measurement technique. For instance, magnetometry is sensitive to FM, AFM and PM field-induced responses, while only FM order (i.e., net magnetisation) is observable by PNR. Hence, PM impurities in the substrate could contribute to the magnetometry signal (and evolve with annealing); however, do not influence the magnetic signal obtained by PNR. Throughout the irradiation zone the overall effect of annealing results in the formation of two FM volumes separated by a layer-averaged non-FM section, which has effectively increased the number of magnetic interfaces within the bilayer. The location of the non-FM region within the irradiation layer suggests that annealing causes a re-crystallisation of the chemically ordered phase of $FePt_3$ which propagates from the centre of the ion-impacted layer. The remaining FM regions within the irradiation layer of the annealed film have reduced magnetic SLDs in comparison to the same section of film prior to annealing. This indicates that the irradiation layer is no longer uniformly chemically disordered, but rather consists of some partial mixture among FM (chemical disorder), AFM (chemical order) and PM domains, as confirmed by SAED measurements. In addition to this, the boundary between the irradiated and non-irradiated regions develops a root-mean-square roughness of approximately 10 nm once annealed. This suggests that the heightened EB observed by magnetometry is due to the combined effects of magnetic roughness at the non-irradiated/irradiated interface [261, 209], in addition to self-EB [244] created at boundaries between neighbouring FM and AFM domains within the irradiation layer (i.e., within the nominally FM layer) of the $FePt_3$ FM/AFM bilayer. Overall, the magnetic model developed from fitting the characteristic PNR spectral features of the $FePt_3$ FM/AFM bilayer annealed at 840 K validates the EB and microstructural properties obtained experimentally via magnetometry and TEM.

3.7 Conclusion

The work presented in this chapter reports the fundamental sharpness of a FM/non-FM interface formed by He^+ irradiation of a chemically ordered $FePt_3$ film. The implication of the result facilitates a comprehension of the definitive size of FM elements, such as dots and wires, which may be formed by stylus-type ion-beam writing, and therefore the result may help to broaden the future capacity of magnetic technologies synthesised by ion beams. The complementarity of TEM, magnetometry and PNR data confirms that ion irradiation is an effective tool which can be used to manipulate the chemical order, and subsequently generate room-temperature ferromagnetism in $FePt_3$. Monte Carlo simulations were used to establish the sharpness of the structural phase transformation set to take place within the $FePt_3$ target resulting from the He^+ irradiation. However, due to the special peculiarities of the $FePt_3$ magnetic phase diagram, it was found that the gradient of the ion-beam induced structural transition did not linearly correlate to the magnetic changes, resulting in discrepancies between the depth and the sharpness of the structural and magnetic phase boundaries. Subsequently, it is revealed that ion-induced structural and magnetic phase transformations in single crystalline $FePt_3$ are defined by two different spatial boundaries, where the latter exhibits a very sharp magnetic interface on the order of 10 unit cells between the ferromagnetically-active volume and the encompassing PM matrix. Using DFT, we pinpointed the type of defects required to drive the low-temperature AFM-to-FM transition in $FePt_3$. According to the calculations, a stable FM state can be achieved by flipping approximately 25% of the initially chemically ordered Fe-Pt sites. Combining these results with the findings of the three-dimensional TRIM calculations presented in Figure 3.18, it seems feasible that ion beams could be used to pattern 10 nm FM-bit periodicities (dependent on the ion energy). This could ultimately support 6.5

Tbit in^{-2} storage densities in ultra-high density magnetic recording devices utilising ion-beam designed FM elements and high magnetic anisotropy materials, such as $L1_0$ FePt or FePd.

Collectively, the results of our investigations into the irradiated $FePt_3$ film confirm that magnetically saturated FM elements which exhibit distinct interfaces can be formed by low-energy ion irradiation, and successfully probed with high-resolution experimental techniques. While very sharp magnetic interfaces may be useful in certain applications such as magnetic data storage, in others, where strongly exchange biased FM/AFM interfaces are required, it may not be so suitable. This is because the interfaces formed by ion irradiation may be too planar and would prevent a strong exchange coupling among FM and AFM domains from being achieved. As such, the low-temperature EB properties of the irradiated $FePt_3$ FM/AFM bilayer film were investigated and tailored through post-irradiation annealing. The volume-averaged magnetisation of the specimen systematically declined as the annealing temperature was raised, indicating a progressive growth of chemically higher-ordered domains within the nominally FM layer of the structure. Annealing at a moderate temperature of 840 K resulted in a peak EB behaviour which was further investigated by TEM and PNR. The domain morphology of the film was heavily dependent upon the annealing temperature, while the film's single crystallinity was preserved after each treatment. Magnetic depth-profiles obtained for the $FePt_3$ FM/AFM bilayer annealed at 840 K showed two main effects that can be attributed to the enhanced EB: magnetic roughening of the FM/AFM interface at the non-irradiated/irradiated boundary, in addition to the presence of partial chemical order/disorder domains within the nominally FM layer which self-EB with their neighbouring anti-domain. The experimental results indicate that EB is hindered at interfaces which are both chemically and magnetically perfect, and annealing can be used to tailor the magnetic roughness, and hence the

EB properties, of the FM/AFM interface for various applications.

Chapter 4

Hydrogen-Driven Switching of the Magnetic Surface Anisotropy at the Co/Pd Interface

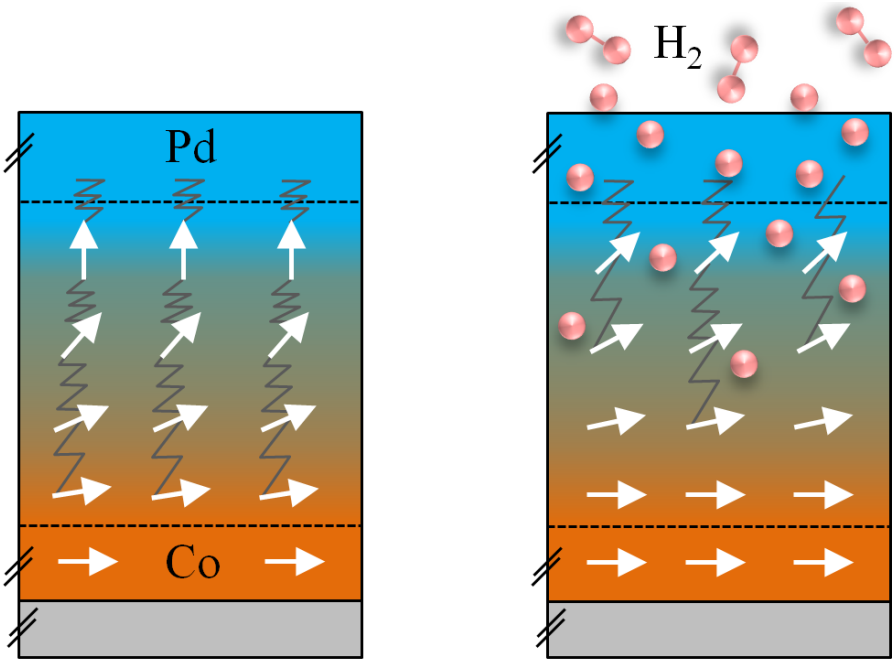

(left) Illustration of the FM spin directions across the Co/Pd interface (under magnification) and the resulting perpendicular magnetic anisotropy. (right) After the absorption of hydrogen gas, the anisotropy energy of the Co/Pd interface is weakened and the FM spins increase their projection into the film plane.

4.1 Motivation

In the race to find clean, renewable and abundant energy alternatives to fossil fuels, a spotlight has been shone on hydrogen as a 'green' option due to its zero emissions capability [1, 260]. An early focus of this green-energy revolution has been the internal combustion engine with the prospect of replacing it with hydrogen fuel-cells which work by converting hydrogen and oxygen into electricity, heat and water [256, 18]. Despite the first hydrogen fuel-cell vehicles becoming commercially available in 2014 [295], the high flammability and explosiveness of hydrogen gas [97], has to date, and to a large extent, hindered this revolution globally [76, 184, 273]. To provide peace-of-mind to consumers, robust hydrogen technologies which address safety and other technical issues associated with the storage and usage of hydrogen fuel are now in high demand.

In recent years, it has been proposed to equip vehicles with hydrogen-gas-sensing thin-film devices which would work to assist in the detection of gas leakages from fuel-cells and tanks, into the open atmosphere and/or within vehicle cabins [117, 37]. Of the many HGSs already proposed, several designs utilise Pd as the hydrogen-gas-sensing element [119, 121, 102, 163, 304]. This is because the phase diagram of Pd uniquely supports the absorption of large volumetric quantities of hydrogen gas at room temperature and atmospheric pressure [156, 125]. The absorbed hydrogen chemically binds to the metallic lattice which accompanies several changes to the physical properties of Pd, including: an 80% reduction in the electrical conductivity [156, 65], an increase in the refractive index [11, 127, 283], and an elastic expansion of the lattice by up to 3.6% in bulk specimens [124]. Another distinctive feature of Pd is that it is virtually unresponsive to other commonly found gases, such as CO, Cl_2, SO_2, H_2S, NO_x and hydrocarbons, making it a suitable material for hydrogen sensing applications [102, 284]. Of further convenience, is that the absorption of

hydrogen by Pd is completely reversible in most circumstances [156]. Hence, there is great potential to incorporate the abovementioned modifications which occur upon the hydrogenation of Pd into modern HGS design. The challenge to reach the application stage lies in how to most effectively sense the hydrogen-induced changes. Current sensors have numerous shortcomings including poor sensitivity, slow response times and high power consumption [118]. Specifically, resistance sensors are plagued by flammability concerns arising from electrical arcing in the presence of hydrogen [149], optical sensors require sophisticated detection systems [304, 102], while mechanical sensors are susceptible by hydrogen-induced aging effects [117]. Consequently, no single pre-existing HGS model is without a drawback.

Recently, a novel HGS concept was proposed by Kostylev *et al.* which utilises a lesser known property of Pd which is modified by hydrogen — magnetism [47]. In general, the prototype magnetic HGS employs microwave spectroscopy to register hydrogen-induced changes to the magnetic anisotropy of interfacial Pd within FM/Pd thin-film bilayers. This sensing strategy has numerous advantages over other HGSs. Namely, compact microwave transducers are routinely used in the telecommunications industry [169], and therefore this technology can be integrated inexpensively into magnetic HGSs. Sensing can be performed remotely through non-transparent walls and is therefore less complicated than optical-sensor readouts [47]. The design has enhanced fire-safety with respect to electrical sensors, because DC currents are prevented from exposure to hydrogen through the microwave shielding effect [138, 139]. Also, magnetic HGSs are projected to have longer lifetimes than mechanical sensors because they do not rely on inducing a structural transformation throughout the Pd layer of the device [65, 150]. Extensive work by Lueng *et al.* showed that the sensitivity of Co/Pd-based HGSs are optimised when the thickness of the magnetically active layer is restricted to 5 nm [170, 168]. It was further demonstrated that Co/Pd bilayers are capable of

accurately detecting a broad spectrum of hydrogen concentrations in air (i.e., 0.2 − 100%) [171], which is often outside the performance-range of many single competing HGS designs [117, 118]. Furthermore, by nanostructuring continuous Co/Pd films into wires Lueng *et al.* reported a subsequent 40% decrease in the response time of the device [169]. Overall, research into the feasibility of magnetism-based HGSs has been positive, with canonical examples demonstrating non-hysteretic changes in the presence of hydrogen gas, which can be tuned as a function of the hydrogen partial pressure at room temperature [47, 148, 160, 197, 172, 198, 159, 158]. While significant progress has been made from the application side, a complete picture of the fundamental mechanism which drives the changes to the Pd magnetisation at the FM/Pd interface upon hydrogenation is still lacking. For instance, it is well-recognised that electronic hybridisation due to alloying at the FM/Pd interface crucially affects device performance [160], yet it is difficult to access the interface and isolate its characteristics. Furthermore, while it is frequently reported that the uptake of hydrogen by Pd is completely reversible [160, 159, 105], the process is largely sample-dependent. Several studies on polycrystalline films have shown semi-reversible characteristics in which the first cyclic-exposure to hydrogen produces distinctly different characteristics to all higher-order exposures [197, 212, 215, 69, 233]. Therefore, even though the first exposure may be the most interesting, it is seldom characterised due to its quasi-reversible nature. To bypass the irreversibility problem requires the use of an experimental probe capable of simultaneously recording a sample's state of magnetic anisotropy and net-magnetisation step-wise throughout a single exposure to hydrogen gas, and which is also sensitive to buried chemical and magnetic interfaces.

The work presented in this chapter outlines a unique experimental methodology which has been developed to aid in mutually determining the static, quasi-static and dynamic magnetisation behaviours of FM films in the presence of external thermo-

dynamic stimuli. By innovatively combining the technique of PNR with the spectroscopic method of ferromagnetic resonance (FMR), we show that a correlation can be obtained between the layer-averaged static magnetic characteristics and the macroscopic magneto-dynamic behaviours of a FM film as a function of hydrogen partial pressure. Section 4.2 presents the proposed scheme, data acquisition routine and the sample environment commissioned for recording PNR with *in situ* FMR measurements on the PLATYPUS beamline at ACNS, ANSTO. Feasibility studies reveal the profound capacity for the PNR with *in situ* FMR measurement approach in being able to detect minute changes between extrinsically driven states of matter. In Section 4.3 the PNR with *in situ* FMR method is employed to characterise the hydrogen-induced irreversible modifications to the magnetic anisotropy of polycrystalline Co/Pd bilayers. The modifications are observed and examined in detail through simultaneously probing the FMR of a Co layer in contact with a Pd layer, and studying the changing chemical and magnetic depth-profiles across the entire bilayer with PNR during primary hydrogen-gas absorption.

4.1.1 Magnetic Anisotropy

Thin films are essentially two-dimensional nanostructures which range in thickness from a few atomic monolayers to hundreds of nanometres. Due to the finite size of the lattice and the large surface-to-volume ratio of the atoms in thin films, exchange interactions at the surface and at the film-substrate interface are altered. These new interactions can stabilise alternate phases and modify the properties of a material which would otherwise be uncharacteristic of the bulk three-dimensional state. The magnitude of magnetic moments [9, 287], the directions of magnetic easy-axes, the magnetic transition temperatures [147, 188], and (of importance to this study) the

magnetic anisotropy energies may all be modified by the lower dimensionality state characteristic of thin films [281, 239].

In general, there are four contributions to the magnetic anisotropy energy of a FM film [217]. These are: the magneto-static E_{MS}, the magneto-crystalline E_{MC}, the magneto-elastic E_{ME} and the surface E_{S} anisotropy energies. E_{MS} is related to the shape and/or volume of the film. E_{MC} originates from the coupling between the magnetic and crystalline lattices of the film. E_{ME} is caused by external stresses which induce volume-relaxation of the lattice. E_{S} arises from the broken symmetry of the lattice at the surface and interfaces within the film [123]. For polycrystalline films, subtle contributions from both the E_{MC} and the E_{ME} energies are deemed negligible (e.g., $E_{\mathrm{MC}} = 27$ kJ m^{-1} for bulk face-centred-cubic Co which decreases upon nanostructuring [28]) with respect to the E_{MS} and E_{S} energies [217]. The relative magnitudes of the latter two contributions – that is, the surface and the shape anisotropies – depends on the thickness of the FM film. In atomically-thin FM films (or near an interface), the surface anisotropy term dominates over the shape anisotropy which causes the film's FM magnetisation vector to lie normal to the film surface, resulting in a PMA [120, 193, 254]. As the film thickness is increased, a reduction in the surface-to-shape anisotropy energy fraction and an enhancement to the coordination of the lattice sees the magnetisation vector preferentially reorient into the plane of the film [126]. The transition from a perpendicular to an in-plane preferred direction of the magnetic easy-axis occurs continuously over a finite range in proximity to the film surface and/or auxiliary chemical interfaces. As an example, the strong surface-PMA field of monolayer Co (> 1.8 T [238]) coherently rotates into the film plane (at room temperature) as the Co layer thickness is increased to 1 nm [75, 4], which, driven by shape anisotropy energetically retains an in-plane alignment at sufficiently larger thicknesses.

4.1.2 Magnetic Proximity Effect

Although heavy-metal Pd is a bulk PM, it exhibits the largest magnetic susceptibility among the 4d transition metals [280], such that it is virtually on the cusp of displaying FM characteristics. The magnetic predisposition of Pd can be provoked through proximity to a FM which will initiate spontaneous polarisation of the PM spins [95]. If Pd is interfaced to (or embedded within) thin FM layers which exhibit PMA surface-termination, this PMA will propagate across the chemical boundary and manifest within the first few atomic planes of the Pd lattice at each FM/Pd interface within the heterostructure [72]. If the PMA of the interfacial Pd is modified, say, through the application of a thermodynamic stimulus (e.g., an oxidising atmosphere, elastic strain, temperature or pressure), because it is exchange coupled to the FM lattice, then these modifications will also be experienced by the bulk of the neighbouring FM layer. The modifications to the global magnetic anisotropy response of the system can subsequently be detected via spectroscopy.

4.1.3 Ferromagnetic Resonance

Ferromagnetic resonance (FMR) is an established spectroscopic method commonly used to investigate the magnetisation dynamics of FM films [179]. Specifically, the FMR technique yields direct information about the Curie temperature T_{C}, the saturation magnetisation M_{S}, the gyromagnetic ratio γ, and the bulk and interface magnetic anisotropies of FM specimens [129, 52]. FMR was first observed by Griffiths in 1946 while attempting to measure the permeability of FM metals at centimetre wavelengths [98], and the first theoretical description of the phenomenon was contributed by Kittel [132, 133]. Extensive reviews of the FMR technique can be found in the literature

[179, 109, 12, 110].

In the simplest case, FMR is the occurrence of FM spin precession about an equilibrium position [103]. For continuous films, the precession of spins is spatially uniform across the sample dimension such that the precession can be described by a macroscopic magnetisation vector $\mathbf{M}$ [179]. Figure 4.1 depicts the typical FMR geometry. At equilibrium, the direction of $\mathbf{M}$ is governed by the anisotropy of the specimen and subsequently lies parallel to the sample's effective magnetic field $\mathbf{H}_{\text{eff}}$ [179]. A transverse in-plane AC magnetic field $\mathbf{H}_{\text{ac}}$ is used to perturb the static direction of $\mathbf{M}$, placing it into gyroscopic motion about $\mathbf{H}_{\text{eff}}$. The precessional motion of $\mathbf{M}$ about its equilibrium position is described by the Landau-Lifshitz Equation [110],

$$\frac{\partial \mathbf{M}}{\partial t} = -\gamma \left(\mathbf{M} \times \mathbf{H}_{\text{eff}}\right) + \frac{G}{\gamma M^2}\left(\mathbf{M} \times \frac{\partial \mathbf{M}}{\partial t}\right), \tag{4.1}$$

where G is the Gilbert damping constant which accounts for the magnetic relaxation of the system [12]. The precession represents a resonance process, such that the angle (amplitude) of precession reaches a maximum when the frequency of $\mathbf{H}_{\text{ac}}$ coincides

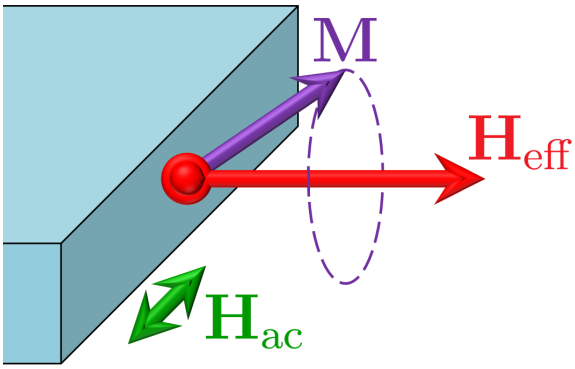

Figure 4.1: Schematic of the typical geometry employed in the measurement of the FMR of a FM film. An AC magnetic field $\mathbf{H}_{\text{ac}}$ is used to perturb the equilibrium (static) direction of $\mathbf{M}$, placing it into gyroscopic motion about $\mathbf{H}_{\text{eff}}$. The resonance condition is met when the frequency of $\mathbf{H}_{\text{ac}}$ coincides with the precessional eigenfrequency of $\mathbf{M}$.

with the precessional eigenfrequency of **M**. The distinct frequency at which resonance is met is termed the FMR frequency f [110]. The FMR frequency of a material depends on a number of magnetic sample parameters (e.g., γ, M_S, T_C etc.) including the sample shape [179]. For the specific case of a thin film magnetised in-plane but known to possess a small component of perpendicular-to-plane magnetic anisotropy (or PMA), the FMR frequency is given by the Kittel equation [110],

$$f = \gamma\sqrt{H_{res}(H_{res} + M_{\parallel} - H_{PMA})}, \tag{4.2}$$

where H_{res} is the FMR resonance field, $M_{\parallel}$ is the in-plane FM magnetisation (which is assumed to approximate M_S) and H_{PMA} is the effective perpendicular-to-plane anisotropy field of the specimen. Because FM materials possess large γ values (e.g., $\gamma_{Co} = 3.2$ MHz Oe^{-1}), the FMR frequency lies in the microwave frequency range between 0.1 and 100 GHz. Hence, microwave technology is used to aid in registering FMR responses. One useful approach for taking FMR spectra is with a microwave stripline transducer [179]. The advantage of this method is the possibility of taking measurements over a very broad range of microwave frequencies, allowing the magnetic parameters of the specimen under investigation to be accurately determined [255]. Furthermore, and contrary to the much older microwave cavity method [103], the stripline FMR fixture can be miniaturised, allowing it to be embedded into, say, small-volume pressure-tight chambers, which is especially important for measurements requiring flammable or explosive gases such as hydrogen.

It is noted that formulae similar to Equation 4.2 exist for other types of magnetic anisotropies, as well as for more complicated systems containing several magnetically exchange-coupled layers [99]. Numerical models have also been built which allow for the calculations of the FMR frequencies of films with arbitrary magnetic profiles across

the film thickness, as well as for in-plane patterned films [100]. However, in saying this, the simplistic form of Equation 4.2 is relevant to the work described in this chapter, which in combination with the FMR geometry of Figure 4.1, has been applied to probe the H_{PMA} of Co/Pd bilayers.

4.1.4 Pd-Hydride Phase Diagram: Bulk and Thin Film

The mechanism of hydrogen-gas absorption by bulk Pd lattices is well-documented (for references see [155, 83, 89, 10]). Hydrogen molecules (H_2) readily dissociate into unbound hydrogen (H) atoms on the surface of Pd at room temperature, through strong Pd-H interactions which elongate the H-H bond distance [20, 78]. The small radius of the chemisorbed atomic H (i.e., 0.052 nm [160]) then diffuses with a very high mobility (i.e., 3.8 $\times 10^{-7}$ cm^2 s^{-1} at 298 K [199]) into the bulk of the Pd lattice as an octahedral interstitial impurity. The resulting α-phase solid-solution of Pd-hydride (PdH_x) retains the symmetry of the primary face-centered-cubic Pd lattice ($a = 0.3887$ nm) up to a maximum H concentration of $x = 0.017$ (corresponding to $a = 0.3895$ nm) [181]. Beyond $PdH_{0.017}$ the system enters a mixed ($\alpha + \alpha'$) phase which then tracks towards stoichiometric PdH characterised by the full occupation of the octahedral interstitial sites. A transition into the pure α'-phase occurs when the absorbed hydrogen concentration exceeds the maximum solid solubility. As shown in Figure 4.2(a), this occurs at room temperature for $PdH_{0.6}$ and is identified by a distinct lattice parameter of $a = 0.4025$ nm [156]. In the α'-phase, not only are the structural (mechanical) properties of Pd modified but also are the optical [148, 158, 157, 219], electronic [151, 83, 258, 245] and magnetic properties [2, 197, 198, 47]. In particular, the magnetic susceptibility of Pd lessens upon hydrogen absorption and decreases to zero upon reaching the α'-phase transition [2, 220, 208]. Upon desorption, hydrogen

atoms in the α'-phase quickly diffuse from the lattice, while the more stable α-phase atoms migrate slowly between the interstitials within the bulk of the lattice before desorbing from the surface of the material [159, 160].

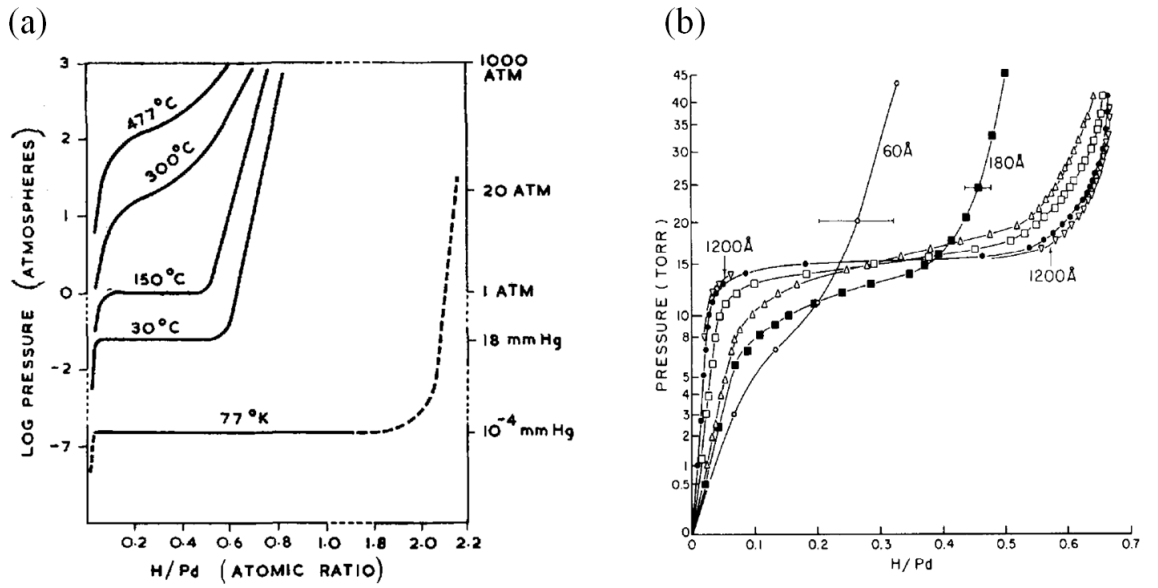

Figure 4.2: Pd-H phase diagrams. (a) The pressure-concentration isotherms of bulk Pd (available from [155] under Creative Commons from Johnson Matthey Plc). At room temperature the α'-phase boundary is located at $PdH_{0.6}$ (or $PdH_{0.57}$ at 30 °C). (b) The room-temperature pressure-concentration isotherms of nanoscale Pd (reprinted from [83] with permission from Elsevier). As the Pd thickness decreases the maximum hydrogen solubility reduces.

In the lower dimensionality environment of a thin film, the phase behaviour of PdH_x differs significantly from the bulk [83, 153]. In general, the pressure-concentration isotherms of nanoscale PdH_x exhibit lower critical temperatures, and accordingly display truncated miscibility gaps between the pure α and α' phases compared to bulk PdH_x [83]. As a consequence, the maximum H solubility of Pd at any given temperature and pressure is decreased with respect to bulk Pd as shown in Figure 4.2(b). The abovementioned behaviours are consistent with a weakening of the H-H interaction energy within the two-dimensional Pd lattice [83, 156]. A further source of this behaviour arises from charge transfer to neighbouring material layers within het-

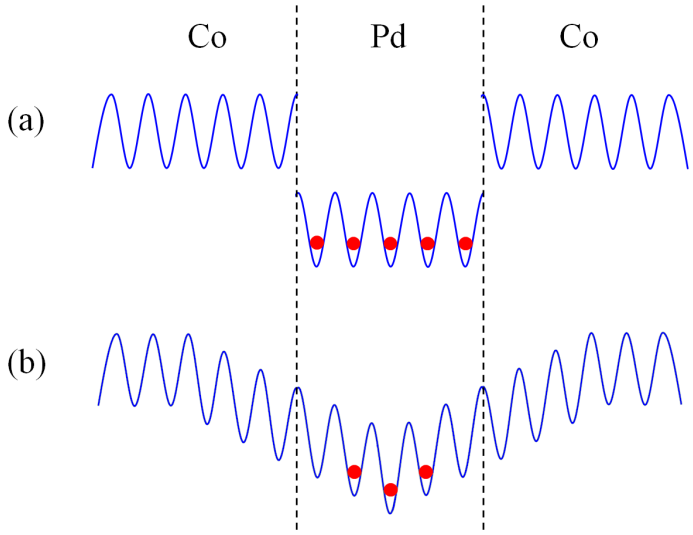

Figure 4.3: Schematic of the chemical potential across the Co/Pd-hydride/Co interface. (a) Isolated lattices of Co and Pd have low and high hydrogen solubilities, respectively. (b) Upon nanostructuring, the chemical potential of interfacial Pd increases which reduces the density of energetically favourable hydrogen absorption sites (denoted in red).

erostructure films [40]. As shown in Figure 4.3, electronic hybridisation as a result of chemical alloying increases the chemical potential of interfacial Pd lowering its ability to absorb hydrogen. As this effect occurs only in proximity to chemical interfaces, the average hydrogen solubility is therefore dependent upon the thickness of the Pd film [199]. In turn, the chemical interface which binds the Pd film to the substrate also needs to be considered for its impact on the hydrogen solubility. Usually in charging bulk Pd with hydrogen, an isotropic, three-dimensional expansion of the crystalline lattice is observed, as shown in Figure 4.4(a). The relative change in the Pd lattice parameter $\Delta a/a_0$ increases linearly as a function of the hydrogen concentration C_{H} and is given by the proportionality factor $\Delta a/a_0 = 0.063 \cdot C_{\mathrm{H}}$ [224], where C_{H} is expressed as a ratio of the number of H atoms per Pd atom. However, in thin films due to the lateral clamping effect provided by the substrate, any in-plane expansion of the lattice is strongly prohibited. As a result, for thin films an anisotropic, one-dimensional volumetric expansion of the lattice is observed in the out-of-plane direction only [194],

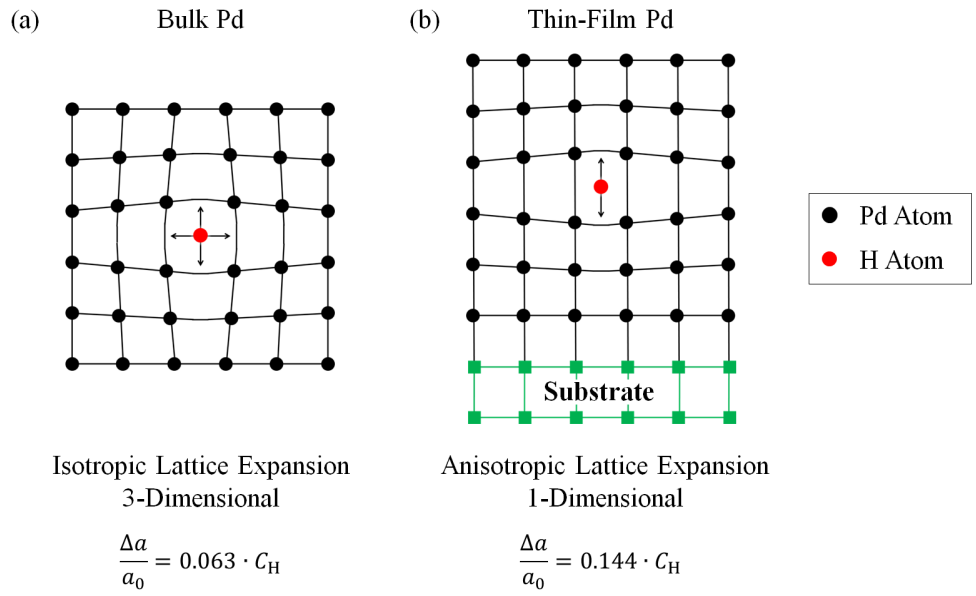

Figure 4.4: Comparison of the (a) isotropic three-dimensional expansion of bulk crystalline Pd lattices after hydrogen absorption, and the (b) anisotropic one-dimensional expansion of thin-film crystalline Pd lattices after hydrogen absorption.

as shown in Figure 4.4(b). Theoretically, one would expect a modified proportionality factor of $\Delta a/a_0 = 0.144 \cdot C_H$ [35]. At increased concentrations (or increased film thicknesses) the magnitude of the in-plane stresses generated by the uni-directional expansion of the crystalline lattice may exceed the yield stress of the two-dimensional film [40, 105]. Should this occur, the stress will be released through the formation of destructive folds and dislocations, or may even lead to a complete delamination of the film from the substrate. For example, Lee *et al.* showed that the hydrogen-induced delamination of Pd films occurred for film thicknesses > 30 nm in a 2% hydrogen partial pressure, whereas thinner films could withstand equivalent stresses without deformation but were nevertheless susceptible to cold-annealing by hydrogen [150]. Hydrogen annealing is a 'one-off' process which can occur during the first cyclic exposure of a film to hydrogen gas [87]. The process removes defect volumes (e.g., vacancies, dislocations and grain boundaries) which may innately occupy the lattices of thin films, leading to a plastic deformation which irreversibly alters the chemical and electronic energy

landscape of the film (during the first exposure) such that reproducible responses are then obtainable throughout the second and subsequent exposures.

4.1.5 Neutrons and Hydrogen

As established throughout Chapter 2, the macroscopic SLD of a non-magnetic material is calculated as the summation over the SLDs of the individual elements (for X-rays) or the elemental isotopes (for neutrons) which constitute the material. Hence, a Pd film which absorbs hydrogen will have its primary SLD modified, and will subsequently acquire the SLD characteristics of atomic hydrogen. The degree of SLD modification will depend upon the C_{H} absorbed by the Pd film (i.e., the number of H atoms per Pd atom). Furthermore, as the SLD of a given volume-element is proportional to the bound coherent scattering length b within that volume-element — where b is a probe-dependent quantity — the change in SLD of Pd at any fixed C_{H} will differ when observed under X-rays or neutrons. Table 4.1 compares the X-ray and neutron scattering lengths of hydrogen b_{H} and palladium b_{Pd}.

	b_{H} (fm)	b_{Pd} (fm)
X-ray	2.81	129.26
neutron	−3.74	5.92

Table 4.1: Comparison of the X-ray and neutron scattering lengths of hydrogen and palladium.

As shown in Table 4.1, the positive X-ray b_{H} is almost two orders of magnitude smaller than the X-ray b_{Pd}, whereas the neutron b_{H} is comparatively large and negative with respect to the neutron b_{Pd}. As a result, the presence of hydrogen in Pd is virtually

indistinguishable when viewed under X-rays, however can be straightforwardly investigated with neutrons. Consequently, neutrons are routinely employed in the study of hydrogenation dynamics in bulk materials [89], as well as to investigate hydrogen absorption and desorption behaviours in thin films (as has been done in this work) [199, 197, 198, 232, 136, 88, 114, 86]. The unique attribute that hydrogen possesses a negative neutron scattering length, means that it is an effective modifier of the neutron SLD of many materials, including Pd. In particular, by employing neutrons to study the reflectometry of Pd films upon hydrogenation, direct and simultaneous information regarding the concentration of absorbed hydrogen and the expansion of the film in the hydrogenated state can be obtained. Specifically, by assuming a one-dimensional expansion of the Pd film upon hydrogenation (as in Figure 4.4(b)), the relative change in the neutron SLD of a Pd film before ($\mathrm{SLD_{Pd}}$) and after hydrogenation ($\mathrm{SLD_{Pd+H}}$) can be used to calculate the average concentration of absorbed hydrogen C_{H},

$$C_{\mathrm{H}} = \frac{b_{\mathrm{Pd}}}{b_{\mathrm{H}}} \left[\frac{\mathrm{SLD_{Pd+H}}}{\mathrm{SLD_{Pd}}} \cdot \frac{d_{\mathrm{Pd+H}}}{d_{\mathrm{Pd}}} - 1 \right], \tag{4.3}$$

within the Pd film in the hydrogenated state [232]. Here, C_{H} is expressed in terms of the number of H atoms per Pd atom, and d accounts for the thickness of the Pd film before (d_{Pd}) and after hydrogenation ($d_{\mathrm{Pd+H}}$).

4.2 Commissioning of Sample Environment

The previous section outlined various physical mechanisms which can be employed in synergy to approach the design of novel HGS which utilises magnetic interface effects. Concisely, a magnetic HGS which is based on a Co/Pd bilayer construction would function in such a way that as hydrogen gas is absorbed by Pd its magnetic susceptibility

will be reduced, which will subsequently reduce the strength of the interfacial PMA to the underlying Co layer [47]. The state of the system's magnetic anisotropy can be monitored directly by microwave spectroscopy through measurements of the sample's FMR spectrum to provide real-time detection of hydrogen gas [171, 169, 170, 172]. However, in order to extract anisotropy information from an FMR spectrum to allow comprehensive characterisation of the sample's magnetic state, independent knowledge of the in-plane magnetisation of the material under study is needed. Often, it is a non-trivial task to extract the absolute in-plane magnetisation of a thin film, especially if the magnetisation varies non-uniformly across the film thickness or as a function of an external thermodynamic stimulus, such as temperature, pressure and/or chemical atmosphere [160]. The technique of PNR can be employed in such circumstances. In contrast to the conventional magneto-optical Kerr effect, PNR can provide the absolute value of a sample's in-plane magnetisation as well as its distribution across a film thickness. Furthermore, unconventional stimuli such as hydrogen gas, oxidising atmospheres and/or elastic strain can be provided to the sample *in situ* during a PNR measurement, unlike with commercial magnetometry systems. Therefore, PNR and FMR represent complementary techniques for the study of magnetically anisotropic FM films because different magnetic parameters are accessible via each method. When used in combination the techniques of PNR and FMR have the ability to quantitatively solve Equation 4.2 to facilitate characterisation of externally-driven modifications to the static, quasi-static, and dynamic magnetisation behaviours of FM films.

Another complementary feature of combining PNR with *in situ* FMR stems from the difference between the data acquisition times required by each method. PNR measurement times are mostly sample-size and neutron-flux dependent, but generally the method demands several hours per spin state in order to obtain good statistics over a sufficiently large Q_z range. In comparison, FMR measurements can be completed

within $2 - 15$ minutes for reasonable- to high-quality data sets, respectively. Therefore, the FMR technique can be used to probe short-lived processes and/or transient states, while PNR would record the average of these changing states of the specimen over a relatively extended measurement period. A notable exception, of course, is when the process being driven by the external stimulus results in completely reversible changes to the sample's properties. Here, the PNR data acquisition system can be used to time-stamp the state of the sample over multiple cycles relative to the external modifier. This capability is, for example, utilised in pump-probe type measurements. However, in general, data acquisition times of a few hours are still required.

As a final point, the true worth of combining PNR with *in situ* FMR is demonstrated in cases where the external stimulus causes irreversible (or semi-reversible) property modifications to the sample. Under these circumstances, it is essential to record as much detail about the sample step-wise throughout a single cycle (or during a single exposure), because once perturbed by the environment, the initial state of the sample is unable to be revisited at any later stage. In this way, PNR with *in situ* FMR offers the capability to simultaneously probe a vast range of material properties during a single measurement cycle, rather than retrospectively after the fact. The work presented in this chapter deals specifically with the example of using PNR with *in situ* FMR to characterise the irreversible changes which occur to the magnetic anisotropy of Co/Pd bilayers upon exposure to hydrogen gas.

4.2.1 PNR with *in situ* FMR Chamber

Figure 4.5 displays a schematic of the sample environment commissioned during the course of this thesis to provide PNR with *in situ* FMR characterisation on the PLATYPUS beamline at ACNS, ANSTO. The current design of the chamber allows thin-film

characterisation to be carried out in the presence of a broad range of gas atmospheres. The side panels of the atmospheric pressure-tight chamber are made of thick aluminium. In each panel, a centralised 20 × 5 mm (length × height) window is comprised of a thin aluminium foil to allow incident and reflected neutron passage during PNR measurement. The remaining area of the chamber face incident to neutrons is coated in cadmium to prevent unintentional neutron scattering events taking place through the thick aluminium chamber walls. Gas inlets and outlets, respectively located in the roof and floor of the sample chamber, provide steady gas flow through the sample space during measurement which is continually regulated by a mass-flow controller. Positioned towards the base of the chamber, but still suspended above the chamber floor, is a 29 × 12 mm (length × width) sample stage upon which the thin-film specimen for PNR with *in situ* FMR measurement is placed. The sample stage is made from a

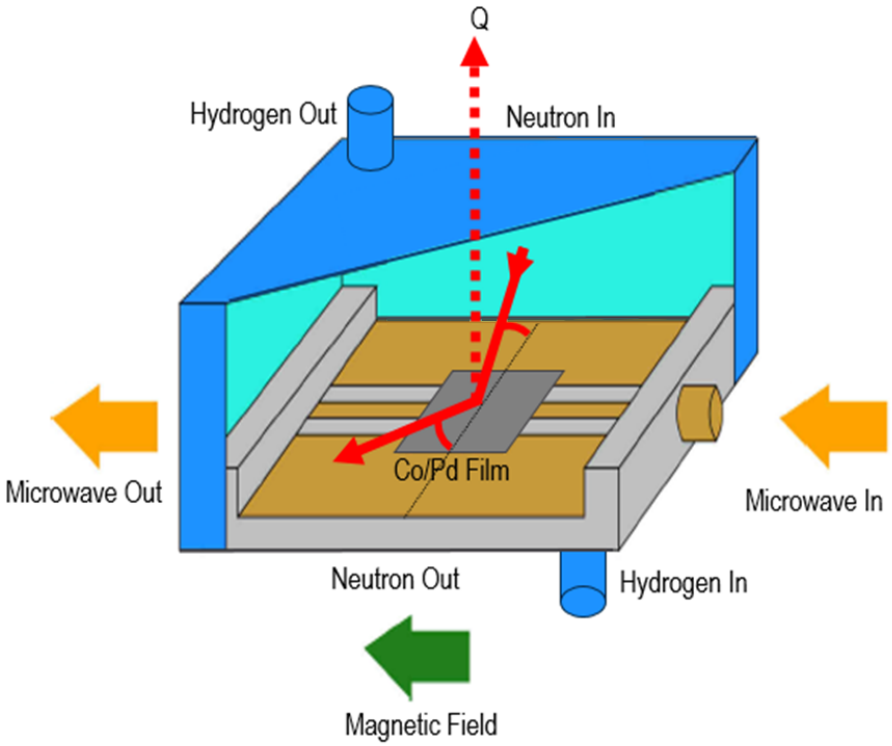

Figure 4.5: Cross-sectional schematic and beamline geometry of the PNR with *in situ* FMR sample chamber.

microwave-quality composite material Duroid (Rogers Corp., USA) which represents a microwave electromagnetic waveguide referred to as a backed coplanar stripline [179]. The coplanar stripline has the shape of two parallel grooves etched into the metallised surface of the dielectric Duroid plate. The grooves act to separate the central electrode, referred to as the signal line, from two metallic half-planes, referred to as ground lines.

External to the sample chamber, the remaining experimental circuitry required to facilitate PNR with *in situ* FMR measurements is shown in Figure 4.6. Here, microwave coaxial cables are joined via end-launch connectors through the insulating front and back walls of the sample chamber (parallel to the neutron beam) to each end of the coplanar stripline. One end of the stripline feeds to a miniature USB-controlled microwave generator while the other is connected to a microwave diode. The output of the microwave diode is fed into a lock-in amplifier. To enable instantaneous communication between the electromagnet of the PLATYPUS instrument and the FMR set-up, a hand-held computer-controlled magnetometer by MagnetPhysik is employed [175]. The Hall probe of the magnetometer is placed near the sample chamber between the poles of the electromagnet on the beamline. The PNR control software is used to produce a stepped magnetic field sequence of the electromagnet with constant wait times

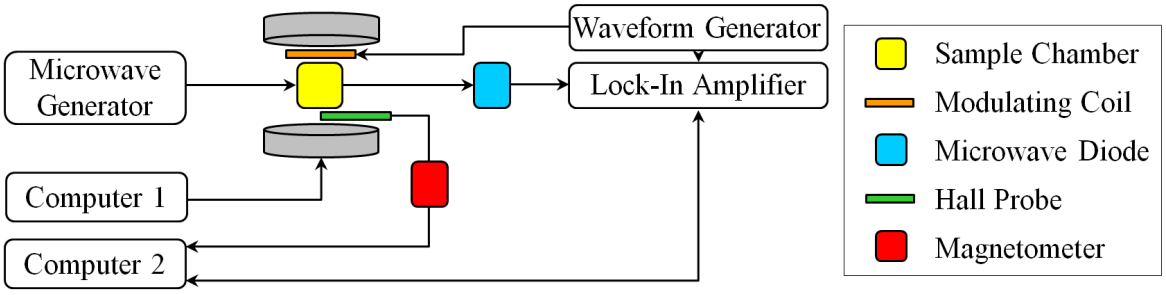

Figure 4.6: External circuitry required to facilitate PNR with *in situ* FMR measurements. The sample chamber described in Figure 4.5 (denoted in yellow) is placed between the poles of an electromagnet (denoted in grey).

between subsequent field (current) settings [203, 204]. The FMR control software repeatedly then reads off the outputs of the lock-in amplifier and of the magnetometer with the same period as the wait command of the resultant field of the electromagnet. In addition, a small modulating coil is placed on one of the external surfaces of the insulating (i.e., plastic) side walls of the sample chamber. A sinusoidal AC voltage with a frequency of 220 Hz and a peak-to-peak amplitude of 10 V is applied to the modulating coil from the waveform generator, which also references the lock-in amplifier. The current in the coil produces an AC magnetic field with a root-mean-square amplitude of approximately 6 Oe, which weakly modulates the static field provided by the electromagnet across the sample position. This arrangement, which is called field-modulated FMR, strongly increases the sensitivity of the set-up and makes small FMR absorption signals easily detectable. The microwave AC field drives magnetisation dynamics in the neighbouring FM film which is placed on top of the stripline. At resonance, the microwave energy is absorbed by the film and is seen as a sharp drop in the output DC voltage of the microwave diode. The drop has the shape of a Lorentzian function with respect to the applied magnetic field, typical for any resonance [110]. However, because the lock-in amplifier is insensitive to DC voltages, this drop is not seen directly. Instead, the registered signal of the field-modulated FMR method yields the first derivative of the Lorentzian function with respect to the sweeping parameter (i.e., the applied field) [12]. The resulting data set is often referred to as a differential absorption FMR spectrum.

In our neutron-beamline FMR assembly, the FM film sits face-up on the microwave stripline, separated by its substrate (the typical substrate thickness is 0.5 – 1 mm). This orientation is stipulated by the PNR measurement geometry, however is atypical of an FMR measurement, where usually the film itself (not the substrate) faces the coplanar stripline. The resulting separation distance between the film and the stripline

results in a significant decrease in the coupling of the film's magnetisation dynamics to the microwave driving field. This leads to a decrease in the amplitude of the FMR response, which can be smaller by two orders of magnitude with respect to typical FMR experiments. However, because the amplitude of FMR absorption scales with the length of the stripline [179, 138], the signal strength can be easily increased by using large-area films, as also stipulated by the PNR technique. Accordingly, the standard size of a film measured in the chamber is 20 × 15 mm (length × width), where the size along the stripline is 20 mm. To further aid in this, a wide (0.5 mm) signal line is employed to increase the vertical spread of the stripline's microwave Oersted field to ensure it can easily penetrate through the dielectric substrate of the film to reach the FM layer [17].

Another important consideration to make is that the current implementation of the sample chamber presupposes that PNR and FMR measurements probe differing timescales of a film's FM response. Specifically, FMR probes microwave dynamics, while PNR is used to probe static magnetic properties. There is no cross-coupling between the two measurements types, principally because FMR is recorded in the linear (small signal) regime, where the magnetisation precession angle is negligible (i.e., on the order of 1°). Hence, the precessional motion will have little effect upon the length of the static magnetisation vector (i.e., below the resolution of the PNR technique). Furthermore, precession is only excited in the region of the film which is in close proximity to the stripline, and a large volume fraction of the film (more than 90%) is not driven to resonance. The small volume driven to FMR is sufficient enough to produce well-resolved FMR spectra, while the much larger total surface area of the film is used to acquire high-quality PNR data sets.

A FMR spectrum can be obtained by following either frequency- or field-resolved methodologies. During a frequency-resolved measurement the applied field is kept con-

stant and the microwave power is swept across the resonance, while for field-resolved measurements the microwave frequency is fixed and the external magnetic field swept. It is well known that the characteristics of microwave transmission lines are generally frequency dependent, such that the first methodology often produces artefacts which either distort or hide the FMR absorption peak. This is generally overcome by employing sophisticated microwave network analysers [179]; however, these instruments are expensive and bulky and can be easily damaged during transportation to a neutron facility. A more practical way is to take field-resolved measurements (as has been done in this work). Field-resolved measurements are not affected by frequency dependent artefacts as the measurements are taken at a single frequency and also because the data sets contain only magnetic field dependent responses, such as the FMR absorption peak. Furthermore, field-resolved measurements can be achieved by inexpensive and portable devices measuring no more than 60 × 30 × 20 cm (excluding the lock-in amplifier and waveform generator) if the microwave circuitry is simply restricted to a single generator and diode. This is especially useful for transporting the chamber to and from neutron facilities, if needed.

4.2.2 Methodology

In general, the sequence for acquiring PNR with *in situ* FMR data on a FM film during hydrogen-gas cycling comprises of three stages, as follows.

(I) First, FMR and PNR data are recorded in the presence of pure nitrogen gas. In this state, typically two field-resolved FMR data sets are taken at different frequencies (acquisition time ≈ 15 minutes each), which are then followed by a PNR measurement of the R^+ and R^- channels (acquisition time ≈ 12 hours). Upon completion of the PNR measurement, it is advisable to record a further field-resolved FMR spectrum in

order to show that a stable state was reached prior to commencing PNR and/or did not change over the course of the PNR measurement.

(II) Secondly, simultaneous time-resolved FMR [169] and R^+ PNR scans are measured during hydrogen-gas absorption. To this end, the time-resolved FMR spectrum commences before the initial admission of hydrogen gas into the sample chamber (in order to establish a baseline recording in the nitrogen atmosphere), and is acquired until the completion of the hydrogenation process. During these measurements the applied field is set to the maximum slope of the field-resolved differential absorption FMR spectrum taken at the preceding step, and outputs of the lock-in amplifier are read periodically. Because the applied field is set to a constant value during the time-resolved FMR measurement, reflectometry can be measured in parallel. Here, to assist in prompt measurement timings, only R^+ reflectivities are recorded with somewhat limited statistical accuracy (acquisition time $\approx$ 40 minutes). These simultaneous measurements are capable of mapping the dynamic chemical and magnetic states of the sample during the hydrogen absorption process via two separate routes (i.e., FMR and PNR), which each deliver information on different aspects of the transient process. Once the time-resolved FMR data set reaches a plateau with respect to the absorption amplitude and the features of the PNR data sets are invariant between consecutive acquisitions, hydrogenation of the sample is complete. The hydrogenation process depends on various factors, including chemical composition, film thickness and temperature. Therefore, the time required for completion of the hydrogenation process can vary widely from sample to sample, such that it may be necessary to record several R^+ reflectometry sequences in order to capture the period over which the stable hydrogenated state is reached.

(III) Finally, once the time-resolved FMR data set plateaus with respect to the absorption amplitude, signalling the end of the transient process, field-resolved FMR

as well as R^+ and R^- PNR data sets are re-measured in the hydrogenated state (using the same procedure as set out in stage I). By comparing the data sets of stages I and III, the effect of hydrogenation on the depth-dependence of the sample's in-plane magnetic moment and chemical-density profile, as well as changes to the global magnetisation dynamics of the sample, can be determined. Accessing such detailed information over such a wide class of magnetic sample parameters is achieved only by adding the technically relatively simple, but highly effective, FMR set-up to the PNR beamline.

4.2.3 Feasibility Study

To investigate the effectiveness and practicality of the proposed PNR with *in situ* FMR method, feasibility measurements were performed on a ternary cobalt-nickel-palladium (CNP) alloy film in the presence of hydrogen gas. As one of the primary purposes for conducting feasibility studies on commissioned equipment is to test the absolute capacity of the set-up, the proceeding section relates to results obtained on a *palladium-deficient* CNP alloy film exposed to a *dilute* hydrogen atmosphere. Similar to Co/Pd bilayers, FM-metal alloy films containing Pd are also prospective candidates for future hydrogen-sensing applications [2, 160]. Therefore, it is also important to carry out characterisation of these materials *in situ* with hydrogen-gas atmospheres.

A CNP alloy film comprised of 24% cobalt, 36% nickel and 40% palladium was grown by DC magnetron sputter deposition at the University of California-Berkeley. The film was deposited onto a silicon substrate and grown to a nominal thickness of 60 nm. The coercive field of the alloy film obtained from magnetometry measurements was approximately 300 Oe at 300 K (characterisation performed at the University of California-Berkeley). The film was loaded into the PNR with *in situ* FMR sample

chamber (outlined in Figure 4.5) on the PLATYPUS beamline at ACNS, ANSTO and positioned between the poles of the 10 kOe electromagnet. The electromagnet of the PLATYPUS instrument provided a sweeping sample field (700 Oe − 1500 Oe) during field-resolved FMR measurements, a 1658 Oe sample field during time-resolved FMR measurements and a 1 kOe sample field for all PNR measurements presented in this section. A constant microwave frequency of 8 GHz was used for the acquisition of all FMR spectra presented in this section. A mass-flow controller was used to deliver pure N_2 gas or a dilute H_2/N_2 gas mixture (3.5% hydrogen partial pressure) to the sample chamber at a constant flow rate of 4.2 $\times 10^{-6}$ m^3 s^{-1} (250 ml min^{-1}), corresponding to an effective hydrogen partial pressure of 35.5 mbar (assuming 1 bar total pressure) within the chamber at an ambient temperature of 298 K.

Figure 4.7 displays the field-resolved FMR data sets obtained for the CNP alloy film (a) before hydrogenation in the presence of nitrogen gas (solid green line), (b) in the hydrogenated state after 1.5 hours of hydrogen gas flow through the sample chamber (solid blue line) and (c) in the hydrogenated state after 12 hours of hydrogen gas flow through the sample chamber (dotted blue line). Upon the initial uptake of hydrogen gas (i.e., a $\rightarrow$ b), the FMR resonance linewidth narrows while the resonance position shifts from 1658 Oe (before hydrogenation) to 1582 Oe. Each of these behaviours is indicative of an increase to the effective magnetisation $4\pi M_{\text{eff}}$ of the CNP alloy film in the hydrogenated state, where $4\pi M_{\text{eff}} = 4\pi(M_{\parallel} - H_{\text{PMA}})$ from Equation 4.2. After a continued 12 hours in the presence of hydrogen (i.e., b $\rightarrow$ c), a subsequent FMR spectrum (recorded after the R^+ and R^- PNR measurement of stage III as outlined in Section 4.2.2) reveals a slight increase to the resonance position of the film with respect to the applied field. As the increase is greater than the experimental error of the measurement, this suggests the possibility of two competing processes taking place during the hydrogenation of the CNP alloy film. The dominant contribution

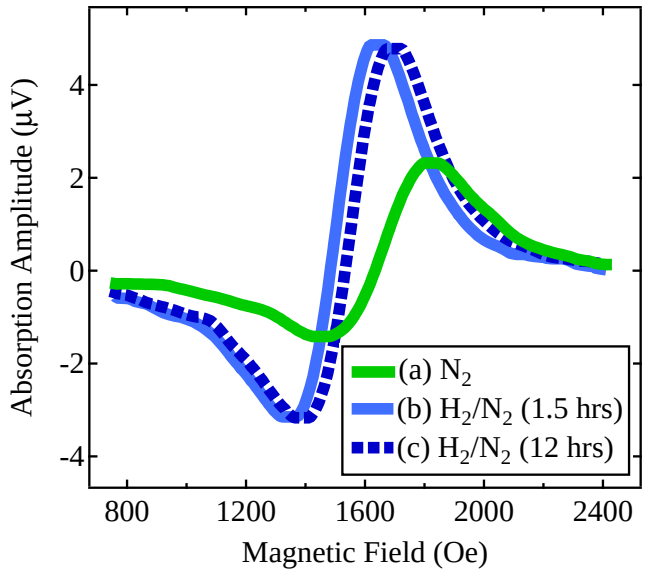

Figure 4.7: Field-resolved FMR spectra of the CNP alloy film recorded (a) before hydrogenation in the presence of nitrogen gas (solid green line), (b) in the hydrogenated state after 1.5 hours of hydrogen gas flow (solid blue line) and (c) in the hydrogenated state, after 12 hours of hydrogen gas flow (dotted blue line). All data sets were measured at a microwave frequency of 8 GHz.

proceeds at a fast rate and decreases the resonance position of the CNP alloy film, while a second (minor) contribution evolves more steadily and acts to increase the resonance position.

Figure 4.8 displays the results of the simultaneous time-resolved FMR and R^+ PNR measurements performed on the CNP alloy film during the initial stages of hydrogen-gas absorption. Throughout these measurements the applied external magnetic field was set to 1658 Oe, which corresponds to the maximum slope of the field-resolved FMR differential absorption peak of the CNP alloy film before hydrogenation (as in Figure 4.7(a)). At time $t = 300$ s (vertical red line) of the time-resolved FMR spectrum in Figure 4.8(a), hydrogen gas first enters the sample chamber, replacing the former pure nitrogen gas atmosphere (depicted by data points $t < 300$ s). The gradual increase in the FMR absorption amplitude observed over the course of the measurement indicates

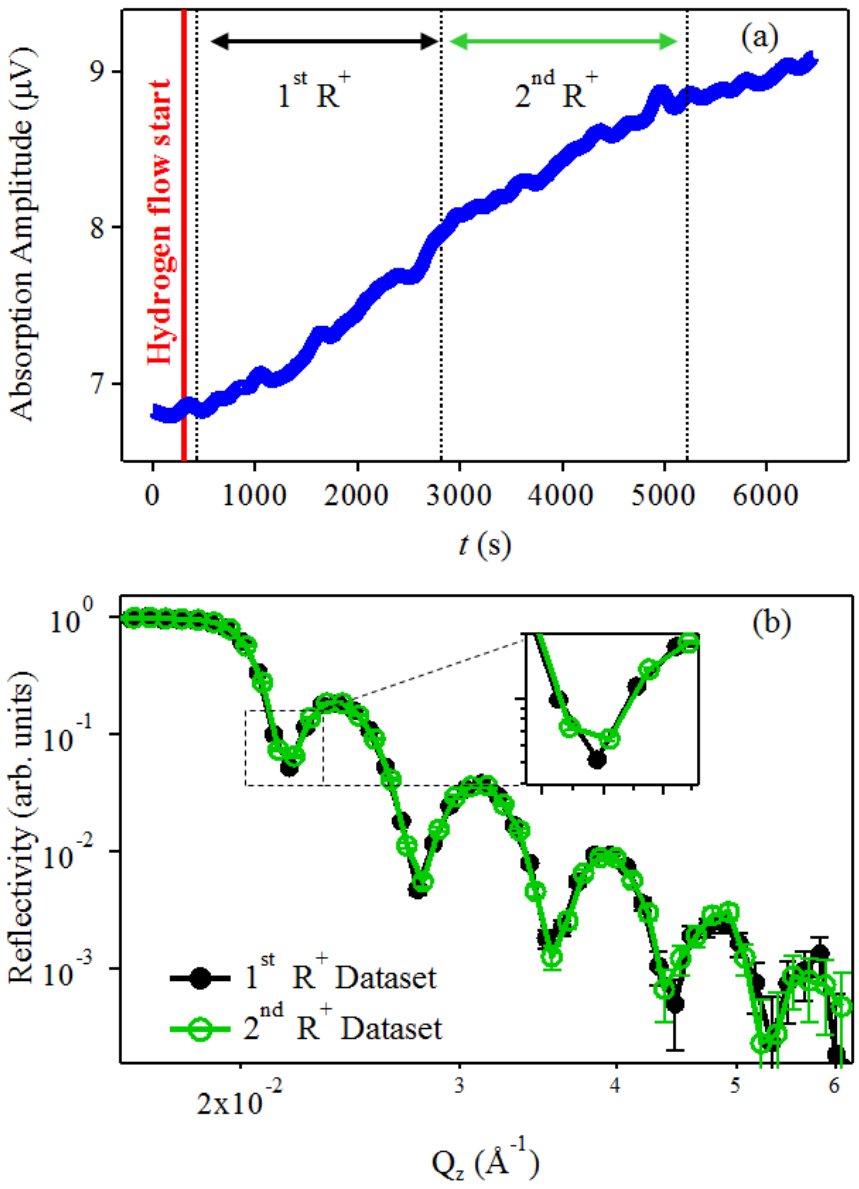

Figure 4.8: (a) Time-resolved FMR spectrum of the CNP alloy film during the initial stages of hydrogen-gas absorption. (b) Consecutive R^+ PNR patterns measured in parallel with the data of pane (a).

that the magnetisation dynamics of the CNP alloy evolve steadily in the presence of hydrogen gas. The slow development of the transient process, which is yet to plateau even after $>$ 2 hours in the presence of hydrogen gas, is illustrative for the purposes of the commissioning measurements because it allows a good demonstration of the usefulness of recording R^+ PNR patterns in parallel to time-resolved FMR spectra.

The two R^+ PNR absorption measurements acquired in parallel to the time-resolved FMR spectrum are shown in Figure 4.8(b). The first R^+ absorption data set commenced at $t = 420$ s of the time-resolved FMR spectrum and was acquired until $t = 2820$ s, at which time the second R^+ absorption data set begun. Only very minor deviations between the first and the second R^+ absorption data sets are observed, despite the clear evidence provided by FMR measurements that the dynamical magnetic properties of the CNP alloy are changing in the presence of hydrogen gas. Having the ability to sense changes to the dynamic magnetisation behaviour of a film, before significant changes to structure and/or static magnetisation behaviour are detectable by PNR, further vindicates the usefulness of combining PNR and FMR into a single experimental set-up.

Figure 4.9 shows the (a) R^+ and the (b) R^- PNR patterns obtained for the CNP alloy film before hydrogenation (red data symbols and fitting curves) and in the hydrogenated state (blue data symbols and fitting curves). Each PNR data set is, respectively, analogous to the field-resolved FMR spectra displayed in Figure 4.7(a) and (b). The nuclear and magnetic SLD profiles extracted from fitting the PNR data in each state are shown in the inset of Figure 4.9.

To obtain a suitable fit to the PNR data before hydrogenation, the chemical profile of the CNP alloy film was divided into several discrete layers, each approximately 10 nm in thickness, and each occupying marginally dissimilar nuclear SLD values. In this model, the nuclear SLD (Figure 4.9 inset, dashed black line) tends to decrease steadily towards the film surface. This can be explained by assuming an inhomogeneous alloy composition across the sample depth. In the hydrogenated state, the nuclear SLD of the CNP alloy film will be reduced because (as discussed in Section 4.1.5) hydrogen possessing a negative neutron scattering length of $b_{\mathrm{H}} = -3.74$ fm. In fitting the data, an insignificant amount of hydrogen was found to have been absorbed by the film, such

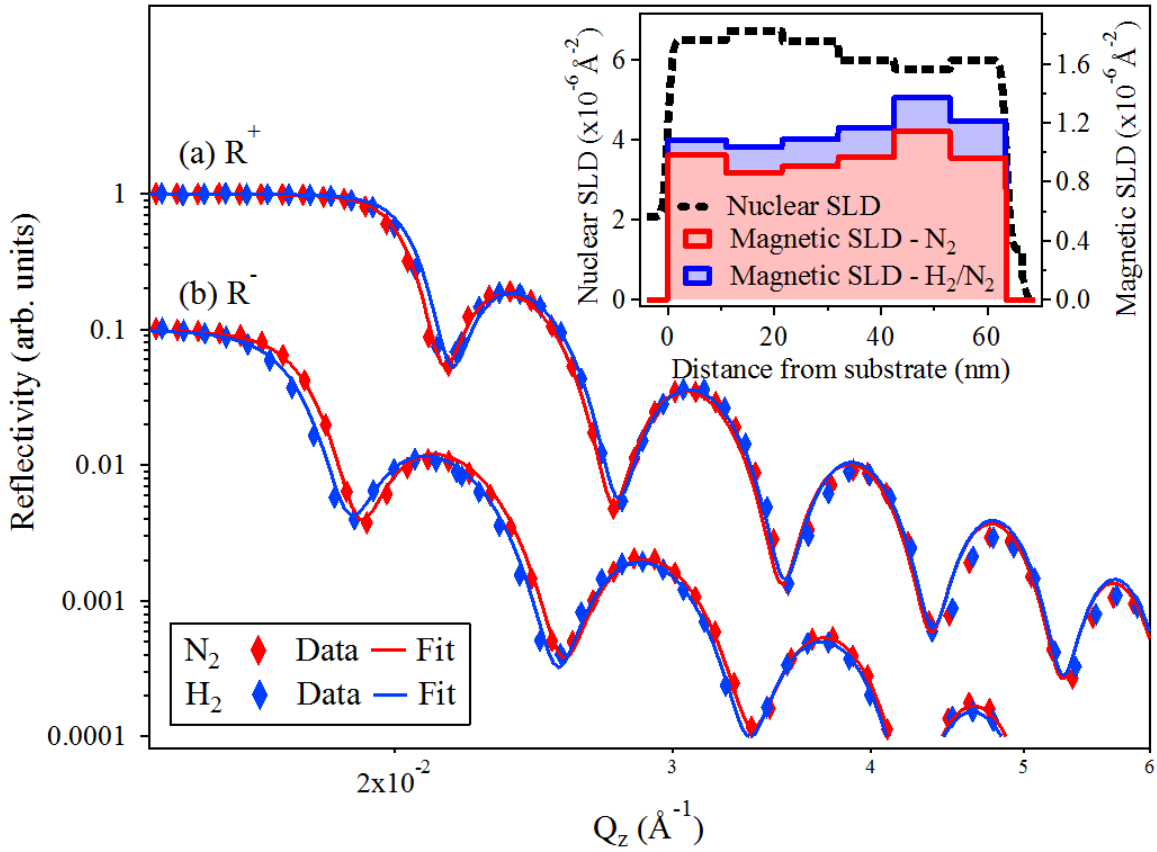

Figure 4.9: (a) R^+ and (b) R^- PNR patterns obtained for the CNP alloy film before hydrogenation (red data points and fits) and in the hydrogenated state (blue data points and fits). For clarity, the R^- data sets have been offset by an order of magnitude on the ordinate axis. Error bars lie within the data set symbols. (Inset) The nuclear and magnetic SLD profiles extracted from fitting the PNR data before hydrogenation (red) and in the hydrogenated state (blue).

that the reduction to the nuclear SLD in the hydrogenated state remained below the detection limit of the PNR instrument. Using this information in conjunction with Equation 4.3, an upper-bound limit of the number-density ratio between hydrogen atoms and CNP alloy atoms of 0.04:1 was established for the CNP alloy film in the hydrogenated state. The magnetic SLD profile, which is sensitive only to the in-plane FM moment of the film, does however increase almost monotonically over the sample depth in the presence of hydrogen gas (Figure 4.9 inset, red and blue profiles). Further, the sign of the change agrees with the field-resolved FMR results of Figure 4.7, where

a decrease in the FMR resonance position was found upon hydrogenation. This is consistent with an increase in the in-plane magnetic moment ($M_{\parallel}$ of Equation 4.2) of the film, as confirmed by PNR.

By extracting the in-plane FM moment of the film from the magnetic SLD profile and acknowledging the FMR resonance position, the H_{PMA} for the CNP alloy film before and after hydrogenation can be calculated from Equation 4.2. Doing so allows for an evaluation of the strength of the PMA and how it quantitatively changes as a function of the external stimulus. More precisely, insight can be gained as to whether the observed shift to the FMR resonance position is solely due to an increase in $M_{\parallel}$ upon hydrogenation, or whether these changes are also a result of contributions from modifications to the film's PMA in the presence of hydrogen gas. Performing the above calculation for the CNP alloy, the in-plane magnetic moment of the film before hydrogenation and in the hydrogenated state are $4\pi M_{\parallel} = 2090$ G and $4\pi M_{\parallel} = 2500$ G, respectively. Using these values and assuming $3.2 \leq \gamma \leq 3.3$ MHz Oe^{-1}, the upper-bound and lower-bound approximations to the change in the H_{PMA} of the film in the hydrogenated state are calculated to be 150 Oe and 160 Oe, respectively. Interestingly, the lower-bound γ value corresponds to a vanishing H_{PMA} in the virgin state, while the upper-bound γ value returns a H_{PMA} of 202 Oe. As both values are less than 10% of the in-plane magnetic moment of the CNP alloy film before hydrogenation, they lie within the experimental error of the measurement. As a result, it can be concluded that the changes which occur to the magnetic state of the CNP alloy film in the hydrogenated state originate primarily from increases to the in-plane magnetic moment of the sample. This is important result which cannot be obtained from either of the two measurement techniques alone.

4.3 Sample Growth and Characterisation

The previous section established a method for characterising the static magnetic and dynamic magnetisation behaviours of FM films in the presence of hydrogen gas atmospheres. In this section the abovementioned experimental technique is applied to Co/Pd bilayers in order to characterise their changing magnetic behaviours in the presence of hydrogen gas. Prior to the *in situ* investigation, the structural and magnetic properties of the Co/Pd bilayers are first comparatively investigated via several lab-based characterisation methods.

The Co/Pd bilayers studied in this chapter were grown by DC magnetron sputter deposition at the University of Western Australia. Four bilayers were grown and deposited onto 12.5 × 10 mm (100)-oriented thermally-oxidised Si substrates. The base pressure of the chamber was 2.7 $\times 10^{-2}$ mPa prior to deposition. Deposition took place in an ultra-high purity (99.999%) argon gas atmosphere at a working pressure of 1 Pa. The power to the magnetron guns was fixed to 100 W during the deposition of Co, and 60 W during the deposition of Pd. Deposition rates of 0.61 and 1.04 nm s^{-1} were calibrated for the Co and Pd targets, respectively, from preliminary profilometry measurements. The nominal thicknesses of the deposited Co and Pd layers were estimated from the calibrated sputtering rate of the respective target. The sputtering time of the Co target was fixed for each deposition to provide a consistent and nominal Co layer thickness of 5 nm to each sample. It had previously been established through preliminary investigations that a Co layer thickness of 5 nm provided optimum FMR responses [170]. The sputtering time of the Pd target was varied between each deposition to provide nominal thicknesses of 3, 5, 10, 15 nm between the four bilayers, such that thickness-dependent studies in relation to hydrogen-induced behaviour could be carried out. The four deposited bilayers are herein referred to as the: Co/Pd(3 nm),

Co/Pd(5 nm), Co/Pd(10 nm) and Co/Pd(15 nm) bilayers, where the nominal Co layer thickness of each film is a constant (5 nm). The thickness uniformity of each Co/Pd bilayer across the sample dimension was better than 5% [168].

4.3.1 *Ex situ* Characterisation

The chemical depth-profile of each Co/Pd bilayer was examined by XRR. Figure 4.10 displays the XRR data of the four Co/Pd bilayers collected in air at room temperature. Each data set was corrected for the footprint of the X-ray beam incident on the sample surface. Good fits to the data sets of each film were obtained by allowing the real and imaginary parts of the X-ray SLD of the Co and Pd layers to vary between $90 - 100\%$ of the bulk X-ray SLD of Co and Pd, respectively. The X-ray SLD of the Si substrate was restricted to the bulk value throughout all the fitting procedures. The bulk X-ray SLDs of Co, Pd and Si are $(63.02 - 9.14\text{i}) \times 10^{-6}$ Å^{-2}, $(87.62 - 7.57\text{i}) \times 10^{-6}$ Å^{-2}, $(20.05 - 0.45\text{i}) \times 10^{-6}$ Å^{-2}, respectively. The simulated X-ray SLD profiles obtained from best fits to the XRR data are shown in the inset of the corresponding figure (the χ^2 of each fit was < 0.05). Each bilayer exhibits an approximate 2 nm-thick alloyed region at the Co/Pd interfacial boundary. The alloy content trends as $\text{Co}_x\text{Pd}_{1-x}$ for $0 \leq x \leq 1$ across the Co/Pd interface profile which results from the natural diffusion of Pd atoms into the Co layer during room-temperature deposition. The modelled thicknesses of the Co and Pd layers of each film (inclusive of the alloyed interface) are within $\pm$ 1.5 nm of their nominal values. The surface roughness of each film was modelled to be on the order of $1 - 2$ nm. As a result, the Co/Pd(3 nm) and the Co/Pd(5 nm) bilayers have large surface roughnesses relative to the thickness of their Pd layers (and as such are disregarded to a large extent throughout the ensuing analysis). The individual layer thicknesses, interfacial and surface roughness parameters extracted from each

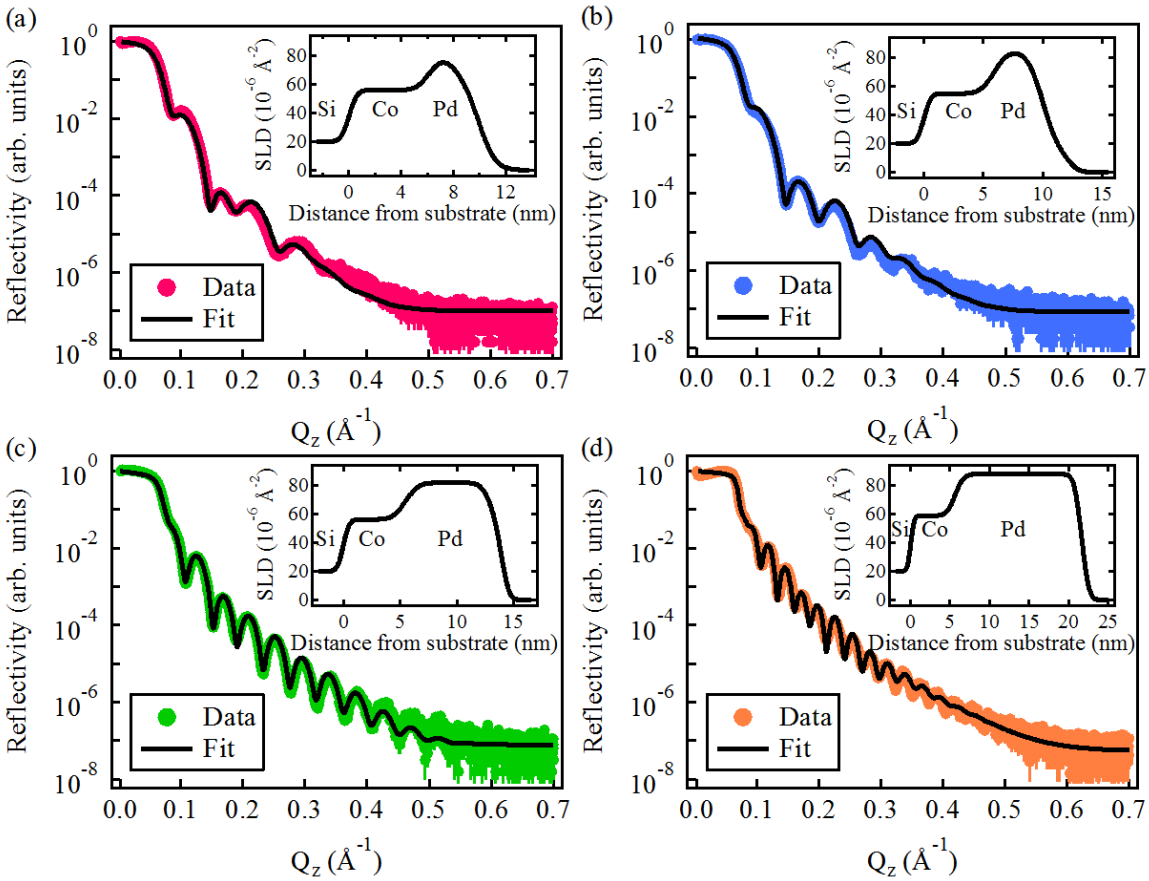

Figure 4.10: XRR data (closed symbols) and best fits (solid curves) to the (a) Co/Pd(3 nm), (b) Co/Pd(5 nm), (c) Co/Pd(10 nm) and (d) Co/Pd(15 nm) bilayers. The X-ray SLD profiles obtained from best fits to the XRR data are correspondingly shown in the inset of each figure. Measurements were recorded in air at room temperature.

XRR chemical depth-profile were used as fixed inputs to model the nuclear SLD of the respective bilayer during the PNR modelling procedure (note: the XRR chemical depth-profile formed the basis of the structural PNR model of each Co/Pd bilayer prior to hydrogen absorption only).

Each Co/Pd bilayer was further structurally characterised by high-angle XRD. Each XRD spectrum was collected over a 2θ range from 20° to 90°, and obtained with a constant ω-offset of 0.04° to diminish the relatively strong intensity of reflections originating from the Si substrate. The XRD peak positions of each Co/Pd bilayer

showed good agreement to face-centred-cubic Pd. Accordingly, the XRD spectrum of the Co/Pd(15 nm) bilayer presented in Figure 4.11 shows evidence of Pd (111) and Pd (113) Bragg reflections which correspond to 2θ locations of 40.14° and 82.22°, respectively. All bilayers possessed high-intensity Pd (113) reflections, whereas the intensity of the Pd (111) reflection was absent (i.e., not observable above background) in the XRD spectra of the thinner bilayers. Similarly, no characteristic face-centred-cubic (or hexagonal closed-packed) Co Bragg reflections were observed in the XRD spectra of any of the Co/Pd bilayers, and is likely a consequence of the small volume and polycrystallinity of the Co layer of each film.

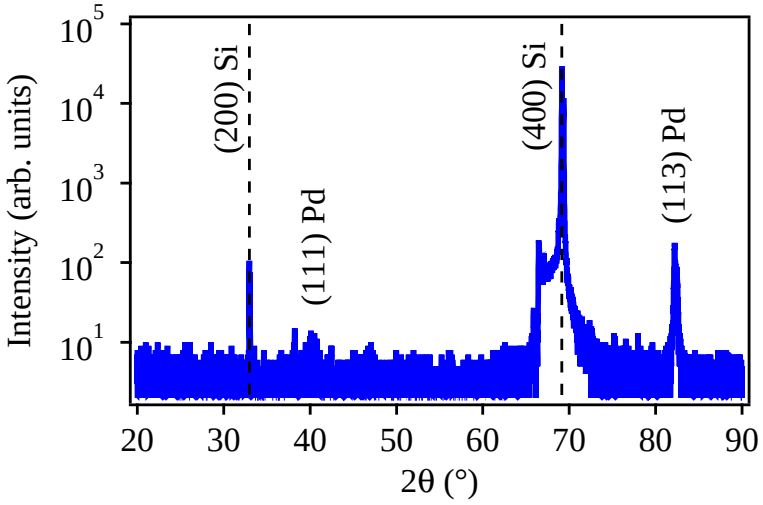

Figure 4.11: High-angle XRD spectrum of the Co/Pd(15 nm) bilayer measured in air at room temperature, showing evidence of the Pd(111) and the Pd(113) Bragg reflections.

In Figure 4.12, filtered HR-TEM images recorded in the [110] zone axis of the Co/Pd(10 nm) bilayer confirms the thickness and polycrystallinity of the Co and Pd layers. FFT verify the collective presence of face-centred-cubic Co and Pd grains. Cross-sectional TEM measurements confirm the presence of an approximate 1 nm-thick oxide layer on the surface of the silicon substrate, which likely results from the oxidation of Co at the $Si/SiO_2/Co$ interface, and is consistent with previous samples

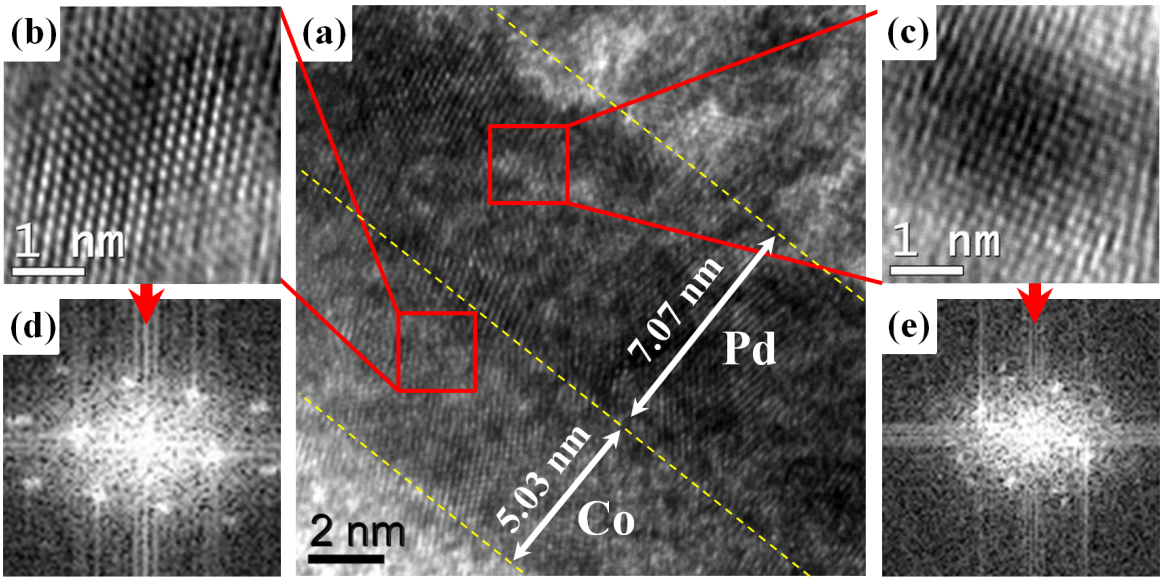

Figure 4.12: (a) Filtered HR-TEM image of the Co/Pd(10 nm) bilayer measured in the [110] zone axis. High-magnification images of the (b) Co layer and the (c) Pd layer taken from the marked areas in (a). FFT of the high-magnification images of the (d) Co layer and the (e) Pd layer which display diffraction patterns consistent with face-centred-cubic Co and Pd, respectively.

grown under the same conditions [171].

The in-plane and the out-of-plane field-induced magnetic responses of each Co/Pd bilayer were investigated by VSM magnetometry. The bilayers were measured in a Quantum Design PPMS VSM located at ACNS, ANSTO. To avoid magnetic artefacts arising in the measured data, the remanent hysteresis of the PPMS device was removed prior to data acquisition by oscillating and dampening the field (current) of the electromagnet between ± 500 Oe. The field-induced magnetic moment of each Co/Pd bilayer was measured at 300 K over a field range of ± 3000 Oe and ± 40 kOe for the in-plane and the out-of-plane measurements, respectively. Magnetisation data was obtained by normalising the measured moment of each Co/Pd bilayer to the volume of the Co layer, using the Co layer thickness extracted from the best fit to the corresponding XRR data set. Magnetisation data were corrected for the diamagnetic response of the substrate. Figure 4.13 displays the 300 K (a) in-plane and (b) out-

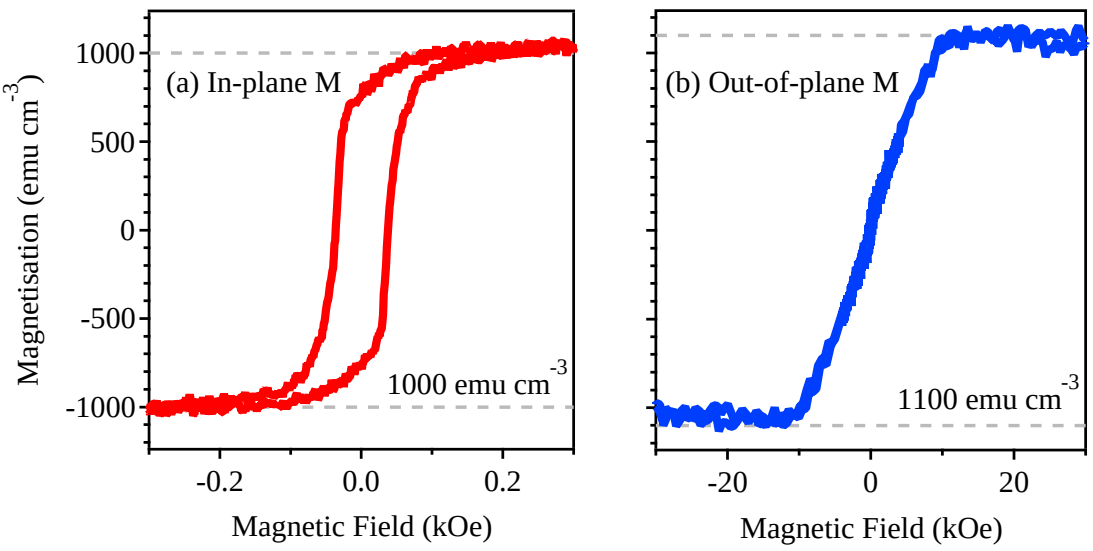

Figure 4.13: The (a) in-plane and the (b) out-of-plane M-H behaviours of the Co/Pd(10 nm) bilayer measured at 300 K. The M-H behaviours shown are representative of all Co/Pd bilayers.

of-plane magnetisation vs field (M-H) variations of the Co/Pd(10 nm) bilayer, which is representative of the M-H behaviours of all other bilayers. Namely, the magnetic anisotropy of each Co/Pd bilayer exhibits an in-plane magnetic easy-axis and an out-of-plane magnetic hard-axis as evidenced by the low- and high-saturation fields of the respective measurement directions. The in-plane H_C of each bilayer is on the order of 50 Oe while the out-of-plane magnetisation saturates under an applied field of approximately 10 kOe. The saturation magnetisation of each Co/Pd bilayer is approximately 1100 emu cm^{-3}, which is in good agreement with the volume-magnetisation of bulk Co (e.g., 1417 emu cm^{-3} at 300 K [51]). Furthermore, in Figure 4.13 the approximate 100 emu cm^{-3} discrepancy in the saturation magnetisation of the Co/Pd(10 nm) between the in-plane (low-field) and the out-of-plane (high-field) M-H variations manifests the volume-averaged magnetic contribution of the interfacial PMA moments. It follows that the interfacial moments which remain perpendicular-to-plane in a 0.3 kOe in-plane applied field, can be saturated in-plane under the application of a 10 kOe

in-plane applied external magnetic field.

4.3.2 PNR with *in situ* FMR Characterisation

PNR and *in situ* FMR data sets of the four Co/Pd bilayers were obtained using the commissioned sample environment and the data acquisition routine outlined in Section 4.2. Each Co/Pd bilayer was sequentially loaded into the PNR with *in situ* FMR sample chamber and measured at room temperature on the PLATYPUS beamline at ACNS, ANSTO. The electromagnet of the PLATYPUS instrument provided sweeping fields during field-resolved FMR measurements and sample-dependent fields during time-resolved FMR measurements. For the acquisition of PNR data, the electromagnet provided a 1 kOe sample field which was sufficient to magnetise the bulk Co moments while being insufficient to saturate the interfacial PMA moments into the plane of the film. The specular reflected R^+ and R^- intensities were recorded as a function of the incident angle θ using a time-of-flight data collection mode. Data was analysed in terms of the wavevector transfer Q_z ($= 4\pi\sin\theta/\lambda$) which is directed normal to the sample surface. The experimental resolution ($\Delta Q_z/Q_z$) of the PNR set-up was 5.2%. A determination of the nuclear and magnetic SLD profiles across each bilayer were obtained by fitting model structures to the respective PNR data sets using the SIMULREFLEC software package. A mass-flow controller was used to deliver pure N_2 gas or 3.5% H_2/N_2 gas mixture to the sample chamber at a flow rate of 4.2 $\times 10^{-6}$ m^3 s^{-1} (250 ml min^{-1}), corresponding to an effective hydrogen partial pressure of 35.5 mbar (assuming 1 bar total pressure) within the chamber at ambient temperature. Although it was found that a 3.5% H_2/N_2 atmosphere was insufficient to produce measurable modifications to the structural SLD of a Pd-alloyed film upon hydrogenation (see Figure 4.9), preliminary reflectivity simulations nevertheless con-

firmed that 3.5% H_2/N_2 would generate sizeable hydrogen-induced variations to the reflectivity of Co/Pd bilayer structures over the measurable Q_z range.

To begin the PNR with *in situ* FMR investigations, it is first necessary to establish qualitatively if the magnetic and structural properties of the Co/Pd bilayers behave reversibly between consecutive exposures to hydrogen gas. Figures 4.14 and 4.15 show the PNR data sets and the *in situ* FMR spectra obtained from the Co/Pd(15 nm) bilayer during the first and second cyclic exposures of the sample to pure N_2 and 3.5% H_2/N_2 atmospheres. A single cycle is defined as moving from an atmosphere of pure N_2 to 3.5% H_2/N_2 (hydrogenated state) before returning to N_2 (dehydrogenated state) and commencing the next cycle. The PNR data sets of Figure 4.14 are organised such that the respective N_2 and H_2/N_2 states of the first and second cyclic exposures can be compared directly. Through qualitative assessment of the PNR data it is quite evident that the reflectivity of the Co/Pd bilayer in the N_2 state of the first cycle is inconsistent with the N_2 state of the second cycle. On the other hand, the H_2/N_2 states of the first and second cycles are comparable (within the error bar) at each Q_z location across the reflectivity spectrum. The distinct differences observed in the reflectivity of the Co/Pd bilayer between the sequential N_2 states is attributed to the Pd layer succumbing to hydrogen-induced annealing during the initial cycle after hydrogen gas is first desorbed from the Pd layer (as described in Section 4.1.4). The series of FMR spectra presented in Figure 4.15 also document an irreversible change to the magnetic anisotropy landscape of the Co/Pd(15 nm) bilayer during hydrogen-gas cycling. In the H_2/N_2 state, the characteristic FMR resonance position shifts to lower in applied field with respect to the N_2 state of the corresponding cycle, indicating a weakened PMA of the Co/Pd bilayer upon hydrogen-gas absorption. However, it is apparent that there is a fundamental change in the magnetic anisotropy of the bilayer between the consecutive exposures which prevents the FMR responses of the first cycle from

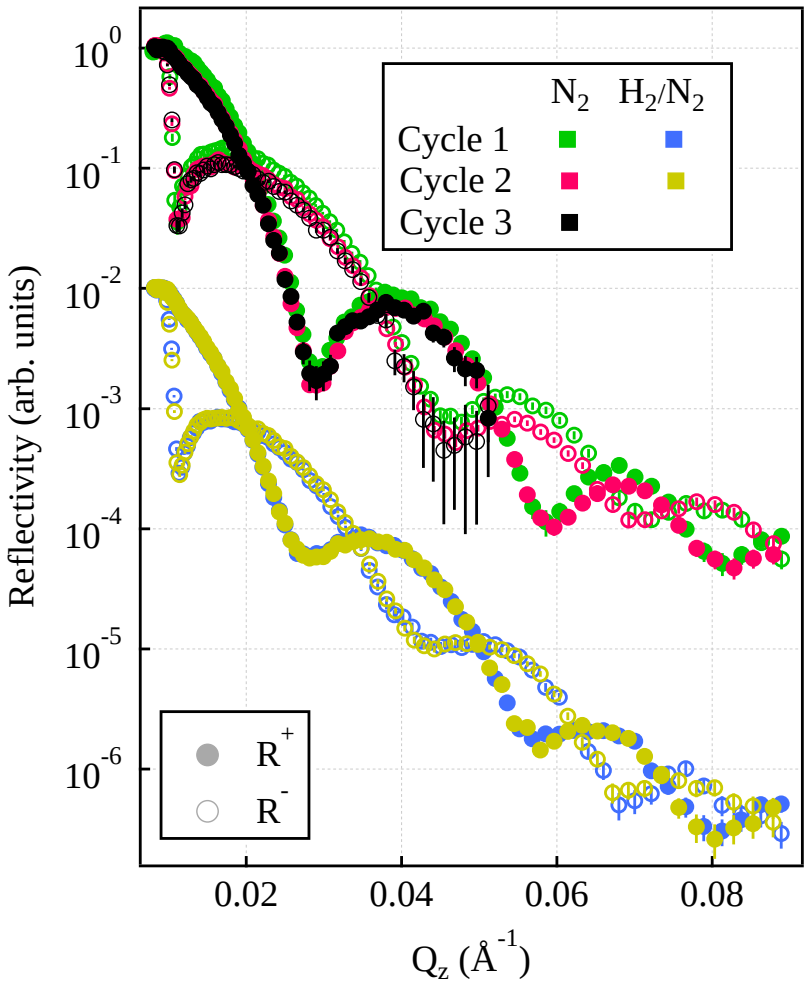

Figure 4.14: PNR data sets of the Co/Pd(15 nm) bilayer during the first and second cyclic exposures to a 3.5% H_2/N_2 atmosphere. The H_2/N_2 data sets are shifted on the ordinate axis for clarity.

coinciding with the FMR responses of the second cycle. By cycling the Co/Pd bilayer a third consecutive time, the reflectivity and magnetic resonance (data not shown) of the bilayer were found to be consistent with the data sets recorded during the second cyclic exposure in the corresponding atmosphere. This verifies that the structural and magnetic properties of the Co/Pd bilayer respond reversibly to hydrogen gas only after the polycrystalline Pd lattice is first annealed by hydrogen during the initial cycle. From establishing reversible properties between the higher-order exposures, the key aim of the ensuing work is to characterise the irreversible modifications which

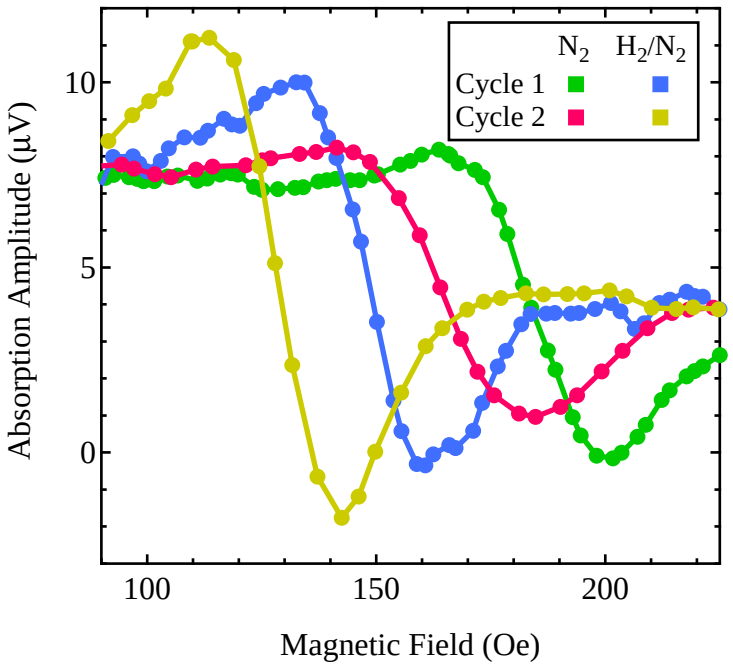

Figure 4.15: FMR spectra of the Co/Pd(15 nm) bilayer during the first and second cyclic exposures to a 3.5% H_2/N_2 atmosphere. All data sets were acquired at a microwave frequency of 4.4 GHz.

occur to the magnetism and structure of polycrystalline Co/Pd bilayers upon *primary* hydrogen-gas absorption. In the proceeding section, in the interest of characterising the properties of all four Co/Pd bilayers while keeping data presentation to a minimum, only the PNR and *in situ* FMR data sets of the Co/Pd(10 nm) bilayer will be presented, and will be analysed in terms of the equivalent behaviours observed in the Co/Pd(3, 5, 15 nm) bilayers.

Figure 4.16 displays the sequential room-temperature PNR data sets collected during the first cyclic exposure of the Co/Pd(10 nm) bilayer to a 3.5% H_2/N_2 gas mixture. Open symbols denote the specular reflected R^+ and R^- cross-sections measured with the incident neutron polarisation oriented parallel (+) and antiparallel (−) with respect to a 1 kOe sample field. Solid curves superimposed on the PNR data sets denote the best-fit models. The simulated nuclear and magnetic SLD profiles of

the Co/Pd(10 nm) bilayer obtained from the best fits to the PNR data at each stage during the hydrogenation cycle are presented in Figure 4.17.

Prior to recording the PNR data sets of Figures 4.16(b) and (c), the changing magnetic state of the Co/Pd(10 nm) bilayer during the initial stages of hydrogen-gas absorption and desorption were monitored by time-resolved FMR measurements. Figure 4.18 shows the time-resolved FMR spectra collected on the Co/Pd(10 nm) film during (a) hydrogenation and (b) dehydrogenation. At time $t = 300$ s of Figure 4.18(a) (depicted by the grey dotted line), 3.5% H_2/N_2 gas first enters the sample chamber, replacing the former pure N_2 atmosphere (depicted by data points at time $t < 300$ s). The gradual increase in the FMR absorption amplitude observed over the course of the measurement indicates that the magnetisation dynamics of the Co/Pd(10 nm) bilayer evolve steadily during the first exposure to hydrogen gas. Once the time-resolved FMR data set reaches a plateau with respect to the absorption amplitude at time $t = 8000$ s, hydrogenation of the film is complete, and recording of the PNR data set of Figure 4.16(b) commenced. During the dehydrogenation of the Co/Pd(10 nm) bilayer in Figure 4.18(b), pure N_2 gas first enters the chamber at time $t = 60$ s (depicted by the grey dotted line), replacing the former 3.5% H_2/N_2 atmosphere. Unlike the gradual changes observed in the time-resolved FMR spectrum during primary hydrogen-gas absorption, a rapid decrease (≈ -1.75 μV) in the FMR absorption amplitude is observed within the first 40 s from the initial admission of N_2 gas. This corresponds to the removal of α'-phase hydrogen atoms from the Pd layer of the Co/Pd bilayer. The gradual slope of the data from time $t = 100$ s corresponds to the desorption of the more stable α-phase hydrogen atoms from the Pd lattice. Again, the irreversibility of the first cyclic exposure is apparent in the time-resolved FMR data. Firstly, the primary absorption process occurs over a greater time period than the subsequent desorption process, as has been observed by other authors [150, 232]. Secondly, the change in the

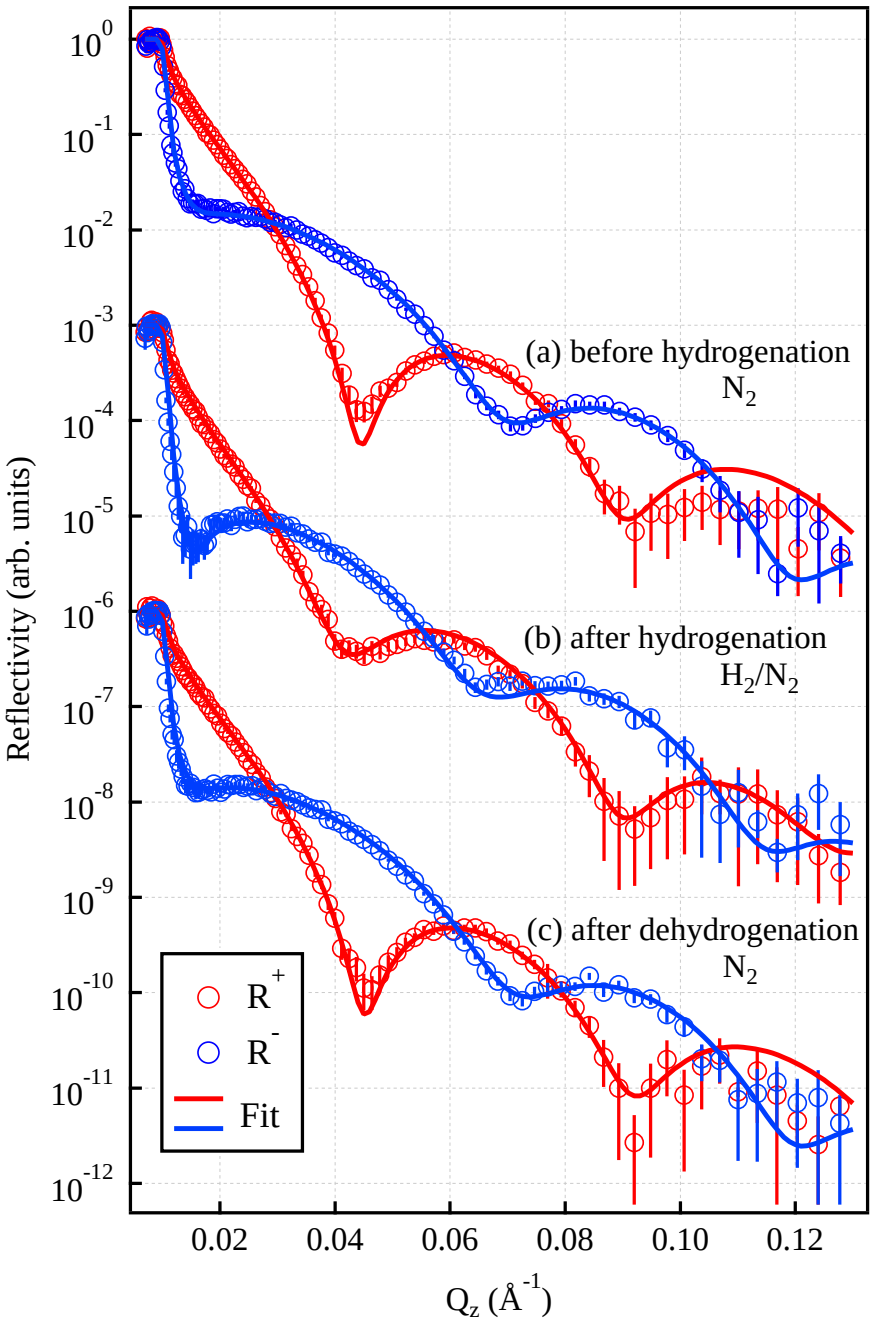

Figure 4.16: PNR data (open symbols) and best fits (solid curves) to the R^+ and R^- cross-sections of the Co/Pd(10 nm) bilayer (a) before hydrogenation (measured in N_2), (b) after hydrogenation (measured in 3.5% H_2/N_2), and (c) after dehydrogenation (measured in N_2). Data sets (b) and (c) are shifted on the ordinate axis for clarity.

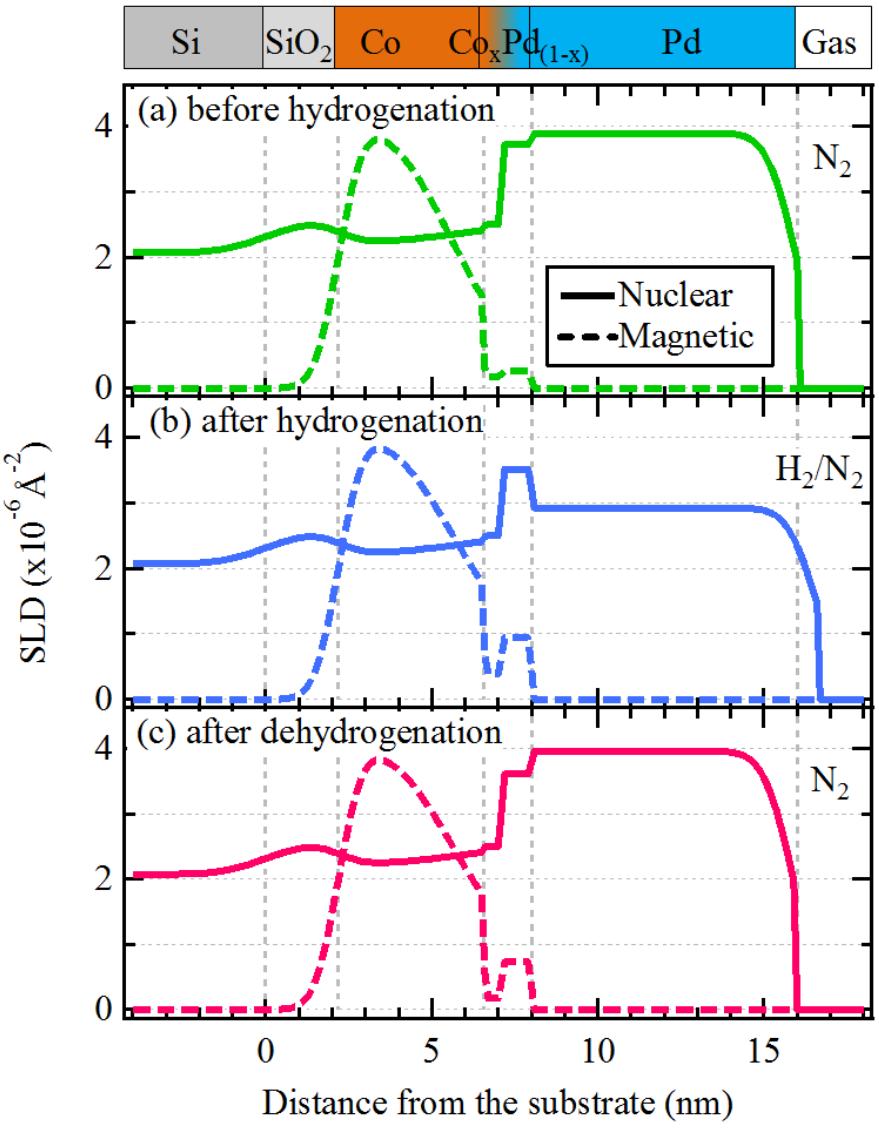

Figure 4.17: Nuclear and magnetic SLD profiles of the Co/Pd(10 nm) bilayer (a) before hydrogenation (measured in N_2), (b) after hydrogenation (measured in 3.5% H_2/N_2) and (c) after dehydrogenation (measured in N_2). Modelled SLDs are obtained from best fits to the PNR data and are plotted as a function of sample depth from the SiO_2-terminated Si substrate. Solid and dashed lines denote the SLD arising from nuclear and magnetic components of the bilayer, respectively.

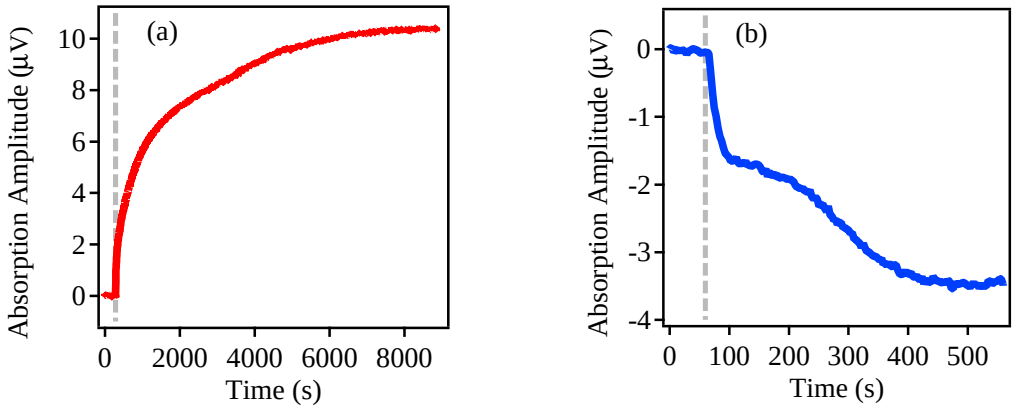

Figure 4.18: Time-resolved FMR spectra of the Co/Pd(10 nm) bilayer during the initial stages of (a) hydrogen-gas absorption and (b) hydrogen-gas desorption.

FMR absorption amplitude occurring over the course of the desorption of hydrogen atoms from the Co/Pd(10 nm) bilayer (i.e., $|\Delta| \approx 4\ \mu$V) does not compensate for the magnitude of changes occurring during the initial hydrogenation of the bilayer (i.e., $|\Delta| \approx 10\ \mu$V).

Returning to Figure 4.16, the oscillatory behaviour of each PNR data set is namely attributed to the scattering contrast provided by the differing chemical characteristics of the Co and Pd layers of the film, while the separation between the R^+ and R^- channels is indicative of an in-plane FM magnetisation which is encoded in the Q_z-dependence of the spin-asymmetry. After the absorption of hydrogen gas, minima in the reflectivity shift to lower positions in Q_z indicating an increase in the total physical thickness of the bilayer, while dampened fringe oscillations suggest a reduction in the film's chemical scattering contrast. Data analysis indicates a remarkable 7.5% increase in the overall Pd layer thickness in the presence of hydrogen gas. This increase is greater than the three-dimensional 3.6% expansion expected for bulk Pd in the α'-phase [124], and results from the anisotropic influence of the substrate which changes the proportionality factor during hydrogen absorption by largely preventing any in-plane expansion of the thin-film Pd lattice (as previously discussed in Section

4.1.4). By comparing the SLD profiles of Figure 4.17(a) and (b) it is confirmed that the chemistry and magnetism of the bulk of the Co layer are unaffected by the presence of the 3.5% H_2/N_2 atmosphere. Furthermore, the Co layer displays a linearly degrading magnetic SLD in proximity to the Pd layer, indicative of a coherent rotation of the layer's magnetisation vector from an in-plane to an out-of-plane direction (but could also suggest minor alloy formation). In comparison, between Figures 4.17(a) and (b), the Pd layer features a pronounced and uniform reduction in nuclear SLD which is indicative of a homogeneous concentration of hydrogen atoms throughout the layer. Examining the modifications to the thickness and SLD of the Pd layer upon hydrogenation, the average C_{H} within the Pd lattice in the hydrogenated state can be estimated using Equation 4.3 and the best-fit parameters to the PNR data listed in Table 4.2. From this analysis it is determined that for every 1 Pd atom there are 0.31 hydrogen atoms (on average) occupying the Pd lattice of the Co/Pd(10 nm) bilayer in the presence of a 3.5% H_2/N_2 atmosphere. Referring to Figure 4.2(b), this establishes that the hydrogenated Co/Pd(10 nm) bilayer is most likely situated towards the end of miscibility gap at the α'-phase boundary of the Pd-hydride phase diagram. Applying the same analysis to the remaining Co/Pd(3, 5, 15 nm) bilayers using the best-fit parameters to the PNR data sets provided in Table 4.2, it is found that the thickness of the hydrogen-absorbing layer has a strong influence on the maximum C_{H} which can be absorbed by the Co/Pd bilayer in a given atmosphere of hydrogen. Specifically, when exposed to a 3.5% H_2/N_2 atmosphere the C_{H} absorbed in the four Co/Pd bilayers trends as 0.048, 0.052, 0.31 and 0.42 as a function of increasing Pd layer thickness. This inherent dependence is accredited to electronic effects (as previously discussed in Section 4.1.4). Close to the Co/Pd interface of each bilayer, within the first few monolayers of the Pd layer, drastic deviations from bulk behaviour may occur due to charge-transfer with the Co atoms which fill holes at the Fermi level of the Pd 4d-band

which lowers the density of available states [198]. The transfer of electrons from Co to Pd within the alloyed portion of the bilayer lowers the solubility of hydrogen (as depicted in Figure 4.3), and results in a comparatively reduced absorption of hydrogen atoms in Co/Pd bilayers with larger interface-to-bulk Pd volume ratios.

Bilayer	SLD_{Pd} ($\times 10^{-6}$ Å^{-2})	SLD_{Pd+H} ($\times 10^{-6}$ Å^{-2})	t_{Pd} (nm)	t_{Pd+H} (nm)	C_H (H/Pd at.%)
Co/Pd(3 nm)	3.42	2.99	3.07	3.40	0.048
Co/Pd(5 nm)	3.27	3.12	5.48	5.55	0.052
Co/Pd(10 nm)	3.91	2.93	8.00	8.60	0.31
Co/Pd(15 nm)	3.86	2.66	15.39	16.48	0.42

Table 4.2: Parameters used in the calculation of the average C_H absorbed by the Pd layer of each Co/Pd bilayer in a 3.5% H_2/N_2 atmosphere. Parameters were obtained from best fits to the PNR data sets of each bilayer between the N_2 (subscript: Pd) and the 3.5% H_2/N_2 (subscript: Pd+H) atmospheres of the first cyclic exposure.

Upon the complete removal of hydrogen from the Co/Pd(10 nm) bilayer, the PNR spectrum in Figure 4.16(c) appears to return to a state qualitatively similar to the data set of Figure 4.16(a). However, minor differences in the PNR spectral features parameterised by the SLD profiles in Figures 4.17(a) and (c) reveal that the Pd layer component of the film features an increased SLD (1.51%) in addition to a reduced thickness (1.75%) relative to the primary film. Both variations are ascribed to the cold-annealing of the Pd layer by hydrogen (as previously characterised for the Co/Pd(15 nm) bilayer) which changes the stress state of the film [200]. Through the removal of defect volume, the annealing process leads to an inadvertent increase in the atomic-packing factor of the thin-film lattice which simultaneously increases the SLD (i.e., the atomic density component) while reducing the total thickness of the Pd layer upon dehydrogenation. Subsequent XRR characterisation of the Co/Pd(10 nm) bilayer after

dehydrogenation also confirms this behaviour. Figure 4.19 compares the XRR data and best fits to the Co/Pd(10 nm) before hydrogenation and after dehydrogenation. From best fits to the XRR data, the thickness of the Pd layer (relative to the primary film) contracts by 2.24% and increases in SLD by 1.05% after hydrogen-annealing. The magnitudes of the changes obtained from best fits to the XRR data are consistent with the PNR best fits.

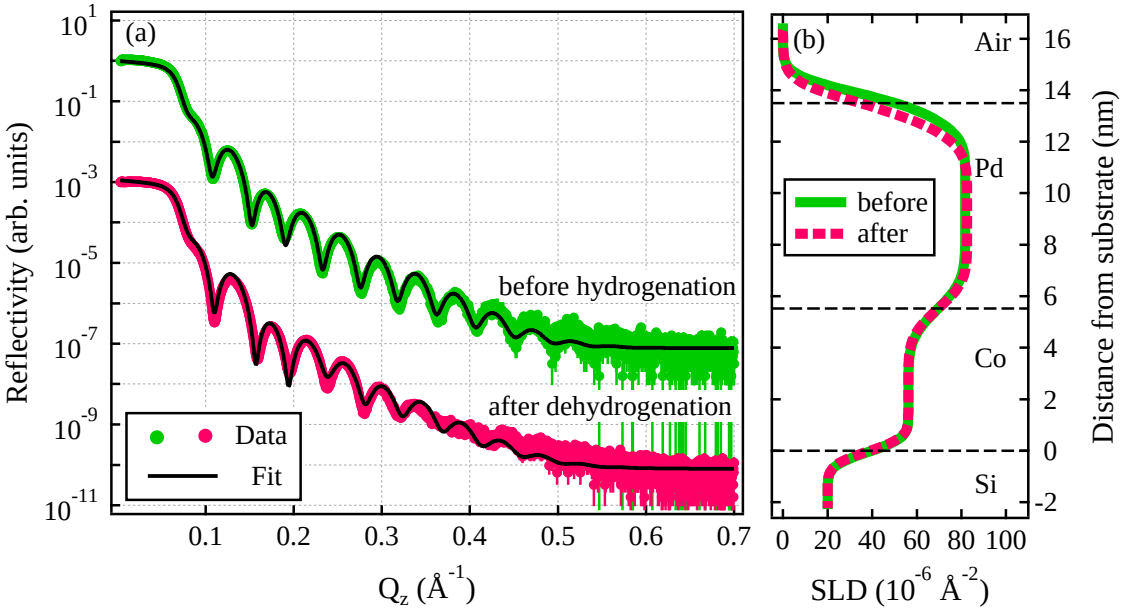

Figure 4.19: (a) XRR data (closed symbols) and best fits (solid curves) to the Co/Pd(10 nm) bilayer before hydrogenation and after dehydrogenation. (b) Corresponding X-ray SLD profiles obtained from best fits to the XRR data in either state. Measurements were recorded in air at room temperature.

In Figure 4.17 the bilayer's Co/Pd interface is modelled as a 1.4 nm-thick region which exhibits a complex chemical and magnetic depth-profile resulting from the room-temperature diffusion of Pd atoms into the deposited Co layer during film growth. Contingent on the precise Co_xPd_{1-x} stoichiometry (for $0 \leq x \leq 1$) of each layer-averaged section of the alloyed interface, the chemical and magnetic signatures can vary widely. For example, with $x = 0$ the nuclear and magnetic SLDs are 4.02 $\times 10^{-6}$ Å^{-2} and 0 $\times 10^{-6}$ Å^{-2}, respectively, and conversely 2.23 $\times 10^{-6}$ Å^{-2} and 4.11

$\times 10^{-6}$ Å^{-2} with $x = 1$. The combined nuclear and magnetic SLD of the Co_xPd_{1-x} diffusion profile therefore nominally trends as $(2.32x + 4.02)$ $\times 10^{-6}$ Å^{-2} across the interface. However, because of competing electronic effects and the FM polarisation of Pd at the interface [95, 72, 2], it would be an invalid assumption to separate the chemical and magnetic components of the alloyed region based on SLD considerations alone. Instead, to decouple the magnetic response of the alloyed interface from its complex chemical profile, the spin-asymmetry of the bilayer at each stage during the hydrogenation cycle is analysed in Figure 4.20(a). The non-zero Q_z-dependence of the spin-asymmetry arises from the asymmetric influence of the sample's in-plane FM magnetisation on the R^+ and R^- scattering potentials. As established earlier, the magnetisation of the bulk of the Co layer remains invariant between the N_2 and the H_2/N_2 atmospheres. Therefore, any changes to the spin-asymmetry of the film in the hydrogenated and dehydrogenated states must originate from modifications to the in-plane magnetisation of the alloyed interface only. Namely, the spin-asymmetry at the critical-edge location of $Q_c = 0.010$ Å^{-1}, shown enlarged in Figure 4.20(b), is proportional to the total in-plane FM magnetisation of the interface. Prior to hydrogen absorption, the full Q_z-range of the spin-asymmetry in Figure 4.20(a) in addition to the Q_c curvature of the data points in Figure 4.20(b) can be suitably modelled by an average in-plane interfacial magnetisation of 176 emu cm^{-3}, which increases to 402 emu cm^{-3} in the presence of hydrogen gas. In the desorbed state, the magnetisation decreases to 336 emu cm^{-3}; however, remains enhanced magnetically relative to the primary film (all values are calculated as averages over the interfacial thickness). The result confirms that a greater portion of interfacial moments turn into the plane of the film in the presence of hydrogen gas. Furthermore, the effect is irreversible because the primary magnetisation of the film is not recovered by the succeeding N_2 atmosphere. Equivalent trends have indeed been identified in CoPd alloys [160, 212]

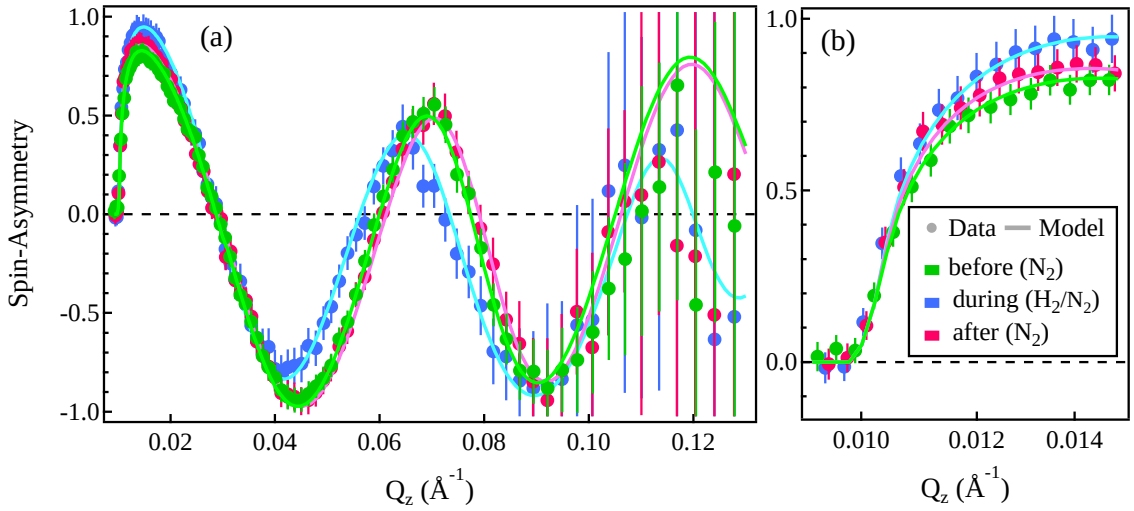

Figure 4.20: Evolution of the spin-asymmetry of the Co/Pd(10 nm) bilayer during primary hydrogen-gas absorption. Closed symbols denote data points, and solid lines denote magnetic models obtained from fitting the asymmetric influence of the samples' in-plane FM magnetisation on the R^+ and R^- scattering potentials. (b) The magnified critical-edge region of the spin-asymmetry, which is proportional to the total in-plane FM magnetisation of the interface.

and in atomically thin Co/Pd multilayers [197, 198] via sample-averaged magnetometry and magneto-optical Kerr effect measurements, and has been attributed to an irreversible reduction in the PMA of the specimen upon primary hydrogen absorption. However, we further observe that the relative change in the magnetic response of the Co/Pd bilayer between the primary and hydrogenated states exhibits a dependence on the thickness of the Pd layer. Figure 4.21 compares the spin-asymmetry of the (a) Co/Pd(3 nm), (b) Co/Pd(5 nm) and (c) Co/Pd(15 nm) bilayers at each stage during the hydrogenation cycle. It is evident that the spin-asymmetries of the two thinnest Co/Pd bilayers remain almost invariant (within the error bar) throughout the hydrogenation cycle, whereas the thickest bilayer displays the largest relative change in magnetic response in the presence of hydrogen gas. The increased frequency of the spin-asymmetry in the hydrogenated state of the Co/Pd(15 nm) bilayer in Figure 4.21(c) is a consequence of the hydrogen-induced expansion of the Pd layer. The

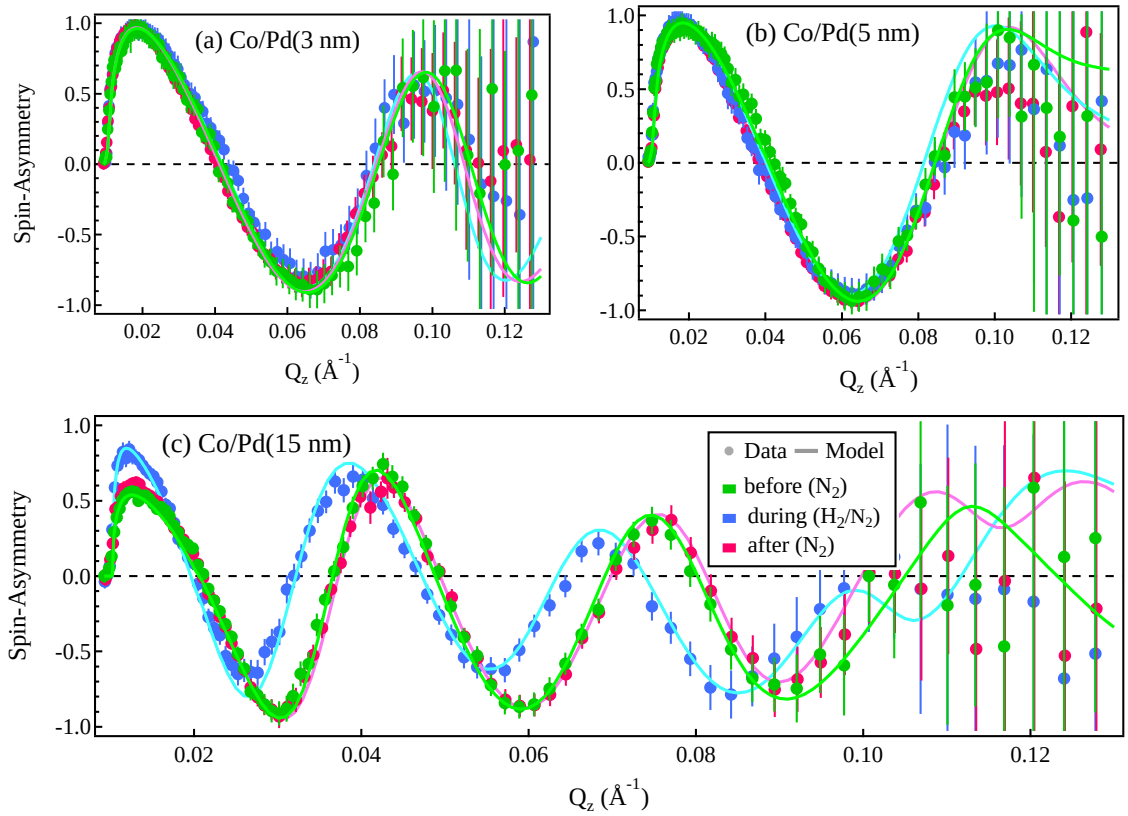

Figure 4.21: Evolution of the spin-asymmetry of the (a) Co/Pd(3 nm), (b) Co/Pd(5 nm), and (c) Co/Pd(15 nm) bilayers during primary hydrogen-gas absorption. Closed symbols denote the data points, and solid lines denote the magnetic models obtained from fitting the asymmetric influence of each film's in-plane FM magnetisation on the R^+ and R^- scattering potentials.

increased amplitude of the spin-asymmetry in proximity to the film's critical edge of reflectivity (at $Q_c = 0.010$ Å^{-1}) identifies a sizeable enhancement to the total in-plane magnetisation of the bilayer upon hydrogen-gas absorption. The magnitude of the enhancement is greater than that observed at the Q_c location of the Co/Pd(10 nm) bilayer upon hydrogenation. It is therefore determined that as the thickness of the Pd layer increases so too does the relative increase in the interfacial FM magnetisation of the Co/Pd bilayer upon hydrogen-gas absorption (in a given hydrogen atmosphere). These trends most likely share a common connection to the behaviours established in Table 4.2 where it was found that Co/Pd bilayers with reduced interface-to-bulk Pd

volume ratios have enhanced hydrogen solubilities [40]. However, before the inherent relationship can be scrutinised the magnetic anisotropies of the Co/Pd bilayers before and after hydrogen absorption must first be analysed.

To determine the magnetic anisotropy contribution to the changes observed to the in-plane FM magnetisation of the Co/Pd(10 nm) bilayer upon hydrogenation, field-resolved FMR spectra were collected *in situ* during the first cyclic exposure of the bilayer to a 3.5% H_2/N_2 gas mixture. Figure 4.22 shows the field-resolved FMR spectra of the Co/Pd(10 nm) bilayer recorded at each stage during the hydrogenation cycle. The film was driven to resonance by sweeping an external field across the resonance of the microwave cavity, which was held at a frequency of $f = 9.354$ GHz. Before the admission of hydrogen gas, the bilayer exhibits a broad FMR spectrum which reaches resonance at an applied field of $H_{\text{res}} = 819$ Oe. After the absorption of hydrogen gas, the bilayer is able to generate resonance in a reduced field of $H_{\text{res}} = 707$ Oe. This specifies an increase to the effective magnetisation $4\pi M_{\text{eff}}$ ($= 4\pi(M_{\parallel} - H_{\text{PMA}})$) of the Co/Pd bilayer upon hydrogenation, which is synonymous with a decrease in the PMA of the specimen and is in-line with previous works [47, 172]. Solving Equation 4.2 for $4\pi M_{\text{eff}}$ and using the resonance fields outlined above, the $4\pi M_{\text{eff}}$ of the Co/Pd(10 nm) bilayer before and after hydrogen absorption are calculated to be 10,670 G and 12,600 G, respectively. Furthermore, in the hydrogen atmosphere it is found that the FMR amplitude increases, while the resonance linewidth narrows relative to the FMR response of the bilayer prior to hydrogen exposure. These secondary variations to the appearance of the FMR spectrum agree with previous reports [47, 171], and mutually indicate that the precessional angle of the magnetisation vector throughout the FM volume of the Co/Pd bilayer increases in the presence of hydrogen gas. This is caused by a reduction in the magnetic damping coefficient of the Co layer (and the FM component of the alloyed interface) which is intrinsically linked to the layer's ability

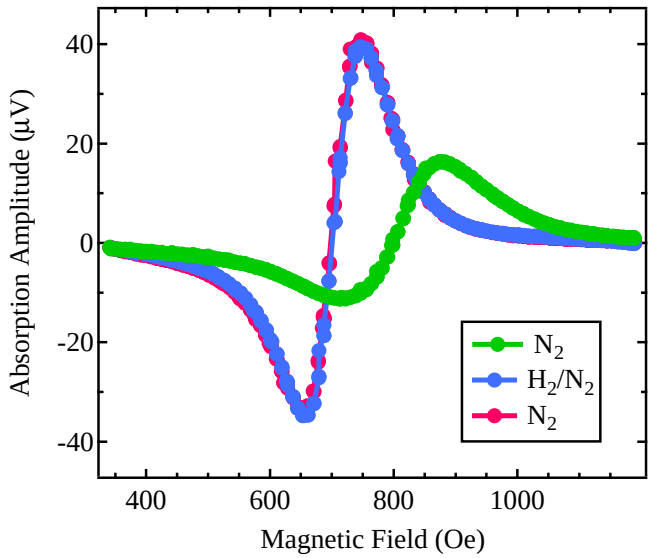

Figure 4.22: Field-resolved FMR spectra of the Co/Pd(10 nm) bilayer during primary hydrogen absorption. All data sets were measured at a microwave frequency of 9.354 GHz.

to generate an efficient spin current through the Pd layer [235]. After the desorption of hydrogen gas, the bilayer retains consistent magnetisation dynamics in relation to the hydrogenated film (within experimental error). This highlights that the PMA of the Co/Pd(10 nm) bilayer is irreversibly modified and weakened through the primary exposure to hydrogen gas, which is in-line with our PNR models, and previous works [47, 169, 171, 170].

Uniquely, by combining the knowledge obtained from the PNR with *in situ* FMR measurements, we can numerically evaluate via Equation 4.2 the magnitude of interfacial PMA in the Co/Pd(10 nm) bilayer and its modification upon hydrogen-gas absorption. From the magnetic SLD profiles of Figure 4.17, the Co/Pd(10 nm) bilayer before hydrogenation exhibits an average in-plane FM magnetisation of $4\pi M_{\parallel} =$ 14,427 G, which increases by 5% in the presence of hydrogen gas to 15,124 G. These values are calculated as a thickness-averaged magnetisation over the Co layer and the interfacial FM moments which contribute to the FMR response of the film. It follows

from Equation 4.2 that the interfacial PMA of the bilayer before hydrogen absorption decreases from $H_{\mathrm{PMA}} = 3757$ Oe to 2524 Oe after hydrogenation.

By consolidating all the above-described experimental behaviours, a unified model of the interfacial moments of the Co/Pd bilayers emerges. The proposed mechanism, which can account for the drastic change in the PMA of the bilayers upon hydrogen absorption and the dependence on the thickness of the Pd layer, is as follows. The hydrogen atoms which are initially chemisorbed on the surface of the Pd film diffuse into the layer to contribute their bound coherent scattering length and atomic volume to the Pd layer of the Co/Pd bilayer. This leads to a simultaneous decrease in the effective neutron SLD and an increase in the out-of-plane thickness of the Pd layer (as observed in Figure 4.17). The highly mobile hydrogen atoms diffuse throughout the Pd layer and eventually encounter the Co/Pd interface. The alloyed interface represents a change in the electronic and magnetic environment of the film where the density of Pd atoms continually decline (over a range of approximately 1.4 nm) and are substituted by atomic densities of Co in approach to the underlying Co layer (see Figure 4.17). The spin-orbit coupling of the interfacial Pd atoms are altered through short-range electron spill-over effects with neighbouring Co atoms [87]. Furthermore, the PM spins of the Pd atoms become ferromagnetically polarised through proximity to the alloyed Co content to provide an extra energy term to the surface anisotropy of the Co layer. At each discrete location across the interface profile, the polarised Pd spins adopt the local FM-spin direction. That is, the PM spins predominantly align perpendicular-to-plane (via surface anisotropy) at the Pd-side of the interface and contribute to the PMA of the system and then coherently rotate into the film plane (via shape anisotropy) over a finite distance in approach to the underlying Co layer. The solubility of hydrogen within the interface region decreases proportional to the local Co alloy content [160]. It has been shown that even a minor $\mathrm{Co}_x\mathrm{Pd}_{1-x}$ alloy

concentration of $x = 0.15$ reduces the maximum room-temperature solubility of Pd from $PdH_{0.6}$ (in bulk) to $PdH_{0.1}$ [285]. As a result, the hydrogen-induced structural transformation which occurs throughout alloyed interface is more subtle than in the pure Pd layer. Although extremely dilute, the C_H which is absorbed by the interface is sufficient to affect the electronic and magnetic properties of the interfacial Pd atoms. Namely, as hydrogen is absorbed by the interface the magnetic susceptibility of the Pd atoms is suppressed. This essentially 'switches off' the component of the PMA field contributed by the interfacial Pd atoms leading to a reduction in the system's PMA which is observed via FMR (see Figure 4.22). This process correlates with an increase in the density of interfacial moments which possess weak-local anisotropy fields. The weakened anisotropy of the interfacial Co moments are therefore more susceptible to external fields, and will preferentially tilt into the plane of the film along the direction of the 1 kOe sample field. The increased projection of the FM spins onto the film plane yields the enhanced spin-asymmetry signals observed for the Co/Pd bilayer in the hydrogenation state (see Figure 4.20). The effect is dependent upon the thickness of the Pd layer because thicker Pd layers can absorb greater average concentrations of hydrogen (see Table 4.2). We speculate that this behaviour allows a more efficient transfer of H atoms to the Co/Pd interface (of thicker Pd layers) to then afford a greater reduction in the magnetic susceptibility of the interfacial Pd atoms (compared to thinner Pd layers). In turn this further reduces the local anisotropy of the interfacial moments leaving them more susceptible to be influenced by the 1 kOe in-plane sample field. As a result, Co/Pd bilayers with thicker Pd layers have a greater density of interfacial moments which preferentially turn into the film plane upon hydrogenation to give larger relative increases to the spin-asymmetry signals compared to thinner Pd layers (see Figure 4.21).

4.4 Conclusion

The work presented in this chapter first outlines an innovative PNR beamline instrumentation concept which incorporates FMR. We show that by combining PNR with *in situ* FMR each term of the Kittel equation can be accounted for, such that, the in-plane magnetic moment and the magnetic anisotropy of a FM specimen can be quantitatively solved. The strength of the technique is showcased in circumstances where external stimuli (e.g., elastic strain, temperature, pressure and/or oxidising atmospheres) cause irreversible or semi-reversible modifications to the static and dynamic magnetisation behaviours of the FM specimen under study. Here, PNR with *in situ* FMR offers the capability to simultaneously probe a vast range of material properties step-wise throughout a single cycle (or during a single exposure) before irreversible changes are incurred to the initial state of the material. Accordingly, a PNR with *in situ* FMR sample chamber was custom-developed during the course of this thesis to allow thin-film characterisation to be carried out in the presence of gas atmospheres. The commissioned sample environment was implemented on the PLATYPUS beamline at ACNS, ANSTO, and a three-step methodology for acquiring PNR with *in situ* FMR data sets was developed. Feasibility measurements were conducted on a Pd-deficient CNP alloy film in the presence of a dilute hydrogen-gas atmosphere. During hydrogenation the static and dynamic magnetisation behaviours of the CNP alloy film were mapped and correlated across two independent channels (i.e., PNR and FMR). It was found that the sensitivity of FMR was able to detect minute changes to the dynamic magnetisation behaviour of the film, before significant changes to the structure and/or static magnetisation behaviour were detectable via PNR. The advantages of recording time-resolved FMR spectra on the PNR beamline were also highlighted. Such measurements provide rapid insights into the current magnetic state of the sample

under investigation, including whether it be equilibrated or transient, to ensure that the sample sitting on the beamline is in exactly the state as needed, or desired, before commencing investigations by PNR.

The PNR with *in situ* FMR measurement approach was then employed to characterise the PMA present at the chemical interface within Co/Pd bilayers and its modification upon exposure to hydrogen gas. Through repeatedly cycling the Co/Pd bilayers between pure N_2 and 3.5% H_2/N_2 atmospheres it was established that the polycrystalline films succumbed to hydrogen annealing during the first exposure to hydrogen gas. The process removed defect volumes from the Pd layer of the film leading to an observed decrease in the overall Pd layer thickness together with an increase in the Pd layer density between the primary and secondary N_2 states. Owing to the isolated nature of the annealing process, completely reversible responses — both in reflectivity and in magnetic resonance — were then established throughout all the higher-order exposures. With an inherent curiosity to investigate the irreversible modifications to the magnetic anisotropy and structural properties of the Co/Pd bilayers upon primary hydrogen-gas absorption, each film was then characterised at each stage during the first cyclic exposure to hydrogen gas. Under a constant temperature and hydrogen partial pressure it was found that Co/Pd bilayers with thicker Pd layers were able to absorb greater concentrations of hydrogen (on the layer average). This is attributed to charge-transfer between interfacial Co and Pd atoms, which increases the chemical potential of interfacial Pd lowering its ability to absorb hydrogen, and subsequently results in a reduced average concentration of absorbed hydrogen in Co/Pd bilayers with thinner Pd layers. For the specific case of a Co/Pd(10 nm) bilayer, a 7.5% increase in the overall thickness of the Pd layer upon exposure to a 3.5% H_2/N_2 partial pressure at room temperature was observed. The out-of-plane expansion of the film is approximately twice that expected for bulk Pd exposed to hydrogen under

the same conditions and can be attributed to the in-plane structural clamp provided by the substrate which effectively diverts the three-dimensional expansion (expected for bulk Pd) into a one-dimensional expansion of the Pd thin-film layer in the out-of-plane direction only. Chemical and magnetic depth-profiles of Co/Pd(10 nm) bilayer reveal that the chemistry and magnetism of the bulk of the Co layer remain invariant before and after hydrogenation, while the Co/Pd interface features an approximate two-fold increase in in-plane magnetic moment. Furthermore, the Co/Pd bilayer is able to generate resonance in a reduced field in the presence of hydrogen gas. By correlating these changes and employing the Kittel equation it is confirmed that the PMA of the Co/Pd(10 nm) bilayer decreases in the presence of hydrogen gas. This is an important result which cannot be obtained from either of the two measurement techniques alone. Nor would a consistent or valid result have been obtained if the two techniques were employed in sequence (i.e., PNR followed by FMR, and vice versa), due to the irreversible nature of the first hydrogenation cycle.

Chapter 5

Summary and Outlook

> *Scientific discovery is not yet predictable. If you have an exciting road to follow do not be put off by those who say that there is nothing at the end of it; they do not know. Persevere, and enjoy the excitement of the unknown.*
>
> — Joseph Chatt [49]

Together, the studies presented in this thesis embody the philosophies of Feynman and Kroemer and investigate the occurrence of magnetic interface phenomena in low-dimensional thin-film structures. The interface — be it magnetic and/or chemical in character — plays a vital role in mediating the pertinent physics of the structure which is confined to the nanometre length scale. By controlling interfacial properties, for example, through ion-beam disorder or exposure to gas atmospheres, the system can be tailored towards a desired functionality. However, it is often impossible to predict the immediate outcomes of fundamental scientific research, as Joseph Chatt's statement above articulates. If in fact outcomes were predicable then there would be no need

to conduct investigations in the first instance. What seems to be more unpredictable, however, is knowing just how useful the scientific outcomes will be and/or where the research will find application. In saying this, it is hoped that the results of the studies presented in this thesis will be of use, that they will stimulate further research activity and subsequently lead to the development of future technological devices. The following text summarises the main conclusions of the thesis and provides some suggestions for the future directions of each project.

The study presented in Chapter 3 investigated the sharpness of magnetic interfaces which can be formed locally by driving magnetic phase transitions in materials using ion beams. The work provided, for the first time, a lower-bound numerical estimate of the spatial definition of FM volumes which can be formed in materials exclusively from the ion-matter interaction gradient resulting from an irradiation (under the conditions we have applied). This was achieved by illuminating the surface of a film with a broad-ion beam, such that the created ion-cascade volume was free of additional lateral and/or projected straggling influences which are often compounded during masked irradiations (because the scattering profile is dependent upon the effectiveness of the etching chemicals used to prepare the lithography mask). The irradiations were performed on the prototype $FePt_3$ template to exploit the materials unique quantum chemical feature which allows either a PM or FM state to be selected at room temperature depending on the level of atomic-site disorder in the alloy. A detailed microstructural analysis of ion irradiation $FePt_3$ was presented using a complementarity of magnetometry, TEM and PNR techniques. By modelling the characteristic features of the irradiated $FePt_3$ film's PNR spectra, the magnetic interface was observed to transition from FM to PM over a length scale on the order of 2.5 – 3 nm. Monte Carlo simulations and TEM imaging identified that the structural transformation occurred over a broader length scale, causing the ion-induced structural and magnetic

phase transformations of single crystalline $FePt_3$ to be defined by two different spatial boundaries. The result is in-line with a long-reported ideal that ion-induced magnetic property changes are not related in a simple way to the structural property changes of a material, and in most cases, magnetic transitions appear sharper than the structural one [48]. The disorder-induced magnetic transition of $FePt_3$ was then investigated through theoretical modelling, and the first DFT results for the entire suite of potential long-range magnetically ordered states of $FePt_3$ were presented. In doing so, the (½ ½ 0) c-type $FePt_3$ structure was identified as the energetically favourable ground-state spin structure, in agreement with previous neutron diffraction experiments [173]. Furthermore, by analysing several localised defect structures which may form in $FePt_3$ under ion-irradiation, it was revealed that disorder is driven by the mechanism of anti-site disorder which involves an interchange of Fe and Pt atoms between their respective sites. By modelling the lowest energy state of (½ ½ 0) c-type $FePt_3$ under varying degrees of anti-site disorder, it was determined that a stable FM state could be achieved by interchanging 25% of the initially chemically ordered Fe and Pt sites. It was proposed that the subtle 'threshold' nature of the level of anti-site disorder required to catalyse the transformation from PM to FM in $FePt_3$, may be the physical origin of the abrupt magnetic interface observed experimentally by PNR.

The experimental findings reported in Chapter 3 position ion irradiation (albeit performed with a focussed-ion beam) as a particularly attractive method for fabricating magnetically-isolated, single-domain and topologically flat FM elements ideally suited to the tribology of next-generation patterned-media devices, as well as for the direct stylus-type writing of ferromagnetism for spintronic, logic-gate and racetrack memories. Now that we have successfully demonstrated the principal concept using the template material of $FePt_3$, the next step will be to develop the technique further by bringing materials into play which have favourable properties. Materials consid-

ered for memory applications will need to be developed such that they also respond to ion-induced disorder with a PM-to-FM phase transition, in addition to exhibiting a high coercivity and an out-of-plane magnetic easy axis. One example can be found in PM $A1$ FePt, which can be transformed into the highly anisotropic FM $L1_0$ FePt through ion irradiation. However, the search for materials displaying this feature is not restricted to already known bulk materials. For example, PM-to-FM phase transitions could be generated locally by tuning lattice strain with an ion beam. Furthermore, it will be interesting to establish through future investigations as to whether the abrupt magnetic phase boundary reported in this work is unique to intermetallic alloys (e.g., CoFe, FeV, FeAl, FePt, NiFe, CoZr etc.), or whether such interface quality could be achieved in a diverse range of materials (e.g., oxides, superconductors, multiferroics etc.) which could then go on to support an even greater range of applications.

The study contained in Chapter 4 introduced a PNR with *in situ* FMR method which can be employed to characterise irreversible modifications to the layer-averaged static magnetic characteristics and the macroscopic magneto-dynamic behaviours of FM films, while sample properties are gradually transformed in the presence of external stimuli. A three-step methodology for acquiring high-quality data sets was developed, a sample environment was commissioned, and feasibility studies were performed. The current design of the chamber allows thin-film characterisation to be carried out in the presence of a broad range of gas atmospheres. However, simple modifications to the chamber could allow forthcoming characterisations of irreversible magnetic behaviours of thin films to be performed in the presence of chemical, mechanical and/or other thermodynamic stimulants. For example, there are already several irreversible thin-film processes published in the literature which could benefit from combined PNR with *in situ* FMR measurements. These include: the dissolution of FM metals in aqueous environments [292], voltage-moderated oxygen migration in Co films [93],

elastic stresses applied to FM films grown on flexible substrates [101], and the epitaxial growth of Fe layers with *in situ* PNR [141].

The PNR with *in situ* FMR method was then used to characterise the simultaneous and irreversible modifications which occur to the magnetic surface anisotropy and the in-plane magnetisation of Co/Pd bilayers upon exposure to hydrogen gas. For the case of a Co/Pd(10 nm) bilayer exposed to a 3.5% H_2/N_2 atmosphere at room temperature, the sample was able to be driven to resonance in a reduced field upon hydrogenation, while the sample's in-plane magnetic moment also increased. Furthermore, neither parameter returned to its primary state upon dehydrogenation. These modifications are indicative of an irreversible reduction in the PMA of the Co/Pd bilayer, which was calculated via the Kittel equation to have decreased by more than 30% in the presence of hydrogen gas. The behaviour was attributed to the suppression of the magnetic susceptibility of interfacial Pd atoms upon hydrogenation. This resulted in a weakening of the local anisotropy fields across the interface causing the interfacial Co moments to become more susceptible to the applied (in-plane) field and increase their projection into the film plane. The occurrence of interface PMA in Co/Pd bilayers and its modification upon hydrogen-gas absorption unavoidably begs the question — if the pertinent physics takes place at the interface (where the Co and Pd atoms are alloyed) could similar results be obtained by exposing the interface directly to a hydrogen atmosphere? The latter could be answered by performing systematic investigations on alloyed CoPd films of differing Pd stoichiometries in the presence of hydrogen gas. As we found during the feasibility studies, measurable changes were observed to the FMR response of a cobalt-nickel-palladium alloy in the presence of a dilute hydrogen concentration. In addition, an almost uniform increase in magnetisation across the film volume was observed. This suggests that the magnetic anisotropy of an alloyed system behaves as a bulk PMA rather than an interface PMA, and could form the

basis of a more robust hydrogen-gas detection system. In terms of the Co/Pd bilayers, it is clear that a more thorough experimental and theoretical understanding of the interfacial moments is required. X-ray resonant magnetic reflectometry could be used to provide element-specific depth-sensitive magnetic information to supplement the magnetic information obtained by PNR and FMR. There is also potential to develop a more sophisticated numerical model than that of the Kittel equation to account for the intricate dependencies of the strength of the exchange coupling of the moments across the interface profile. To provide more clarity in this area, DFT calculations are currently being executed. However, at the time of writing, these calculations are incomplete due to the complexities in modelling anisotropy and also due to the large number of atoms involved in the simulation. Nevertheless, the early computations are yielding some promising results.

Appendix A

Units of Measurement

Throughout this thesis a combination of SI and CGS units are used depending on the suitability of a given unit in a particular situation and/or the unit commonly employed in the relevant field of science[1]. Table A.1 lists the main magnetic units of measurement used in this thesis in addition to the relevant conversion factors between SI and CGS units [96].

Quantity	Symbol	SI Unit	CGS Unit	Conversion Factor
Magnetic Induction	$\mathbf{B}$	T	G	10^4
Magnetic Field	$\mathbf{H}$	A m^{-1}	Oe	$4\pi/10^3$
Magnetic Moment	m	Am^2	emu	10^3
Magnetisation	$\mathbf{M}$	A m^{-1}	emu cm^{-3}	10^{-3}
Vacuum Permeability	μ_0	H m^{-1}	dimensionless	$10^7/4\pi$
Gyromagnetic Ratio	γ	m A^{-1} s^{-1}	Oe^{-1} s^{-1}	$10^3/4\pi$

Table A.1: List of magnetic quantities and the corresponding SI and CGS units. To obtain the values of the quantities in CGS units, the corresponding SI unit should be multiplied by the conversion factor.

[1]The Angstrom Å ($= 1 \times 10^{-10}$ m) is an internationally recognised unit of length and is commonly used in the presentation of scattering data; however, is not an SI unit.

Bibliography

[1] T. Abbasi and S. A. Abbasi. 'Renewable' hydrogen: Prospects and challenges. *Renew. Sust. Energ. Rev.*, **15**:3034–3040, (2011).

[2] S. Akamaru, T. Matsumoto, M. Hara, K. Nishimura, N. Nunomura, and M. Matsuyama. Magnetic susceptibility of the Pd-Co-H system. *J. Alloy. Compd.*, **580**:S102–S104, (2013).

[3] M. Ali, P. Adie, C. H. Marrows, D. Greig, B. J. Hickey, and R. L. Stamps. Exchange bias using a spin glass. *Nat. Mater.*, **6**:70, (2007).

[4] R. Allenspach, M. Stampanoni, and A. Bischof. Magnetic domains in thin epitaxial Co/Au(111) films. *Phys. Rev. Lett.*, **65**:3344–3347, (1990).

[5] J. U. Andersen. Notes on channeling. http://phys.au.dk/fileadmin/site_files/publikationer/Lecture_notes/JUA-Channeling20151012total-2.pdf.

[6] J. F. Ankner and G. P. Felcher. Polarized-neutron reflectometry. *J. Magn. Magn. Mater*, **200**:741–754, (1999).

[7] B. Antonini, F. Lucari, F. Menzinger, and A. Paoletti. Magnetization distribution in ferromagnetic $MnPt_3$ by a polarized-neutron investigation. *Phys. Rev.*, **187**:611–618, (1969).

[8] V. N. Antonov, B. N. Harmon, and A. N. Yaresko. Electronic structure and X-ray magnetic circular dichroism in Cu_3Au-type transition metal platinum alloys. *Phys. Rev. B*, **64**:024402, (2001).

[9] S. E. Apsel, J. W. Emmert, J. Deng, and L. A. Bloomfield. Surface-enhanced magnetism in nickel clusters. *Phys. Rev. Lett.*, **76**:1441, (1996).

[10] H. Araki, M. Nakamura, S. Harada, T. Obata, N. Mikhin, V. Syvokon, and M. Kubota. Phase diagram of hydrogen in palladium. *J. Low Temp. Phys.*, **134**:1145–1151, (2004).

[11] J. I. Avila, R. J. Matelon, R. Trabol, M. Favre, D. Lederman, U. G. Volkmann, and A. L. Cabrera. Optical properties of Pd thin films exposed to hydrogen studied by transmittance and reflectance spectroscopy. *J. Appl. Phys.*, **107**:023504, (2010).

[12] K. Baberschke. *Handbook of magnetism and advanced magnetic materials.* Investigation of ultrathin ferromagnetic films by magnetic resonance. John Wiley and Sons, (2007).

[13] G. Bacon. *X-ray and neutron diffraction.* Pergamon Press, (1966).

[14] G. E. Bacon and J. Crangle. Chemical and magnetic order in platinum-rich Pt+Fe alloys. *Proc. R. Soc. Lond. A*, **272**:387–405, (1963).

[15] S. D. Bader and S. S. P. Parkin. Spintronics. *Annu. Rev. Condens. Matter Phys.*, **1**:71–88, (2010).

[16] M. N. Baibich, J. M. Broto, A. Fert, F. Nguyen Van Dau, F. Petroff, P. Etienne, G. Creuzet, A. Friederich, and J. Chazelas. Giant magnetoresistance of (001)Fe/(001)Cr magnetic superlattices. *Phys. Rev. Lett.*, **61**:2472–475, (1988).

[17] S. Balaji and M. Kostylev. A two dimensional analytical model for the study of ferromagnetic resonance responses of single and multilayer films. *J. Appl. Phys.*, **121**:123906, (2017).

[18] M. Balat. Potential importance of hydrogen as a future solution to environmental and transportation problems. *Int. J. Hydrogen Energ.*, **33**:4013–4029, (2008).

[19] R. Bali, S. Wintz, F. Meutzner, R. Hübner, R. Boucher, A. A. Ünal, S. Valencia, A. Neudert, K. Potzger, J. Bauch, F. Kronast, S. Facsko, J. Lindner, and J. Fassbender. Printing nearly-discrete magnetic patterns using chemical disorder induced ferromagnetism. *Nano Lett.*, **14**:435–441, (2014).

[20] W. M. Bartczak and J. Stawowska. Interaction of dihydrogen with transition metal (Pd, Ni, Ag, Cu) clusters. *Struct. Chem.*, **15**:447–459, (2004).

[21] M. Belmeguenai, H. Tuzcuoglu, M. S. Gabor, T. Petrisor, C. Tiusan, F. Zighem, S. M. Chérif, and P. Moch. Co_2FeAl Heusler thin films grown on Si and MgO substrates: Annealing temperature effect. *J. Appl. Phys.*, **115**:043918, (2014).

[22] J. P. C. Bernards. Design of a detection coil system for a biaxial vibrating sample magnetometer and some applications. *Rev. Sci. Instrum.*, **64**:1918–1930, (1993).

[23] H. Bernas, J.-Ph. Attané, K.-H. Heinig, D. Halley, D. Ravelosona, A. Marty, P. Auric, C. Chappert, and Y. Samson. Ordering intermetallic alloys by ion irradiation: A way to tailor magnetic media. *Phys. Rev. Lett.*, **91**:077203, (2003).

[24] M. J. Besnus and A. J. P. Meyer. Magnetic properties of the ordered and disordered $CrPt_3$ and CrPt phases. *Phys. Status Solidi B*, **58**:533–542, (1973).

[25] H. Bethe and W. Heitler. On the stopping of fast particles and on the creation of positive electrons. *Proc. R. Soc. Lond. A*, **146**:83–112, (1934).

[26] S. G. Bhat and P. S. Anil Kumar. Defect mediated exchange bias in oriented (111) Fe_3O_4/(100) GaAs. *Thin Solid Films*, **621**:26–31, (2017).

[27] S. Bhatti, R. Sbiaa, A. Hirohata, H. Ohno, S. Fukami, and S. N. Piramanayagam. Spintronics based random access memory: A review. *Mater. Today*, **20**:530–548, (2017).

[28] I. M. Billas, A. Chatelain, and W. A. der Heer. Magnetism from the atom to the bulk in iron, cobalt and nickel clusters. *Science*, **265**:1682, (1994).

[29] G. Binasch, P. Grünberg, F. Saurenbach, and W. Zinn. Enhanced magnetoresistance in layered magnetic structures with antiferromagnetic interlayer exchange. *Phys. Rev. B*, **39**:4828–4830, (1989).

[30] M. Birkholz. *Thin film analysis by X-ray scattering*. Wiley-VCH Verlag GmbH & Co., (2005).

[31] P. Blaha, K. Schwarz, G. K. H. Madsen, D. Kvasnicka, and J. Luitz. *WIEN2k: An augmented plane wave and local orbitals program for calculating crystal properties*. Vienna University of Technology, Austria, (2001).

[32] N. Bohr. The penetration of atomic particles through matter. *Mat. Fys. Medd. Dan. Vid. Selsk.*, **18**:1–144, (1948).

[33] C. Borschel, R. Niepelt, S. Geburt, C. Gutsche, I. Regolin, W. Prost, F.-J. Tegude, D. Stichtenoth, D. Schwen, and C. Ronning. Alignment of semiconductor nanowires using ion beams. *Small*, **5**:2576–2580, (2009).

[34] W. L. Bragg. The diffraction of short electromagnetic waves by a crystal. *Proc. Camb. Philos. Soc.*, **17**:43–57, (1912).

[35] E. A. Brandes, G. B. Brook, and P. Paufler. Smithells metals reference book. Butterworth-Heinemann Ltd. *Cryst. Res. Technol.*, **28**:530–530, (1992).

[36] J. C. Bravman and R. Sinclair. The preparation of cross-section specimens for transmission electron microscopy. *J. Electron Microsc.*, **1**:53–61, (1984).

[37] W. Buttner, M. B. Post, R. Burgess, and C. Rivkin. An overview of hydrogen safety sensors and requirements. *Int. J. Hydrogen Energ.*, **36**:2462–2470, (2014).

[38] L. J. Cabri and Feather C. E. Platinum-iron alloys: A nomenclature based on a study of the natural and synthetic alloys. *Can. Mineral*, **13**:117–126, (1975).

[39] M. C. Cadeville, C. E. Dahmani, and F. Kern. Magnetism and spatial order in Ni−Pt and Co−Pt alloys. *J. Magn. Magn. Mater.*, **54-57**:1055–1056, (1986).

[40] S. J. Callori, C. Rehm, G. L. Causer, M. Kostylev, and F. Klose. Hydrogen absorption in metal thin films and heterostructures investigated *in situ* with neutron and X-ray scattering. *Metals*, **6**:125, (2016).

[41] P. F. Carcia, A. D. Meinhaldt, and A. Suna. Perpendicular magnetic anisotropy in Pd/Co thin film layered structures. *Appl. Phys. Lett.*, **47**:178–180, (1985).

[42] P. F. Carcia, S. I. Shah, and W. B. Zeper. Effect of energetic bombardment on the magnetic coercivity of sputtered Pt/Co thin-film multilayers. *Appl. Phys. Lett.*, **56**:2345–2347, (1990).

[43] G. L. Causer, D. L. Cortie, H. Zhu, M. Ionescu, G. J. Mankey, X. L. Wang, and F. Klose. Direct measurement of the intrinsic sharpness of magnetic interfaces formed by chemical disorder using a He^+ beam. *ACS Appl. Mater. Interfaces*, **10**:16216–16224, (2018).

[44] G. L. Causer, M. Kostylev, D. L. Cortie, C. Lueng, S. J. Callori, X. L. Wang, and F. Klose. Hydrogen-driven switching of the magnetic surface anisotropy at the Co/Pd interface. *In preparation*, (2018).

[45] G. L. Causer, H. Zhu, J. Davis, M. Ionescu, G. J. Mankey, X. L. Wang, and F. Klose. The microstructural evolution of chemical disorder and ferromagnetism in He^+ irradiated $FePt_3$ films. *Appl. Surf. Sci*, **459**:672–677, (2018).

[46] G. L. Causer, H. Zhu, M. Ionescu, G. J Mankey, X. L Wang, and F. Klose. Tailoring exchange bias in ferro/antiferromagnetic $FePt_3$ bilayers created by He^+ beams. *J. Phys.: Condens. Matter*, **30**:315804, (2018).

[47] C. S. Chang, M. Kostylev, and E. Ivanov. Metallic spintronic thin film as a hydrogen sensor. *Appl. Phys. Lett.*, **102**:142405, (2013).

[48] C. Chappert, H. Bernas, J. Ferré, V. Kottler, J.-P. Jamet, Y. Chen, E. Cambril, T. Devolder, F. Rousseaux, V. Mathet, and H. Launois. Planar patterned magnetic media obtained by ion irradiation. *Science*, **280**:1919–1922, (1998).

[49] J. Chatt. A half century of platinum metal chemistry. Reminiscences of progress from academic backwater to industrial importance. *Platin. Met. Rev.*, **29**:126–130, (1985).

[50] H. Chen, N. E. Brener, and J. Callaway. Electronic structure, optical and magnetic properties of fcc palladium. *Phys. Rev. B*, **40**:1443–1449, (1989).

[51] A. Chtchelkanova, S.Wolf, and Y. Idzerda. *Magnetic Interactions and Spin Transport*. Kluwer Academic/Plenum Publishers, (2003).

[52] O. Chubykalo-Fesenko, U. Nowak, R. W. Chantrell, and D. Garanin. Dynamic approach for micromagnetics close to the Curie temperature. *Phys. Rev. B*, **74**:094436, (2006).

[53] R. L. Compton, M. J. Pechan, S. Maat, and E. E. Fullerton. Probing the magnetic transitions in exchange-biased $FePt_3$/Fe bilayers. *Phys. Rev. B*, **66**:054411, (2002).

[54] D. L. Cortie, Y. Khaydukov, T. Keller, D. J. Sprouster, J. S. Hughes, J. P. Sullivan, X. L. Wang, A. P. Le Brun, J. Bertinshaw, S. J. Callori, R. Aughterson, M. James, P. J. Evans, G. Triani, and F. Klose. Enhanced magnetization of cobalt defect clusters embedded in $TiO_{2-\delta}$ films. *ACS Appl. Mater. Interfaces*, **9**:8783–8795, (2017).

[55] S. Couet, J. Demeter, E. Menéndez, R. Rüffer, C. J. Kinane, B. Laenens, A. Teichert, S. Tripathi, F. Almeida, A. Vantomme, and K. Temst. The magnetic structure of exchange coupled FePt/$FePt_3$ thin films. *J. Appl. Phys.*, **113**:013909, (2013).

[56] F. Cousin and A. Menelle. Neutron reflectivity. *EPJ Web Conf.*, **104**:01005, (2015).

[57] J. Crangle. Some magnetic properties of platinum-rich Pt−Fe alloys. *J. Phys. Radium*, **20**:435–437, (1959).

[58] D. Creagh. Tables of X-ray absorption corrections and dispersion corrections: The new versus the old. *Nucl. Instrum. Methods Phys. Res. A*, **295**:417–434, (1990).

[59] C. D. Cress, S. W. Schmucker, A. L. Friedman, P. Dev, J. C. Culbertson, J. W. Lyding, and J. T. Robinson. Nitrogen-doped graphene and twisted bilayer graphene via hyperthermal ion implantation with depth control. *ACS Nano*, **10**:3714–3722, (2016).

[60] D. T. Cromer and J. B. Mann. X-ray scattering factors computed from numerical Hartree-Fock wave functions. *Acta Cryst.*, **24**:321–324, (1968).

[61] Crystalmaker^{TM} Software Ltd. Oxford, England, (2017). Software available at www.crystalmaker.com.

[62] R. Cubitt, G. Fragneto, R. E. Ghosh, and A. R. Rennie. REFILL2002. Advances in the study of interfaces with neutron reflection. *Langmuir*, **19**:7685–7687, (2003).

[63] B. D. Cullity. *Elements of X-ray diffraction.* Addison-Wesley Publishing Company, (1956).

[64] S. Cybart, E. Cho, T. Wong, B. Wehlin, M. Ma, C. Huynh, and R. Dynes. Nano Josephson superconducting tunnel junctions in $YBa_2Cu_3O_{7-\delta}$ directly patterned with a focused helium ion beam. *Nat. Nanotechnol.*, **10**:598–602, (2015).

[65] O. Dankert and A. Pundt. Hydrogen-induced percolation in discontinuous films. *Appl. Phys. Lett.*, **81**:1618–1620, (2002).

[66] T. Devolder, C. Chappert, Y. Chen, E. Cambril, H. Bernas, J. P. Jamet, and J. Ferré. Sub-50 nm planar magnetic nanostructures fabricated by ion irradiation. *Appl. Phys. Lett.*, **74**:3383–3385, (1999).

[67] T. Devolder, J. Ferré, C. Chappert, H. Bernas, J.-P. Jamet, and V. Mathet. Magnetic properties of He^+-irradiated Pt/Co/Pt ultrathin films. *Phys. Rev. B*, **64**:064415, (2001).

[68] S. Dietrich and A. Haase. Scattering of X-rays and neutrons at interfaces. *Phys. Rep.*, **260**:1–138, (1995).

[69] R. Dus, R. Nowakowski, and E. Nowicka. Chemical and structural components of work function changes in the process of palladium hydride formation with thin Pd film. *J. Alloys Compd.*, **404**:284–287, (2005).

[70] Editorial. The interface is still the device. *Nat. Mater.*, **11**:91, (2012).

[71] H. Enge. *Introduction to nuclear physics*. Addison Wesley, (1966).

[72] B. N. Engel, C. D. England, R. A. Van Leeuwen, M. H. Wiedmann, and C. M. Falco. Interface magnetic anisotropy in epitaxial superlattices. *Phys. Rev. Lett.*, **67**:1910–1913, (1991).

[73] J. Fassbender and J. McCord. Magnetic patterning by means of ion irradiation and implantation. *J. Magn. Magn. Mater.*, **320**:579–596, (2008).

[74] J. Fassbender, D. Ravelosona, and Y. Samson. Tailoring magnetism by light-ion irradiation. *J. Phys. D: Appl. Phys.*, **37**:R179, (2004).

[75] C. Favieres, C. Aroca, M. C. Sánchez, and V. Madurga. Continuous change of surface magnetization direction from perpendicular to planar in soft magnetic CoP multilayers. *J. Appl. Phys.*, **91**:9995–10002, (2002).

[76] H. Fayaz, R. Saidur, N. Razali, F. S. Anuar, A. R. Saleman, and M. R. Islam. An overview of hydrogen as a vehicle fuel. *Renew. Sust. Energ. Rev.*, **16**:5511–5528, (2012).

[77] J. Ferré, T. Devolder, H. Bernas, J. P. Jamet, V. Repain, M. Bauer, N. Vernier, and C. Chappert. Magnetic phase diagrams of He ion-irradiated Pt/Co/Pt ultrathin films. *J. Phys. D: Appl. Phys.*, **36**:3103, (2003).

[78] P. Ferrin, S. Kandoi, A. U. Nilekar, and M. Mavrikakis. Hydrogen adsorption,

absorption and diffusion on and in transition metal surfaces: A DFT study. *Surf. Sci.*, **606**:679–689, (2012).

[79] R. P. Feynman. There's plenty of room at the bottom. An invitation to enter a new field of physics. *Caltech J. Engineer. Sci.*, **23**:22–36, (1959).

[80] M. Fitzsimmons and C. F. Majkrak. *Application of polarized neutron reflectometry to studies of artificially structured magnetic materials.* Modern techniques for characterising magnetic materials. Springer, (2005).

[81] S. Foner. Versatile and sensitive vibrating-sample magnetometer. *Rev. Sci. Instrum.*, **30**:548–557, (1959).

[82] NIST Center for Neutron Research. Neutron scattering length and cross section. https://www.ncnr.nist.gov/resources/n-lengths/list.html.

[83] G. A. Frazier and R. Glosser. Characterizations of thin films of the palladium-hydrogen system. *J. Less Common Met.*, **74**:89–96, (1980).

[84] S. Friedensen, J. T. Mlack, and M. Drndić. Materials analysis and focused ion beam nanofabrication of topological insulator Bi_2Se_3. *Sci. Rep.*, **7**:13466, (2017).

[85] H. Fritzsche. *Neutron Reflectometry.* Characterization of Materials. John Wiley and Sons, Inc., (2012).

[86] H. Fritzsche, W. P. Kalisvaart, B. Zahiri, R. Flacau, and D. Mitlin. The catalytic effect of Fe and Cr on hydrogen and deuterium absorption in Mg thin films. *Int. J. Hydrogen Energ.*, **37**:3540–3547, (2012).

[87] H. Fritzsche, F. Klose, C. Rehm, Z. Tun, M. Wolff, and B. Hjörvarsson. *Neutron Reflectometry.* Neutron Scattering and Other Nuclear Techniques for Hydrogen

in Materials. Neutron Scattering Applications and Techniques. Springer International Publishing, (2016).

[88] H. Fritzsche, M. Saoudi, J. Haagsma, C. Ophus, E. Luber, C. T. Harrower, and D. Mitlin. Neutron reflectometry study of hydrogen desorption in destabilized MgAl alloy thin films. *Appl. Phys. Lett.*, **92**:121917, (2008).

[89] Y. Fukai. *The hydrogen-metal system: Basic bulk properties.* Springer-Verlag, 2nd edition, (2005).

[90] B. Fultz and J. M. Howe. *Transmission Electron Microscopy and Diffractometry of Materials.* Springer, 4th edition, (2012).

[91] A. Furrer, J. Mescot, and T. Strässle. *Neutron scattering in condensed matter physics.* Series on neutron techniques and applications. World Scientific, (2009).

[92] L. A. Giannuzzi. *Ion-solid interactions.* Introduction to Focused Ion Beams: Instrumentation, Theory, Techniques and Practice. Springer, (1990).

[93] D. A. Gilbert, A. J. Grutter, E. Arenholz, K. Liu, B. J. Kirby, J. A. Borchers, and B. B. Maranville. Structural and magnetic depth profile of magneto-ionic heterostructures beyond the interface limit. *Nat. Commun.*, **7**:12264, (2016).

[94] A. Giri, S. H. Wee, S. Jain, O. Hellwig, and P. E. Hopkins. Influence of chemical ordering on the thermal conductivity and electronic relaxation in FePt thin films in heat assisted magnetic recording applications. *Sci. Rep.*, **6**:32077, (2016).

[95] U. Gradmann. Magnetic surface anisotropies. *J. Magn. Magn. Mater*, **54**:733, (1986).

[96] F. Grandjean and G. J. Long. *Fundamental Concepts and Units in Magnetism.* Supermagnets, Hard Magnetic Materials. Springer, (1991).

[97] F. Greco, L. Ventrelli, P. Dario, B. Mazzolai, and V. Mattoli. Micro-wrinkled palladium surface for hydrogen sensing and switched detection of lower flammability limit. *Int. J. Hydrogen Energ.*, **37**:17529–17539, (2012).

[98] J. H. E. Griffiths. Anomolous high-frequency resistance of ferromagnetic metals. *Nature*, **158**:670, (1946).

[99] P. Grünberg. Layered magnetic structures in research and application. *Acta Mater.*, **48**:239–251, (2000).

[100] G. Gubbiotti, P. Malagò, S. Fin, S. Tacchi, L. Giovannini, D. Bisero, M. Madami, G. Carlotti, J. Ding, A. O. Adeyeye, and R. Zivieri. Magnetic normal modes of bicomponent permalloy/cobalt structures in the parallel and antiparallel ground state. *Phys. Rev. B*, **90**:024419, (2014).

[101] M. Gueye, F. Zighem, M. Belmeguenai, M. Gabor, C. Tiusan, and D. Faurie. Ferromagnetic resonance in thin films submitted to multiaxial stress state: Application of the uniaxial equivalent stress concept and experimental validation. *J. Phys. D: Appl. Phys.*, **49**:265001, (2016).

[102] R. Gupta, A. A. Sagade, and G. U. Kulkarni. A low cost optical hydrogen sensing device using nanocrystalline Pd grating. *Int. J. Hydrogen Energ.*, **37**:9443–9449, (2012).

[103] A. G. Gurevich and G. A. Melkov. *Magnetisation oscillation and waves*. C.R.C. Press, (1996).

[104] F. D. M. Haldane. Model for a Quantum Hall effect without Landau levels: Condensed-matter realization of the "parity anomaly". *Phys. Rev. Lett.*, **61**:2015–2018, (1988).

[105] M. Hamm, V. Burlaka, S. Wagner, and A. Pundt. Achieving reversibility of ultra-high mechanical stress by hydrogen loading of thin films. *Appl. Phys. Lett.*, **106**:243108, (2015).

[106] C. Hammond. *The basics of crystallography and diffraction*. Oxford University Press, (2001).

[107] T. P. A. Hase, M. S. Brewer, U. B. Arnalds, M. Ahlberg, V. Kapaklis, M. Björck, L. Bouchenoire, P. Thompson, D. Haskel, Y. Choi, J. Lang, C. Sánchez-Hanke, and B. Hjörvarsson. Proximity effects on dimensionality and magnetic ordering in Pd/Fe/Pd trialyers. *Phys. Rev. B*, **90**:104403, (2014).

[108] A. Heidarian, R. Bali, J. Grenzer, R. A. Wilhelm, R. Heller, O. Yildirim, J. Lindner, and K. Potzger. Tuning the antiferromagnetic to ferromagnetic phase transition in FeRh thin films by means of low-energy/low-fluence ion irradiation. *Nucl. Instrum. Methods Phys. Res. B*, **358**:251–254, (2015).

[109] B. Heinrich. *Ultrathin magnetic structures*. Springer, (1994).

[110] B. Heinrich and J. A. C. Bland. *Ultrathin magnetic structures: Measurement techniques and novel magnetic properties*. Springer, (1994).

[111] O. Hellwig, D. Weller, A. J. Kellock, J. E. E. Baglin, and E. E. Fullerton. Magnetic patterning of chemically-ordered $CrPt_3$ films. *Appl. Phys. Lett.*, **79**:1151–1153, (2001).

[112] R. M. Hengstler-Eger, P. Baldo, L. Beck, J. Dorner, K. Ertl, P. B. Hoffmann, C. Hugenschmidt, M. A. Kirk, W. Petry, P. Pikart, and A. Rempel. Heavy ion irradiation induced dislocation loops in AREVA's M5 alloy. *J. Nucl. Mater.*, **423**:170–182, (2012).

[113] T. Herrmannsdörfer, S. Rehmann, W. Wendler, and F. Pobell. Magnetic properties of highly diluted $PdFe_x$ and $PtFe_x$-alloys. Part I. Magnetization at kelvin temperatures. *J. Low Tem. Phys.*, **104**:49–65, (1996).

[114] B. Hjörvarsson, J. Rydén, E. Karlsson, J. Birch, and J.-E. Sundgren. Interface effects of hydrogen uptake in Mo/V single-crystal superlattices. *Phys. Rev. B*, **43**:6440–6445, (1991).

[115] J. Honolka, T. Y. Lee, K. Kuhnke, A. Enders, R. Skomski, S. Bornemann, S. Mankovsky, J. Minár, J. Staunton, H. Ebert, M. Hessler, K. Fauth, G. Schütz, A. Buchsbaum, M. Schmid, P. Varga, and K. Kern. Magnetism of FePt surface alloys. *Phys. Rev. Lett.*, **102**:067207, (2009).

[116] J. H. Hubbell and S. M. Seltzer. NIST Center for Neutron Research. X-ray mass attenuation coefficients, https://www.nist.gov/pml/x-ray-mass-attenuation-coefficients.

[117] T. Hübert, L. Boon-Brett, G. Black, and U. Banach. Hydrogen sensors - A review. *Sens. Actuators B Chem.*, **157**:329–352, (2011).

[118] T. Hübert, L. Boon-Brett, V. Palmisano, and M. A. Bader. Developments in gas sensor technology for hydrogen safety. *Int. J. Hydrogen Energ.*, **39**:20474–20483, (2014).

[119] R. C. Hughes and W. K. Schubert. Thin films of Pd/Ni alloys for detection of high hydrogen concentrations. *J. Appl. Phys.*, **71**:542–544, (1992).

[120] S. Ikeda, K. Miura, H. Yamamoto, K. Mizumuma, H. D. Gan, M. Endo, S. Kanai, J. Hayakawa, F. Matsukura, and H. Ohno. A perpendicular-anisotropy CoFeB-MgO magnetic tunnel junction. *Nat. Mater.*, **9**:721–724, (2010).

[121] Y. Imai, Y. Kimura, and M. Niwano. Organic hydrogen gas sensor with palladium-coated β-phase poly(vinylidene fluoride) thin films. *Appl. Phys. Lett.*, **101**:181907, (2012).

[122] M. James, A. Nelson, S. A. Holt, T. Saerbeck, W. A. Hamilton, and F. Klose. The multipurpose time-of-flight neutron reflectometer "Platypus" at Australia's OPAL reactor. *Nucl. Instrum. Methods Phys. Res. A*, **632**:112–123, (2011).

[123] M. Jamet, W. Wernsdorfer, C. Thirion, D. Mailly, V. Dupuis, P. Mélinon, and A. Pérez. Magnetic anisotropy of a single cobalt nanocluster. *Phys. Rev. Lett.*, **86**:4676–4679, (2001).

[124] H. C. Jamieson, G. C. Weatherly, and F. D. Manchester. The $\beta \rightarrow \alpha$ phase transformation in palladium-hydrogen alloys. *J. Less Common Met.*, 50:85–102, (1976).

[125] L. L. Jewell and B. H. Davis. Review of absorption and adsorption in the hydrogen-palladium system. *Appl. Catal. A*, **310**:1–15, (2006).

[126] M. T. Johnson, P. J. H. Bloemen, F. J. A. den Broeder, and J. J. de Vries. Magnetic anisotropy in magnetic multilayers. *Rep. Prog. Phys.*, **59**:1409, (1996).

[127] K. Kalli, A. Othonos, and C. Christofides. Characterization of reflectivity inversion, α- and β-phase transitions and nanostructure formation in hydrogen activated thin Pd films on silicon based substrates. *J. Appl. Phys.*, **91**:3829–3840, (2002).

[128] T. Kato, S. Iwata, Y. Yamauchi, and S. Tsunashima. Modification of magnetic properties and structure of Kr^+ ion-irradiated $CrPt_3$ films for planar bit patterned media. *J. Appl. Phys.*, **106**:053908, (2009).

[129] R. I. Khaibullin, L. R. Tagirov, B. Z. Rameev, S. Z. Ibragimov, F. Yildiz, and B. Aktaş. High Curie-temperature ferromagnetism in cobalt-implanted single-crystalline rutile. *J. Phys. Condens. Matter*, **16**:L443, (2004).

[130] M. Khalid, A. Setzer, M. Ziese, P. Esquinazi, D. Spemann, A. Pöppl, and E. Goering. Ubiquity of ferromagnetic signals in common diamagnetic oxide crystals. *Phys. Rev. B*, **81**:214414, (2010).

[131] E. Kita, K. Ono, N. Yamaguchi, T. Nishihashi, M. Iura, J. Morishita, Y. Utsumi, K. Mibu, T. Niizeki, K. Z. Suzuki, and H. Yanagihara. Control of magnetization in spinel-type Fe_3O_4 thin films by N_2 ion implantation. *JPN J. Appl. Phys.*, **53**:020306, (2014).

[132] C. Kittel. Interpretation of the anomalous larmor frequencies in ferromagnetic resonance experiment. *Phys. Rev.*, **71**:270, (1947).

[133] C. Kittel. Ferromagnetic resonance. *J. Phys. Radium*, **12**:291, (1951).

[134] C. Kittel. *Introduction to Solid State Physics*. Wiley, (2004).

[135] M. Kiwi. Exchange bias theory. *J. Magn. Magn. Mater.*, **234**:584–595, (2001).

[136] F. Klose, C. Rehm, M. Fieber-Erdmann, E. Holub-Krappe, H. J. Bleif, H. Sowers, R. Goyette, L. Tröger, and H. Maletta. Hydrogen absorption in epitaxial W/Nb(001) and polycrystalline Fe/Nb(110) multilayers studied in situ by X-ray/neutron scattering techniques and X-ray absorption spectroscopy. *Physica B*, **283**:184–188, (2000).

[137] S. Kolesnik, B. Dabrowski, and J. Mais. Structural and magnetic properties of transition metal substituted ZnO. *J. Appl. Phys.*, **95**:2582–2586, (2004).

[138] M. Kostylev. Strong asymmetry of microwave absorption by bilayer conducting ferromagnetic films in the microstrip-line based broadband ferromagnetic resonance. *J. Appl. Phys.*, **106**:043903, (2009).

[139] M. Kostylev. Transmission of microwaves through exchange-coupled bi-layer magnetic films in ferromagnetic and standing spin wave resonances. *J. Appl. Phys.*, **112**:093901, (2012).

[140] M. Kostylev, G. L. Causer, C.-H. Lambert, T. Schefer, C. Weiss, S. J. Callori, S. Salahuddin, X. L. Wang, and F. Klose. *In situ* ferromagnetic resonance capability on a polarized neutron reflectometry beamline. *J. Appl. Cryst.*, **51**:9–16, (2018).

[141] W. Kreuzpaintner, B. Wiedemann, J. Stahn, J.-F. Moulin, S. Mayr, T. Mairoser, A. Schmehl, A. Herrnberger, P. Korelis, M. Haese, J. Ye, M. Pomm, P. Böni, and J. Mannhart. *In situ* polarized neutron reflectometry: Epitaxial thin-film growth of Fe on Cu(001) by dc magnetron sputtering. *Phys. Rev. Applied*, **7**:054004, (2017).

[142] H. Kroemer. *Nobel Lectures in Physics 1996-2000.* World Scientific Publishing Co. Ptc. Ltd., (2000).

[143] W. Kuch, L. I. Chelaru, F. Offi, J. Wang, M. Kostsugi, and J. Kirschner. Tuning the magnetic coupling across ultrathin antiferromagnetic films by controlling atomic-scale roughness. *Nat. Mater.*, **5**:128–133, (2006).

[144] S. Kundu, N. Gaur, S. N. Piramanayagam, S. L. Maurer, H. Yang, and C. S. Bhatia. Ion implantation challenges for patterned media at areal densities over 5 Tbpsi. *IEEE Trans. Magn.*, 50:41–46, 2014.

[145] E. Lage, C. Kirchhof, V. Hrkac, L. Kienle, R. Jahns, R. Knöchel, E. Quandt, and D. Meyners. Exchange biasing of magnetoelectronic composites. *Nat. Mater.*, **11**:523–529, (2012).

[146] C.-H. Lai, C.-H. Yang, and C. C. Chiang. Ion-irradiation-induced direct ordering of $L1_0$ FePt phase. *Appl. Phys. Lett.*, **83**:4550–4552, (2003).

[147] X. Y. Lang, W. T. Zheng, and Q. Jiang. Size and interface effects on ferromagnetic and antiferromagnetic transition temperatures. *Phys. Rev. B*, **73**:224444, (2006).

[148] D. Lederman, Y. Wang, E. H. Morales, R. J. Matelon, G. B. Cabrera, U. G. Volkmann, and A. L. Cabrera. Magnetooptic properties of Fe/Pd and Co/Pd bilayers under hydrogen absorption. *Appl. Phys. Lett.*, **85**:615–617, (2004).

[149] E. Lee, J. Lee, J.-S. Noh, W. Kim, T. Lee, S. Maeng, and W. Lee. Pd-Ni hydrogen sponge for highly sensitive nanogap-based hydrogen sensors. *Int. J. Hydrogen Energ.*, **37**:14702–14706, (2012).

[150] E. Lee, J. M. Lee, J. H. Koo, W. Lee, and T. Lee. Hysteresis behavior of electrical resistance in Pd thin films during the process of absorption and desorption of hydrogen gas. *Int. J. Hydrogen Energ.*, **35**:6984–6991, (2010).

[151] E. Lee, J. M. Lee, E. Lee, J. S. Noh, J. H. Joe, B. Jung, and W. Lee. Hydrogen gas sensing performance of Pd-Ni alloy thin films. *Thin Solid Films*, **519**:880–884, (2010).

[152] H.-R. Lee, K. Lee, J. Cho, Y.-H. Choi, C.-Y. You, M.-H. Jung, F. Bonell, Y. Shiota, S. Miwa, and Y. Suzuki. Spin-orbit torque in a bulk perpendicular magnetic anisotropy Pd/FePd/MgO system. *Sci. Rep.*, **4**:6548, (2014).

[153] M. W. Lee and R. Glosser. Pressure concentration isotherms of thin films of the palladium-hydrogen system as modified by film thickness, hydrogen cycling and stress. *J. Appl. Phys.*, **57**:5236–5239, (1985).

[154] W.-K. Lee, K. E. Whitener, J. T. Robinson, and P. E. Sheehan. Patterning magnetic regions in hydrogenated graphene via e-beam irradiation. *Adv. Mater.*, **27**:1774–1778, (2015).

[155] F. A. Lewis. The hydride of palladium and palladium alloys: A review of recent researches. *Platin. Met. Rev.*, **4**:132–137, (1960).

[156] F. A. Lewis. *The palladium hydrogen system.* Academic Press, (1967).

[157] W.-C. Lin, C.-S. Chi, T.-Y. Ho, and C.-J. Tsai. Hydrogen absorption induced reversible effect on magneto-optical property of Pd/Fe, Pd/Co and Pd/Ni bilayers. *Thin Solid Films*, **531**:487–490, (2013).

[158] W.-C. Lin, C.-S. Chi, T.-Y. Ho, C.-J. Tsai, F.-Y. Lo, H.-C. Chuang, and M.-Y. Chern. Hydrogenation-induced change of magneto optical Kerr effect in Pd/Fe bilayers. *J. Appl. Phy.*, **112**:063914, (2012).

[159] W.-C. Lin, C.-J. Tsai, B.-Y. Wang, C.-H. Kao, and W.-F. Pong. Hydrogenation induced reversible modulation of perpendicular magnetic coercivity in Pd/Co/Pd films. *Appl. Phys. Lett.*, **102**:252404, (2013).

[160] W.-C. Lin, B.-Y. Wang, H.-Y. Huang, C.-J. Tsai, and V. R. Mudinepalli. Hydrogen absorption-induced reversible change in magnetic properties of Co–Pd alloy films. *J. Alloys Compd.*, **661**:20–26, (2016).

[161] J. Lindhard, M. Scharff, and H. E. Schiott. Range concepts and heavy ion ranges. *Mat. Fys. Medd. Dan. Vid. Selsk.*, **33**:1–42, (1963).

[162] D. Litvinov, V. Parekh, C. E, D. Smith, J. O. Rantschler, P. Ruchhoeft, D. Weller, and S. Khizroev. Recording physics, design considerations, and fabrication of nanoscale bit-patterned media. *IEEE Trans. Nanotechnol.*, **7**:463–476, (2008).

[163] N. Liu, M. L. Ting, M. Hentschel, Giessen H, and A. P. Alivisatos. Nanoantenna-enhanced gas sensing in a single tailored nanofocus. *Nat. Mater.*, **10**:631–636, (2011).

[164] D. Lott, F. Klose, H. Ambaye, G. J. Mankey, P. Mani, M. Wolff, A. Schreyer, H. M. Christen, and B. C. Sales. Chemical-order-induced magnetic exchange bias in epitaxial $FePt_3$ films. *Phys. Rev. B*, **77**:132404, (2008).

[165] S. W. Lovesey. *The Theory of Neutron Scattering from Condensed Matter*. Volume I. International Series of Monographs on Physics. Oxford University Press, 4th edition, (1986).

[166] C. Lu, K. Jin, L. K. Béland, F. Zhang, T. Yang, L. Qiao, Y. Zhang, H. Bei, H. M. Christen, R. E. Stoller, and L. Wang. Direct observation of defect range and evolution in ion-irradiated single crystalline Ni and Ni binary alloys. *Sci. Rep.*, **6**:19994, (2016).

[167] Z. Lu, M. J. Walock, P. R. LeClair, G. J. Mankey, P. Mani, D. Lott, F. Klose, H. Ambaye, V. Lauter, M. Wolff, A. Schreyer, H. Christen, and B. C. Sales. Structural and magnetic properties of epitaxial $Fe_{25}Pt_{75}$. *J. Vac. Sci. Technol. A*, **27**:770–775, (2009).

[168] C. Lueng. *Hydrogen gas sensing with magnetic nanomaterials*. PhD thesis, University of Western Australia, (2017).

[169] C. Lueng, P. Lupo, P. J. Metaxas, M. Kostylev, and A. O. Adeyeye. Nanopatterning-enhanced sensitivity and response time of dynamic palladium/cobalt/palladium hydrogen gas sensors. *Adv. Mater. Technol.*, **1**:1600097, (2016).

[170] C. Lueng, P. Metaxas, and M. Kostylev. Pd/Co bi-layer films for microwave-frequency hydrogen gas sensing applications. *IEEE COMMAD Conf. Proc.*, 27-29, (2014).

[171] C. Lueng, P. J. Metaxas, M. Sushruth, and M. Kostylev. Adjustable sensitivity for hydrogen gas sensing using perpendicular-to-plane ferromagnetic resonance in Pd/Co bi-layer films. *Int. J. Hydrogen Energ.*, **42**:3407–3414, (2017).

[172] C. Lueng, F. Zighem, D. Faurie, and M. Kostylev. Ferromagnetic resonance investigation of physical origins of modification of the perpendicular magnetic anisotropy in Pd/Co layered films in the presence of hydrogen gas. *J. Appl. Phys.*, 122 :163901, (2017).

[173] S. Maat, O. Hellwig, G. Zeltzer, E. E. Fullerton, G. J. Mankey, M. L. Crow, and J. L. Robertson. Antiferromagnetic structure of $FePt_3$ films studied by neutron scattering. *Phys. Rev. B*, **63**:134426, (2001).

[174] S. Maat, A. J. Kellock, D. Weller, J. E. E. Baglin, and E. E. Fullerton. Ferromagnetism of $FePt_3$ films induced by ion-beam irradiation. *J. Magn. Magn. Mater.*, **265**:1–6, (2003).

[175] Magnet-Physik. Magnetic field strength meter gauss-/teslameter FH 54, https://www.magnet-physik.de/upload/18658302-10.pdf.

[176] C. F. Majkrak, K. V. O'Donovan, and N. F. Berk. NIST Center for Neutron Research. polarized neutron reflectometry, (2004), https://www.ncnr.nist.gov/staff/hammouda/distance_learning/pnrchapti.pdf.

[177] C. F. Majkrzak. Polarized neutron reflectometry. *Physica B*, **173**:75–88, (1991).

[178] C. F. Majkrzak. Neutron scattering studies of magnetic thin films and multilayers. *Physica B*, **221**:342–356, (1996).

[179] I. Maksymov and M. Kostylev. Broadband stripline ferromagnetic resonance spectroscopy of ferromagnetic films, multilayers and nanostructures. *Phys. E*, **69**:253–293, (2015).

[180] M. Malloy and L. C. Litt. Technology review and assessment of nanoimprint lithography for semiconductor and patterned media manufacturing. *J. Micro-Nanolith. Mem.*, **10**:032001, (2011).

[181] F. D. Manchester, A. San-Martin, and J. M. Pitre. The H-Pd (hydrogen-palladium) system. *J. Phase Equilib.*, **15**:62–83, (1994).

[182] B. Marchon, T. Pitchford, Y.-T. Hsia, and S. Gangopadhyay. The head-disk interface roadmap to an areal density of 4 Tb/in^2. *Adv. Tribology*, **2013**:8, (2013).

[183] C. H. Marrows, L. C. Chapon, and S. Langridge. Spintronics and functional materials. *Mater. Today*, **12**:70–77, (2009).

[184] E. Martin, S. A. Shaheen, T. E. Lipman, and J. R. Lidicker. Behavioral response to hydrogen fuel cell vehicles and refueling: Results of California drive clinics. *Int. J. Hydrogen Energ.*, **34**:8670–8680, (2009).

[185] A. Marynowska, P. Misiuna, S. Lewińska, E. Dynowska, A. Wawro, A. Ślawska-Waniewska, R. Böttger, J. Fassbender, and L. T. Baczewski. Modification of structural and magnetic properties in Fe/Pt (111)-oriented multilayers with ion beam irradiation. *Nucl. Instrum. Methods Phys. Res. B*, **415**:136–141, (2018).

[186] M. Matczak, B. Szymański, P. Kuświk, M. Urbaniak, F. Stobiecki, Z. Kurant, A. Maziewski, D. Lengemann, and A. Ehresmann. Tailoring magnetic anisotropy gradients by ion bombardment for domain wall positioning in magnetic multilayers with perpendicular anisotropy. *Nanoscale Res. Lett.*, **9**:395, (2014).

[187] W. H. Meiklejohn and C. P. Bean. New magnetic anisotropy. *Phys. Rev.*, **102**:1413–1414, (1956).

[188] A. Melville, T. Mairoser, A. Schmehl, T. Birol, T. Heeg, B. Hollander, J. Schubert, C. J. Fennie, and D. G. Schlom. Effect of film thickness and biaxial strain on the Curie temperature of EuO. *Appl. Phys. Lett.*, **102**:062404, (2013).

[189] E. Menéndez, J. Demeter, J. Van Eyken, P. Nawrocki, E. Jedryka, M. Wójcik, J. F. Lopez-Barbera, J. Nogués, A. Vantomme, and K. Temst. Improving the magnetic properties of Co−CoO systems by designed oxygen implantation profiles. *ACS Appl. Mater. Interfaces*, **5**:4320–4327, (2013).

[190] E. Menéndez, M. O. Liedke, J. Fassbender, T. Gemming, A. Weber, L. J. Heyderman, K. V. Rao, S. C. Deevi, S. Suriñach, M. D. Baró, J. Sort, and J. Nogués. Direct magnetic patterning due to the generation of ferromagnetism by selective ion irradiation of paramagnetic FeAl alloys. *Small*, **5**:229–234, (2009).

[191] E. Menéndez, H. Modarresi, C. Petermann, J. Nogués, N. Domingo, H. Liu, B. J. Kirby, A. S. Mohd, Z. Salhi, E. Babcock, S. Mattauch, C. Van Haesendonck, A. Vantomme, and K. Temst. Lateral magnetically modulated multilayers by combining ion implantation and lithography. *Small*, **13**:1603465, (2017).

[192] F. Menzinger and A. Paoletti. Magnetic moments and unpaired-electron densities in $CoPt_3$. *Phys. Rev.*, **143**:365–372, (1966).

[193] P. J. Metaxas, J. P. Jamet, A. Mougin, M. Cormier, J. Ferré, V. Baltz, B. Rodmacq, B. Dieny, and R. L. Stamps. Creep and flow regimes of magnetic domain-wall motion in ultrathin Pt/Co/Pt films with perpendicular anisotropy. *Phys. Rev. Lett.*, **99**:217208, (2007).

[194] P. F. Miceli, H. Zabel, J. A. Dura, and C. P. Flynn. Anomalous lattice expansion of metal-hydrogen thin films. *J. Mater. Res.*, **6**:964–968, (1991).

[195] R. Morales, A. C. Basaran, J. E. Villegas, D. Navas, N. Soriano, B. Mora, C. Redondo, X. Batlle, and I. K. Schuller. Exchange-bias phenomenon: The role of the ferromagnetic spin structure. *Phys. Rev. Lett.*, **114**:097202, (2015).

[196] A. Moser, D. T. Margulies K. Takano, M. Albrecht, Y. Sonobe, Y. Ikeda, S. Sun, and E. E. Fullerton. Magnetic recording: Advancing into the future. *J. Phys. D: Appl. Phys.*, **35**:R157–R167, (2002).

[197] K. Munbodh, F. A. Perez, C. Keenan, D. Lederman, M. Zhernenkov, and M. R. Fitzsimmons. Effects of hydrogen/deuterium absorption on the magnetic properties of Co/Pd multilayers. *Phys. Rev. B*, **83**:094432, (2011).

[198] K. Munbodh, F. A. Perez, and D. Lederman. Changes in magnetic properties of Co/Pd multilayers induced by hydrogen absorption. *J. Appl. Phys.*, **111**:123919, (2012).

[199] A. E. Munter. *Deuterium phase behaviour in thin film Pd.* PhD thesis, University of Illinois at Urbana-Champaign, (1999).

[200] A. E. Munter and B. J. Heuser. Deuterium phase behaviour in thin-film Pd. *Phys. Rev. B*, **58**:678–684, (1998).

[201] A. K. Nayak, M. Nicklas, S. Chadov, P. Khuntia, C. Shekhar, A. Kalache, M. Baenitz, Y. Skourski, V. K. Guduru, A. Puri, U. Zeitler, J. M. D Coey,

and C. Felser. Design of compensated ferrimagnetic Heusler alloys for giant tunable exchange bias. *Nat. Mater.*, **14**:679–684, (2015).

[202] L. Néel. Superficial magnetic anisotropy and orientation substructures. *J. Phys. Radium*, **15**:225–239, (1954).

[203] A. Nelson. Co-refinement of multiple-contrast neutron/X-ray reflectivity data using MOTOFIT. *J. Appl. Cryst.*, **39**:273–276, (2006).

[204] A. Nelson. MOTOFIT - Integrating neutron reflectometry acquisition, reduction and analysis into one, easy to use, package. *J. Phys. Conf. Ser.*, **251**:012094, (2010).

[205] Q. Niu, D. J. Thouless, and Y.-S. Wu. Quantized Hall conductance as a topological invariant. *Phys. Rev. B*, **31**:3372–3377, (1985).

[206] J. Nogués, D. Lederman, T. J. Moran, I. K. Schuller, and K. V. Rao. Large exchange bias and its connection to interface structure in FeF_2-Fe bilayers. *Appl. Phys. Lett.*, **68**:3186–3188, (1996).

[207] J. Nogués, J. Sort, V. Langlais, V. Skumryev, S. Suriñach, J. S. Muñoz, and M.D. Baró. Exchange bias in nanostructures. *Phys. Rep.*, **422**:65–117, (2005).

[208] J. K. Nørskov. Covalent effects in the effective-medium theory of chemical binding: Hydrogen heats of solution in the 3*d* metals. *Phys. Rev. B*, **26**:2875–2885, (1982).

[209] U. Nowak, K. D. Usadel, J. Keller, P. Miltényi, B. Beschoten, and G. Güntherodt. Domain state model for exchange bias. I. Theory. *Phys. Rev. B*, **66**:014430, (2002).

[210] K. O'Grady, L. E. Fernandez-Outon, and G. Vallejo Fernandez. A new paradigm for exchange bias in polycrystalline thin films. *J. Magn. Magn. Mater.*, **322**:883–899, (2010).

[211] J. Okabayashi, Y. Miura, and H. Munekata. Anatomy of interfacial spin-orbit coupling in Co/Pd multilayers using X-ray magnetic circular dichroism and first-principles calculations. *Sci. Rep.*, **8**:8303, (2018).

[212] S. Okamoto, O. Kitakami, and Y. Shimada. Enhancement of magnetic anisotropy of hydrogenated Pd/Co/Pd trilayers. *J. Magn. Magn. Mater.*, **239**:313–315, (2002).

[213] D. Oshima, E. Suharyadi, T. Kato, and S. Iwata. Observation of ferr-nonmagnetic boundary in $CrPt_3$ line-and-space patterned media using a dark-field transmission electron microscope. *J. Magn. Magn. Mater*, **324**:1617–1621, (2012).

[214] D. Oshima, M. Tanimoto, T. Kato, Y. Fujiwara, T. Nakamura, Y. Kotani, S. Tsunashima, and A. Iwata. Modifications to the structure and magnetic properties of $L1_0$ MnAl and MnGa films by Kr^+ ion irradiation. *IEEE Trans. Magn.*, **50**:3203407, (2014).

[215] A. Othonos, K. Kalli, and D. P. Tsai. Optically thin palladium films on silicon-based substrates and nanostructure formation. *Appl. Surf. Sci.*, **161**:54–60, (2000).

[216] F. Ott. SIMULREFLEC (2002). Software and description available form http://www-llb.cea.fr/prism/programs/simulreflec/simulreflec.html.

[217] S. Oyarzún, A. Tamion, F. Tournus, V. Dupuis, and M. Hillenkamp. Size effects

in the magnetic anisotropy of embedded cobalt nanoparticles: From shape to surface. *Sci. Rep.*, **5**:14749, (2015).

[218] D. Palaith, C. W. Kimball, R. S. Preston, and J. Crangle. Magnetic behaviour of the Pt+Fe system near Pt_3Fe. *Phys. Rev.*, **178**:795, (1969).

[219] G. K. Pálsson, A. Bliersbach, M. Wolff, A. Zamani, and B. Hjörvarsson. Using light transmission to watch hydrogen diffuse. *Nat. Commun.*, **3**:892, (2012).

[220] D. A. Papaconstantopoulos, B. M. Klein, E. N. Economou, and L. L. Boyer. Band structure and superconductivity of PdD_x and PdH_x. *Phys. Rev. B*, **17**:141–150, (1978).

[221] L. G. Parratt. Surface studies of solids by total reflection of X-rays. *Phys. Rev.*, **95**:359–369, (1954).

[222] Z. Pastuovic, D. Button, D. Cohen, D. Fink, D. Garton, M. Hotchkis, M. Ionescu, S. Long, V. Levchenko, M. Mann, R. Siegele, A. Smith, and K. Wilcken. SIRIUS – a new 6MV accelerator system for IBA and AMS at ANSTO. *Nucl. Instrum. Methods Phys. Res. B*, **371**:142–147, (2016).

[223] O. P. Pavlova, T. I. Verbitska, I. A. Vladymyrskyi, S. I. Sidorenko, G. L. Katona, D. L. Beke, G. Beddies, M. Albrecht, and I. M. Makogon. Structural and magnetic properties of annealed FePt/Ag/FePt thin films. *Appl. Surf. Sci.*, **266**:100–104, (2013).

[224] H. Peisl. *Hydrogen in Metals I.* Topics in Applied Physics. Springer-Verlag, (1978).

[225] J. Penfold and R. K. Thomas. The application of the specular reflection of neutrons to the study of surfaces and interfaces. *J. Phys. Condens. Matter*, **2**:1369, (1990).

[226] T. Qu, S. C. Pandey, G. S. Sandhu, and R. H. Victora. Theoretical study of magnetic damping and anisotropy of Fe/Pd (001) superlattice. *IEEE Trans. Magn.*, **52**:1–5, (2016).

[227] F. Radu and H. Zabel. *Exchange bias effect of ferro/antiferromagnetic heterostructures*. Magnetic Nanostructures. Springer, (2008).

[228] J. G. Ramirez, T. Saerbeck, S. Wang, J. Trastoy, M. Malnou, J. Lesueur, J.-P. Crocombette, J. E. Villegas, and I. K. Schuller. Effect of disorder on the metal-insulator transition of vanadium oxides: Local versus global effects. *Phys. Rev. B*, **91**:205123, (2015).

[229] Range and stopping powers of ions in various materials. Tables of physical and chemical constants. Kaye and Laby Online. Version 1.0, (2005). Available from http://www.kayelaby.npl.co.uk.

[230] M. Ratner and D. Ratner. *Nanotechnology*. A Gentle Reminder to the Next Big Idea. Pearson Education, (2002).

[231] D. Ravelosona, C. Chappert, V. Mathet, and H. Bernas. Chemical order induced by ion irradiation in FePt (001) films. *Appl. Phys. Lett.*, 76 :236–238, (2000).

[232] C. Rehm, H. Fritzsche, H. Maletta, and F. Klose. Hydrogen concentration and its relation to interplanar spacing and layer thickness of 1000-å Nb(110) films during in situ hydrogen charging experiments. *Phys. Rev. B*, **59**:3142–3152, (1999).

[233] C. Rehm, H. Maletta, M. Fieber-Erdmann, E. Holub-Krappe, and F. Klose. Anomalous layer expansion in thin niobium films during hydrogen absorption. *Phys. Rev. B*, **65**:113404, (2002).

[234] F. Roder, G. Hlawacek, S. Wintz, R. Hubner, L. Bischoff, H. Lichte, K. Potzger, J. Lindner, J. Fassbender, and R. Bali. Direct depth- and lateral- imaging of nanoscale magnets generated by ion impact. *Sci. Rep.*, **5**:16786, (2015).

[235] J.-C. Rojas-Sánchez, N. Reyren, P. Laczkowski, W. Savero, J.-P. Attané, C. Deranlot, M. Jamet, J.-M. George, L. Vila, and H. Jaffrés. Spin pumping and inverse spin Hall effect in platinum: The essential role of spin-memory loss at metallic interfaces. *Phys. Rev. Lett.*, **112**:106602, (2014).

[236] R. M. Rowan-Robinson, A. A. Stashkevich, Y. Roussigné, M. Belmeguenai, S.-M. Chérif, A. Thiaville, T. P. A. Hase, A. T. Hindmarch, and D. Atkinson. The interfacial nature of proximity-induced magnetism and the dzyaloshinskii-moriya interaction at the Pt/Co interface. *Sci. Rep.*, **7**:16835, (2017).

[237] S. Roy, H. L. Meyerheim, A. Ernst, K. Mohseni, C. Tusche, M. G. Vergniory, T. V. Menshchikova, M. M. Otrokov, A. G. Ryabishchenkova, Z. S. Aliev, M. B. Babanly, K. A. Kokh, O. E. Tereshchenko, E. V. Chulkov, J. Schneider, and J. Kirschner. Tuning the Dirac point position in $Bi_2Se_3(0001)$ via surface carbon doping. *Phys. Rev. Lett.*, **113**:116802, (2014).

[238] U. Rüdiger, J. Yu, L. Thomas, S. S. P. Parkin, and A. D. Kent. Magnetoresistance, micromagnetism, and domain-wall scattering in epitaxial hcp Co films. *Phys. Rev. B*, **59**:11914–11918, (1999).

[239] P. Ruiz-Diaz, T. R. Dasa, and V. S. Stepanyuk. Tuning magnetic anisotropy in metallic multilayers by surface charging: An ab initio study. *Phys. Rev. Lett.*, **71**:267203, (2013).

[240] T. Saerbeck. Magnetic exchange phenomena probed by neutron scattering. *Solid State Phys.*, **65**:237–352, (2014).

[241] T. Saerbeck and F. Klose. Neutron scattering and its application to investigate magnetic thin film structures. *Mater. Today*, **12**:70–77, (2009).

[242] T. Saerbeck, F. Klose, A. P. Le Brun, J. Füzi, A. Brule, A. Nelson, S. A. Holt, and M. James. Invited article: Polarization "down under": The polarized time-of-flight neutron reflectometer PLATYPUS. *Rev. Sci. Instrum.*, **83**:081301, (2012).

[243] T. Saerbeck, F. Klose, D. Lott, G. J. Mankey, Z. Lu, P. R. LeClair, W. Schmidt, A. P. J. Stampfl, S. Danilkin, M. Yethiraj, and A. Schreyer. Artificially modulated chemical order in thin films: A different approach to create ferro/antiferromagnetic interfaces. *Phys. Rev. B*, **82**:134409, (2010).

[244] T. Saerbeck, H. Zhu, D. Lott, H. Lee, P. R. LeClair, G. J. Mankey, A. P. J. Stampfl, and F. Klose. Tailoring exchange bias through chemical order in epitaxial $FePt_3$ films. *J. Appl. Phys.*, **114**:013901, (2013).

[245] Y. Sakamoto, K. Takai, I. Takashima, and M. Imada. Electrical resistance measurements as a function of composition of palladium - hydrogen(deuterium) systems by a gas phase method. *J. Phys. Condens. Matter*, **8**:3399, (1996).

[246] K. Sanghoon, L. Soogil, and H. Jongill. An array of ferromagnetic nanoislands nondestructively patterned via a local phase transformation by low-energy proton irradiation. *ACS Nano*, **8**:4698–4704, (2014).

[247] K. Saravanan, C.-H. Kao, Y.-C. Shao, Y.-F. Wang, B.-Y. Wang, H. T. Wang, C.-J. Tsai, W.-C. Lin, C.-W. Pao, H.-M. Tsai, L.-Y. Jang, H. J. Lin, J.-F. Lee, and W.-F. Pong. Magnetic anisotropic properties of Pd/Co/Pd trilayer films studied by X-ray absorption spectroscopy and magnetic circular dichroism. *RSC Adv.*, **5**:19014–19019, (2015).

[248] Sarveena, N. Shrivastava, M. Singh, and S. K. Sharma. *Multifunctional Magnetic Nanostructures: Exchange Bias Model and Applications.* Complex Magnetic Nanostructures: Synthesis, Assembly and Applications. Springer International Publishing, (2017).

[249] C. Scheuner, S. Jankuhn, J. Vogt, S. Pezzagna, C. Trautmann, and J. Meijer. Nanometer collimation of enhancement of ion beams using channelling effects in track-etched mica capillaries. *Sci. Rep.*, **7**:17081, (2017).

[250] A. Schreyer, C. F. Majkrzak, N. F. Berk, H. Grüll, and C. C. Han. Using polarized neutrons to determine the phase of reflection from thin film structures. *J. Phys. Chem. Solids*, **60**:1045–1051, (1999).

[251] I. K. Schuller, R. Morales, X. Batlle, U. Nowak, and G. Güntherodt. Role of the antiferromagnetic bulk spins in exchange bias. *J. Magn. Magn. Mater.*, **416**:2–9, (2016).

[252] V. F. Sears and S. A. Shelley. Debye-Waller factor for elemental crystals. *Acta Cryst.*, **47**:441–446, (1991).

[253] P. A. Sharma, A. L. Lima Sharma, M. Hekmaty, K. Hattar, V. Stavila, R. Goeke, K. Erickson, D. L. Medlin, M. Brahlek, N. Koirala, and S. Oh. Ion beam modification of topological insulator bismuth selenide. *Appl. Phys. Lett.*, **105**:242106, (2014).

[254] J. M. Shaw, H. T. Nembach, and T. J. Silva. Determination of spin pumping as a source of linewidth in sputtered $Co_{90}Fe_{10}$/Pd multilayers by use of broadband ferromagnetic resonance spectroscopy. *Phys. Rev. B*, **85**:054412, (2012).

[255] J. M. Shaw, H. T. Nembach, T. J. Silva, and C. T. Boone. Precise determina-

tion of the spectroscopic g-factor by use of broadband ferromagnetic resonance spectroscopy. *J. Appl. Phys.*, **114**:243906, (2013).

[256] S. Singh, S. Jain, V. PS, A. K. Tiwari, M. R. Nouni, J. K. Pandey, and S. Goel. Hydrogen: A sustainable fuel for future of the transport sector. *Renew. Sust. Energ. Rev.*, **51**:623–633, (2015).

[257] D. S. Sivia. *Elementary Scattering Theory.* Oxford University Press Inc., 1st edition, (2011).

[258] T. Skośkiewicz and B. Baranowski. Investigation of the electrical resistance anomaly in the palladium-hydrogen system. *Phys. Status Solidi B*, **30**, (1968).

[259] V. Skumryev, S. Stoyanov, Y. Zhang, G. Hadjipanayis, D. Givord, and J. Nogués. Beating the superparamagnetic limit with exchange bias. *Nature*, **423**:850–853, (2003).

[260] F. Hernández Sobrino, C. Rodríguez Monroy, and J. L. Hernández Pérez. Critical analysis on hydrogen as an alternative to fossil fuels and biofuels for vehicles in Europe. *Renew. Sust. Energ. Rev.*, **14**:772–780, (2010).

[261] J. Spray and U. Nowak. Exchange bias in ferromagnetic/antiferromagnetic bilayers with imperfect interfaces. *J. Phys. D: Appl. Phys.*, **39**:4536, (2006).

[262] G. L. Squires. *Introduction to the theory of thermal neutron scattering.* Cambridge University Press, 4th edition, (1978).

[263] P. A. Stadelmann. EMS - a software package for electron diffraction analysis and HREM image simulation in materials science. *Ultramicroscopy*, **21**:131–145, (1987).

[264] R. L. Stamps. Mechanisms for exchange bias. *J. Phys. D: Appl. Phys.*, **33**:R247, (2000).

[265] M. Sternik, S. Couet, J. Łażewski, P. T. Jochym, K. Parlinski, A. Vantomme, K. Temst, and P. Piekarz. Dynamical properties of ordered Fe–Pt alloys. *J. Alloy. Compd.*, **651**:528–536, (2015).

[266] E. Suharyadi, T. Kato, S. Tsunashima, and S. Iwata. Magnetic properties of patterned Co/Pd nanostructures by e-beam lithography and Ga ion irradiation. *IEEE Trans. Magn.*, **42**:2972–2974, (2006).

[267] E. Suharyadi, S. Natsume, T. Kato, S. Tsunashima, and S. Iwata. Microstructures and magnetic properties of the FIB irradiated Co-Pd multilayer films. *IEEE Trans. Magn.*, **41**:3595–3597, (2005).

[268] E. Suharyadi, D. Oshima, T. Kato, and S. Iwata. Nanoscale patterning of $CrPt_3$ magnetic thin films by using ion beam irradiation. *Results in Physics*, **6**:186–188, (2016).

[269] S. Takahashi and K. Ikeda. Magnetic interaction in plastically deformed $FePt_3$ alloy. *Phys. Lett. A*, **95**:247–248, (1983).

[270] B. Terris and T. Thomson. Nanofabricated and self-assembled magnetic structures as data storage media. *J. Phys. D: Appl. Phys.*, **38**:R199, (2005).

[271] B. D. Terris. Fabrication challenges for patterned recording media. *J. Magn. Magn. Mater.*, **321**:512–517, (2009).

[272] B. D. Terris, L. Folks, D. Weller, J. E. E. Baglin, A. J. Kellock, H. Rothuizen, and P. Vettiger. Ion-beam patterning of magnetic films using stencil masks. *Appl. Phys. Lett.*, **75**:403–405, (1999).

[273] G. Thesena and O. Langhelle. Awareness, acceptability and attitudes towards hydrogen vehicles and filling stations: A greater stravanger case study and comparisons with London. *Int. J. Hydrogen Energ.*, **33**:5859–5867, (2008).

[274] T. Thomson. *Magnetic properties of metallic thin films*. Metallic films for electronic, optical and magnetic applications. Woodhead Publishing, (2014).

[275] J. Thorsen. *The penetration of atomic particles through matter*. The penetration of charged particles through matter. Addison Wesley, (1987).

[276] T. Tohyama, Y. Ohta, and M. Shimizu. Tight-binding calculations of the electronic structure and magnetic properties in ordered TPt_3 (T=Ti, V, Cr, Mn, Fe and Co) alloys. *J. Phys.: Condens. Matter*, **1**:1789, (1989).

[277] F. Torres, R. Morales, I. K. Schuller, and M. Kiwi. Dipole-induced exchange bias. *Nanoscale*, **9**:17074–17079, (2017).

[278] M. Urbaniak, F. Stobiecki, D. Engel, B. Szymański, and A. Ehresmann. Selective modification of magnetic properties of Co_1/Au/Co_2/Au multilayers by He ion bombardment. *Acta Pys. Pol. A*, **115**:326–328, (2009).

[279] M. Urbaniak, F. Stobiecki, A. Gaul, and A. Ehresmann. Magnetization reversal of Co/Au multilayer stripes with keV-He^+ ion bombardment induced coercivity gradient. *J. Phys. D: Appl. Phys.*, **48**:335003, (2015).

[280] D. A. van Leeuwen, J. M. van Ruitenbeek, G. Schmid, and L. J. de Jongh. Size-dependent stoner factor in Pd and Pt clusters. *Physica B*, **194-196**:263–264, (1994).

[281] C. A. F. Vaz, J. A. C. Bland, and G. Lauhoff. Magnetism in ultrathin film structures. *Rep. Prog. Phys.*, **71**:056501, (2008).

[282] L. G. Vivas, J. Rubín, A. I. Figueroa, F. Bartolomé, L. M. García, C. Deranlot, F. Petroff, L. Ruiz, J. M. González-Calbet, S. Pascarelli, N. B. Brookes, F. Wilhelm, M. Chorro, A. Rogalev, and J. Bartolomé. Perpendicular magnetic anisotropy in granular multilayers of CoPd alloyed nanoparticles. *Phys. Rev. B*, **93**:174410, (2016).

[283] K. von Rottkay, M. Rubin, and P. A. Duine. Refractive index changes of Pd-coated magnesium lanthanide switchable mirrors upon hydrogen insertion. *J. Appl. Phys.*, **85**:408–413, (1999).

[284] E. C. Walter, F. Favier, and R. M. Penner. Palladium mesowire arrays for fast hydrogen sensors and hydrogen-actuated switches. *Anal. Chem.*, **74**:1546–1553, (2002).

[285] D. Wang, K.-Y. Lee, S. Luo, and T. B. Flanagan. The thermodynamics of hydrogen absorption/desorption by Pd–Co alloys. *J. Alloy. Compd.*, **252**:209–218, (1997).

[286] B. E. Warren. *X-ray Diffraction*. Dover Publications, (1990).

[287] X. Wei, R. Skomski, B. Balamurugan, Z. G. Sun, S. Ducharme, and D. J. Sellmyer. Magnetism of TiO_2 nanoclusters. *J. Appl. Phys.*, **105**:07C517, (2009).

[288] D. Weller, J. E. E. Baglin, A. J. Kellock, K. A. Hannibal, M. F. Toney, G. Kusinski, S. Lang, L. Folks, M. E. Best, and B. D. Terris. Ion induced magnetization reorientation in Co/Pt multilayers for patterned media. *J. Appl. Phys.*, **87**:5768–5770, (2000).

[289] D. Weller and A. Moser. Thermal effect limits in ultrahigh-density magnetic recording. *IEEE Trans. Magn.*, **35**:4423–4439, (1999).

[290] D. B. Williams and C. B. Carter. *The transmission electron microscope.* Transmission Electron Microscopy. Springer, (1996).

[291] E. O. Wollan and W. C. Koehler. Neutron diffraction study of the magnetic properties of the series of perovskite-type compounds $[(1-x)\mathrm{La}, x\mathrm{Ca}]\mathrm{MnO}_3$. *Phys. Rev.*, **100**:545–563, (1955).

[292] M. H. Wood, R. J. L. Welbourn, A. Zarbakhsh, P. Gutfreund, and S. M. Clarke. Polarized neutron reflectometry of nickel corrosion inhibitors. *Langmuir*, **31**:7062–7072, (2015).

[293] F. Y. Yang and C. L. Chien. Oscillatory exchange bias due to an antiferromagnet with incommensurate spin-density waves. *Phys. Rev. Lett.*, **90**:147201, (2003).

[294] J. K. W. Yang, Y. Chen, T. Huang, H. Duan, N. Thiyagarajah, H. K. Hui, S. H. Leong, and V. Ng. Fabrication and characterization of bit-patterned media beyond 1.5 Tbit/in^2. *Nanotechnology*, **22**:385301, (2011).

[295] T. Yoshida and K. Kojima. Toyota MIRAI fuel cell vehicle and progress toward a future hydrogen society. *Electrochem. Soc. Interface*, **24**:45–49, (2015).

[296] C. N. T. Yu, A. J. Vick, N. Inami, K. Ono, W. Frost, and A. Hirohata. Exchange bias induced at a $\mathrm{Co_2FeAl_{0.5}Si_{0.5}}$/Cr interface. *J. Phys. D: Appl. Phys.*, **50**:125004, (2017).

[297] F. T. Yuan, J. K. Lin, Y. D. Yao, and S. F. Lee. Exchange bias in spin glass (FeAu)/NiFe thin films. *Appl. Phys. Lett.*, **96**:162502, (2010).

[298] H. Zabel. *X-ray and neutron scattering at thin films.* Festkörperprobleme 30: Plenary Lectures of the Divisions Semiconductor Physics Thin Films Dynamics and Statistical Physics Magnetism Metal Physics Surface Physics Low Temperature

Physics Molecular Physics of the German Physical Society (DPG), Regensburg. Springer, (1990).

[299] L. Zhang, Y. K. Takahashi, A. Perumal, and K. Hono. $L1_0$-ordered high coercivity (FePt)Ag–C granular thin films for perpendicular recording. *J. Magn. Magn. Mater.*, **322**:2658–2664, (2010).

[300] T. Zhu. *Modern techniques for characterizing magnetic materials*. Kluwer Academic Publishers, (2005).

[301] J. F. Ziegler, J. P. Biersack, and M. D. Ziegler. *SRIM - The stopping and range of ions in matter*. Introduction to Focused Ion Beams: Instrumentation, Theory, Techniques and Practice. Lulu Press, 15th edition, (1990).

[302] J. F. Ziegler, U. Littmark, and J. P. Biersack. *The stopping and range of ions in solids*. Pergamon New York, (1985).

[303] J. F. Ziegler, M. D. Ziegler, and J. P. Biersack. SRIM - the stopping and range of ions in matter (2010). *Nucl. Instrum. Methods Phys. Res. B*, **268**:1818–1823, (2010).

[304] I. Zorić, E. M. Larsson, B. Kasemo, and C. Langhammer. Localized surface plasmons shed light on nanoscale metal hydrides. *Adv. Mater.*, **22**:4628–4633, (2010).